



The University of
Nottingham

UNITED KINGDOM • CHINA • MALAYSIA

Extended Equivalent Dipole Model for Radiated Emissions

Chijioke S Obiekezie, MSc

Thesis submitted to the University of Nottingham
for the degree of Doctor of Philosophy

March, 2014

Abstract

This work is on the characterisation of radiated fields from electronic devices. An equivalent dipole approach is used. Previous work showed that this was an effective approach for single layer printed circuit boards where an infinite ground plane can be assumed. In this work, this approach is extended for the characterisation of more complex circuit boards or electronic systems.

For complex electronic radiators with finite ground planes, the main challenge is characterising field diffracting around the edges and boundaries. It is shown that this can be satisfactorily characterised using passive dipoles located along the edge. It is also shown that the number of dipoles used to characterise a device can be further optimised by using a complex location for the dipoles. Novel optimisation approaches such as particle swarm optimisation were also investigated.

It is concluded that characterisation of complex electronic devices can be achieved in 3D space using edge dipoles to represent diffraction effects and available optimisation strategies.

List of Publications

1. C. Obiekezie, D. W. P Thomas, A. Nothofer, S. Greedy and P. Sewell, "Electromagnetic Characterization of 3D Radiators, " presented at EuroEM Conf., Toulouse, France, July 2012.
2. C. Obiekezie, D. W. P Thomas, A. Nothofer, S. Greedy, P. Sewell and C. Christopoulos, "Prediction of Emission from a Source placed inside a Metallic Enclosure over a Finite Ground Plane , " EMC Euro Conf., Rome, Italy, September 2012.
3. C. Obiekezie, D. W. P Thomas, A. Nothofer, S. Greedy, Luk. R Arnaut and P. Sewell, " A Simplified Analytical Solution for Characterizing Edge Currents Along a Finite Ground Plane," ACES Conf., Monterey, CA, March 2013.
4. C. Obiekezie, D. W. P Thomas, A. Nothofer, S. Greedy, Luk. R Arnaut and P. Sewell, "Modeling of Electromagnetic Emissions from a Multilayer PCB," IEEE EMC Int. Symp. on Electromagn. Compat., Denver, Colorado, August 2013.
5. C. Obiekezie, D. W. P Thomas, A. Nothofer, S. Greedy, Luk. R Arnaut and P. Sewell, "A Technique for Analyzing EMC Shielding Effectiveness Based on Near-Field Measurement and Equivalent Dipole Modeling," EMC Euro. Conf., Brugge, Belgium, Sept. 2013.
6. C. Obiekezie, D. W. P Thomas, A. Nothofer, S. Greedy, Luk. R Arnaut and P. Sewell, "Optimization of a Simple Equivalent Dipole Model to include Edge Effects," Int. Conf. of Electromagn. in Adv. Applications, Torino, Italy, Sept. 2013.
7. C. Obiekezie, D. W. P. Thomas, A. Nothofer, S. Greedy, L. R. Arnaut, P.Sewell, "Extended Scheme using Equivalent Dipoles for Characterizing Edge Currents Along a Finite Ground Plane ", *Jour., Applied Comp.*

- Electromagn. Soc.*, vol. 28, nos. 11, pp. 1111-1121, Nov. 2013.
8. C. Obiekezie, D. W. P Thomas, A. Nothofer, S. Greedy, Luk. R Arnaut and P. Sewell, " Accurate Prediction of Magnetic Fields at Higher Planes using Near-Field Measurement," presented at URSI UK workshop, Birmingham, Sept. 2013.
 9. C. Obiekezie, D. W. P Thomas, A. Nothofer, S. Greedy, Luk. R Arnaut and P. Sewell, " Complex Locations of Equivalent Dipoles for Improved Characterization of Radiated Emissions," *IEEE Trans. on Electromag. Comp.*, vol. PP-99, nos. 1-8, 2014.
 10. D. W. P Thomas, C. Obiekezie, A. Nothofer, S. Greedy and P. Sewell, "Characterization of Noisy Electromagnetic Fields from Circuits using the Correlation of Equivalent Sources, " EMC Euro Conf., Rome, Italy, September 2012.
 11. L. R. Arnaut and C. S. Obiekezie, "Identification of UWB Emissions from Printed Circuit Boards Using Principal Component Analysis", EMC Euro Conf., Brugge, Belgium, Sept. 2013.
 12. L. R. Arnaut and C. S. Obiekezie, "UWB radiation modes of printed circuit boards based on principal component analysis," Proc. ICEAA Int. Conf. Electromagn. Adv. Applications, Torino, Italy, Sep. 2013.
 13. L. R. Arnaut and C. S. Obiekezie, "Stochastic analysis of wideband near-field emissions from integrated antennas and circuits", *IEEE Trans. on Electromag. Comp.*, vol. 56, nos. 1, pp. 93-101, 2014.
 14. L. R. Arnaut, C. S. Obiekezie and D. W. P Thomas, "Empirical Emission Eigenmodes of Printed Circuit Boards", *IEEE Trans. on Electromag. Comp.*, vol. 99, pp. 1-11, 2013.

15. D. W. P Thomas, C. Obiekezie, S. Greedy, L. Arnaut, P. Sewell and A. Nothofer, "Analysis of Radiated Fields from PCBs in the Time Domain," submitted to Radio 2014, Mauritius.
16. L. R. Arnaut, C. S. Obiekezie and D. W. P Thomas, " Source separation for wideband Energy Emissions using Complex Independent Component Analysis," *IEEE Trans. on Electromag. Comp.*, vol. PP, nos. 99, pp 1-12, 2014.
17. D. W. P Thomas, C. Obiekezie, A. Nothofer, S. Greedy, L. Arnaut and P. Sewell, "Near-field Characterization of electromagnetic Interference from Multilayered printed circuit boards," Microwave conf. Europe (EuMC), pp.1127-1130, 2013.
18. Arnaut L R, Thomas, D W P and Obiekezie, C S, Complex principal and independent component analyses of radiated emissions for the time-frequency domain, Proc. 2014 EMC Europe – Int. Conf. Electromagnetic Compatibility, Göteborg, Sweden, 1-4 Sep 2014, submitted for presentation.
19. Arnaut L R and Obiekezie C S, Comparison of complex principal and independent component analyses for radiated emissions from printed circuit boards, URSI XXXIst General Assembly and Scientific Symposium, 17-23 Aug 2014, Beijing, China, invited paper.
20. Arnaut L R and Obiekezie C S, Principal and independent components of time-domain wideband radiated emissions, Proc. 1st IEEE Numerical Electromagnetics and Optimization Conference, 14-16 May 2014, Pavia, Italy, invited paper.

Acknowledgements

I remain grateful to God for the grace that saw me through these academic work-packed years.

I wish to appreciate my supervisors Prof. Dave Thomas, Dr. Angela Nothofer and Dr. Luk Arnaut, under whose guidance and support the works presented in this thesis were carried out. And I also extend my appreciation to Dr. Steve Greedy, Prof. Phil Sewell and Prof. Christos Christopoulos for their availability at our meetings and their immense contributions to this work.

I thank the University of Nottingham for offering me the EPSRC studentship and the prestigious Tower Innovation Scholarship, through which my doctorate with the George Green Institute for Electromagnetic Research (GGIEMR) was funded. I am also grateful to other members of staff and researchers in GGIEMR for their friendship and support.

My parents in Nigeria, Mr Fredrick and Mrs Njideka Obiekezie, my siblings Nkem, Obinna, Nneka and Ogoo, Mr JNJ Madueke and other friends and relatives, I thank you all for your love and care, which kept reminding me of my other life apart from research.

And finally to my love Adaora, I say a very big thank you for your support during the tedious correction period.

Contents

ABSTRACT	I
LIST OF PUBLICATIONS	II
ACKNOWLEDGEMENTS	V
CONTENTS	VI
ACRONYMS	X

CHAPTER 1

INTRODUCTION	1
1.1 BACKGROUND	1
1.2 EMC DIRECTIVE	3
1.3 EM BEHAVIOUR OF CIRCUIT COMPONENTS AND PCBs	6
1.4 MEASUREMENT METHODS FOR PCB EMISSIONS	8
1.4.1 Open Area Test Site	9
1.4.2 Anechoic chamber	10
1.4.3 Compact antenna test range	11
1.4.4 TEM cell	12
1.4.5 Reverberation chamber	14
1.4.6 Near field measurement	16
1.4.7 Comparative summary of EM measurement techniques.....	17
1.5 MODELLING TECHNIQUES FOR PCB EMISSIONS	18
1.6 EQUIVALENT DIPOLE MODELLING	22
1.7 CURRENT WORK	23
1.8 CONCLUSION	24
1.7 THESIS OUTLINE.....	25
References.....	26

CHAPTER 2

THEORY OF MEASUREMENT AND MODELLING FOR EQUIVALENT DIPOLE MODELLING	
2.1 INTRODUCTION	39
2.2 RADIATION CHARACTERISTICS OF PCB.....	40

2.2.1 Near field region.....	41
2.2.2 Far field region.....	42
2.2.3 Approximate EM field representation	42
2.3 NEAR FIELD SCANNING	43
2.4 BASIC PRINCIPLE OF EQUIVALENT DIPOLE MODELLING	46
2.4.1 Source equivalence principle	46
2.4.2 Dipole expansion	49
2.4.3 Solution to inverse problem	51
2.5 CONCLUSION.....	52
References.....	52
CHAPTER 3	
NEAR FIELD MEASUREMENT	55
3.1 INTRODUCTION	55
3.2 NEAR FIELD MEASUREMENT APPLICATION.....	56
3.3 NEAR FIELD MEASUREMENT TEST BENCH.....	58
3.4 MOTION CONTROL	62
3.4.1 PC based control.....	63
3.5 DATA ACQUISITION.....	64
3.5.1 Measurement using vector network analyzer	65
3.5.2 Measurement using spectrum analyzer	68
3.6 NEAR FIELD MEASUREMENT PROBE	69
3.6.1 Electric field probe	70
3.6.2 Magnetic field probe	71
3.7 ERROR ANALYSIS AND PROBE CORRECTION.....	74
3.7.1 Error Analysis.....	75
3.7.2 Near field probe correction	76
3.8 NEAR FIELD MEASUREMENT VALIDATION WITH SIMULATION.....	87
3.9 CONCLUSION	88
References.....	90
CHAPTER 4	
EQUIVALENT DIPOLE MODELLING APPLICATIONS AND LIMITATIONS. 95	
4.1 INTRODUCTION	95
4.2 EQUIVALENT DIPOLE MODELLING IN FREE SPACE	96

4.3 GROUND PLANE APPROXIMATION.....	99
4.4 INFINITE GROUND PLANE APPROXIMATION	99
4.4.1 Image theory	100
4.4.2 Radiating loop over a large ground plane	101
4.4.3 3D radiator over an infinite ground plane	104
4.5 SOURCES OF ERROR IN EQUIVALENT DIPOLE MODELLING.....	108
4.5.1 Deviation in modelling height	108
4.5.2 Sampling resolution	110
4.5.3 Sampling plane	113
4.5.4 Dipole spatial resolution	114
4.6 FINITE GROUND PLANE APPROXIMATION	117
4.6.1 Diffraction effects	119
4.6.2 Diffraction relative to source position.....	123
4.6.3 Solutions to diffraction	126
4.7 Conclusion.....	137
References.....	138

CHAPTER 5

EXTENDED EQUIVALENT DIPOLE MODELLING.....	141
5.1 INTRODUCTION	141
5.2 PASSIVE DIPOLES	142
5.3 EEDM VALIDATION	149
5.3.1 Single layer PCB	149
5.3.2 Multilayer PCB.....	157
5.3.3 A conducting enclosure with aperture	166
5.4 CONCLUSION	171
References.....	171

CHAPTER 6

TECHNIQUES FOR IMPROVING THE PERFORMANCE OF EQUIVALENT DIPOLE MODELLING	173
6.1 INTRODUCTION	173
6.2 COMPLEX SOURCE POINT	174

6.3 CSP VALIDATION	176
6.3.1 <i>Developing Equivalent dipole model</i>	176
6.3.2 <i>CSP example: Experimental Validation</i>	181
6.4 PARTICLE SWARM OPTIMISATION	182
6.5 FEATURE SELECTIVE VALIDATION	188
6.6 GA VS PSO	191
6.7 CONCLUSION	194
<i>References</i>	195
CHAPTER 7	
CONCLUSION AND FUTURE WORK	199
CONCLUSION	199
FUTURE WORK	202
<i>References</i>	203
APPENDIX A	
<i>System automation</i>	205
APPENDIX B	
<i>Equivalent dipole modelling accuracy dependence on</i>	
<i>Dipole resolution</i>	215
APPENDIX D	
<i>Infinitesimal radiation variation with distance</i>	216
APPENDIX E	
<i>Basic 1-D FSV formulation</i>	217

Acronyms

2-D	Two Dimensional
3-D	Three Dimensional
CATR	Compact Antenna Test Range
CEM	Computational Electromagnetics
DUT	Device Under Test
E Field	Electric field
EDM	Equivalent Dipole Modelling
EEDM	Extended Equivalent Dipole Modelling
EM	Electromagnetic
EMC	Electromagnetic Compatibility
EMI	Electromagnetic Interference
FDTD	Finite Difference Time Domain
FEM	Finite Element Method
FSV	Feature Selective Validation
GA	Genetic Algorithm
GGIEMR	George Green Institute of Electromagnetics
GO	Geometrical Optics
GPIB	General Purpose Interface Bus
GTD	Geometric Theory of Diffraction
GTEM	Gigahertz TEM cell
PCB	Printed Circuit Board
H field	Magnetic field
IC	Integrated Circuit
MoM	Method of Moment
MSE	Mean Square Error
NPL	National Physical Laboratory
OATS	Open Area Test Site
PEC	Perfect Electric Conductor
PEEC	Partial Element Equivalent Circuit
PO	Physical Optics
PSO	Particle Swarm Optimisation
PTD	Physical Theory of Diffraction
PUT	Probe under Test
RAM	Radiation Absorbent Material

List of Tables

RF	Radio Frequency
RMS	Root Mean Square
SA	Spectrum Analyzer
SCPI	Standard Command for Programmable Instrument
SVD	Singular Value Decomposition
TDR	Time Domain Reflectometer
TEM	Transverse Electromagnetic Mode
TLM	Transmission Line Matrix
UTD	Uniform Theory of Diffraction
VNA	Vector Network Analyser
VSWR	Voltage Standing Wave Ratio

Chapter 1

INTRODUCTION

1.1 Background

According to Christopoulos [1], "Electromagnetic Compatibility (EMC) is the branch of science and engineering concerned with the design and operation of equipment in a manner that makes them immune to certain amounts of electromagnetic interference (EMI), while at the same time keeping equipment-generated interference within specified limits".

The need to properly characterize the EM behaviour to ensure EMC compliance of electrical/electronic systems and devices continues to be of concern. New international EMC standards are constantly being developed, or existing standards revised, and new guidelines issued to keep pace with development in the electrical and electronic industry. These standards cover the various EMI propagation channels which include radiation, conduction, capacitive and inductive coupling [2].

Ideally EMC should be considered during the design process, however this can be difficult due to the complexity of modern systems and devices. Simulation tools are difficult to apply as the field interactions between devices and components are not easily modelled due to the range of feature sizes and complexities. Also, circuit detail is often unknown or limited due to commercial confidentiality reasons. An accurate model, results in a high computational cost (in terms of both time and memory) making it impractical and there are few

situations where simple analytical solutions can be applied. Often, an iterative process is applied where prototypes are tested and then adjusted as necessary to meet the required standards. To reduce development time, efficient and more accurate models of devices are required that not only predict the emissions but can faithfully represent their interaction in their EM environment.

The aim of the work presented in this thesis is to characterize the electromagnetic (EM) emissions from practical electronic devices. This approach offers a simplified way of predicting the EM characteristics of practical electronic devices without requiring complex far field measurement methods or computationally expensive numerical simulation techniques.

PCBs are the major source of unintentional electromagnetic interference in an electrical and electronic system. PCB design complexity continues to increase with the inclusion of high-density interconnects, embedded components, gigabit data rates and other technologies. This is driven by the ever increasing demand for mobile devices and the services integrated in them, consequently, making PCBs more effective radiators on a wider spectrum up to 3GHz. Previously in [3]-[5], it was demonstrated that the equivalent source approach can be used in characterising the EM properties of printed circuit boards (PCBs). This work had assumed an infinite ground plane and only used a top surface field scan in characterising the PCBs. In the approach, equivalent sources in the form of infinitesimal dipoles were used to represent the active current sources on the PCB. However, in a more practical case, the PCB ground plane is finite which gives rise to induced currents propagating along the edges of the PCB which are induced by the active current sources on the PCB through edge excitation [6].

These additional currents at the edge makes the approach presented in [3]-[5] insufficient in characterising the radiation effects of a practical PCB.

In addressing the limitations of previous works, an analytical solution that can fully characterize the EM properties of a practical PCB is developed in this work, which also offers ways of optimizing the equivalent sources. By so doing, the analytical solution extends the capability of the conventional equivalent source approach in characterizing a practical PCB by accounting for the finiteness of the ground plane. Furthermore, a modified 3D near field scanner was used to extract the field information from all sides of a PCB as required by the new model. The developed approach that can predict emissions from a practical PCB can then be used in the assessment of EMC compliance for household and other commercial electronics to the relevant EMC standards or directives in a far more efficient way.

In this chapter the requirements for EMC assessment of PCB is examined and the limitations of current approaches explained. The requirements and objectives of the presented work will then be defined.

1.2 EMC Directive

The European Commission EMC directive is a performance directive for ensuring that electrical equipment is compliant to both electromagnetic emission and immunity standards. Other nation states have similar legislation that enforces compliance to standards. The International Electrotechnical Commission (IEC), which also works closely with the International Standard Organisation (ISO), recommends international standards, which the national committees are

expected to work with [7]. Tasks are divided into technical committees (TC), whose remit is to address specific product sectors.

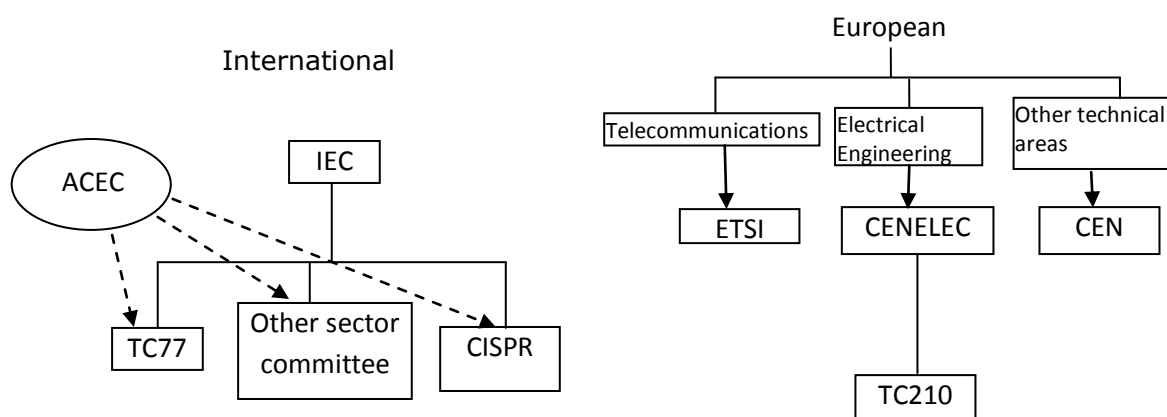


Fig. 1.1 EMC standards structure

As shown in Fig. 1.1, the TC77 (for EMC between equipment including networks) and the CISPR (International Special Committee on Radio Interference) are the two IEC technical committees devoted to EMC work. The various outputs of TC77 are provided in the IEC Publication 61000.

The ACEC (Advisory Committee on EMC), co-ordinates the IEC's work on EMC between various committees so as to prevent the development of conflicting standards. More on this can be found in the literature [7]-[9].

In Europe, CENELEC (the European Committee for Electrotechnical Standardization) has been mandated by the European Commission to develop EMC standards for use with the European EMC Directive. The European Telecommunications Standards Institute (ETSI) develops standards for telecommunications equipment. The TC210 is the committee charged with developing EMC related standards [10]-[11]. Also some harmonised EMC standards are published by the European Committee for Standardization (CEN), which is for non-electrotechnical subjects. The compilation of the product

standard including the requirements for the EMC emissions and immunity test are given in [9], [11]-[16].

As an example, the European emission requirement for Class B (for domestic use) information technology (IT) equipment stipulated by the EN 55022 [17] is shown in Fig. 1.2.

Following this directive, all Class B IT equipment is expected to have a maximum electric field emission as specified in the limits in Fig. 1.2 for the various applicable frequency bands in order to comply with the EN 55022 standard.

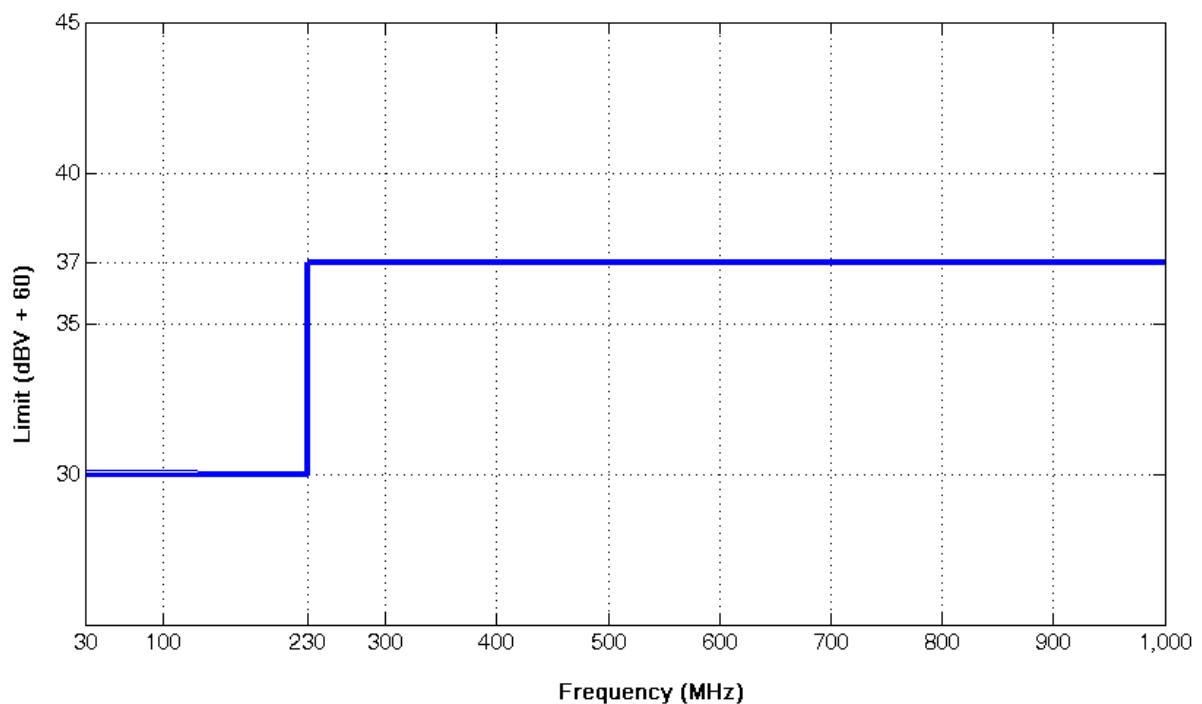


Fig. 1.2 Class B EN 55022 radiated electric field emission standard at 10m

To ensure that an electronic product is compliant with the relevant radiated emission standard, the emissions can either be measured or estimated. The latter being based on a good understanding of the EM characteristics of the current sources on the PCB (i.e. radiation characteristics of the PCB).

1.3 EM Behaviour of Circuit components and PCBs

A Radio Frequency (RF) device according to the Federal Communications Commission (FCC in the United States), is defined as any "device that in its operation is capable of intentionally or unintentionally emitting radio frequency energy by radiation, conduction or some other means" [1]. Depending on the frequency of operation, dimensions of the board and feature sizes PCBs may act as effective RF radiators.

The sources of EMI in an electronic device include the circuit components, PCBs, power and signal cables. However, PCBs have been shown to contribute most to the EMC issues encountered in electronic devices. Therefore, inclusion of EMC assessments in PCB designs will help reduce the EMI noise [18]-[21]. Most PCBs contain a number of active and passive electronic components, hosting billions of switching events per second. The complex design layout often adopted by the PCB designers to optimize available board space makes its assessment difficult from an electromagnetic field characterisation perspective [22]-[25]. The cabling that bring signals in and out of the PCB also constitute a valid source of EM noise, however this problem is often mitigated through cable screening and the use of filter circuits at the cable terminations.

The electromagnetic characteristics of most electronic components change as they are assembled to form an electronic device, because of the mutual coupling between them. The resulting electromagnetic characteristics of the device are therefore not easily deduced from the individual behaviour of the discrete electronic components. Therefore the inclusion of appropriate EMC tests at every stage of the product cycle (design, development, validation and production) will significantly reduce the unwanted EMI by identifying the interference sources

and then proffering appropriate mitigation measures. According to [26], ignoring EMC assessment in a products early design stage leads to an increase in cost. This increased cost is as a result of the shielding options, which at this stage is less costly than redesigning when EMC issues arise during prototype test. In [27], the cost accrued due to the shielding option adopted at the later stage of an electronic production project was shown to be higher than the cost of mitigating EMC issues at an earlier stage.

Table 1.1 shows variation in the EMC rescue cost with respect to the various phases of a product's production cycle. The cost becomes very high towards the end phase particularly in the production phase where little or nothing could be done to salvage the design. However, most EMC solutions here would use a shield or containment in the form of Faraday's cage [26], which will not only increase the cost but can also distort the product's original physical design and size.

Table 1.1. EMC cost as a function of product phase [8].

Product phase	Design	Development	Validation	Production
EMC solution	<i>Many</i>	<i>Some</i>	<i>Few</i>	<i>None</i>
EMC cost	<i>Low</i>	<i>Medium</i>	<i>High</i>	<i>Very High</i>

Therefore, including EMC evaluation throughout the product design stage would help in reducing the expense and complication in rectifying the EMC problem. Table 1.2 shows the PCB emissions as a function of its complexity and operational frequency. The table shows that the cost of remedying EMC issues

increases with the complexity of the PCB especially at higher frequencies [9], [27].

Table 1.2. EMI dependence on PCBs complexity and operational frequency [23].

Complexity Frequency	Low	Medium	Large
< 10MHz	<i>Low</i>	<i>Medium</i>	<i>Medium to high</i>
10-100MHz	<i>Medium</i>	<i>Medium to High</i>	<i>High to very high</i>
>100MHz	<i>High</i>	<i>High to very high</i>	<i>Very high</i>

Therefore there is the need for the development of simple techniques for assessing the EMC compliance of PCBs to relevant EMC directives, which can easily be applied to any of the production stages. These techniques are either in the form of measurements or modelling.

In the measurement only based approach for characterising the EM properties of a practical current source, a repeat of the measurement will be required whenever the EM characteristics of the DUT changes. A good alternative is the use of mathematical model to extend the capabilities of these measurement techniques where the mathematical model is developed using the information gathered from the field measurement.

1.4 Measurement Methods for PCB Emissions

Presently, many approaches exist for measuring emissions from practical devices. Choosing the appropriate measurement type depends on the signal strength, availability of resources, dimensions of the device to test, operational frequency etc. The facilities used for measuring the radiated fields from a practical device include Open area test site (OATS), anechoic chamber, compact

antenna test range, transverse electromagnetic (TEM) cells, reverberation chamber and near field scanner. The magnitude of the field measured using the above facilities can then be compared to recommended limits to ascertain compliance to the relevant standards.

1.4.1 Open Area Test Site

A plane wave, theoretically characterized by its uniform amplitude and phase, is usually generated at far field distances of a radiator. The Open area test site (OATS) [28] and its setup as shown in Fig. 1.3 is used for measuring and characterising this plane wave or far field radiation pattern. The device under test (DUT) is placed at a specified far field distance, r , away from the receiver antenna for radiated emissions measurements. The reference measurement antenna is of known radiation properties i.e. its gain and antenna calibration factor over the test frequency range have been validated.

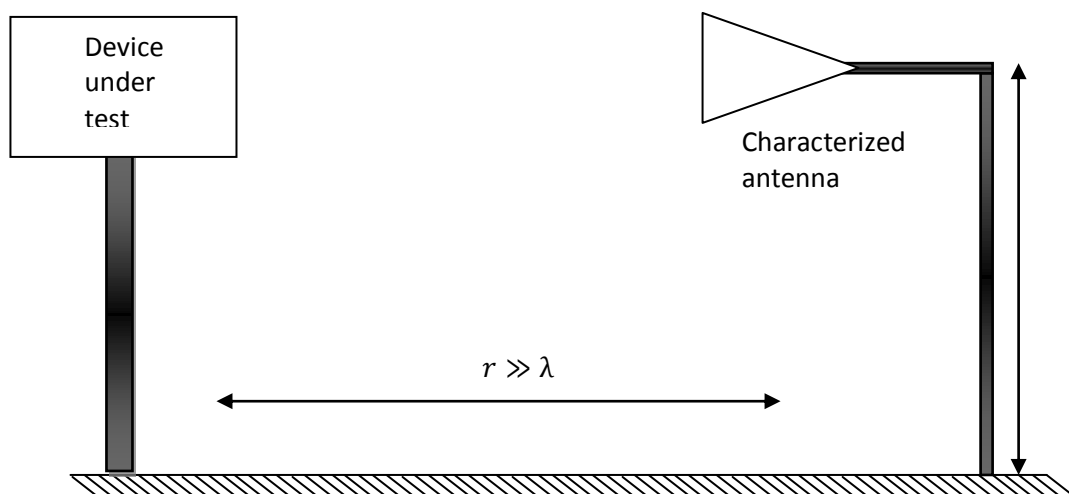


Fig. 1.3. Open Area Test Site measurement setup.

In the emission test, the DUT is used as the source while the characterised antenna is connected to the field receiver. A reverse setup is used for the immunity test, where the DUT and antenna are connected as the receiver and source respectively. The OATS provides very accurate measurement results for

far field measurement in a relatively shorter time compared to other techniques presented below, however it is very expensive to set-up and the required space may not be available.

In addition, possible interaction with the environment as the setup is not shielded from it, reflections and DUT- antenna positioning are the major sources of inconsistency in this set-up. The positioning of the DUT, which is required to measure different orientation of the DUT and to ensure that the strongest emissions from the DUT has been measured, can lead to DUT positioning error. Other variations of the technique exist such as elevated range or ground reflected range [28]-[30] but they all suffer from the same limitations. Also the far field result measured using the OATS does not provide sufficient information for characterizing unknown current sources.

1.4.2 Anechoic chamber

An anechoic chamber provides a more controlled environment with less demand for space unlike the OATS measurement that requires a wider space. Normally, the anechoic chamber is covered with Radiation Absorbent Material (RAM) as shown in Fig. 1.4.

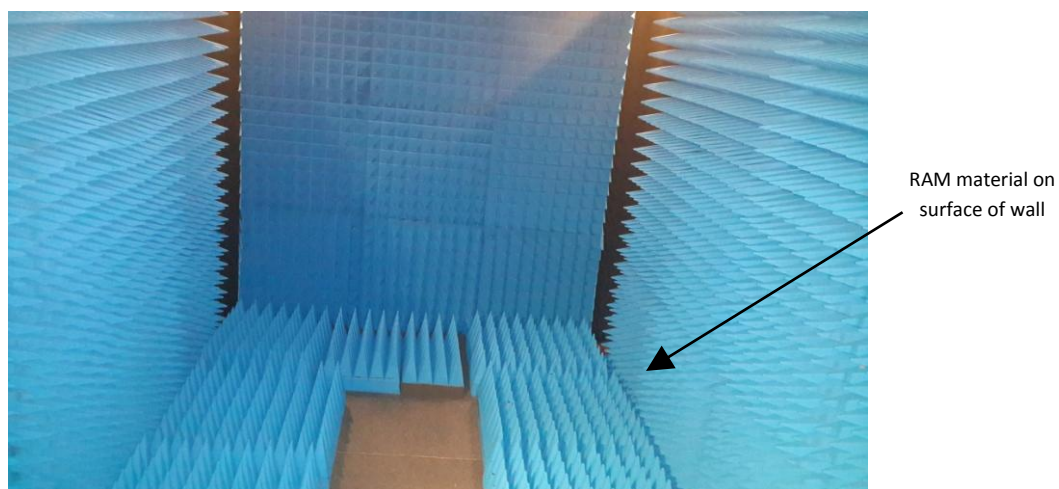


Fig .1.4. Anechoic chamber (GGIEMR, University of Nottingham).

The RAM absorbs the incident fields during the experiment. It is more appropriate at microwave frequencies and tends to be more complicated and expensive as the test frequency lowers. This is because at lower frequencies, a much thicker RAM is required to maintain the required reflectivity performance because of the increased wavelength [31]-[33]. Layers of ferrites are often used to overcome this due to being physically thinner. The addition of ferrites can be expensive to deploy and due to weight may have additional costs associated with the supporting structure. Similar to the OATS, an anechoic chamber is also used to measure the far field radiation pattern directly in a relatively shorter time however this provides little information on the actual source of the radiation in a complex DUT such as a PCB.

1.4.3 Compact antenna test range

The Compact Antenna Test Range (CATR) is used to characterize the plane wave or radiation pattern of a DUT in a relatively shorter time without requiring the availability of a large open space as for the OATS or an expensive anechoic chamber. The plane wave is generated in the near field using curved reflectors with special configurations like parabolic, Cassegrain etc as shown in Fig. 1.5. The parabolic reflector transforms a spherical wave to plane wave over a short range [31], [34]-[36].

In the immunity test, the DUT is positioned at the region where a definable plane wave is present as shown in Fig. 1.5 [31] [35]. Furthermore, by replacing the CATR source by a CATR receiver and using the DUT as the source, the CATR can be used for emission testing [36][37].

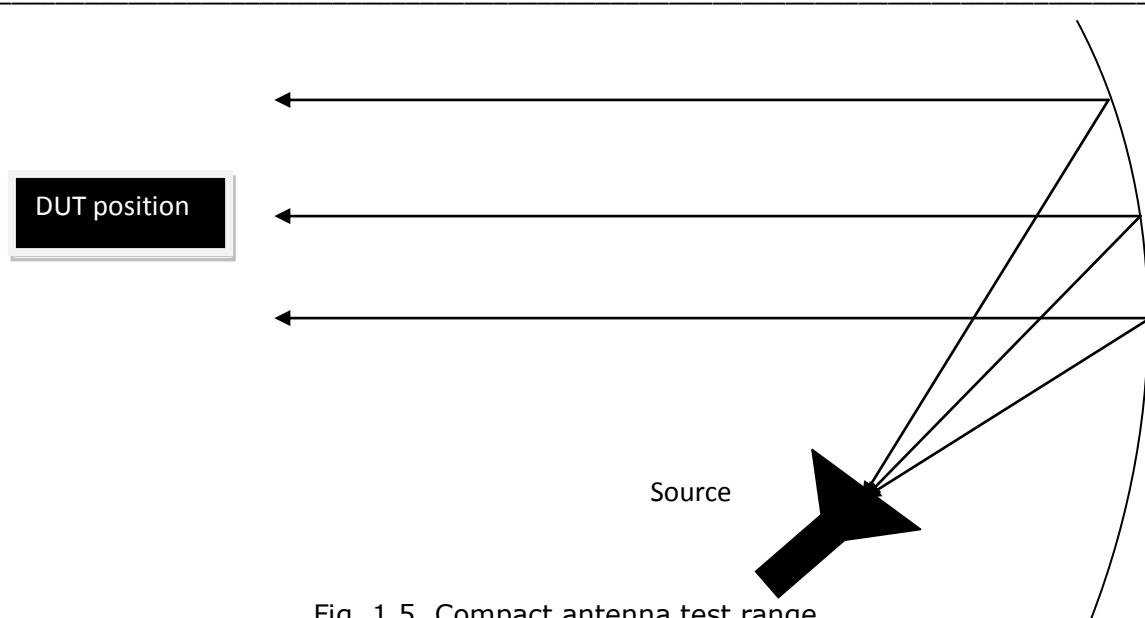


Fig. 1.5. Compact antenna test range.

However, incorrect positioning of the feed or the DUT can result in direct interaction with the DUT and this is a major problem when using this setup [31], [34]. There are also possible diffractions from the edges of the reflector which will generate a non-uniform field that limits this technique. Different modifications e.g. use of a tri-reflector system as presented in [31] have been employed to improve the performance of the CATR. These modifications however, tend to increase the complexities of the system.

1.4.4 TEM Cell

A Transverse Electromagnetic (TEM) cell is a shielded transmission line system in which the electric and magnetic fields are both perpendicular to the direction of propagation. The TEM cell [38], [39] is a tapered structure which provides a smooth field transition from the coaxial feed to large cross-sectional area region big enough to enclose the device under test (DUT). It is designed in such a way to provide the required shielding from the environment and maintain constant characteristic impedance of 50Ω which ensures that the voltage standing wave ratio (VSWR) is minimized. Emissions from DUTs can be measured in a TEM cell

as they couple into the TEM propagating mode. It requires less space than the OATS.

The TEM cell comes as either the low frequency standard TEM cell or the high frequency Gigahertz TEM (GTEM) cell. Figure 1.6 shows the cross section of a standard TEM cell which is a two port device. In normal operation, port 1 is terminated with a load equal to the characteristic impedance of 50Ω and port 2 is connected to a receiver. With the DUT placed inside the cell, the electromagnetic emission from the DUT can be measured.

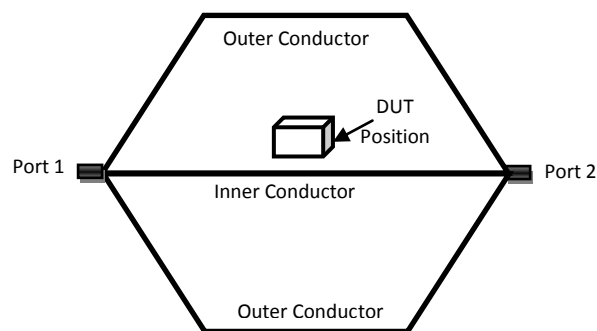


Fig. 1.6. Standard TEM cell.

The operating frequency range of a standard TEM cell is 150Hz to 1GHz above which higher-order modes are generated which disrupt the measurement. Conversely the GTEM cell is a single port device with the second port replaced by a matched termination as shown in Fig. 1.7.

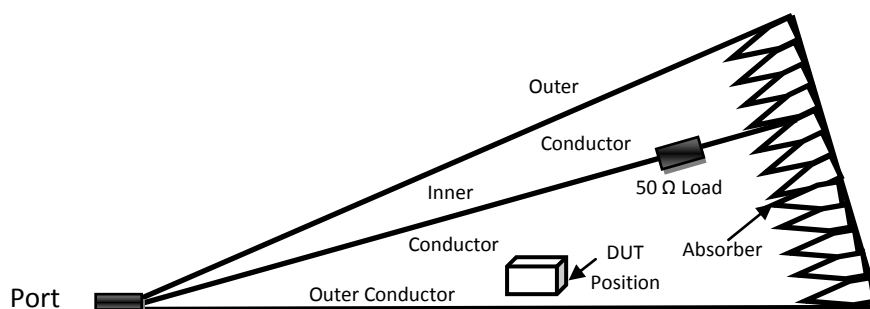


Fig. 1.7 GTEM Cell

The termination consists of a combination of a resistive load which operates at low frequency and a RAM coating on the termination surface which acts as a high frequency load. A complete emission measurement in a TEM cell requires several orientations of the DUT to be tested. This leads to a long measurement time and can create problems such as a situation where the DUT cannot be operated upside down (e.g. laser printers, where the toners may spill) [16] and DUT positioning error. In addition, there are practical limitations in the size of the DUT when compared with OATS. Also field uniformity across the whole volume of the TEM cell may limit the versatility of this technique. In contrast to OATS and anechoic chamber measurements, analytical processing of the output of TEM cell or GTEM cell measurement must be applied to estimate the radiation pattern of the DUT resulting in a higher overall experimental time. This approach has been demonstrated in references [16], [38]-[39] and a good correlation between the OATS and TEM cell measurement was shown.

1.4.5 Reverberation Chamber

The reverberation chamber has been in use for more than forty years [39] in carrying out emission and susceptibility tests for frequencies up to 18GHz. Reverberation chambers do not require expensive RF absorption material on their walls which makes them less expensive and means they are a preferred choice to the anechoic chamber. It does not require large space like in OATS or DUT positioning like in the techniques discussed earlier. They also allow for the generation of high fields for modest input power [40], [41] due to internal resonances.

A schematic of a reverberation chamber is shown in Fig. 1.8. The chamber is made of an enclosed and highly conductive cavity which contains rotating blades

for stirring the fields [42]. This blade rotation enhances the uniformity of the field through blade stirring or blade tuning. For the former, the blades are continually rotated and samples averaged over few cycles of rotation whereas in the later, the response is determined for each step position [42].

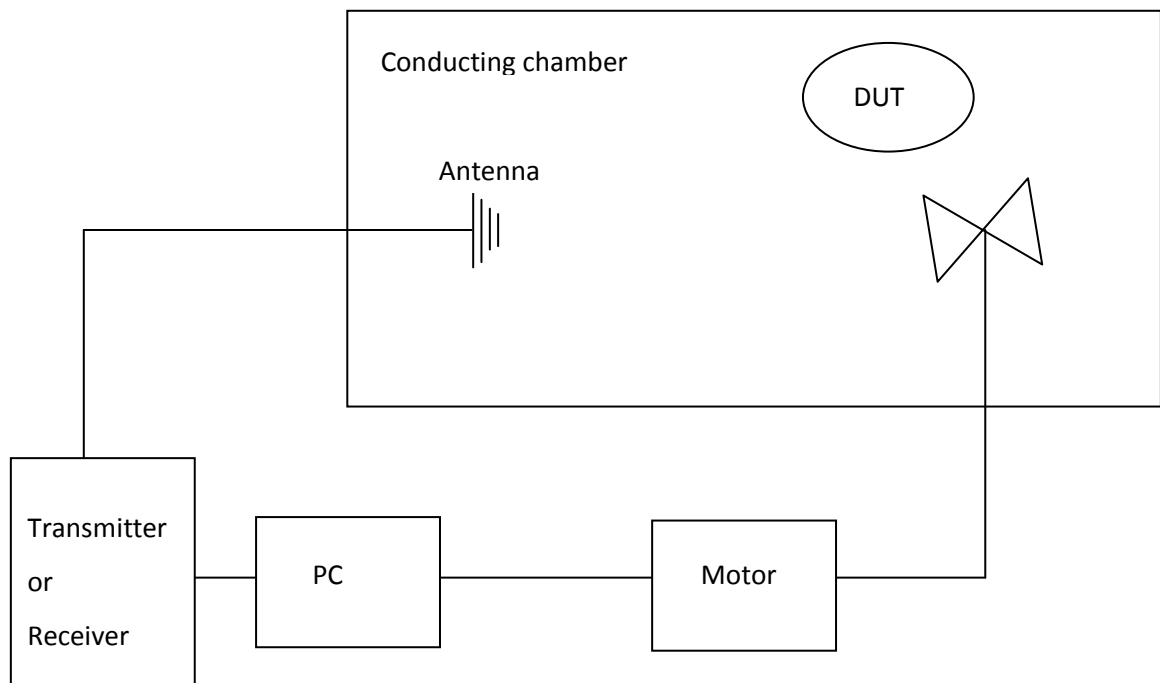


Fig. 1.8. Reverberation chamber.

For emissions testing, the receiver is connected to the receiving antenna and the DUT acts as the transmitter. The field strength can then be analysed from the results recorded by the receiver. According to Freyer et al in [43], [44] the reverberation chamber has smaller and predictable uncertainties than the anechoic chamber. The reverberation chamber does not require DUT re-positioning which often adds precision errors to the measurements and there are no reflection problems as seen in OATS and Anechoic measurements. Also [45] shows that the overall DUT response is obtained without changing its orientation unlike other setups that involve changing the orientation of the DUT. This attribute reduces the measurement time and the possibility of introducing positioning errors. Other advantages of reverberation chambers are presented in

the works [45]-[48]. However, the results from reverberation chamber are not enough to identify the properties of a complex radiator such as a practical PCB.

1.4.6 Near Field Measurement

Near field measurement is an indoor technique that has been widely used for the emission measurements of PCBs and other small radiators [3]-[5]. Near field measurement test bench is easy to set-up, does not require large space compared to OATS and is less expensive than anechoic chamber. It also does not require the movement of the DUT in most cases as the probe is made to scan through the surfaces of the DUT. This therefore removes error emanating from DUT positioning. Even with these advantages, it still does not compromise the accuracy of the measurement and information extracted through near field measurement can be used in computing the radiation pattern of a PCB. However in computing the radiation pattern, higher overall experimental time will be required compared to OATS. This is because post processing of the near field data is required. This application will be demonstrated later in Chapters 4 and 5.

The near field measurement is performed using a near field scanner which is a mechanical positioning system to move the measurement sensors at desirable locations (in 2D or 3D) for recording the field emissions during near field measurement. Different near field scanning geometries have been employed which depend on suitability, availability of resources and level of complexity.

Besides emissions, near field measurements can also be used for immunity tests and other interaction studies. The work by Muchaidze et al in [49] demonstrates how near field measurement is applied to determine the EM resonance of a DUT. This system comprises two probes decoupled from each other. The first probe is

used to excite the DUT while the second probe measures the response from the DUT. During the experiment, the transmission coefficient of the DUT is recorded, with the peak indicating relatively high amount of coupling.

1.4.7 Comparative Summary of EM Measurement Techniques

The summary of the key features of EM measurements using the facilities already discussed (e.g. OATS, Anechoic chamber, GTEM, CATR, Reverberation chamber, near field scanner) is presented in Table 1.3. The choice of facility depends on the availability of space and resources. According to Table 1.3, the OATS and Anechoic chambers offer an easy way of measuring the far-field emissions directly, however large spaces are often required and they are very expensive to set-up. Conversely, the near-field is a relatively low cost facility but requires post-processing to estimate the far-field emissions. This near field to far field transformation technique will be demonstrated later in this work.

Table 1.3 Summary of experiment only based approach

Facility	Space	DUT positioning error	Direct Radiation pattern measurement	Setup cost	Complexity (usage)	Experimental time
OATS	Very Large	Low	Yes	Very High	Low	Very Small
Anechoic Chamber	Large	Low	Yes	High	Low	Very Small
Reverberation Chamber	Small	Very Low	Yes	High	High	Small
CATR	Very Small	Low	Yes	Low	High	Small
GTEM	Small	Low	Post processing required	High	Low	High
Near-field Scanner	Small	Very Low	Post processing required	Very Low	High	High

1.5 Modelling Techniques for PCB Emissions

Mathematical models have been combined with measurement techniques in characterizing the emissions from PCBs [3]-[5], [50]-[59]. Here the actual emission characteristics from the practical radiator were extracted via measurement and the measured data then used to develop mathematical models capable of predicting other characteristics of the radiator as its EM environment changes. Maxwell's equations provide mathematical expressions that underlie the principles of electromagnetism [59]. However, solutions to Maxwell's equations are only possible for a limited number of simple structures. Numerical approximate solutions in the form of computational electromagnetics (CEMs) are often used in solving the Maxwell's equation for more complex structures. CEM comprises various techniques which provide acceptable solutions for realistic physical problems. These techniques are based on integral and/or differential forms [60]. Unlike the experimental techniques which can be very costly and time consuming especially when a design has to be optimised, CEM is much less expensive and has saved industry significant design and production costs [61]. This is because with CEM, experiments are easily repeatable, enabling the details of the electromagnetic properties of designs to be studied. The designs can then be deployed when they have met the desired performance. Common CEM techniques can be categorized as follows.

Integral equation solvers based on the Maxwell's integral equations include:

- *Method of Moments*

Method of moments (MoM) is a frequency domain technique that uses a surface mesh approach to solve the expansion functions (currents or charges) of the electric field integral equation (EFIE) or magnetic field

integral equation (MFIE) on the boundary surface of an electromagnetic problem [63]-[67]. Problems with smaller surface to volume ratios [60] are easily solved using MoM; however as MoM solution involves matrix inversion, higher computational resource is required as the size of the problem increases. The conventional MoM solution of N matrix size requires $O(N^2)$ and $O(N^3)$ for memory and operations respectively.

Also due to its surface mesh approach, MoM is not suitable for analysing the interior of conductive enclosures.

- *Generalised Multipole Technique*

The Generalised Multipole Technique (GMT) is a frequency domain technique similar to the MoM [60], [68]-[69]. However the expansion functions of the integral equations are solved at some distance away from the surface where the boundary condition is being enforced. This is unlike the conventional MoM that utilizes the boundary surface approach. Consequently, the GMT avoids the singularities on the boundary and results in reduction to its computational requirements.

- *Partial Element Equivalent Circuit Method*

In the Partial Element Equivalent Circuit (PEEC) method [70]-[73] the integral equation is interpreted as Kirchhoff's voltage law applied to a basic PEEC cell resulting in a complete circuit solution for 3D geometries. This is suitable for combined EM and circuit analysis in time and frequency domain.

The differential solvers based on discretisation of spatial and temporal derivatives of Maxwell's equations include:

- *Finite Difference Time Domain*

In Finite Difference Time Domain (FDTD), Maxwell's equations are solved over the whole discretised volume of the problem as partial differential equation [60], [74]-[76]. Unlike the MoM, the solution does not include matrix inversion. Two interleaved grid points are used to calculate E-fields and H-fields alternately at every half cycle time step. The broadband data is easily generated in a single run and a steady state analysis can also be performed.

However, FDTD requires adequate staircasing in computing the EM fields for problems with curved surfaces (e.g. sharp and acute edges) leading to high computational cost as a result of the smaller grid size that is required. This limits the usefulness of FDTD in solving problems involving curved surfaces.

- *Transmission line matrix*

The transmission line modelling (TLM) is a space and time discretisation method derived from the analogy between the EM fields and a mesh of transmission line [77]-[80]. This is similar to the FDTD in that the entire region is gridded. However, instead of interleaving E-field and H-field grids, a single grid is established and the nodes are interconnected by virtual transmission lines. It is suitable for the computation of complex 3D electromagnetic structures.

- *Finite element method*

In the finite element method (FEM), the approximate solution of the partial differential equation is found by eliminating the time derivatives completely or rendering the partial differential equation into an equivalent ordinary differential equation [81]-[85]. Also like the TLM and FDTD, the FEM technique involves the discretisation of the entire region. However,

the solution is presented in frequency domain (i.e. a single frequency response).

The above techniques are not recommended for problems of a significant number of wavelengths in size. This is because of the high computational requirements (i.e. time and memory) which are as a result of the discretisation approach (mesh, grid etc) adopted by these CEM solutions.

However, the high frequency techniques do not utilize discretisation in solving Maxwell's equation and therefore have relatively less computational requirements compared to the low frequency techniques. Instead the high frequency techniques use ray tracing approach [9], making them suitable for characterizing electrically large radiators. The high frequency techniques include:

- *Geometrical optics*

The geometrical optics (GO) makes use of ray tracing to approximate the effects of reflections and refractions [33].

- *Physical optics*

The physical optics (PO) uses light wave spreading to account for the diffraction, polarisation and interference [86]-[87].

For problems involving diffractions, additional diffraction components are added to arrive at an asymptotic solution [88] which will be discussed further in Chapter 4.

Though the CEM (low frequency and high frequency) techniques offer a useful way of solving complex EM problems, they have been shown to possess limiting properties that make them insufficient on their own for the majority of problems. For example the MoM or FDTD can become computationally expensive for

electrically large problems whereas the GO or PO will not be able to accurately approximate the effects of diffractions. Through hybridization, the strengths of different techniques are combined resulting in more robust techniques. This has been applied successfully in some commercial electromagnetic tools, which include Concept-II [89] based on MoM-PO, CST Microwave studio [90] based on FIT TLM-MoM-PO, and FEKO based on MoM-FEM-PO-UTD [91]. Others include Agilent ADS [92], ANSYS HFSS [93] etc.

However, the draw back in solutions based on these techniques is their reliance on the electrical details of the devices under test. So in characterizing a PCB using these techniques, information on the PCB circuitries and components is required. This is often a problem as the information is not always available because of confidentiality issues. Also the increase in the complexities of the PCBs makes it even more difficult and computationally expensive to characterize using electromagnetic software. These inherent characteristics are major limitations in adopting this approach in most EMC characterisation.

1.6 Equivalent dipole modelling

In previous work [3]-[5], the equivalent dipole model shown in Fig. 1.9, was used in predicting the electromagnetic characteristics of PCBs over a finite ground plane. In the model, which is based on the principle of source equivalence [31], [33], equivalent dipoles that can emulate the radiation behaviour of the current sources on the PCB were determined and then used to characterize other EM properties of the PCB. These equivalent dipoles are determined without a priori knowledge of the content of the PCB except for the field information extracted in the near field planes surrounding the PCB.

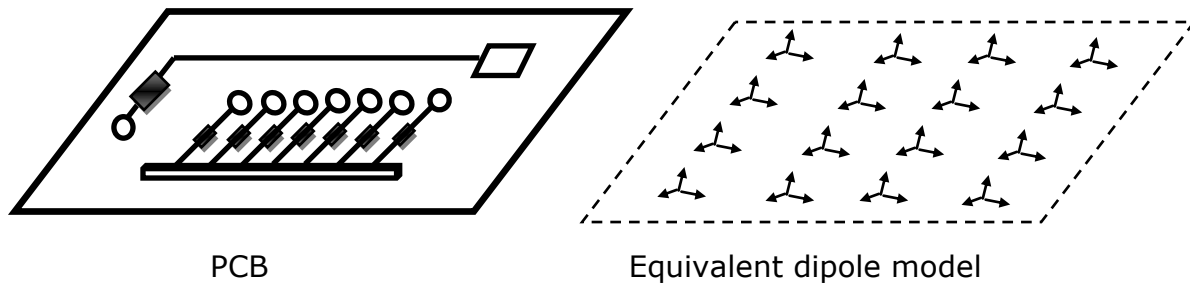


Fig. 1.9 The equivalent dipole model for a practical PCB

In the equivalent dipole model the real current sources on a PCB are replaced by equivalent sources whose properties including their positions and magnitudes (e.g. amps) are estimated from the information extracted at near field or complete circuit simulation.

This approach is shown in this work to be able to characterise the electromagnetic emissions from practical PCBs without requiring the very costly measurements, electrical component details of the PCBs or computationally expensive CEM techniques.

1.7 Current work

The equivalent dipole model implemented in the previous work [94] was validated for problems where an infinite ground plane can be assumed. Thus only a top scan was necessary and effects due to the edge of the finite ground plane were not considered.

However, for practical PCBs the infinite ground plane assumption cannot hold as it does not take into account edge effects such as diffraction. In this work, the planar rectilinear near field measurement is further developed for the measurement of emissions surrounding a 3D PCB. The setup includes an efficient automation mechanism for controlling the motion control and data acquisition processes. The field data extracted from this near field measurement is then

used to develop a mathematical model for characterizing the EM properties of a PCB taking into consideration the finiteness of the ground plane. This will be achieved by extending the capability of the existing equivalent dipole model to account for the induced currents at the edge of the PCB. The input to the model will be the near field emissions measured using a modified 3D near field scanner.

1.8 Conclusion

Different approaches used in characterizing emissions from electronic circuits have been discussed. The measurement only based techniques e.g. those utilising facilities such as anechoic chamber, GTEM cells and reverberation chamber, directly used to measure emissions, have been shown to be insufficient as experiments would have to be repeated for every change in the test condition.

This change can be a different height, different dielectric composition of the medium, time domain to frequency domain etc. To avoid the repetition of the time and resource consuming experiments, modelling becomes very useful. The numerical techniques as discussed also serve as a good alternative, as results can easily be computed at different heights and in any electromagnetic environment. However, the dependence on the detailed knowledge of the PCB and difficulties in simulating very complex PCBs limit the usefulness of these techniques.

An approach based on characterizing a PCB from near field scans and then constructing a computationally efficient equivalent dipole model which does not require a priori information (e.g. technical details of the PCB), is presented in this work. This offers a useful alternative in overcoming the limitations in

characterizing the emissions from practical PCBs. Suffice it to say that the only information required is the electromagnetic emissions measured at near field distances from the PCB. These emissions are then used in determining the properties of the equivalent dipoles that are required to accurately represent the electromagnetic sources on the PCB. As an application, this technique can also be used in identifying unwanted radiators on a PCB hence aiding in the tracking down of possible faults. This work extends previous research in the field by including the effects of finite ground planes.

1.9 Thesis Outline

In Chapter 2 the overview of the equivalent dipole modelling is presented. This comprises a brief introduction to near field measurement and the procedure taken in developing the equivalent dipole model from basic principle. Chapter 3 provides more details on the near field measurement technique employed in this work which was briefly introduced in Chapter 2. The 3D near field scanning required for a complete scan of a 3D object is also presented. The equivalent dipole modelling applications are first presented in Chapter 4 and the conditions for reliable performance of this technique also discussed. This builds from the theories that are presented in Chapter 2. The conditions for the validity of this technique are also provided and its limitation especially in characterizing a finite object is then illustrated. Possible ways of integrating other techniques so as to extend the capability of the equivalent dipole modelling are also presented.

In Chapter 5 the extended equivalent dipole modelling is presented. Here, passive dipoles were added to the basic equivalent dipole modelling in such a way to emulate the electromagnetic characteristics of the induced current at the

edges of the finite ground plane. Other validation results in modelling several complete PCB board designs and an application of this technique in predicting electromagnetic field shielding effectiveness are shown.

In Chapter 6, other ways of improving the performance of the equivalent dipole modelling are presented. This includes complex localization of the dipole sources, whereby the equivalent dipoles that represent the actual sources of emissions are placed in the complex space and Particle Swarm Optimization (PSO). The PSO is a swarm intelligent method that utilizes an iterative algorithm for optimizing the solution of a problem with regard to a defined measure of quality [95]-[97]. The PSO arrives at its optimal solution by moving a swarm of candidate solutions around the search space. The populations are at first selected at random and their movements guided by their own local best position in the search space (p_{best}) as well as the global swarm best (g_{best}). Also in Chapter 6 results are validated using the feature selective validation (FSV) technique, which combines and compares the amplitude and feature aspects of the two data sets being compared [98]-[100]. FSV provides information that is essential for the formal validation of numerical modelling data in a way that appears to provide a good approximation to the group response of visual assessment [98]. The outcome is then presented in a natural language thereby making FSV easy to interpret.

The conclusion of this thesis and suggestion for future works are then presented in Chapter 7.

References

- 1 C. Christopoulos, *Principles and Techniques of Electromagnetic Compatibility*, CRC Press, Ann Arbor, 1995.

- 2 M. Golio "*The RF and Microwave Handbook*," Boca Raton: CRC Press LLC, 2001.
- 3 X. Tong, *Simplified Equivalent Modelling of Electromagnetic Emissions from Printed Circuit Boards*, PhD Thesis, University of Nottingham, May 2010.
- 4 Y. Vives-Gilabert, C. Arcambal, A. Louis, F. de Daran, P. Eudeline, and B. Mazari, "Modeling magnetic radiations of electronic circuits using near-field scanning method," *IEEE Trans. Electromagn. Compat.*, vol. 49, no. 2, pp. 391–400, May 2007.
- 5 L. Beghou, B. Liu, L. Pichon and F. Costa, *Synthesis of Equivalent 3-D Models from Near Field Measurements - Application to the EMC of Power Printed Circuit Boards*, *IEEE Transactions on Magnetics*, Vol. 45, no. 3, pp 1650-1653, 2009.
- 6 C. Obiekezie, D. W. Thomas, A. Nothofer, S. Greedy, L. R. Arnaut, P. Sewell, "Extended Scheme using Equivalent Dipoles for Characterizing Edge Currents Along a Finite Ground Plane," *Applied Comp. Electromagn. Soc.*, vol. 28, nos. 11, pp. 1111-1121, Nov. 2013.
- 7 R. Kay, "Co-ordination of IEC standards on EMC and the importance of participating in standards work ", *IEE 7th International Conference on EMC*, York 28-31st Aug. 1990, pp. 1-6.
- 8 C. Marshman, *The Guide to EMC Directive*, McGraw-Hill, 5th ed., 1988.
- 9 T. Williams, *EMC for Product Designers*, 2nd Ed., Reed Educational and Professional Publishing Ltd, 1996.
- 10 M. Campbell, *Everybody needs standards*, BSI, IEE News pp. 14, 3rd October 1991.

- 11 M. C. Vrolijk, " The Availability of Standards ", *Nederlandse Philips Bedrijven BV*, EMC 91- Direct to Compliance, ERA Technology, February 1991.
- 12 EN50082-1:1995. Electromagnetic compatibility generic emission standard-part 1: Residential, commercial and light industry. European Committee for Electrotechnical Standardization, Brussels, Belgium, 1992.
- 13 EN50082-1:1994. Electromagnetic compatibility generic emission standard-part 2: Residential, commercial and light industry. European Committee for Electrotechnical Standardization, Brussels, Belgium, 1994.
- 14 EN50082-1:1998. Electromagnetic compatibility generic immunity standard-part 1: Residential, commercial and light industry. European Committee for Electrotechnical Standardization, Brussels, Belgium, 1998.
- 15 EN50082-1:1995. Electromagnetic compatibility generic immunity standard-part 2: Residential, commercial and light industry. European Committee for Electrotechnical Standardization, Brussels, Belgium, 1995.
- 16 A. Nothofer, *Cross-Polar Coupling in GTEM Cells used for Radiated Emission Measurements*, PhD Thesis, University of York, York, 2000.
- 17 EN 55022: (2010). Information technology equipment- Radiation disturbance characteristics-Limits and methods of measurement, Brussels, Belgium 2010.
- 18 M. Mardiguan, *Controlling Radiated Emission by Design*, New York, Van Nostrand Reinhold, 1993.
- 19 V. Doren, *Circuit Board Layout to Reduce Electromagnetic Emission and Susceptibility*, Seminar Notes, 1995.
- 20 O. Hartal, *Electromagnetic Compatibility by Design*, Conshohocken, PA: R & B Enterprises, 1994.

- 21 J. Liu and L. Qi, "The EMC analyzing and optimizing with high frequency interference in PCB Design", *IEEE International Symposium on Electromagnetic Compatibility*, 2006, pp.187 - 190.
- 22 Y. Villavicencio, F. Musolino, F. Fiori, "Electrical model of microcontrollers for the prediction of electromagnetic emissions," *IEEE Trans. VLSI Syst.*, vol. 19, no. 7, pp. 1205–1217, Jul. 2011.
- 23 C. Labussi`ere-Dorgan, S. Bendhia, E. Sicard, J. Tao, H. J. Quaresma, C. Lochot, and B. Vrignon, "Modeling the electromagnetic emission of a microcontroller using a single model," *IEEE Trans. Electromagn. Compat.*, vol. 50, no. 1, pp. 22-34, Feb. 2008.
- 24 S. Wu and J. Fan, "Analytical prediction of crosstalk among vias in multilayer printed circuit boards", *IEEE J. Solid-State Circuits*, vol. 54, no. 2, pp. 413–420, Apr. 2012.
- 25 C. Su and T. H. Hubing, "Improvements to a method for estimating the maximum radiated emissions from PCBs with cables", *IEEE Trans. Electromagn. Compat.*, vol. 53, no. 4, pp. 1087–1091, Feb. 2011.
- 26 D. Morgan, *Handbook for EMC Testing and Measurement*, The IET, London, 2007.
- 27 M. I. Montrose, *EMC and the Printed Circuit Board: Design, Theory and Layout Made Simple*, IEEE press, New York, 1999.
- 28 Golio, Mike "The RF and Microwave Handbook," Boca Raton: CRC Press LLC, 2001.
- 29 (2013) Agilent technologies - Introduction to antenna measurement. [online]. Available <http://www.home.agilent.com/>.
- 30 Antenna standards committee, "IEEE standard test procedures for antennas", *IEEE Trans. Antennas Propagation*, vol.149, 1979.

- 31 C. A. Balanis, *Antenna Theory Analysis and Design*, John Wiley and Sons, New York, 2005, 3rd ed.
- 32 C. R. Paul, *Introduction to Electromagnetic Compatibility*, Wiley, New York, 1992.
- 33 C. A. Balanis, *Advanced engineering electromagnetic*, New York: Wiley, 1989.
- 34 W. L. Stutzman and G. A. Thiele, *Antenna theory and design*, New York: Wiley, 1981.
- 35 R. C. Johnson, R. J. Poinsett, " Compact Antenna Range Techniques ", Georgia Institute of Technology, Tech. Report No. RADDC-TR-66-15, 1966.
- 36 M. Philippakis and C.G. Parini, "Compact antenna range performance evaluation using simulated pattern measurement," *IEE Proc.-Microw. Antennas Propag* ,Vol.143, No.3, June 1996.
- 37 A. J. Rowell, D. W. Welsh, A. D. Papatsoris, " Practical Limits for EMC Emission Testing at Frequencies Above 1GHz ", The Radio Communication Agency, York EMC service, York, Final Report.
- 38 P. Wilson, "On Correlating TEM Cell and OATS Emission Measurements," *IEEE Trans. On electromagn. Compat*, VOL. 31, NO.1, February 1995.
- 39 M. Crawford, "Generation of standard EM fields using TEM transmission cells," *IEEE Trans. on Electromagn. Compat.*, vol. 16, no. 4, pp. 189-195, Nov. 1974.
- 40 P. Corona, G. Latmiral, E. Paolini and L. Piccioli, "Use of a reverberating enclosure for measurements of radiated power in the microwave range," *IEEE Trans. on Electromagn. Compat.*, vol. 18, no. 2, p.54-59, May 1976.

- 41 F. B. J. Leferink, "Using reverberation chambers for EM measurements Software", *Telecommunications and Computer Networks (SoftCOM)*, pg1-5, Nov. 2010.
- 42 P. Corona, G. Latmiral, E. Paolini and L. Piccioli, "Use of a reverberating enclosure for measurements of radiated power in the microwave range," *IEEE Trans. on Electromagn. Compat.*, vol. 18, no. 2, p.54-59, May 1976.
- 43 G. J. Freyer and M. G. Bäckström, "Comparison of Anechoic and Reverberation Chamber Coupling Data as a Function of Directivity Pattern", IEEE International Symposium on EMC, Washington, August 2000.
- 44 G. J. Freyer and M. G. Bäckström, "Comparison of anechoic & reverberation chamber coupling data as a function of directivity pattern-II," in *Proc.*, IEEE 2001 International Symposium on EMC, Montreal, pp. 286–291, August 2001.
- 45 G. Gradoni, F. Moglie, A. Pastore and V. M. Primiani, "Numerical and experimental analysis of the field to enclosure coupling in reverberation chamber and comparison with anechoic chamber," *IEEE Trans. on Electromagn. Compat.*, Vol. 48, No. 1, pp. 203-211, February 2006.
- 46 L. R. Arnaut and P. D. West, "Electromagnetic reverberation near a perfectly conducting boundary," *IEEE Trans. Electromagn. Compat.*, vol. 48, no. 2, pp. 359–371, May 2006.
- 47 F. Moglie, "Convergence of the reverberation chambers to the equilibrium analyzed with the finite-difference time-domain algorithm," *IEEE Trans. Electromagn. Compat.*, vol. 46, no. 3, pp. 469–476, Aug. 2004.
- 48 IEC 61000-4-21: Electromagnetic Compatibility (EMC)–Part 4-21: Testing and Measurement Techniques–Reverberation chamber test methods,

- International Electrotechnical Commission, IEC SC77B-CISPR/A JWG REV, Geneva, Switzerland, 2nd ed., Jan 2011.
- 49 G. Muchaidze, W. Huang, J. Min, P. Shao, J. Drewniak and D. Pommerenke, "Automated Near-Field Scanning to Identify Resonances," *Electromagnetic Compatibility - EMC Europe, 2008 International Symposium on*, pp. 1-5, Sept. 2008.
- 50 B. Bae, Y. Shim, K. Koo, J. Cho, J. S. Pak and J. Kim, "Modelling and measurement of power supply noise effects on an analog-to-digital converter based on a chip-PCB hierarchical power distribution network analysis," *IEEE Trans. Electromagn. Compat.*, vol. 55, no. 6, pp. 1260–1270, Dec. 2013.
- 51 J. Regué, M. Ribó and J. Garell, Antonio Martin, "A Genetic Algorithm Based Method for Source Identification and Far Field Radiated Emissions Prediction from Near-Field Measurements for PCB Characterization", *IEEE Trans. On Electromagnetic Compatibility*, vol. 43, no.4, November, 2001
- 52 R. Pierri, G. D'Elia and F. Soldovieri, "A two probes scanning phaseless near-field far-field transformation technique", *IEEE Trans. Antennas Propogat.*, vol. 47, pp.792-802, May, 1999
- 53 T. Isernia, G. Leone and R. Pierri, "Radiation pattern evaluation from nearfield intensities on planes", *IEEE Trans. Antennas Propogat.*, vol. 44, pp.701-710, May, 1996
- 54 T. Isernia, G. Leone and R. Pierri, "Radiation Pattern Evaluation from Near-Field Intensities on Planes", *IEEE Transaction on Antennas and Propagation*, vol. 44, no.5, May, 1996
- 55 J. Jia; D. Rinas and S. Frei, "An alternative method for measurement of radiated emissions according to CISPR 25", *Electromagnetic Compatibility*

- (EMC EUROPE), 2013 International Symposium on, On page(s): 304 - 309, Volume: Issue: , 2-6 Sept. 2013
- 56 J. Jia, D. Rinas and S. Frei, "Prediction of radiated fields from cable bundles based on current distribution measurements", *Electromagnetic Compatibility (EMC EUROPE), 2012 International Symposium on*, On page(s): 1 - 7
- 57 W. T. Smith, K. Frazier, "Prediction of Anechoic Chamber Radiated Emissions Measurements through Use of Empirically-Derived Transfer Functions and Laboratory Common-Mode Current Measurements", IEEE International Symposium on Electromagnetic Compatibility, Aug. 1998.
- 58 D. Rinas, S. Niedzwiedz, J. Jia, S. Frei, "Optimization methods for equivalent source identification and electromagnetic model creation based on near-field measurements", EMC Europe 2011, York, Sept. 2011, pp. 298-303.
- 59 D.B. Davidson, *Computational Electromagnetics for RF and Microwave Engineering*, 2nd Edition, Cambridge: Cambridge University Press, 2011.
- 60 T. Hubing, "Survey of numerical electromagnetic modelling techniques," University of Missouri Rolla, EMC Lab., Report TR91-1-1-001.3, 1991.
- 61 R. Garg, *Analytical and Computational Methods in Electromagnetics*, Artech House, Norwood, MA, 2008.
- 62 R. F. Harrington, *Field Computation by Moment Methods*, The Macmillan Co., New York, 1968.
- 63 G. J. Burke and A. J. Poggio, "Numerical Electromagnetic Code (NEC) - Method of Moments," Naval Ocean Syst. Center, San Diego, CA, NOSC Tech. Document 116 , Jan. 1981.

- 64 F. Bogdanov, R. Jobava, A. Gheonjian, A. Demurov, B. Khvitia, Z. Kut Chadze "Modeling of printed circuit boards and microstrip antennas based on the MoM Hybridized with special Green's function and multiport network approach", Proc. AP-S/URSI-2011, Spokane, Washington, USA, 2011, pp. 1581-1584.
- 65 M. W. Ali , T. H. Hubing and J. L. Drewniak "A Hybrid FEM/MOM Technique for Electromagnetic Scattering and Radiation from Dielectric Objects with Attached Wires", *IEEE Trans. on Electromagnetic Compatibility*, vol. 39, pp.304 -314 1997
- 66 J.-S. Wang, "On edge based finite elements and method of moments solutions of electromagnetic scattering and coupling," Ph.D. dissertation, University of Akron, OH, 1992.
- 67 B. Wong and A. Cantoni, "MoM validation of the predicted radiated emissions of two signal integrity damping schemes on PCB microstrips", Environmental Electromagnetics (CEEM), 2012 6th Asia-Pacific Conference on, On page(s): 175 – 177.
- 68 Th. Wriedt (ed.), Generalized Multipole Techniques for Electromagnetic and Light Scattering, Elsevier, 1999.
- 69 F. Obelleiro, L. Landesa, J. L. Rodriguez, M. R. Pino, R. V. Sabariego, and Y. Leviatan, "Localized Iterative Generalized Multipole Technique for Large Two-Dimensional Scattering Problems," *IEEE Transactions on Antennas and Propagation*, AP-49, 6, 2001, pp. 961-970.
- 70 J. Ekman, "Electromagnetic Modelling Using the Partial Element Equivalent Circuit Method" Ph.D. thesis, Lulea University of Technology, Sweden, March 2003.

- 71 J. Cui and M. Zhang, "Transient Analysis of PCB EMC Problem," International Symposium on Antennas, Propagation and EM Theory, pp.1111-1114, 2008
- 72 V. Vahrenholt and H.D. Brüns, H. Singer, "Fast EMC Analysis of Systems Consisting of PCBs and Metallic Antenna Structures by a Hybridization of PEEC and MoM", *Electromagnetic Compatibility, IEEE Transactions on*, On page(s): 962 - 973 Volume: 52, Issue: 4, Nov. 2010
- 73 H. Heeb, A. E. Ruehli, "Three-dimensional interconnect analysis using partial element equivalent circuits", *IEEE Trans. on CAS-1*. Vol. 39, n. 11, Nov. 1992, pp 974-982.
- 74 E. Fomberg, A. Byers, M. Picket-May, C. L. Holloway, "FDTD Modeling of Printed Circuit Board Signal Integrity and Radiation", IEEE 2000 Int. Symp. on Electromagnetic Compatibility, August 2000, pp. 21-25.
- 75 D. Hockanson, J. L. Drewniak, T. H. Hubing, and T. P. Vandoren, "FDTD modeling of thin wire structures for simulating commonmode radiation from structures with attached cables," in Proc. IEEE Electromag. Compat. Symp., Atlanta, GA, 1995, pp. 168-173
- 76 Y. Kim. "FDTD analysis on the current and electric field distribution in a PCB stripline structure," IEEE International Symposium on Electromagnetic Compatibility, 2000, 2: 691-694.
- 77 C. Christopoulos, "The Transmission-Line Modelling Method: TLM," IEEE Press, New York, 1995.
- 78 C. Christopoulos, "Application of the TLM Method to Equipment Shielding Problems", Proceedings of the 1998 IEEE International Symposium on Electromagnetic Compatibility, vol. 1, pp.182 -187 1998

- 79 Y. Cui, H. Lu, Z. Qiu, W. Zhang and H. Zhang, "Shielding effectiveness characterization of metallic enclosure with apertures," International Symposium on Antennas, Propagation and EM Theory, pp.1039-1042, 2010
- 80 J.S. Pak et al., "Modeling and Measurement of Radiated Field Emission from a Power/Ground Plane Cavity Edge Excited by a Through-Hole Signal Via Based on a Balanced TLM and Via Coupling Model," *IEEE Trans. Advanced Packaging*, vol. 30, no. 1, Feb. 2007, pp. 73—85.
- 81 G. L. Maile, "Three-Dimensional Analysis of Electromagnetic Problems by Finite Element Methods," Ph.D. dissertation, University of Cambridge, December 1979.
- 82 R. Laroussi and G.I. Costache, "Finite-Element Method Applied to EMC Problems", *EEE Trans. on EMC*, W. 35, No. 2, May 1993
- 83 Y. Ji, J Chen, T. H. Hubing, J. L. Drewniak, "Application of a hybrid FEM/MOM method to a canonical PCB problem", 1999 Int. Symp. on Electromagnetic Compatibility, August 1999, pp. 91-95.
- 84 S. Tanabe et al., "3D-FEM Analysis of Electromagnetic Emission from PCB", To be published and presented at IEEE 1996 International Symposium on Electromagnetic Compatibility, Santa Clara, California, August 19-23, 1996
- 85 J. Jin, *The Finite Element Method in Electromagnetics*, New York: McGraw-Hill, 1995.
- 86 P. Meinke, O. Breinbjerg and E. Jorgensen, "An exact line integral representation of the magnetic field physical optics scattered field," *IEEE Trans. Antennas Propag.*, vol. 51, no. 6, pp. 1395–1398, Jun. 2003.

- 87 S.Maci, P.Ya.Ufimtsev, and R. Tiberio, "Equivalence between physical optics and aperture integration for radiation from open-ended waveguides," *IEEE Trans. Antennas Propag.*, vol. 45, no. 1, pp.183–185, Jan. 1997.
- 88 W. L. Stutzman and G. A. Thiele, *Antenna theory and design*, New York: Wiley, 1981.
- 89 Concept-II(2009)[online]. Available:[http://www .tet .tuharburg .de /concept /index.en.html](http://www.tet.tuharburg.de/concept/index.en.html).
- 90 CST- CST MWS, Germany. (2011) [online]. Available: <http://www.cst.com/Content/Products/MWS/Solvers.aspx>.
- 91 FEKO – Product detail. (2011) [online]. Available: http://www.feko.info/product-detail/numerical_methods.
- 92 Agilent Technologies, *Advanced Design System (ADS)*. (2013) [online]. Available: <http://www.home.agilent.com/>
- 93 ANSYS, *HFSS*. (2013)[Online]. Available: <http://www.ansys.com>.
- 94 X. Tong, D. W. P. Thomas, A. Nothofer, P. Sewell, and C. Christopoulos, "Modelling electromagnetic emissions from printed circuit boards in closed environments using equivalent dipoles", on *IEEE Trans. Electromagn. Compat.*, vol.52,no.2,pp.462-470, 2010.
- 95 J. Kennedy and R.G Eberhart, *Particle Swarm Optimization*, IEEE International Conference on Neural Networks, (Perth, Australia), IEEE Service Center, Piscataway, NJ, IV: 1942-1948, 1995.
- 96 J. Kennedy and R.G Eberhart, 1997, "A discrete binary version of the particle swarm algorithm," Proc. 1997 Conf. on Systems, Man, and Cybernetics, Piscataway, NJ: IEEE Service Genter, pp. 4104-4109.

- 97 P.G. Ko and P.G Lin, 2004, "A hybrid swarm intelligence based mechanism for earning forecast," in: Proc. 2nd Int. Conf. on Information Technology and Applications (ICITA 2004).
- 98 V. Rajamani, C.F. Bunting, A. Orlandi and A. Duffy, "Introduction to feature selective validation (FSV) ," IEEE International Symposium Antennas and Propagation, 2006, pp.601-604.
- 99 A. Orlandi, A. P. Duffy, B. Archambeault, G. Antonini, D. E. Coleby, and S. Connor, "Feature selective validation (FSV) for validation of computational electromagnetics (CEM): Part II. Assessment of FSV performance," *IEEE Trans. Electromagn. Compat.* , vol. 48, no. 3, pp. 460–467, Aug. 2006.
- 100 IEEE, "Standard for validation of computational electromagnetics computer modeling and simulation," IEEE Std 1597.1, Piscataway, NJ, 2009.

Chapter 2

Theory of Measurement and Modelling for Equivalent dipole modelling

2.1 Introduction

In this Chapter an overview of equivalent dipole modelling for characterising the electromagnetic (EM) emissions from a Printed Circuit Board (PCB) is presented. Here the development of the equivalent dipole modelling from first principle is presented. In this approach, EM field information is extracted at the near field of the PCB through near field scanning and then used to determine the equivalent dipoles that can reproduce the EM characteristics of the PCB.

Though far field measurements [1] can also extract some information that may be used in characterizing emissions from a PCB, the information extracted is not sufficient in characterising problems with multiple current sources. This is because far field measurement results are not easily mapped to the actual current sources. Consequently making the location, polarisation, amplitude and phase of the individual current sources required for characterising PCBs in different EM environment, undetermined. In this work, near field measurement is demonstrated as a suitable method for extracting sufficient information required for characterizing a practical PCB. This set of information is then used to develop a model based on equivalent dipoles that is capable of emulating the EM characteristics of the PCB.

2.2 Radiation Characteristics of PCBs

Radiation from PCBs is primarily due to the time varying currents and voltages on the tracks [2], [3]. The EM fields can be related to the track current, I along the path dl through the following expressions:

$$\oint H \cdot dl = I_{enc} + \int_s \frac{\partial D}{\partial t} ds \quad (2.1)$$

$$\oint E \cdot dl = - \int_s \frac{\partial B}{\partial t} ds \quad (2.2)$$

where I_{enc} , D and B are the enclosed current, displacement current and magnetic flux density.

The EM effects of the PCB track currents and active circuitry components on the PCB can be represented by dipoles. This is because the EM properties of dipoles are well known and can be easily represented analytically. In this work, the infinitesimal dipole is used which serves as a good choice, as it can be said to represent the simplest possible source of electromagnetic field and serves as a building block for more complex problems. This will be demonstrated later in Chapter 4 to Chapter 6. As the infinitesimal dipoles are very small (*length*, $l \ll \lambda$, *thickness*, $a \ll \lambda$) [1][4][5], it is appropriate to assume a constant spatial variation of the current (i.e. $I\Delta l$).

The radiation from an infinitesimal electric dipole given in Fig. 2.1 for a distance r from an observation point, P is given by

$$\begin{aligned} E_r &= \eta \frac{Il \cos \theta}{2\pi r^2} \left[1 + \frac{1}{jkr} \right] e^{-jkr} \\ E_\theta &= j\eta \frac{kIl \sin \theta}{4\pi r} \left[1 + \frac{1}{jkr} - \frac{1}{(kr)^2} \right] e^{-jkr} \\ H_\phi &= j \frac{kIl \sin \theta}{4\pi r} \left[1 + \frac{1}{jkr} \right] e^{-jkr} \end{aligned} \quad (2.3)$$

where k and η are the wave number and intrinsic impedance of the medium respectively.

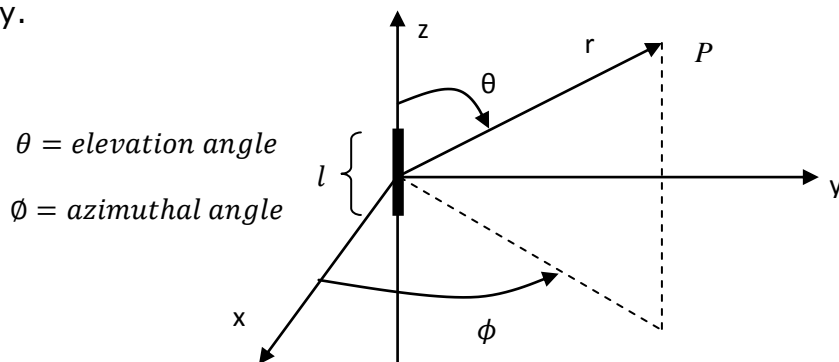


Fig. 2.1 Infinitesimal dipole

The radiating properties of an electromagnetic source (e.g. an infinitesimal dipole) vary as a function of distance away from the source. This variation is subdivided into the near field and far field regions as shown in Fig. 2.2.

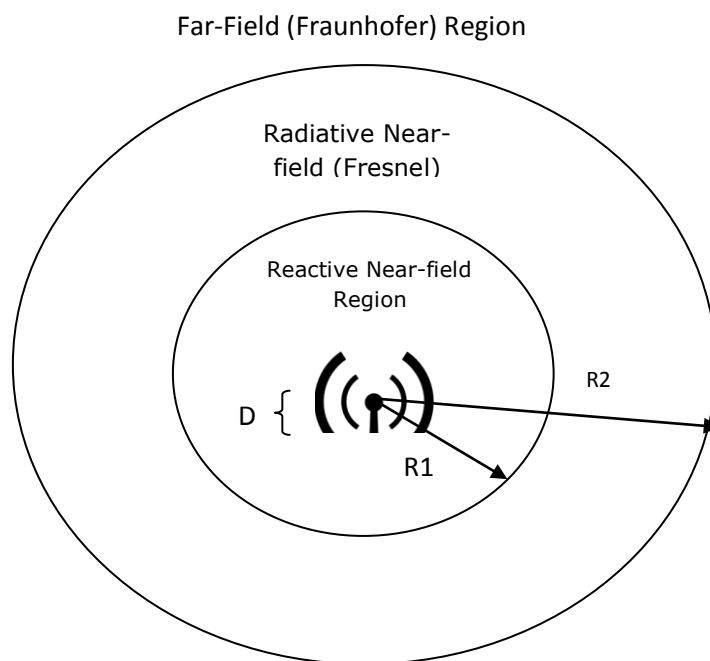


Fig. 2.2 Electromagnetic field regions

2.2.1 Near field region

The near field region comprises reactive and radiating sub-regions [1][4][5] as shown in Fig. 2.2. The reactive near field region is the closest region to the source where the electric field (E) and magnetic field (H) are out of phase by 90°

to each other. For most radiators this region exists at distances less than $0.62\sqrt{\frac{D^3}{\lambda}}$ to the surface of the radiator, where D is the largest dimension of the radiator. The radiating near field region also known as the Fresnel zone covers the distances that are bounded by $0.62\sqrt{\frac{D^3}{\lambda}}$ (inner boundary) and $2\frac{D^2}{\lambda}$ (outer boundary) for large D compared to wavelength (i.e. $D > \lambda$). However, this region may not exist when D is significantly smaller than λ .

2.2.2 Far field region

The far field (also known as Fraunhofer region) is the region where the angular field distribution is independent of the distances from the radiator. The far field region is taken to exist at distances greater than $2\frac{D^2}{\lambda}$ from the surface of the radiator [1]. In the far field region, the electric and magnetic fields are orthogonal and the magnitude of the wave impedance in free space Z_0 , is given by

$$Z_0 = \sqrt{\frac{\mu_0}{\epsilon_0}} \quad (\approx 377\Omega) \quad (2.4)$$

where μ_0 and ϵ_0 are the magnetic (permeability) and electric (permittivity) constants in free space. In a homogenous medium, the wave impedance Z_m is a function of the dielectric property of that medium.

2.2.3 Approximate EM fields representation

As the exact boundary between the regions are ambiguous for mathematical simplicity the near field region is approximately defined as the region within the radius $r \ll \frac{\lambda}{2\pi}$ and where the magnitude of the fields decay rapidly as $\frac{1}{r^3}$. On the

other hand, at the far-field region where $r \gg \frac{\lambda}{2\pi}$, the $\frac{1}{r^2}$ and $\frac{1}{r^3}$ terms given in (2.3) approach zero hence only the $\frac{1}{r}$ term is required to compute the electromagnetic fields in the region. The electric dipole far-field expression is then approximated as

$$\begin{aligned} E_r &\approx 0 \\ E_\theta &\approx j\eta \frac{kIl\sin\theta}{4\pi r} \\ H_\phi &\approx j \frac{kIl\sin\theta}{4\pi r} \end{aligned} \quad (2.5)$$

In this region, the energy radiates away to infinity and is not reflected back towards the source. The approximate expressions in (2.5) show that the magnitude of the field is inversely proportional to r .

The far field and near field phenomena have been introduced in section 2.2 to help understand the rest of the thesis. However, as presented in Chapter 1, near field measurement offers cost effective advantage compared to other measurement methods, which is the reason why it was adopted in this work. Following this, only near field measurement method will be discussed in the remaining part of this thesis.

2.3 Near Field Measurement

Near field measurements can be carried using different geometries and Fig. 2.3 shows the three that are commonly applied. The major difference apart from their physical geometries are:

- set-up complexities,
- total time for complete scan,

- degrees of introduced error,
- mathematical complexities etc

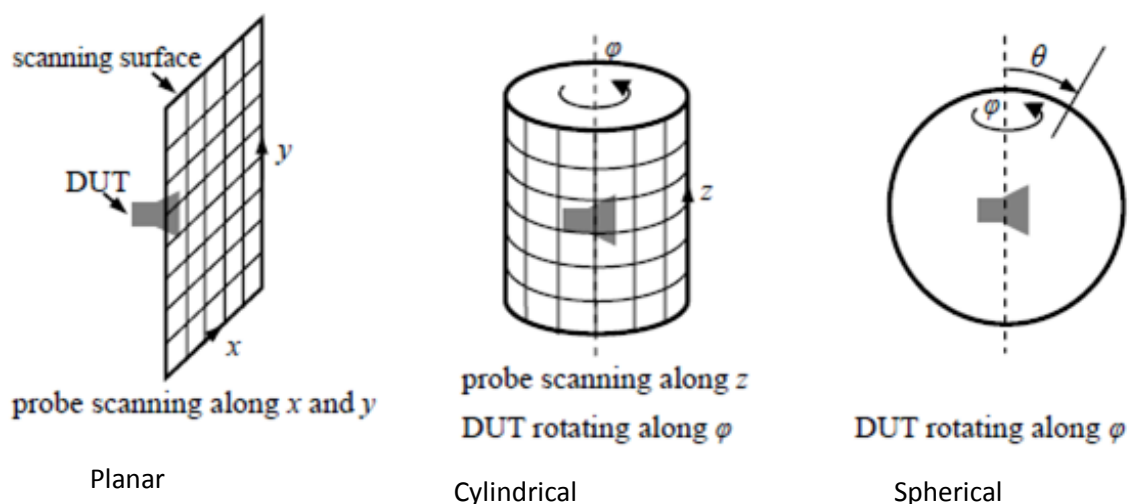


Fig. 2.3. Basic geometries for near-field scanning [6].

In the spherical near field scanning (SNFS), the DUT is rotated through 360° in the ϕ and θ direction whilst the probe is kept stationary. This can be complex to set up initially and errors are introduced due to DUT positioning. However, a complete scan of the DUT can be achieved in a single measurement, hence resulting in a minimized experiment time. It is best suited for low gain and omnidirectional antennas [6] and achieved through the use of dual axis rotators.

The cylindrical near-field scan (CNFS) utilizes a hybrid measurement configuration (involving the movement of both probe and DUT) where the probe is moved linearly along the z-axis and the DUT rotated along ϕ direction. Similar to the SNFS, the CNFS also introduces an error due to the DUT positioning. It also requires a smaller experimental time than the planar technique, as the complete scan is covered in single experiment. However, it is difficult to set up as it involves an apparatus that will support the movement of the probe and

DUT. Probe positioning errors introduced during measurement also limits the application of the CNFS.

The planar near field scanning (PNFS), unlike the SNFS and CNFS, is carried out by moving the probe only instead of the DUT or probe-DUT. As a result, the error due to DUT positioning is eliminated as the DUT remains stationary. Though some planar near field scanning techniques may require the movement of probe and DUT, 3D scanner can be used instead to avoid the movement of DUT.

To capture the entire fields surrounding the DUT, the planar scan is repeated over the planes surrounding it. This invariably results in a significant increase in the experimental time when compared to SNFS and CNFS. However, due to higher computational cost of the SNFS and CNFS, the PNFS is often preferred.

Data acquisition in the planar near field measurement can be achieved through three different configurations which are; plane bipolar, plane polar and plane rectilinear configuration as shown in Fig. 2.4.

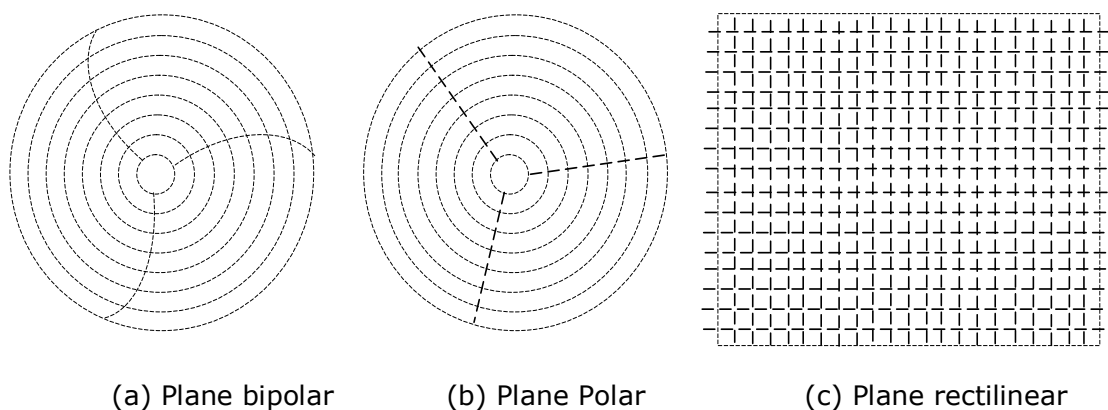


Fig. 2.4. Planar near-field scanning configuration [7].

The plane bipolar and plane polar configurations involve an arc shape movement of the probe [7]-[10]. In the plane bipolar, the probe sweeps out an arc in 2 dimensions whereas in the plane polar, the probe sweeps out an arc in one

dimension as shown in Fig. 2.4a and Fig. 2.4b respectively. The plane bipolar and plane polar techniques involve a reduced mechanical complexity as only a single linear trajectory is required [7]. However their plane pattern corrections are complex and are often solved by the use of numerical approximations. Computational efficiency and accuracy can be maximized by using the plane rectilinear configuration as shown in Fig. 2.4c. Although a more complex physical mechanism is employed here, the mathematical simplicity it offers and the avoidance of numerical approximations, which invariably introduce numerical errors, have made it the most popular configuration of the three.

Once the near field information surrounding the PCB has been extracted through near field measurement technique as described above, a model based on infinitesimal dipoles that is capable of emulating the electromagnetic properties of the PCB, can then be developed.

2.4 Basic Principle of Equivalent Dipole Modelling

In the equivalent dipole modelling, a set of dipoles which are capable of emulating the electromagnetic characteristics of the PCB is used to replace the actual current sources on the PCB. This is based on the principle of source equivalence.

2.4.1 Source Equivalence Principle

In the source equivalence principle, the actual sources are replaced by fictitious equivalent sources. These fictitious sources are said to be equivalent within a region if they produce the same amount of fields within that region to that of the actual sources.

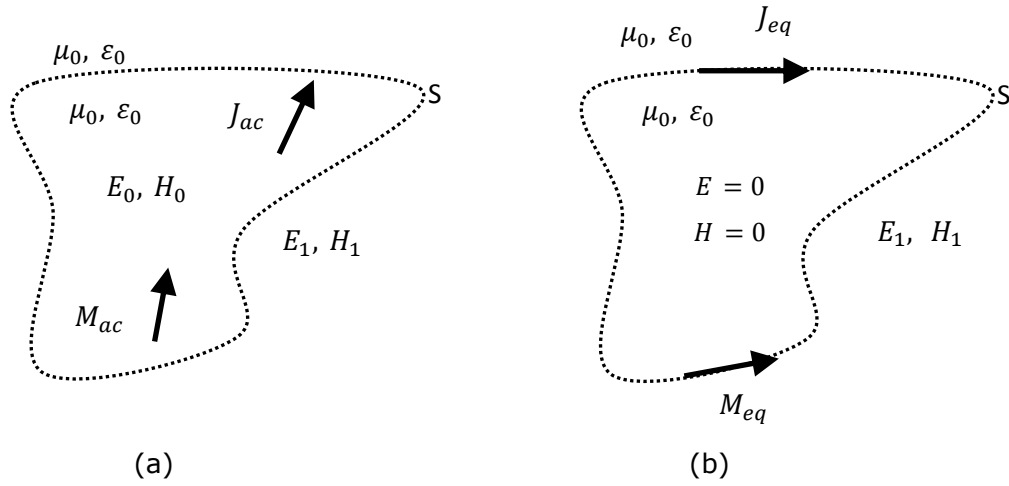


Fig. 2.5. Actual and equivalent source model.

Figure 2.5 illustrates the principle of field equivalence. For a given body, the fields produced by the actual electric, J_{ac} and magnetic, M_{ac} sources are equal to the fields E_1 and H_1 produced by the equivalent sources J_{eq} and M_{eq} which lie on an imaginary surface, S enclosing the actual sources. Electromagnetic fields (E, H) are not assumed to exist inside S of Fig. 2.5 (b) [1]. It is worth mentioning that for this assumption to hold, they must satisfy the boundary conditions on the tangential electromagnetic field components [5].

Therefore,

$$J_{eq} = \hat{n} \times (H_1 - H) \quad (2.6)$$

$$M_{eq} = -\hat{n} \times (E_1 - E) \quad (2.7)$$

The equivalent problem can be simplified further through Love's equivalence principle [11]. In Love's equivalence principle a null field is produced within the imaginary surface (i.e. $H = E = 0$), and giving

$$J_{eq} = \hat{n} \times (H_1) \quad (2.8)$$

$$M_{eq} = -\hat{n} \times (E_1) \quad (2.9)$$

Expressions (2.8) and (2.9) show that only the tangential components of the electric or the magnetic fields are required to determine the equivalent sources.

This principle was introduced by S. A. Schelkunoff in 1936 [12] and can be said to be another form of the Huygens principle [13]. The Huygens principle states that, "Each *point on a primary wavefront can be a new source of a secondary spherical wave and that a secondary wavefront can be constructed as the envelope of these secondary spherical waves.*" However unlike the Huygens theorem, the equivalent sources here are not necessarily placed on the arbitrary surface but in a closed near field observation surface. Also in the generalised source equivalence theory [14], two sources are said to be equivalent if they radiate the same field over a region in space.

From the uniqueness theorem for a lossy region of volume V , bounded by a surface S , the solution is unique if the following are specified [15]-[18]

- The tangential electric field over S or
- The tangential magnetic field over S or
- The tangential electric field over part of S and the tangential magnetic field over the remaining region of S

Thus once the tangential electric or magnetic fields are known over a closed surface, the fields in the outside region can be estimated [5].

In this work, these equivalent sources are represented as infinitesimal dipoles and each infinitesimal dipole is decomposed into its three orthogonal components through dipole expansion.

2.4.2 Dipole expansion

Through dipole expansion [19] a simple arbitrary orientated current source, D can be modelled by 3 orthogonal electric and (or) magnetic dipoles

$$D = (D_x, D_y, D_z), \quad (2.10)$$

where D_x, D_y, D_z are the 3 orthogonal dipoles along the x, y and z coordinates.

The solution is further derived as follows:

The magnetic field H_e from an electric dipole is determined from

$$H_e = \frac{1}{\mu} \nabla \times \vec{A}, \quad (2.11)$$

and for a magnetic dipole as

$$H_m = -j\omega F - \frac{j}{\omega\mu\epsilon} \nabla(\nabla \cdot \vec{F}), \quad (2.12)$$

where \vec{A} and \vec{F} are the magnetic and electric vector potentials respectively and μ and ϵ the permeability and permittivity of the surrounding media respectively.

For a z -directed point dipole, the vector potentials are derived from electric source I_e for \vec{A} and magnetic source I_m for \vec{F} [1][5]

$$\vec{A}(r) = \frac{\mu}{4\pi} I_e dl \frac{e^{-jkr}}{r} \vec{z}_0 \quad (2.13)$$

$$\vec{F}(r) = \frac{\epsilon}{4\pi} I_m dl \frac{e^{-jkr}}{r} \vec{z}_0 \quad (2.14)$$

For an electric dipole at (x_0, y_0, z_0) oriented along the z -axis, the magnetic (x, y, z) field at a distance r is evaluated by substituting (2.13) into (2.11) and given by:

$$H_x = -Pz \frac{jke^{-jkr}}{4\pi r^2} \left[1 + \frac{1}{jkr}\right] (y - y_0), \quad (2.15)$$

$$H_y = Pz \frac{jke^{-jkr}}{4\pi r^2} \left[1 + \frac{1}{jkr}\right] (x - x_0), \quad (2.16)$$

$$H_z = 0. \quad (2.17)$$

Whereas by substituting (2.14) into (2.12) the expression for the magnetic field for a magnetic dipole at (x_0, y_0, z_0) oriented in the z direction is given by

$$H_x = M^z \frac{jk e^{-jkr}}{4\pi r^4} (x - x_0)(z - z_0) \left(jkr + 3 + \frac{3}{jkr} \right), \quad (2.18)$$

$$H_y = M^z \frac{jk e^{-jkr}}{4\pi r^4} (y - y_0)(z - z_0) \left(jkr + 3 + \frac{3}{jkr} \right), \quad (2.19)$$

$$H_z = M^z \frac{jk^2 e^{-jkr}}{4\pi r} \left[\frac{(z - z_0)^2}{r^2} \left(j + \frac{3}{kr} + \frac{3}{jk^2 r^2} \right) - \left(j + \frac{1}{kr} + \frac{1}{jk^2 r^2} \right) \right]. \quad (2.20)$$

where P^z and M^z are the radiated electric and magnetic dipole moments respectively. By taking into account the contributions from other dipole coordinates (x and y), we can formulate the relationship between the magnetic field and the dipole moments for an N sampling point as

$$\begin{bmatrix} H_x \\ H_y \\ H_z \end{bmatrix}_N = \begin{bmatrix} G_x^x & G_y^x & G_z^x \\ G_x^y & G_y^y & G_z^y \\ G_x^z & G_y^z & G_z^z \end{bmatrix}_{N \times M} \begin{bmatrix} D_x \\ D_y \\ D_z \end{bmatrix}_M \quad (2.21)$$

The coefficient elements G_x^x, G_y^y, G_z^z are as given in (2.15) - (2.20) and D is either an electric dipole, magnetic dipole M or both.

Or compactly, (2.16) can be given as

$$[H] = [G][D]. \quad (2.22)$$

In this approach, the field H is extracted in the near field region of the DUT through near field measurement or complete circuit simulation. Therefore once the coefficient matrix G , which is derived from (2.15 to 2.20) or from the dyadic Greens function [5], is computed, the moment vector for the dipoles represented by D can then be determined. As the expression (2.22) involves ill-conditioned matrices, the dipole vector D which can be electric, magnetic or combination of both is determined through the solution to the inverse problem.

2.4.3 Solution to inverse problem

In principle, a sufficient number of sampling points are required to properly compute the moments of the dipoles. i.e.

$$N^s \geq N^m, \quad (2.23)$$

where N^s and N^m are the total number of sampling points and dipoles respectively. For

$$N^s = N^m,$$

The inverse problem involves a square matrix and basic techniques like Gaussian elimination can be used. But this becomes unfeasible as the size of the problem increases, thereby increasing the computational cost of this solution. In practice,

$$N^s \gg N^m. \quad (2.24)$$

leading to an over determined solution. Furthermore, as the positions of the infinitesimal dipoles are quite close, their coefficient matrix with respect to the observation points becomes similar. This accounts for the increase in the condition number of the matrix. The condition number of a matrix is a measure of how much the solution changes with introduction of error (e.g. measurement errors) in the problem [20]. The condition number of a matrix G is given by

$$\text{cond}(G) = \|G\| \cdot \|G\|^{-1} \quad (2.25)$$

where the operator $\|\cdot\|$ is the Euclidean norm [20, Chapter 3].

For this reason, a more robust technique is required in solving this ill-posed and near singular inverse problem. More on condition number of a matrix with respect to dipole modelling is presented in [20, Chapter 3].

So for a linear least square problem [21]

$$\min_x \|Ax - b\|_2, \quad A \in \mathbf{R}^{m \times n}, \quad m > n \quad (2.26)$$

the singular value decomposition (SVD) technique has been demonstrated to offer a unique solution for the inverse problem. The SVD of A is given by

$$SVD(A) = U \Sigma V^T, \quad (2.27)$$

in such a way that they also satisfy

$$A = U \Sigma V^T, \quad (2.28)$$

where U ($U^T U = I$) and V ($V^T = V^{-1}$) are matrices with orthonormal columns and Σ is a non-singular diagonal matrix.

Therefore the inverse problem for the unknown x , can be solved [21],

$$x = A^{-1}b = V \Sigma^{-1} U^T b \quad (2.29)$$

2.5 Conclusion

A simple method for characterising the electromagnetic emissions from PCBs has been presented in this Chapter. It has been shown that electromagnetic field information extracted at near field to PCB using the near field scanner can easily be used to develop a simple analytical solution based on equivalent dipoles. This model is then used to predict other desirable characteristics of the PCB.

References

- 1 C. A. Balanis, *Antenna Theory Analysis and Design*, John Wiley and Sons, New York, 2005, 3rd ed.
- 2 Golio, Mike "The RF and Microwave Handbook," Boca Raton: CRC Press LLC, 2001.

- 3 Jie Liu, Lanfang Qi, "The EMC analyzing and optimizing with high frequency interference in PCB Design", *IEEE International Symposium on Electromagnetic Compatibility*, 2006, pp.187 - 190.
- 4 C. R. Paul, *Introduction to Electromagnetic Compatibility*, Wiley, New York, 1992.
- 5 C. A. Balanis, *Advanced engineering electromagnetic*, New York: Wiley, 1989.
- 6 L. Butler, "Transmission Lines and Measurement of their Characteristics," *Amateur Radio*, October 1989.
- 7 S. Gregson, J. McCormick and C. Parini, *Principles of Planar Near-Field Antenna Measurements*, London: The IET, 2007.
- 8 L. I. Williams, Y. Rahmat-Samii, and R. G. Yaccarino, "The bi-polar planar near-field measurement technique, Part I: implementation and measurement comparisons," *IEEE Trans. on Antennas and Propagation*, vol. AP-42, pp. 184-195, February 1994.
- 9 R. G. Yaccarino, Y. Rahmat-Samii, and L. I. Williams, "The bi-polar planar near-field measurement technique Part 11: near-field to far-field transformation and holographic imaging methods," *IEEE Transactions on Antennas and Propagation*, AP-42, February 1994, pp. 196-204.
- 10 A D Yaghjian, "An overview of near-field antenna measurements," *IEEE Transactions on Antenna and Propagation*, AP-34, January 1986, pp 30-45.
- 11 A. E. H. Love, " The integration of the equation of propagation of electric waves," *Phil. Trans. Roy. Soc. London, Ser. A*, vol. 197, pp. 1-45, 1901.

- 12 S. A. Schelkunoff, "Some Equivalence Theorems of Electromagnetics and Their Application to Radiation Problems," *Bell Syst. Tech. J.* Vol. 15, pp. 92-112, 1936.
- 13 C. Huygens, *Traite de la Lumiere*, Leyden, 1660. Translated into English by S. P. Thompson, London, 1912, reprinted by The University of Chicago Press.
- 14 I. V. Lindell, *Methods for Electromagnetic Field Analysis*, Oxford Science Publications, 1992.
- 15 J. A. Stratton, *Electromagnetic Theory*. New York McGraw-Hill, 1944.
- 16 R. F. Harrington, *Time-Harmonic Electromagnetic Fields*. New York: McGraw-Hill, 1961.
- 17 R. E. Collin, *Foundations for Microwave Engineering*. New York: McGraw-Hill, 1966.
- 18 J. D. Kraai, *Electromagnetics*. New York McGraw-Hill, 1953.
- 19 J.P Wikswo and K.R. Swinney, " Scalar multipole expansions and their dipole equivalents," *J. Appl. Phys.* 57, 4301 (1985).
- 20 X. Tong, *Simplified Equivalent Modelling of Electromagnetic Emissions from Printed Circuit Boards*, PhD Thesis, University of Nottingham, May 2010.
- 21 P. C. Hansen, " Regularization Tools: A Matlab Package for Analysis and Solution of Discrete Ill-Posed Problems," *Numer. Algo.*, vol. 46, pp 189-194, March 2008.

Chapter 3

Near Field Measurement

3.1 Introduction

In this Chapter, the near field measurement technique employed in this work is presented. The existing 2D scanner used for the previous work [1] is further developed to a 3D near field scanner that is required for a complete scan of a practical PCB.

In characterizing the EM properties of PCBs and other radiating elements, details on their electrical contents are often required. The details of the electrical content of PCBs may not readily be available because of confidentiality purposes and even when available, can be computationally expensive to model on a full wave solution because of the complexities of the present day PCBs as mentioned in Chapter 1.

The equivalent dipole modelling simplifies the characterization of emissions from PCBs by not requiring a priori knowledge on the electrical content of the PCB. However, in determining the properties of the equivalent dipoles required in the equivalent dipole model, only the information on the electromagnetic field surrounding the PCB is required. The near field measurement [2] is presented in more details in this Chapter as a more efficient way of extracting the electromagnetic field information required for the equivalent dipole modelling.

In near field measurement, a low gain, low scattering cross section probe that is also electrically small is used in measuring the EM field. An output that is proportional to the field surrounding the DUT is induced in the near field probe

and recorded by an appropriate receiver. A 3D scanner is required for extracting the information, which includes the emissions at the sides of a PCB, required for characterising a practical PCB.

In this work, a loop probe is used in measuring the magnetic fields and a 3D test bench reconstructed for proper positioning of the probe. The DUT is held stationary as the probe is moved to each grid point on the measurement plane. Figure 3.1 shows the details of the measurement plane for a rectilinear planar near field measurement as employed in this work. For a 3D representation, individual planes are scanned and then combined.

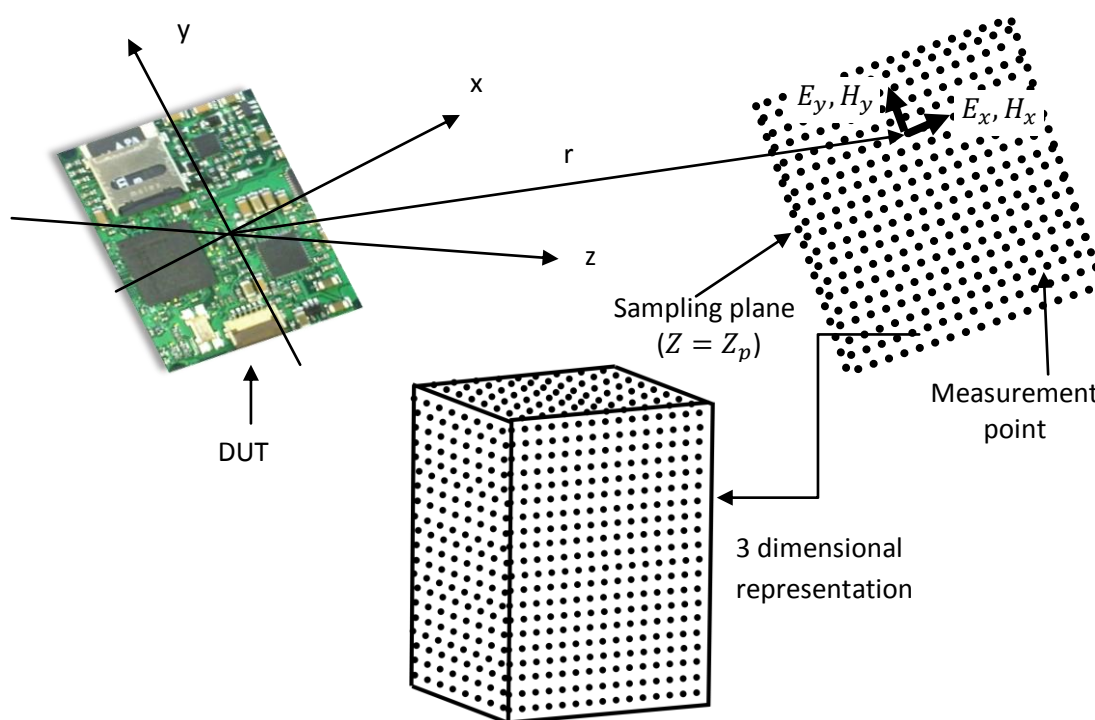


Fig. 3.1 Near field rectilinear measurement plane and the 3-D representation.

3.2 Near field measurement applications

Near field measurement is also useful in locating faults due to noisy components on complex PCBs. This application of near field scanning was carried out in the course of this work and is now presented.

The experiment was performed as a troubleshooting step to identify unintended emission sources on a Bluetooth device as shown in Fig. 3.2. This is a device placed on the body of pregnant women for monitoring foetus development. Ideally, only the Bluetooth planar antenna as shown was meant to be radiating but the performance of the device indicated the possible interference due to other unwanted radiators in the device and their coupling with the antenna.

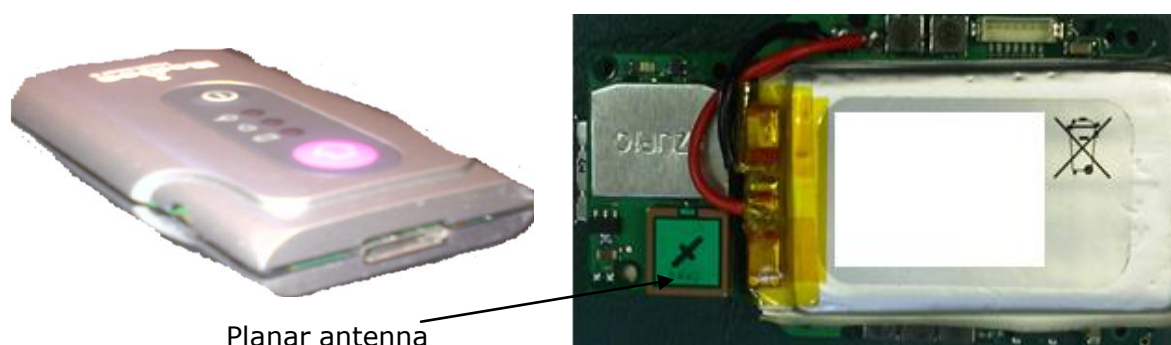


Fig. 3.2. PCB with a Bluetooth Module.

A planar near-field scan was carried out using the near field scanner at the GGIEMR Lab., University of Nottingham, while the device was in operation mode. The operation mode of the device was achieved by connecting a set of resistor components to the device electrode, which ideally simulates the human body characteristics assumed for the device performance while operating. The near field scanning was done for both the front and back of the PCB.

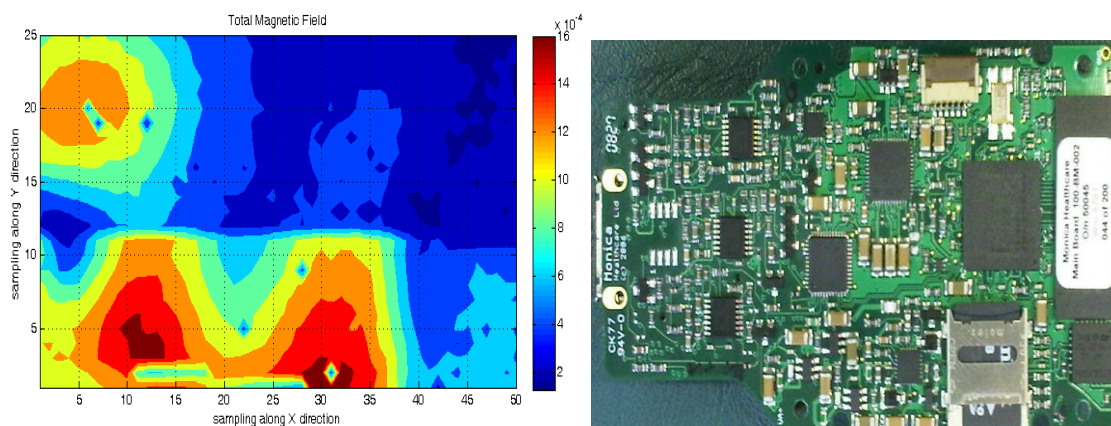


Fig. 3.3. Hot spot identification using near-field method.

This near field scanning was carried out over the full Bluetooth radio operation range (i.e. 2.4GHz -2.48GHz). At each scanning point the Max. Hold feature on the receiver (spectrum analyser EXA N9010A), a pessimistic approach, was used to pick up amplitude of the emission across the entire band. The above approach was adopted as the Bluetooth normally hops about 1600 times per second hence the centre frequency changes rapidly. Figure 3.3 shows the results of the scan on the bottom side that contains most of the electronic components. The hot spots were easily identified from the field plot. This then aided the design engineer in locating the unwanted radiating components.

3.3 Near Field Measurement Test Bench

For the purpose of characterizing EM emissions from a DUT, sufficient near field sampling points, capable of representing the near field properties of the DUT, are required. Consequently, this results in scanning over a number of points, which can easily run into thousands for a moderate PCB size. To achieve this within an acceptable experimental time and with minimised probe positioning error, automated positioner has been used. The near-field measurement is basically divided into motion control, data acquisition and data export. Whilst the latter is mostly software based, the motion control and data acquisition involve both software and hardware aspects. Therefore, to harness all these processes, automation software implemented in a control system is used.

Essentially, a program was developed that coordinates the communications between the various equipment as shown in the near field test bench schematics in Fig. 3.4. The program is expected to allow communication between the

connected devices for an intelligent triggering of subsequent processes. These processes comprise the motion control and data acquisition.

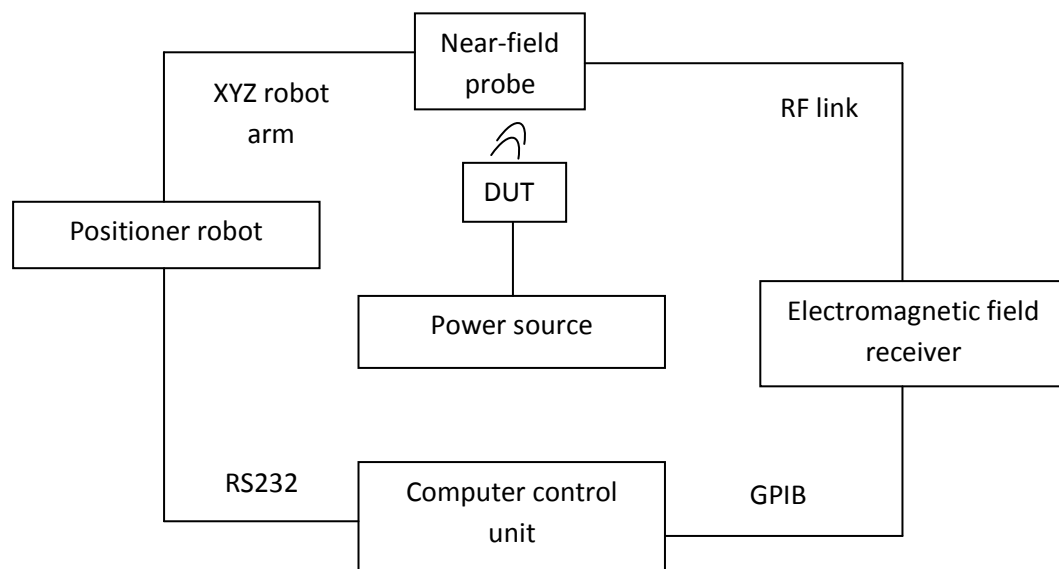


Fig. 3.4. Schematic of a basic near-field test bench.

The 3D scanning robot was modified to provide a larger scanning volume with enough isolation from the conducting parts of the robot. Consequently, the complete near field scanning of a 3D PCB is achievable with minimal perturbations that are due to the metallic parts of the scanner.

Figure 3.5 shows the test bench for near field measurement used in this work as physically implemented at the George Green Institute for Electromagnetic Research (GGIEMR), University of Nottingham, UK. RAM materials are also placed around the scanner when more isolation from environmental noise is desired especially when carrying out measurements in the ISM or GSM spectrum.

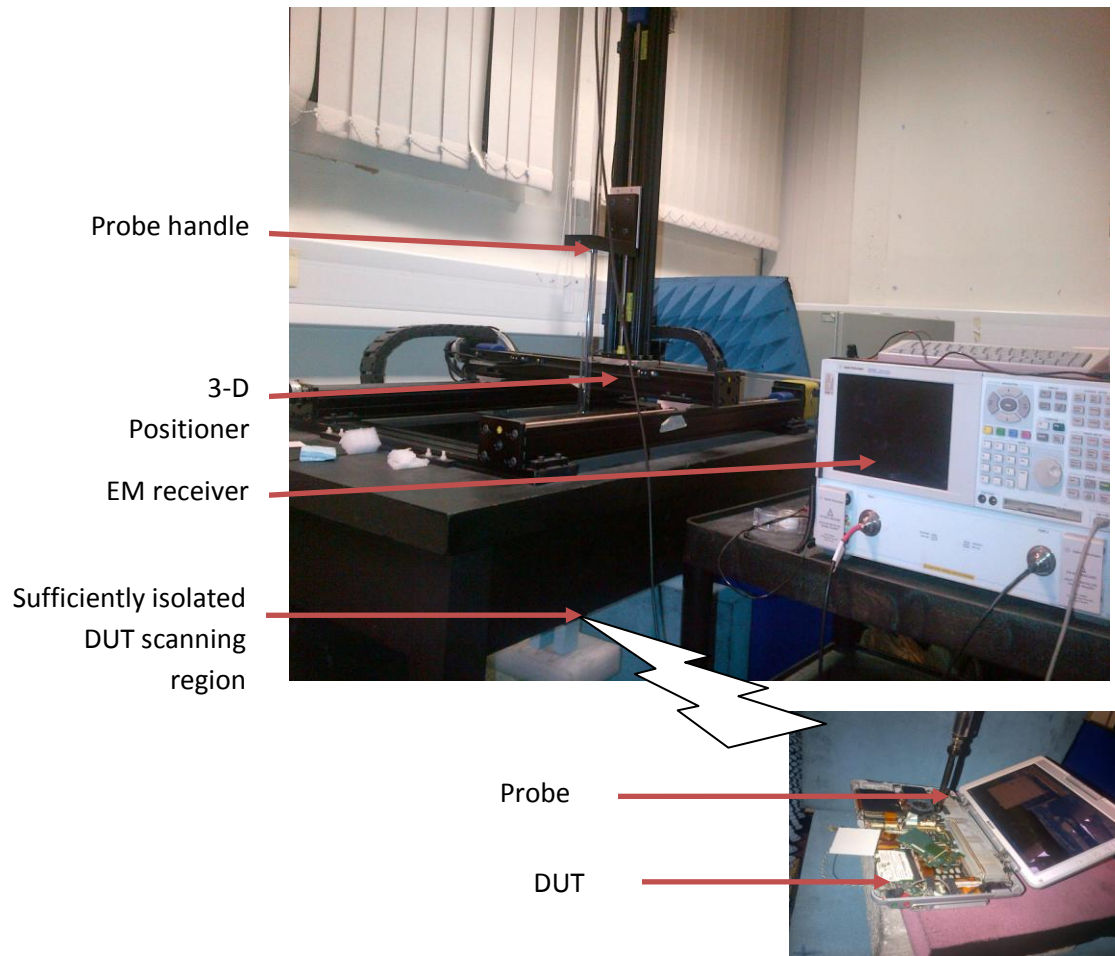


Fig. 3.5. Physical test bench for near-field measurement
(GGIEMR University of Nottingham, UK).

A simple routine for performing the near field measurement is illustrated in the flow chart diagram in Fig. 3.6. Firstly, the step sizes ($\Delta x, \Delta y$) and number of steps (width, x and length, y) are initialized.

Data is acquired after every step Δx along the width. This is repeated for x number of steps, then the probe is returned to the origin along the width whilst incrementing by a step Δy along the length. The whole process is then repeated

for y number of times. Through this, samples of thousands of points can easily be collated automatically without requiring human interaction.

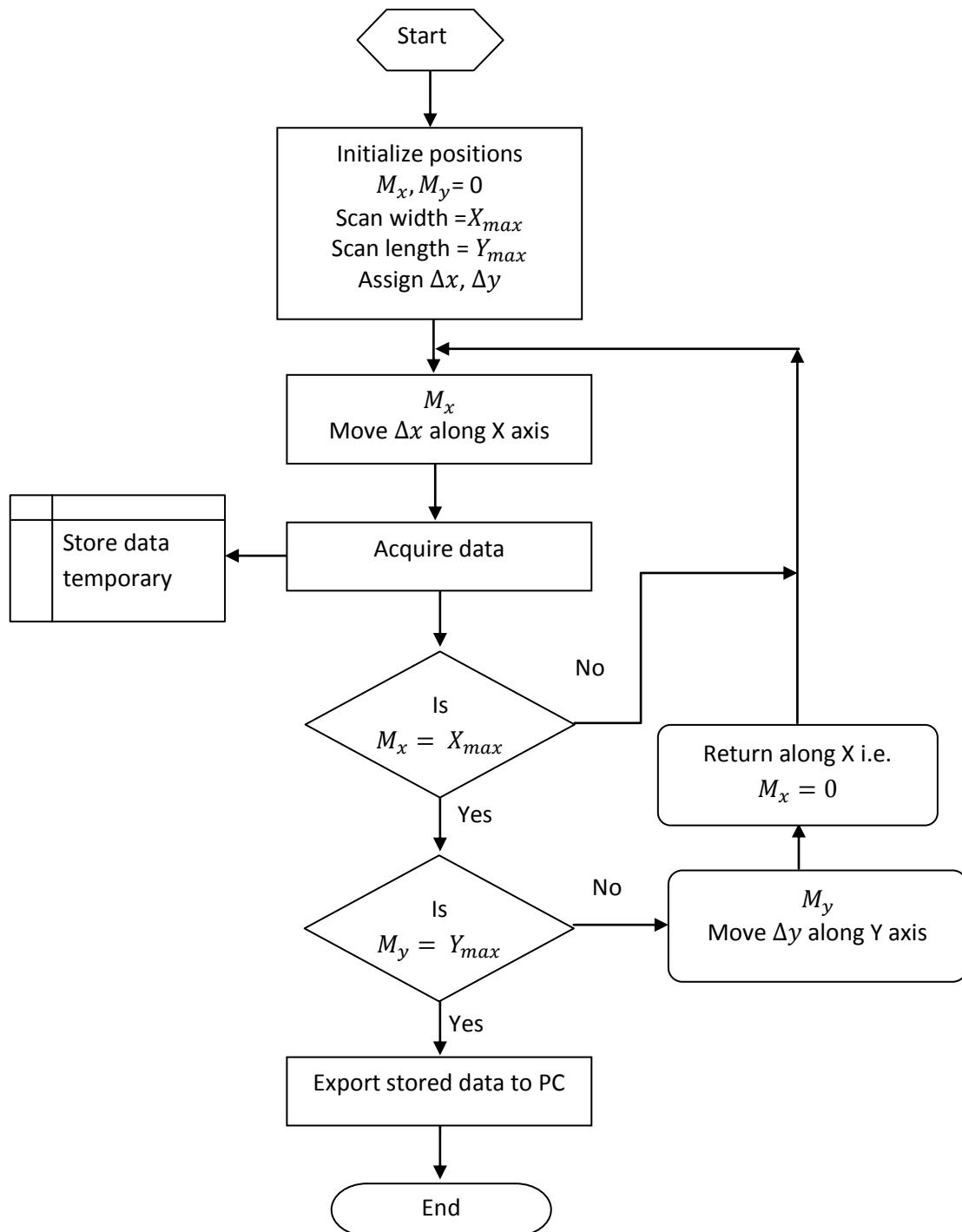


Fig. 3.6. Near-field measurement routine (Flow chart).

The trajectory for the planar scanning shown in Fig. 3.7 involves measurement in one direction. The forward movement (along x), which in this case is a uniform step, involves data acquisition whereas the backward movement only returns the probe to its origin along x as well as incrementing along y .

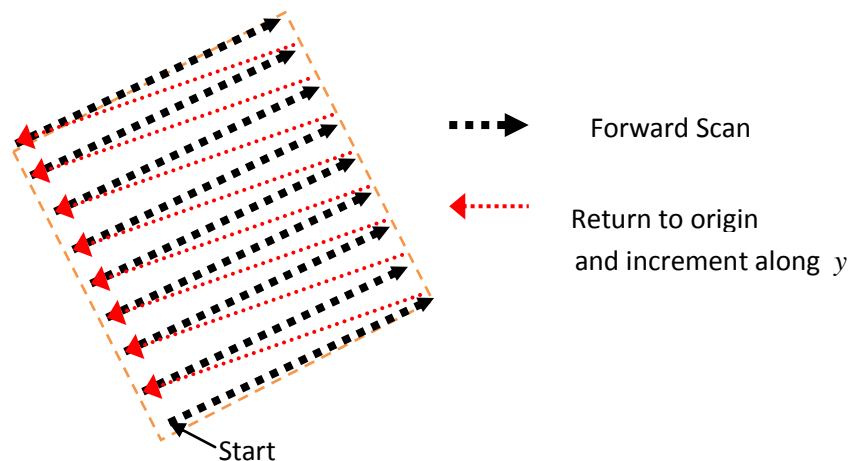


Fig. 3.7. Near-field measurement routine (Scanning trajectory).

3.4 Motion Control

Motion control involves the precise movement of objects (e.g. machines or part of machine) from one desired location to another as a function of speed, load, direction etc. Here, the 3D positioning system is used. The system comprises the 3 trajectory arms, 3 stepper motors, the intelligent microstep drives/controllers and a control PC. The basic function is to move the measurement probe to specific locations, in a 3D trajectory relative to the DUT during the measurement.

At each point, the field measurement is acquired. The set-up is shown in Fig. 3.8. The mechanical structure or control element comprises 3-axis robotic arms in the x , y and z directions. Each contains a separate stepper motor for moving the load or probe along its axis.

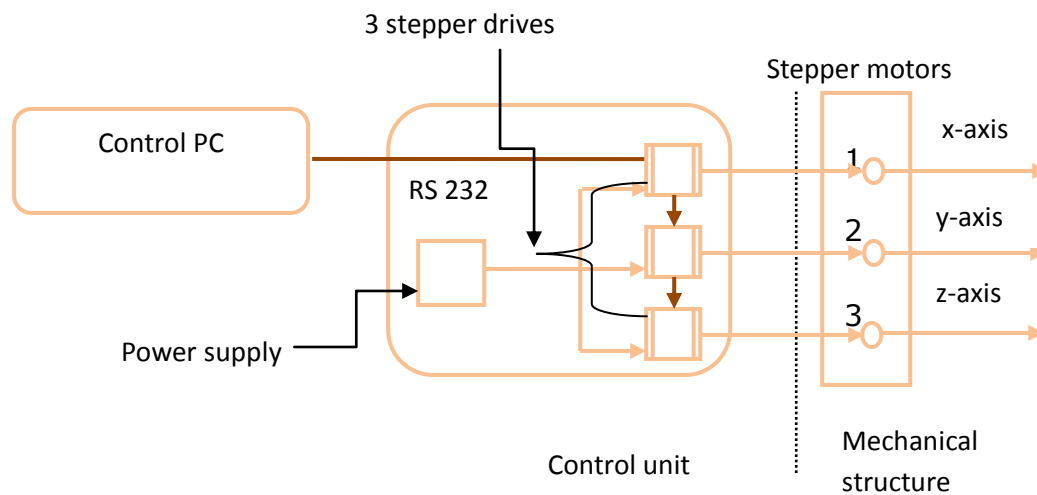


Fig. 3.8. Motion control system.

As these arms are metallic, a good isolation is required from the measurement domain so as not to perturb the experiments. The mechanical structure in a motion control system is as good as its mountings. A shaky mounting would most likely limit the stability of the mechanical structure. However, a robust mounting ensures consistency and reliable performance. The control unit contains the control software implemented on a PC and the intelligent microstep drives/controller. The microstep controller controls the stepper drives that directly communicate with the stepper motors. The stepper motors are able to produce linear motion in either forward or backward directions and they are special type of DC motors often preferred because of their robustness, high torque, reliability and simplicity in interfacing with digital controllers. Other mechanisms like hydraulic systems and linear actuators [3]-[8] can also be used to generate the mechanical energy required to produce linear movements along the arms.

3.4.1 PC based control

A Labview program ver.12 [9]-[10] was used as the automation software. It performs real time motion control operations, which include triggering movement on any specific axis and updating the distance travelled. After each

movement, the Labview triggers the receiver to acquire particular field data. As this involves many scan points, the acquired data are stored temporarily on Labview cache and then exported to the hard drive of the control PC after the experiment. The sequence of routine for automating the near field measurement has been summarised in the flow chart in Fig. 3.6 with the resulting scanning route shown in Fig. 3.7.

The routine for motion control implemented in Labview allows customization of the scan to be carried out according to the any particular PCB. These involve specifying the scanning resolution, scanning height, motor speed, scanning dimension (dependent on the PCB's dimension) etc. More details on the Labview program for motion control are provided in Appendix A.

3.5 Data Acquisition

Electromagnetic measurements are performed in the frequency or time domain. The choice of approach depends on the peculiarities of the problem and convenience. While time domain measurements can be more expensive to set-up and requires a more rigorous approach to ensure repeatability, frequency domain measurements on the other hand are easier to set-up and to perform. It is easier to get good SNR in the frequency domain using heterodyne receivers [11], [12]. Only recently have efficient time domain measurement equipment based on Fast Fourier Transform Method been made available [13]. The near field procedures discussed in this chapter is based in frequency domain.

A signal generator is sometimes used as the power source and when higher power excitation is desired an amplifier is included. At the receiving end, a spectrum analyzer (SA) is used. Alternatively a vector network analyser (VNA)

can be used as both source and signal receiver. A VNA greatly simplifies the measurement procedure when phase information is required.

The probe motor controller or scanner needs to be coordinated with the VNA or SA typically by a PC operating an interface and control program. In this work, Labview program based on the Standard Command for Programming Instrument language (SCPI) for Agilent's equipment [11] and the virtual instrument software architecture (VISA), which is a standard I/O language for instrumentation programming, was used to carry out the data acquisition. More details are provided in Appendix A.

3.5.1 Measurement using the Vector Network Analyzer

A VNA enables the field amplitude and phase measurements required for characterizing linear networks [12]. This is also useful for estimating the complex impedance for evaluating the matching of a network and building an effective error model. The vector network analyser (VNA) offers an easy way of determining the amplitude and phase of any particular measurement through its S-parameters. In order to understand the operation of VNA a brief summary of power transfer along a transmission line is provided.

The Transmission Line

Electromagnetic near field measurement setup using a VNA can be represented by the characterisation of a transmission line network. The intention here is not to provide a detailed discussion on transmission line but to mention the basics deemed necessary in understanding the remaining parts of this thesis. More details are provided in [12],[13]-[15]. A perfect impedance matched connection or link is required in order to fully transfer power from a source to the connected

load in a transmission line system. Consider the transmission line with characteristic impedance represented as Z_0 in Fig. 3.9 where a voltage source with an internal impedance Z_S , is connected to one end and then terminated in a load impedance Z_L at the other end.

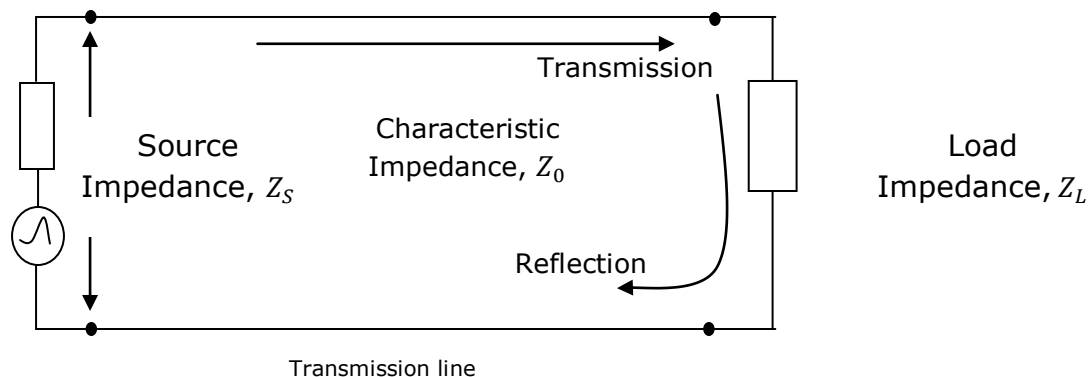


Fig. 3.9. Transmission line with load termination.

The reflection coefficient, Γ , which can be used to assess the level of the impedance matching in a transmission line network from Fig. 3.9, is given by

$$\Gamma = \frac{Z_L - Z_0}{Z_L + Z_0} \quad (3.1)$$

Through the VNA, properties like the reflection coefficient, loss and gain can be determined from the scattering parameter measurement. The scattering parameter also known as the S-parameter [12] describes the electrical behaviour of any line network as it is being excited.

In S-parameter, the numbering convention is that the immediate number following S denotes the port at which the power is received while the second number denotes the excitation port (i.e. S_{ab} is the ratio of the power in port a as a result of the excitation of port b). This represents power transmission. However when the numbers following S are the same e.g. S_{11} , this will refer to a port reflection. The S-parameter of a 2-port device has been illustrated in Fig. 3.10.

In principle, waves are propagating into and out of each of the ports. Therefore for a linear device in Fig. 3.10 the output waves amplitudes (b_1 and b_2) can be defined in terms of the input waves amplitudes (a_1 and a_2).

$$b_1 = S_{11} a_1 + S_{12} a_2 \quad (3.2)$$

$$b_2 = S_{21} a_1 + S_{22} a_2 \quad (3.3)$$

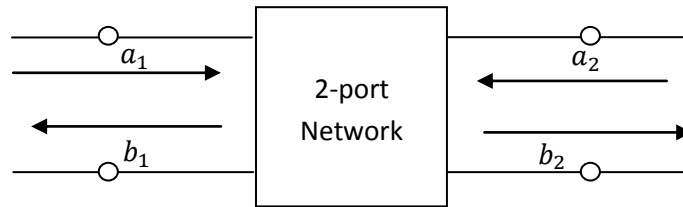


Fig. 3.10. 2-port device represented by S-parameters matrix.

$$\begin{aligned}
 S_{11} &= \frac{\text{Reflected}}{\text{Incident}} = \frac{b_1}{a_1} \Big|_{a_2 = 0} && \text{Port 1} \\
 S_{21} &= \frac{\text{Transmitted}}{\text{Incident}} = \frac{b_2}{a_1} \Big|_{a_2 = 0} && \text{excitation} \\
 S_{22} &= \frac{\text{Reflected}}{\text{Incident}} = \frac{b_2}{a_2} \Big|_{a_1 = 0} && \text{Port 2} \\
 S_{12} &= \frac{\text{Transmitted}}{\text{Incident}} = \frac{b_1}{a_2} \Big|_{a_1 = 0} && \text{excitation}
 \end{aligned} \quad (3.4)$$

Direct outputs in S-parameter formats are measurable using the VNA. These can be used to quantify the reflection and transmission characteristics of the DUT and can be expressed as vector (magnitude and phase), scalar (magnitude only) or phase only quantities.

A VNA excites a DUT with either of its ports to measure the S parameters. This assumes the DUT is a passive device with no internal sources. However, external signals can be fed into the VNA as a reference for self-powered DUTs. This requires careful disabling of the internal signal source in the VNA. Some of the vendors for VNAs offer solutions on how to this can be achieved [14].

3.5.2 Measurement using a Spectrum Analyzer

The spectrum analyzer (SA) allows the measurement of signal absolute values unlike the ratio parameters as mentioned in section 3.5.2 on VNA measurement. The SA settings need to be configured with respect to the measurement type for an optimal performance. In general, two signals of equal-bandwidth can be resolved if their separation is greater than or equal to the 3dB bandwidth of the selected resolution bandwidth filter (RBF) [16]. However, for transient signal measurements, which require a faster sweep time, moderate radio bandwidth is used. This is because the RBW increases that measurement time. Input attenuation are normally used to reduce the mismatch uncertainty [16]. However, this can also reduce the signal to noise ratio (SNR) during measurements.

For low-level signals, minimal input attenuation is required and averaging is used to improve sensitivity. The sensitivity is defined as the minimal amount of EM field that can be measured by the receiver sufficiently above the noise floor. The sensitivity can also be maximized by the use of a high gain, low noise preamplifier. Other ways of improving the performance of the spectrum analyzer include [16]

- The use of built-in amplitude correction function and frequency counter
- Optimization of the dynamic range for distortion measurements
- Use of the appropriate display mode
- The use of time gated spectrum analysis for burst signal measurements

The procedure adopted in this work for carrying out the amplitude and phase measurement using a spectrum analyzer is as explained in [1].

3.6 Near Field Measurement Probe

In most EM field measurements in the near field the DUT is often used as the source and a near field probe is the field sensor. These near field probes are designed and selected in such a way that they will perturb the experiment the least while maintaining sensitivity. Probes are also designed in such a way as to couple well in the direction of the specific field axis.

A substrate integrated waveguide and a waveguide with a suspended substrate have been used in [17] for the near field measurements of reflect array antennas. In [18], [19] an open boundary quad-ridged horn antenna has been designed and used for spherical near field measurement. This work exploited the broadband nature of a typical horn antenna and used a circular ground plane to suppress the side lobes at lower bands, thus improving its directivity.

An optically modulated scatterer technique (OMS) developed by NPL [20] has also been used for near field measurements [21]-[23]. The technique provides an electrical isolation by employing fibre optics between the receiver and the probe. Also optical probe is used, which then offers immunity to electrical loading of the DUT even at close range resulting in a minimal perturbation of the electromagnetic field being measured. This might be a good solution in extreme cases where measurements are taken at the very reactive near field. However, it can be more expensive and its cost increases with increase in the test frequency.

Other techniques like the scanning force microscopy [24], photo emission sampling [25], electro-optic sampling [26] and electron beam sampling [27] have also been used in near field mapping. However, most of these techniques can be quite expensive to set-up.

Probes in the form of monopole or dipole antennas are used in this work for receiving electric fields whereas those in the form of loop antennas are used for magnetic fields. Figure 3.11 shows a typical set of commercial probes for near field measurements.



Fig. 3.11. Commercial near field measurement probe [27].

3.6.1 Electric field probe

A short dipole antenna is used as a standard for electric field measurement [28]-[29]. The input impedance of a short dipole is strongly capacitive [30]-[31] therefore frequency independent response characteristic can be achieved by capacitive loading of a short dipole antenna. Also according to [32]-[33], a diode is added to rectify the induced RF voltage. The circuit diagram for a short dipole is as shown in Fig. 3.12.

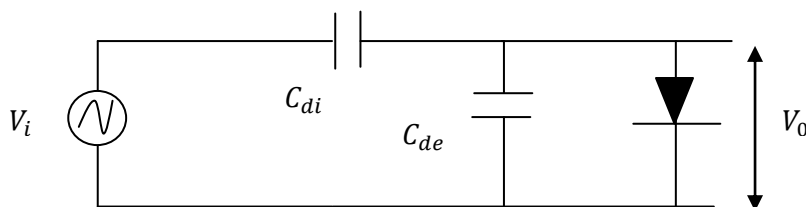


Fig. 3.12. Equivalent circuit of an electrically short dipole with a diode load.

The RF voltage induced in the dipole by the electric field is represented with V_i , where C_{di} and C_{de} are the self-capacitance of the short dipole and the gap

capacitance across the centre terminals which also comprises the diode capacitance respectively. The RF voltage output appearing across the gap and diode at the centre of the dipole is represented with V_0 . Therefore the expression for the output voltage is given as

$$V_0 = \frac{C_{di}}{C_{di}+C_{de}} V_i \quad (3.5)$$

The signal is demodulated by the diode while the diode capacitance ensures a flat frequency response of the probe up to its first natural resonance. Resistive loading of the short dipole is used to attain flat frequency response at higher frequencies than the natural resonance. This is achieved by suppressing the natural resonance through resistive tapering [33]-[36]. Figure 3.13 shows a simple dipole for transverse electric field measurement with two outputs. The measured electric field is determined by the linear combination of the outputs. For the tangential electric field component, the differential mode voltage of the probe outputs is used. For measuring the normal electric fields, the monopole antenna is used. Also for higher sensitivity, a standard half-wave dipole can be used.



Fig. 3.13. Fabricated E-field probe [21].

3.6.2 Magnetic field probe

The magnetic field probes consist of electrically small loop antennas. The loop probes are able to couple well with magnetic fields because of their inductive properties. With a loop probe design, a flat frequency response is achieved through resistive loading [30]. The equivalent circuit diagram for a loop probe is

given in Fig. 3.14. The resonance of the loop probe is determined by the loop inductance and loop capacitance as shown in Fig. 3.14. However to achieve a flat response in the frequency range of interest, the quality factor Q is reduced by the means of loading resistance.

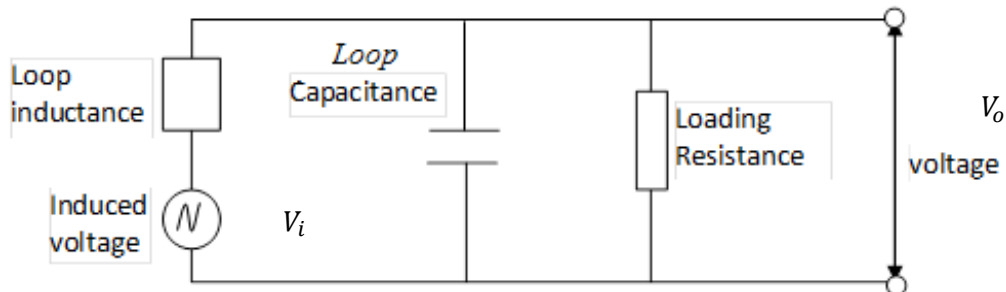


Fig. 3.14. Equivalent circuit for an electrically small loop antenna.

The induced voltage, V_i can be determined through the Maxwell-Faraday's law and given by the integral

$$V_i = \int_0^{2\pi} E_i \cdot dl = -j\omega\mu H_i NS \quad (3.6)$$

where E_i , μ , H_i are the incident field, permeability of the loop region and normal component of the magnetic field. l , N and S are the circumference, number of turns and the area of the loop respectively. At low frequencies, the loop capacitance can be neglected, the output voltage, $V_o \approx V_i$.

Figure 3.15a shows the fabricated loop probes (probes 1, 2, 3) and a commercial loop from ETS Lindgren. The S11 plot in Fig. 3.15b was used to study the probes' return loss as presented in section 3.5.1. While the commercial probe maintains a near flat response, the fabricated probes also maintain flat frequency response before their first resonance. However the return losses including that for the large probe are higher than -10dB. The probes can be said to have a good frequency response in the range from dc to about 1GHz. Probe 1, Probe 2 and Probe 3 have their 1st resonances at 1.5GHz, 1.75GHz and 2.3GHz

respectively as summarised in Table 3.1. They maintain good performance at frequencies below these resonances. However, the commercial probe showed a broader performance up to 3GHz.

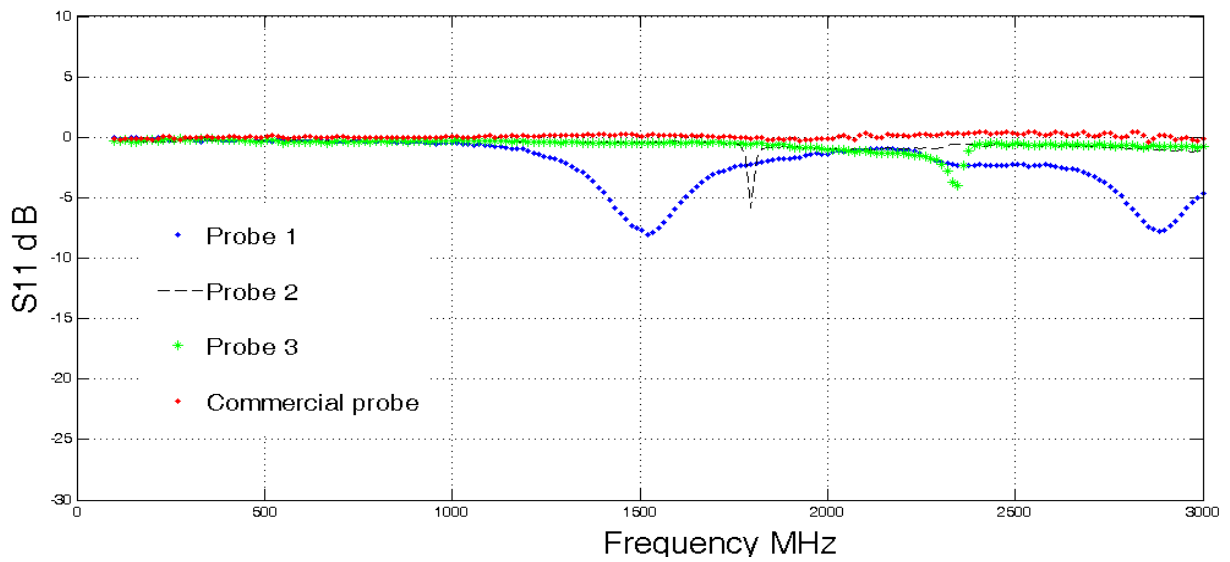
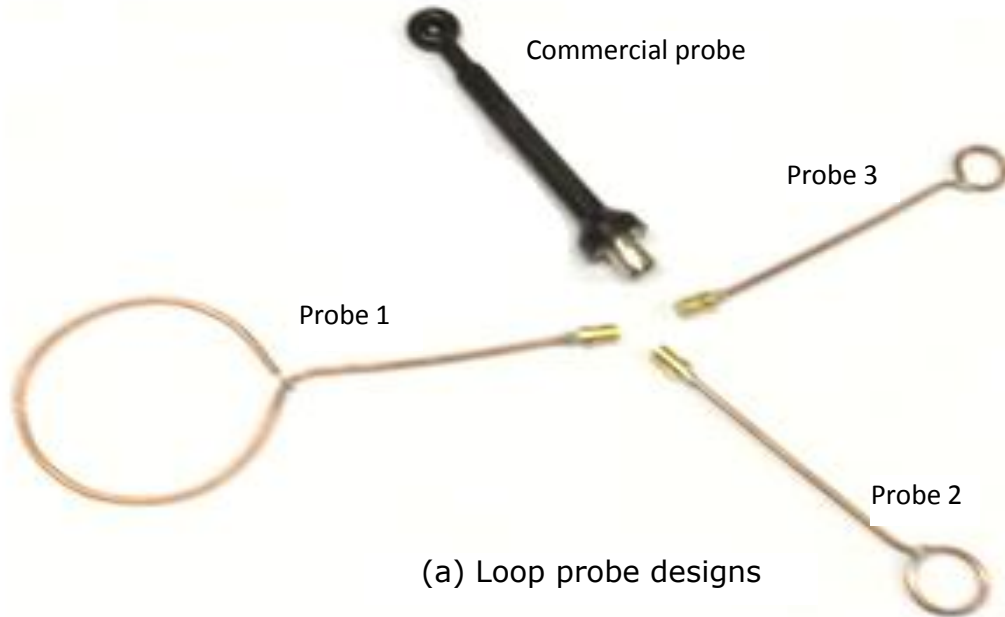


Fig. 3.15. Loop probe characteristics.

The loop probes were designed and fabricated by Harikrishna Patel as part of his BEng project, under my guidance with Dr Angela Nothofer as his main supervisor

Table. 3.1. Probe characteristics.

Probe	Diameter	Upper resonance
Probe 1	65mm	1.52GHz
Probe 2	20mm	1.8GHz
Probe 3	15mm	2.35GHz
Commercial probe	10mm	-

3.7 Error Analysis and Probe Correction

Verification and validation of measurements are required for repeatability. The numerical techniques based software packages, Concept-II [37] and CST [38] microwave, were used to validate the planar near field measurements. The Concept-II is a method of moments (MoM) [37] based solver that employs the surface integration of currents in solving EM field problems in frequency domain. CST Microwave is a volume discretisation based finite integration technique (FIT) [38] for solving EM problems in both frequency and time domain. Comparisons for the results from these EM tools and planar near field measurement are shown later. Also these techniques are used for the validation of the modelling in the subsequent chapters.

To aid comparison of experiments, the same assumption is adopted to minimize the possible differences in setting up the various experiments. A typical set up is shown in Fig. 3.16.

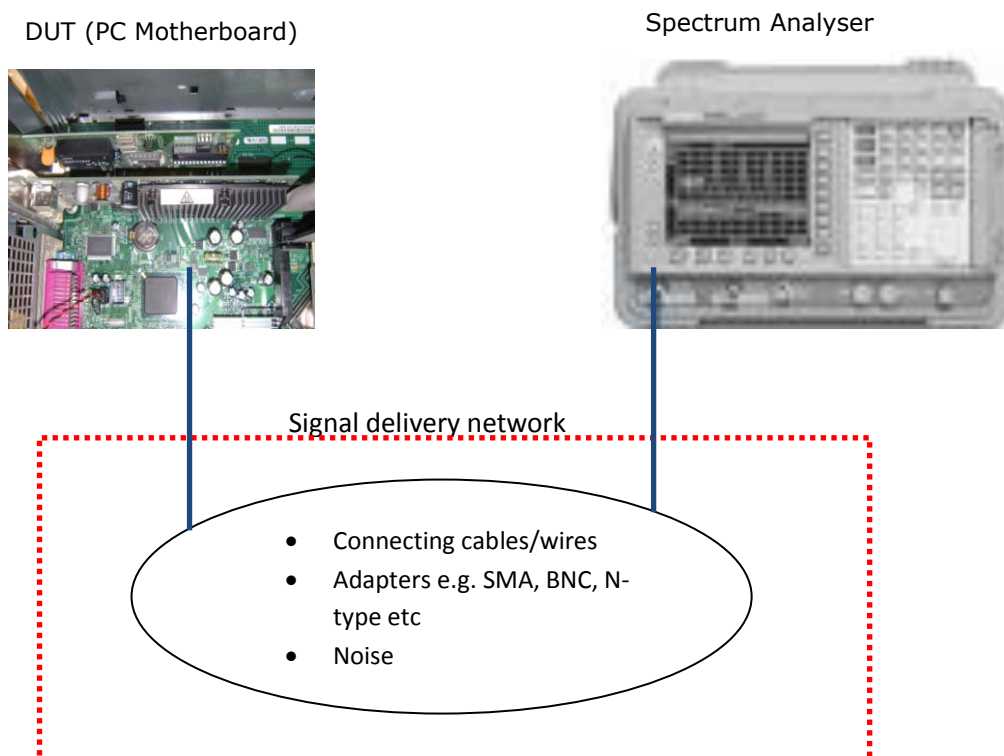


Fig. 3.16. Signal delivery network in a near-field measurement.

In comparing measurement results with those from simulation techniques, there is a need to calibrate out the contributions from the signal delivery network as shown in Fig. 3.16 which is often not accurately represented in the simulation approximations and leads to systematic errors.

The signal delivery network involves the contributions from the environment in the form of noise, the properties of the connecting cables and RF adapters in addition to the probe parameters. These effects are minimized through error correction.

3.7.1 Error analysis

The model of a measurement procedure can be viewed theoretically [39] as a transfer function on the input measurand q , being mapped to an output value of the measurand, n . However, in practice, such an ideal system is not easily achievable. This is because of uncertainties and other sources of errors introduced in the experiment. Figure 3.17 represents a more realistic block diagram for a practical measurement.

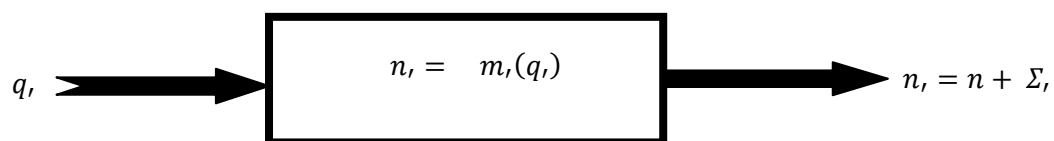


Fig. 3.17. Functional block diagram of a realistic measurement.

The additional term Σ_r represents the errors in the experiment. These errors are introduced at the input and mapping stages. Therefore the total error, Σ_r , has to be systematically determined and quantified where possible, then removed by post processing to minimize the ambiguity in experimental results. This is achieved through error correction [40]. The errors are grouped into systematic and random errors. Whilst the random errors are not deterministic, the systematic errors are due to probe parameters, environmental coupling, receiver

unit, positioning and the connecting links. The total error in the near field scanning is evaluated from the expression [41]

$$\Sigma_{\zeta} = \sqrt{3\delta_R^2 + \Sigma_i \epsilon_i^2} \quad (3.7)$$

where δ_R and ϵ_i are the standard deviation of the random noise and the systematic uncertainties.

3.7.2 Near field probe correction

Ideal near field probes possess a number of important characteristics. These include broadband, non-resonant, electrically short, minimal perturbation to measurement, strong coupling to the measured field but good isolation from all other fields (i.e. other coordinates and field types [E or H]) and output proportional to the measured field. Although the voltage measured may not be the exact voltage induced by the incident field, linearity is expected for different power levels. Furthermore, the probe performance factor (*PPF*) can then be used to determine the appropriate fields from the voltage at the output of the probe, V_p for any particular frequency at the probe's position.

The *PPF* for the electric field, E_{Cr} is given by

$$PPF = \frac{E_{Cr}}{V_p} \quad (3.8)$$

Probe performance factor using GTEM cell

The probe performance factor, which is a function of uncertainties and irregularities in manufacturing, is needed for converting the voltage output of the probe to its absolute field. This is carried out through the calibration process. An experimentally based calibration process is demonstrated.

Firstly, this was carried out on a calibrated GTEM cell, which provides stable and predictable fields that are not significantly disturbed by the insertion of probes under test (PUT) [42]. Figure 3.18 shows the set-up for the experiment.

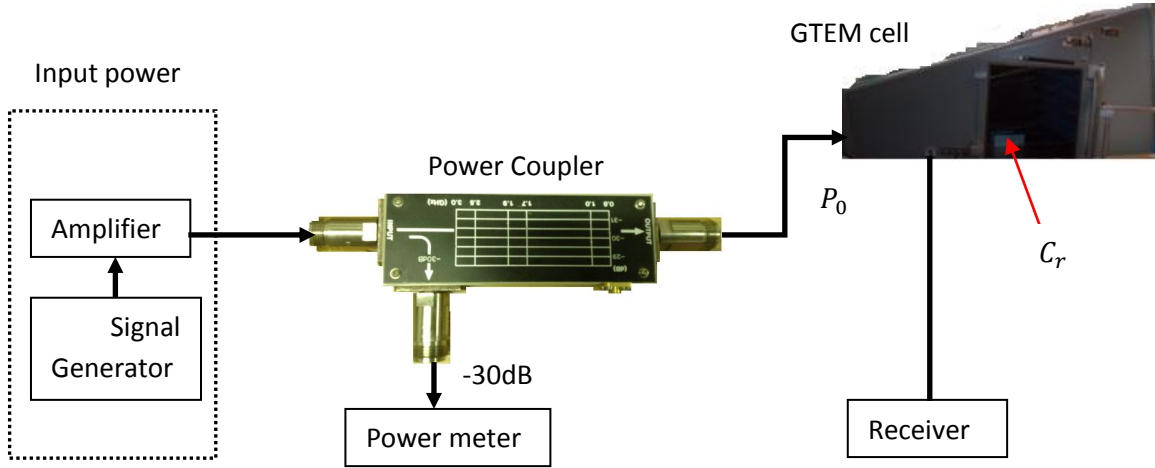


Fig. 3.18. GTEM set-up for probe calibration.

The receiver is either the optical electric field probe receiver or the spectrum analyzer depending on which field probe is being used. The input power to the GTEM cell is monitored via a power coupler with a power meter. In order to verify the proper functioning of the GTEM, a full traceable, calibrated E-field probe and optical receiver unit was initially used to directly measure the E-field for the GTEM excited with a known power, P_0 . The optical probe was used to take reading, E_1 in V/m a calibrated region C_r , in the GTEM cell. The GTEM cell is then used to calibrate the probe once its performance is confirmed by the optical E field probe.

The field, E_{C_r} at an observation point C_r within the GTEM cell, can be approximated by

$$E_{C_r} = \frac{V_0}{h_{C_r}} (V/m) \quad (3.9)$$

where V_0 and h_{C_r} are the voltage at the GTEM's input and the septum height at region C_r respectively. Assuming good impedance matching at the input to the

GTEM cell, the voltage at the GTEM input can be assumed to be the same as that at C_r . For a properly matched GTEM cell, difference in the actual field, E_{C_r} and measured field, E_1 tends to zero such that the ratio F_r given by (3.10) tends to zero.

$$F_r = \frac{E_{C_r} - E_1}{E_{C_r}} \quad (3.10)$$

The frequency variation of F_r is provided in Fig. 3.19. A maximum variation less than 20% at certain frequencies was observed and the variation observed may be due to the sagging of the septum causing impedance mismatch and other wear and tear. Adequate impedance match can be assumed at frequencies with very small F_r values.

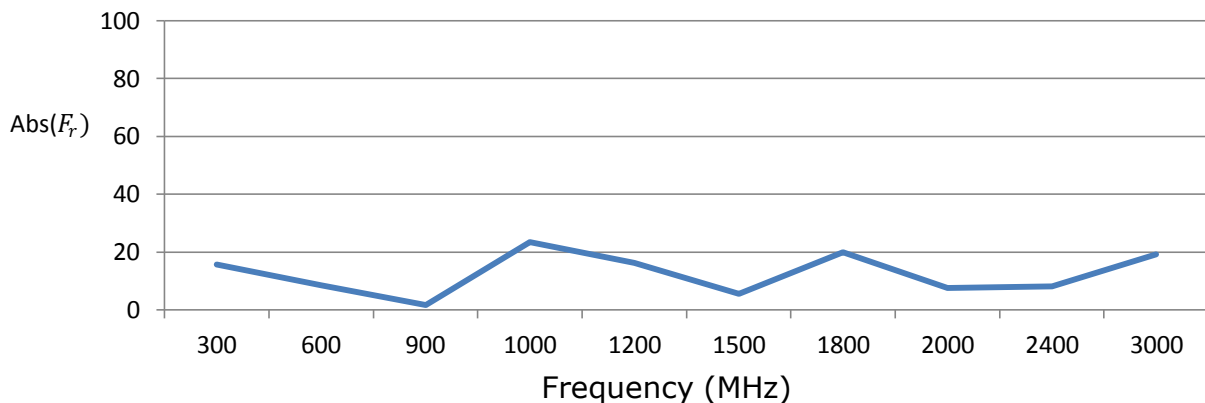


Fig. 3.19 GTEM impedance matching frequency response for 20dBm

The TDR (time domain reflectometer) response at the GTEM terminal was also measured. The result from the TDR measurement is as shown in Fig. 3.20 which shows a uniform impedance match within the range 47-51 Ω . The ripples observed around $t = 0$ is due to the connectors and connecting cables. In TDR measurement, a short pulse is sent into the GTEM cell. A perfectly matched GTEM cell with uniform impedance will result in zero reflection.

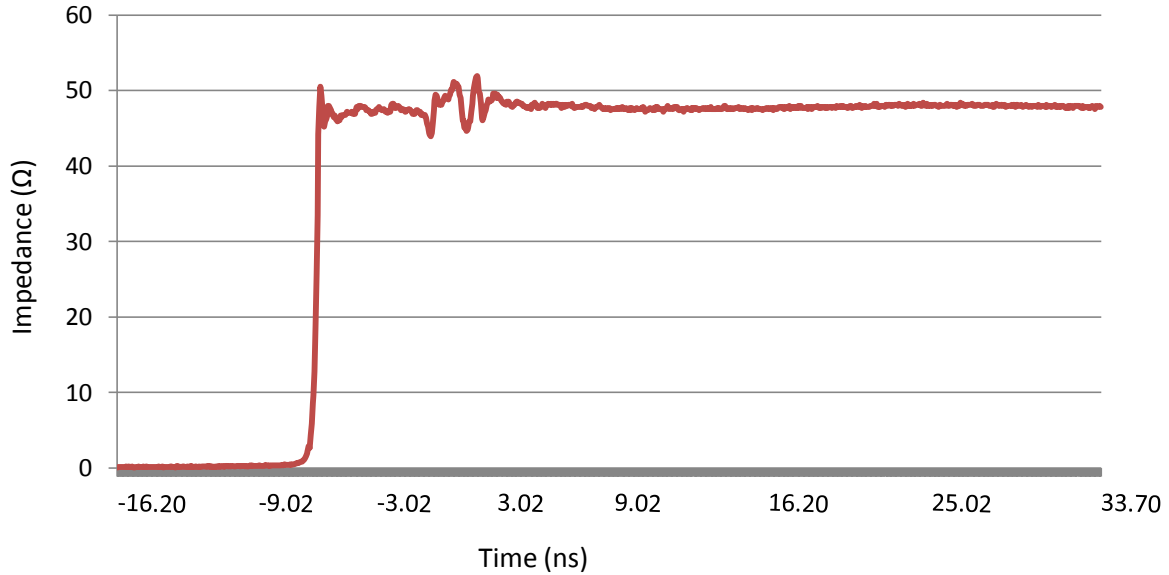


Fig. 3.20. TDR impedance measurement of the GTEM cell.

Therefore, the degree of reflection provides information on the impedance matching of the cell with high reflection meaning insufficient impedance matching and vice versa.

Given satisfactory performance of the GTEM cell, the experiment to calibrate the probe is carried out. The probe under test (PUT) connected to a spectrum analyzer is used as the receiver. The PUT whose probe performance factor (PPF) is to be determined is placed in the calibrated region, C_r . Voltage readings V_p are taken and recorded by the spectrum analyzer. The PPF is then computed through (3.8).

The expression (3.8) is sufficient for an electric PUT. However for a magnetic PUT, an additional step is required. Since the functionality of a GTEM cell ensures close to uniform free space impedance within the calibrated region of the cell, the magnetic probe performance factor for magnetic field, PPF_H is then

$$PPF_H = \frac{PPF}{377} = \frac{H_{cr}}{V_p} \quad (3.11)$$

So for future measurements with the calibrated probes, the received voltage values are multiplied by PPF and PPF_H to get their absolute field values for electric and magnetic field probes respectively. Furthermore, taking into account the measurement uncertainties in a practical setting

$$PPF_H = \left(\frac{H_{cr}}{V_p} \right) + \Sigma_{\zeta} \quad (3.12)$$

where Σ_{ζ} is the total measurement error. The PPF of the magnetic probe used in this work was determined using this technique and is shown in Fig. 3.21 over 0.1-1GHz spectrum.

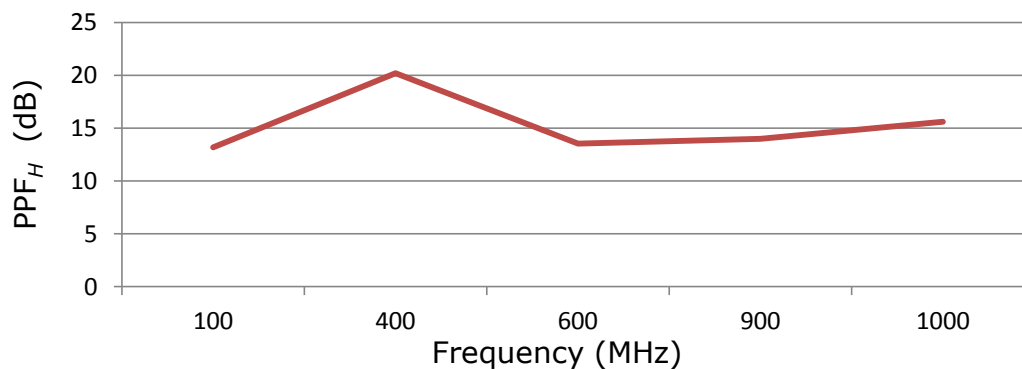


Fig. 3.21. Probe Performance factor for 10mm loop probe, 14 dB at 900MHz.

Performance factor through computer simulation

A simulation technique was also used to estimate this performance factor of the measurement probe. This is demonstrated using the magnetic loop probe of 10mm diameter. A PCB of dimension 80mm X 50mm with a 40mm X 5mm trace was simulated on the MoM-based Concept-II. Figure 3.22 shows the details of the simulation.

A dielectric layer of permittivity 4.6 was included in-between the trace and the ground plane as this is typical of FR4 substrate normally used. The PCB trace was excited with a 500mV CW at 900MHz through a signal generator and

terminated with a 50Ω load as shown in Fig. 2.22. 40×28 Magnetic field samples, H were computed at a parallel plane 10mm above the PCB.

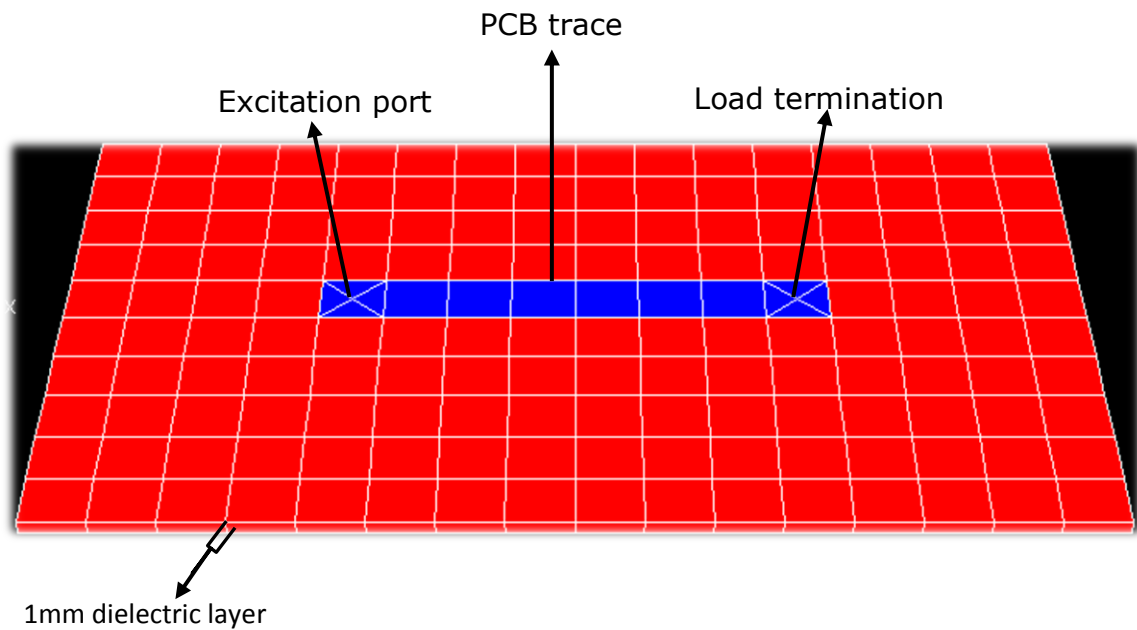


Fig. 3.22. PCB design with a simple trace.

This was also repeated experimentally using the 10mm loop probe and the practical PCB used is shown in Fig. 3.23. The near-field experiment was set-up as in Fig. 3.5 and the probe was used to record 40×28 magnetic field values as probe output voltage samples, V at 10mm above the PCB.

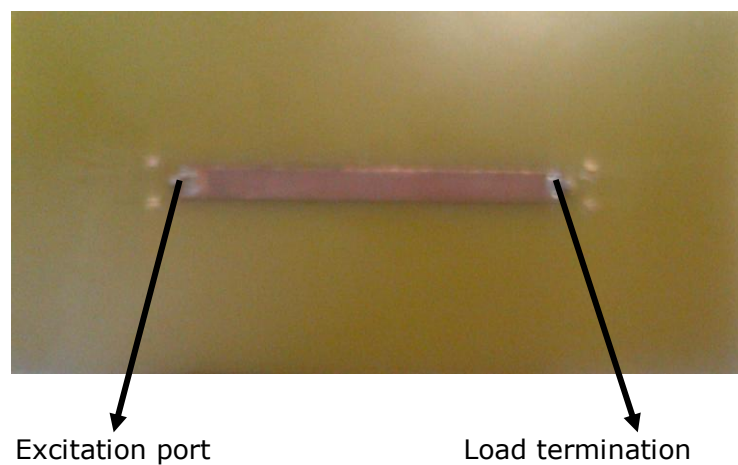


Fig.3.23. Practical PCB with simple trace.

The probe performance factor is then evaluated through the average field method using N samples (where $N = 1120$) giving the result:

$$PPF = \sum_{n=1}^N \left(\frac{H_n}{V_n} \right) / N = 4.47$$

and maximum field gave the result:

$$PPF = \frac{\max H}{\max V} = 4.67$$

These results approximate to the PPF result estimated for the probe using the GTEM cell method (i.e. 14 dB or 5.01 at 900MHz). The difference being the errors in measurement which includes background noise and cable effects. These errors are difficult to estimate experimentally due to the limits of measurable level with the near field scanning apparatus at GGIEMR. The work presented in [45] is an extensive study of the near field measurement errors and are taken as the standard for near field scanning technique. According to [1] the estimate of the errors for the near field apparatus in use at GGIEMR are summarised in Table 3.2 [1] which are amplitude measurement only. However the phase measurement is strongly correlated with the amplitude measurement, therefore phase errors can be estimated from the amplitude errors [46]. If the amplitude A of a measurand vector has an uncertainty Σ_{ζ} , the phase uncertainty is given by

$$\Sigma_{phase} = \sin^{-1} \left[\frac{\Sigma_{\zeta}}{A} \right] \quad (3.13)$$

Table 3.2 Typical bound of error source in near-field measurement

Systematic error budget in near-field measurement	Typical Value (dB)
AUT alignment	0.13
Probe polarisation ratio	
Probe gain measurement	
Probe relative pattern	

Systematic error budget in near-field measurement	Typical Value (dB)
AUT/probe multiple reflections	0.13
Probe alignment error (angular error)	0.05
Probe x, y, z positional errors	
Normalization constant (specific types of gain measurement)	0.00
Data point spacing (aliasing)	0.00
Measurement area truncation	0.00
Impedance mismatch factor	0.25
Receiver nonlinearity	
Receiver dynamic range	
System phase error	
Room scattering	0.05
Leakage and crosstalk	0.05

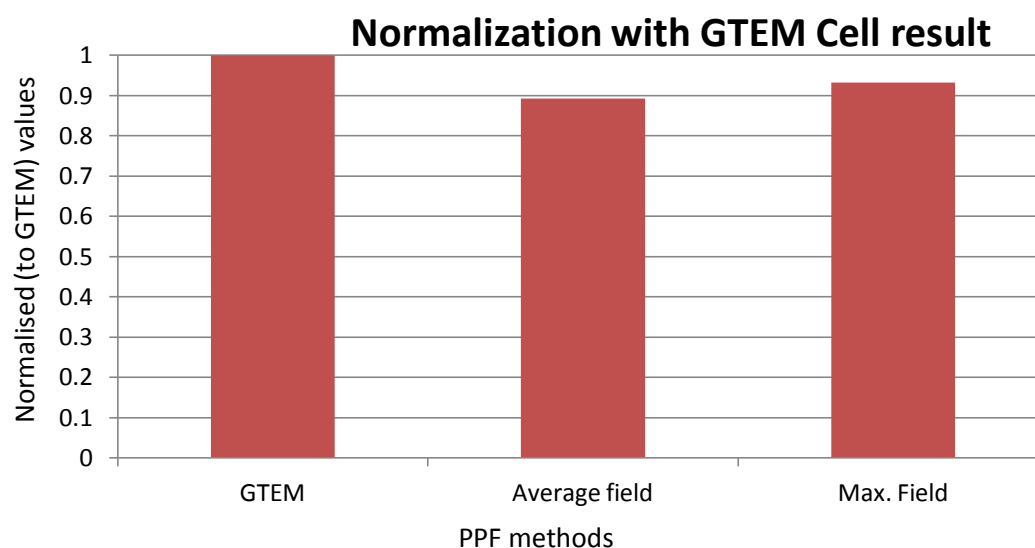


Fig. 3.24. PPF estimation comparison normalised to GTEM result.

Figure 3.24 compares the PPF obtained through the various methods by normalizing these results with that of the GTEM method. A close agreement is observed. In addition, it shows that the PPF obtained by comparing the maximum values (maximum method) yielded a slightly better agreement with

the GTEM measurement than that obtained through averaging (average method). Statistically, this is not expected, however it can be due to the noisy fields picked up at vicinities far away from the current trace on the PCB (random problem). In the averaging method, these noisy signals which may not be accounted for in the simulation are included whereas in the maximum method their effects are reduced.

Probe disturbance factor

Near field probes are selected based on their inherent characteristics. The size of the probe will determine its ability to perturb the fields being measured, with smaller probes having the least disturbance factor. However, the sensitivity of a probe also decreases with the size especially the loop probe according to [1]. A good compromise is then required. Also for a low-level signal experiment that requires minimal distortion, as is often the case, a preamplifier can be used.

Small sized probes offer minimal perturbation to the experiment with good spatial resolution. The spatial resolution of an E-field probe can also be improved by ensuring that the probe is placed at a distance R , to the DUT in such a way that [43], [44]

$$R \ll \frac{\alpha}{2\pi} \quad (3.14)$$

where α is the largest dimension of the DUT.

The probe disturbance factor (*pdf*) was evaluated experimentally. This was performed in the GTEM cell with similar setup as in Fig. 3.18 and is given as

$$pdf = \frac{field_{actual} - field_{perturbed}}{field_{actual}} \quad (3.15)$$

A known power was used to excite the GTEM cell while the electric field optical probe was used to take readings at a calibrated region in the GTEM. The probe under test (PUT) was introduced and positioned directly above the optical probe. The PUT was introduced so as to study the disturbances caused by its presence and was not used to take any reading. Therefore all readings were taken from the optical probe receiver. The readings were taken at different separating distances d , of the PUT from the optical probe. These results were then compared to the recorded measurement results made with the optical probe receiver in the absence of the PUT so as to estimate the PUT's *pdf* using the expression (3.15). This evaluates the effect of the probe to a transverse EM wave in GTEM. In the previous work [1], the planar near field scanner approach was used to characterise the probe. However in this work, the GTEM cell is used.

The probe disturbance factor for the commercial loop probe is shown in Fig. 3.25 for frequencies between 100MHz and 900MHz. Also the *pdf* frequency response, for the fabricated probes are presented in Fig. 3.26.

Figure 3.25 shows the *pdf* to increase with frequency. This coupling as expected also decreases with an increase in the distance of separation. In Fig. 3.26, the larger probe (loop radius) produces more perturbation at any given instant (i.e. the same frequency and the same distance of separation). And like Fig. 3.25, the disturbance also increases with frequency.

Therefore the results from this experiment according to Figs. 3.25 and 3.26 demonstrate that the *pdf* worsens with increase in the size of the loop (loop radius) and at lower wavelengths.

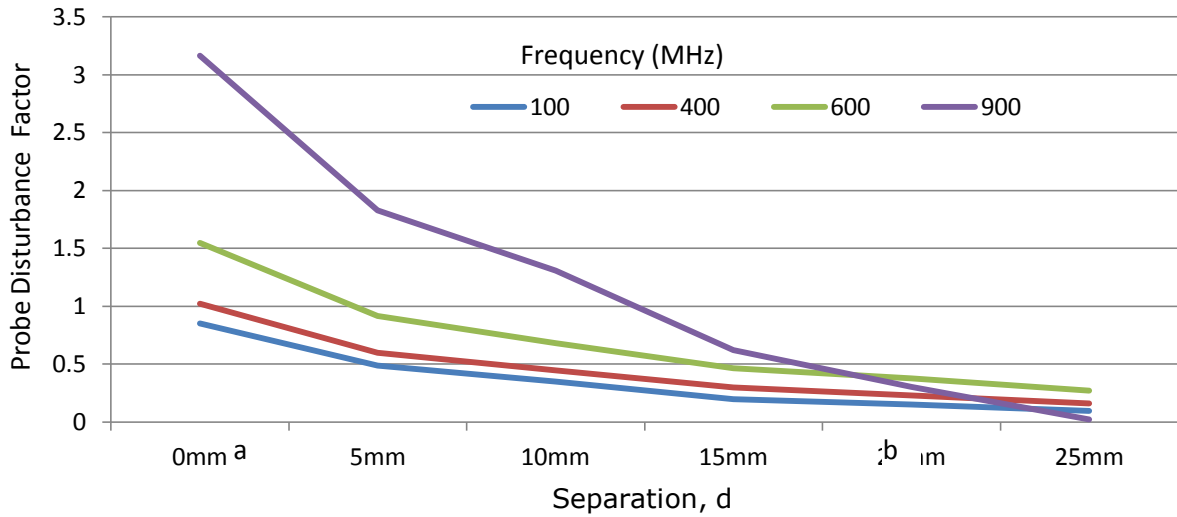


Fig. 3.25. Commercial Loop probe disturbance factor

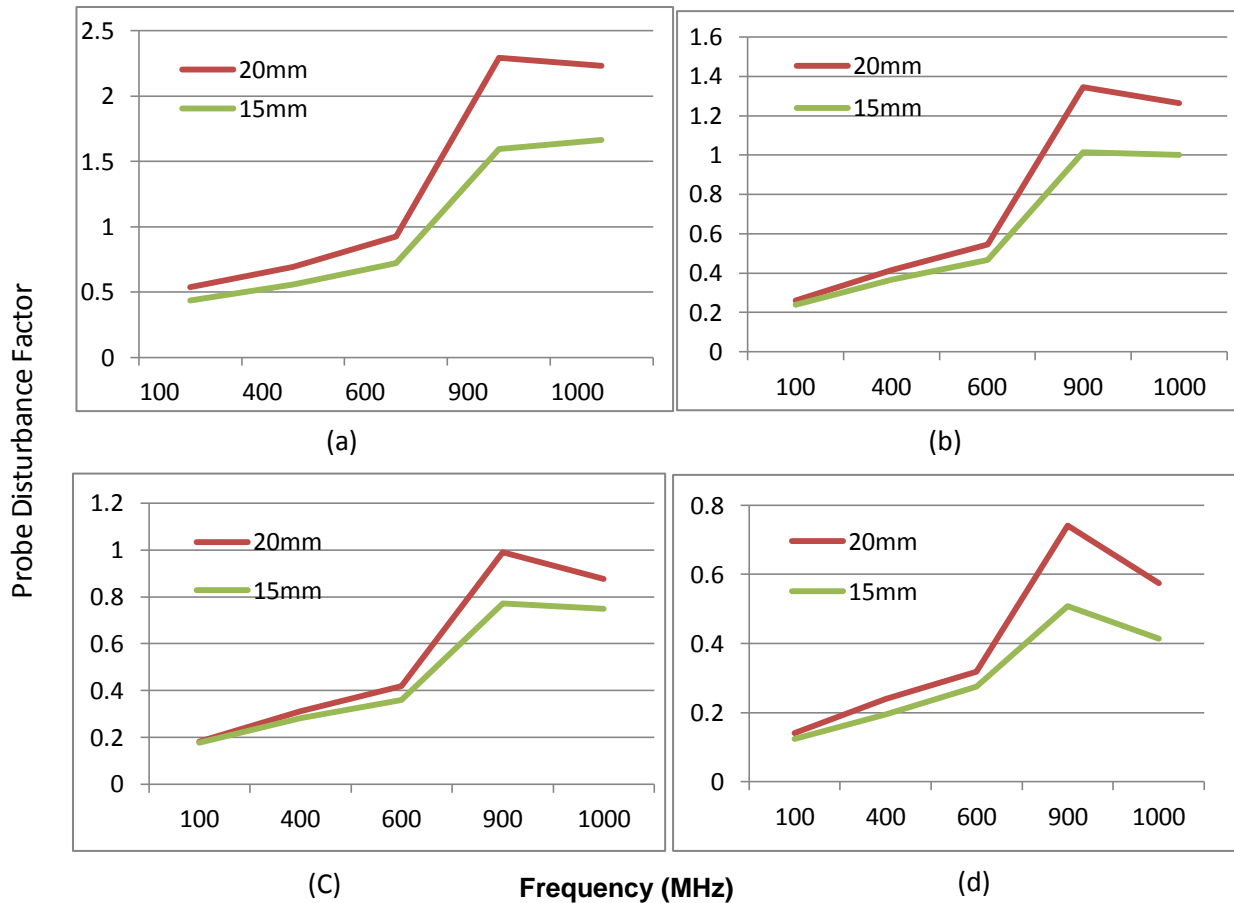


Fig. 3.26. The probe disturbance factor (frequency response) for fabricated probes of 15mm and 20mm diameter at $d =$ (a) 5mm (b) 10mm (c) 15mm (d) 20mm.

3.8 Near Field Measurement Validation with Simulation

The PPF once estimated can be used to convert the voltages picked up by the near field probes to their equivalent field values. In this section, the already determined PPF for the calibrated probes is used in the measurement and the result is compared with an actual simulation.

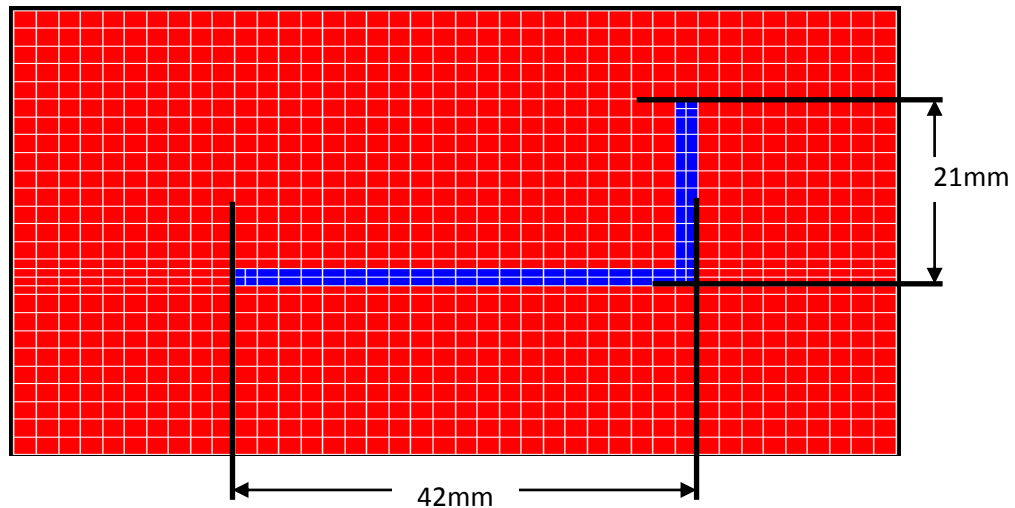


Fig. 3.27. L-trace PCB design.

Here, another PCB was designed on Concept-II. The PCB comprises a 80 × 50mm ground plane and an L trace with dimensions as shown in Fig. 3.27. This L trace was separated from the ground plane using a dielectric layer of same size with the ground plane and permittivity of 4.6. The PCB is excited with 500mV CW using a voltage source at 900MHz.

Then 40 × 28 samples were computed at 10mm above and parallel to the PCB. The near field measurement was set up and carried out as in section 3.6. The same number of near field samples as in the simulation, were also recorded with the spectrum analyser.

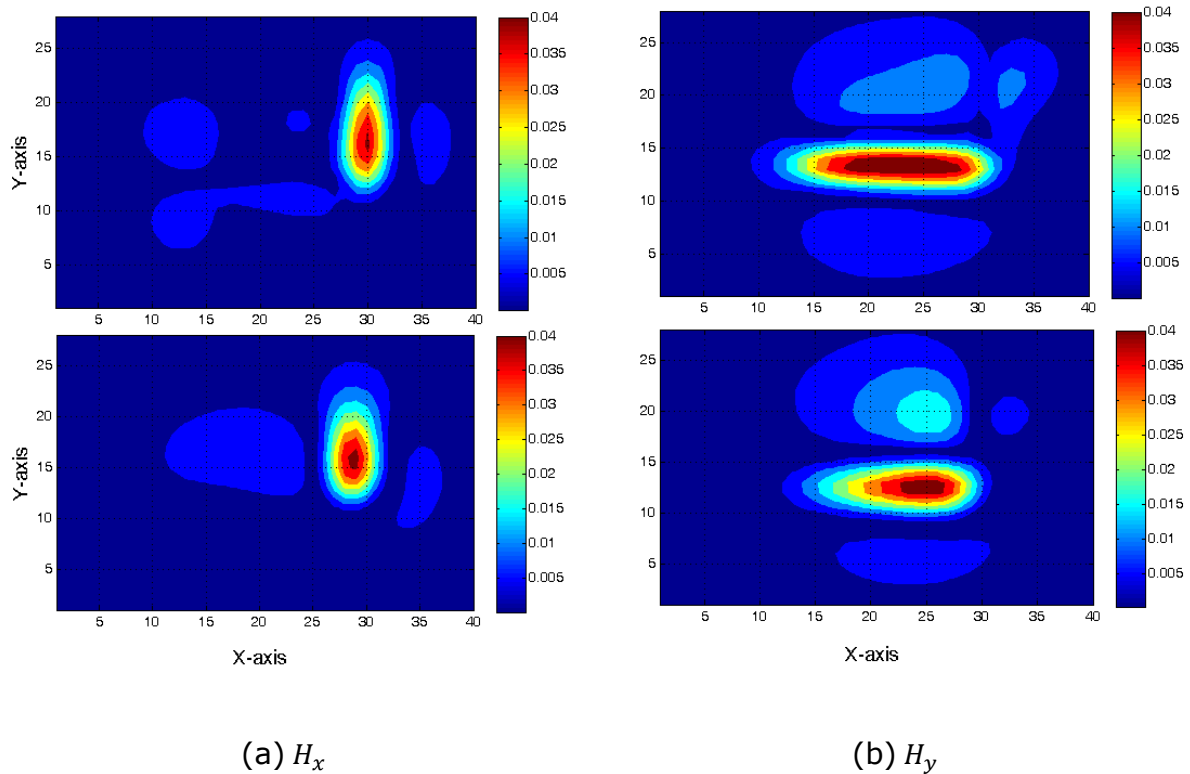


Fig. 3.28. Magnetic near field (magnitude values) results at 10mm above L trace PCB in A/m using near field measurement (1st row) and MoM code (2nd row).

Figure 3.28 compares the H_x and H_y near field measurement results using the 10mm magnetic loop probe and simulation results. The result show a good agreement with the maximum difference in the total magnitude of the magnetic field less than 5 percent.

3.9 Conclusion

A way of performing planar near-field measurement has been described. The information extracted through this process is required for computing the equivalent sources that are capable of representing the actual EM sources on a PCB. An accurate measurement is therefore required for a good representation.

To improve the scanning system and minimize human errors, a full automation of the motion control and data acquisition processes were implemented as

presented. Through this system automation using a robotic positioner and Labview application, thousands of near field scans can be executed without supervision in a relatively short time (up to 50% improvement to the semi-automated system used in the phase 1 of this work [1]).

Though the near field amplitude is easily extracted using most EM receivers, for the development of the equivalent sources both the amplitude and phase values of the near-fields are required. Different ways of extracting both the near-field amplitude and phase for different types of DUTs e.g. self or battery powered DUT (using spectrum analyzer) and externally powered DUT (using vector network analyzer) have also been presented.

Near field probe calibration and characterisation were shown to provide information on the probes performance and predictable error corrections respectively in the measurement. Through calibration, the received voltages are converted to their appropriate fields. The electrical and physical properties of the probe determined through characterisation are used in estimating measurement errors. The most significant of these errors are those due to probe perturbation. For the various probes considered in this work, the 10mm commercial probe was shown to have the least perturbation to the experiment and relatively sufficient sensitivity at 10mm distance. Hence 10mm will be used as the scanning height for the remaining part of this work. The near field measurement using the calibrated 10mm probe has been shown to have a close agreement with simulation.

References

1. X. Tong, Simplified Equivalent Modelling of Electromagnetic Emissions from Printed Circuit Boards, PhD Thesis, University of Nottingham, May 2010.
2. A.D. Yaghjian, " An overview of Near field Antenna Measurements," *IEEE Trans. on Antennas and Propagation.*, vol. AP-34, nos.1, pp. 30-45, January 1986.
3. K. Li, A. Sadighi and Z. Sun, " Motion control of a hydraulic free piston engine", *American Control Conf.*, Montréal, June 2012.
4. J. A. Dworak and K. Srinivasan, " Application of controller design techniques to an electro hydraulic circuit for coordinated motion control" , *American Control Conf.*, Minneapolis,1987.
5. Parker Hannifin Corporation, " Linear Actuators", August 2010.
6. L. J. Kamm, *Understanding Electro Mechanical Engineering* , Piscataway, NJ: IEEE press, 1996.
7. L. C. Westphal, *Handbook of Control System Engineering*, 2nd ed., Norwell, MA: Kluwer Academic, 2001.
8. T. K. Kiong, L. T. Heng, D. Huifang and H. Sunan, Precision Motion Control, London: Springer-Verlag, 2001.
9. Online, (2013). National Instrument, <http://www.ni.com/labview/>. National Instruments, "LabVIEW User Manual", National Instruments, Jan. 1998 Edition.
10. P.A. Blume, *Labview style book*, 1st Edition, New Jersey: Prentice hall, March 2007.
11. Agilent Technologies, *PNA Series Network Analyzer*, December 2007.

12. Hewlett Packard, " Understanding the Fundamental Principles of Vector Network Analysis", Application Note 1287-1.
13. P. Russer, "EMC measurements in the time-domain," in General Assembly and Scientific Symposium, 2011 XXXth URSI. IEEE, Aug. 2011, pp. 1–35
14. HP E8362B User's Guide, Hewlett-packard Co. Santa Rosa, CA, 2000.
15. L. Butler, " Transmission Lines and Measurement of their Characteristics", *Amateur Radio*, October 1989.
16. Agilent Technologies, *Spectrum Analyzer Basics*, [Online], 2013, <http://www.agilent.com>.
17. S. Dieter and W. Menzel, "High-resolution probes for near-field measurements of reflectarray antennas", *IEEE Antennas and Wireless Propagat. Letters*, Vol.8, pp. 157-160, 2009.
18. O. S. Kim, S. Pivnenko and O. Breinbjerg , "Wideband scalable probe for spherical near-field antenna measurements", *Proc. of the 5th European conf. on antenna and propagation (EUCAP)*, pp. 1781-1785, April 2011.
19. V. Rodriguez, "An open-boundary quad-ridged guide horn antenna for use as a source in antenna pattern measurement anechoic chambers," *IEEE Antennas Propagat. Magazine*, vol. 48, no. 2, pp. 157–160, 2006.
20. G. Hygate and J. F. Nye, "Measuring fields directly with an optically modulated scatterer," *Measure. Sci. Technol.*, vol. 1 pp. 703–709, 1990.
21. W. Liang, G. Hygate, J. F. Nye, D. G. Gentle, and R. J. Cook, "A probe for making near-field measurements with minimal disturbance: The optically modulated scatterer", *IEEE Trans. on Antennas and Propagat.*, vol. 45, nos. 5, May 1997.

22. P. McNair, "Improved microwave antenna measurement using a planar near-field scanner," *Microwave Engineering Europe*, pp. 33–39, June/July 1995.
23. R. Lao et al, "High-sensitivity optically modulated scatterer for electromagnetic field measurement", *IEEE Trans. on Instrumentation and Measurement*, Vol. 56, No. 2, pp. 486-490, April 2007.
24. M. S. Hill and A. Gopinath, "Probing Gunn domains at X-band microwave frequencies using a scanning microscope," *J. Phys. D, Appl. Phys.*, vol. 7, pp. 69–77, Jan. 1974.
25. J. Bokor, A. M. Jonson, R. H. Storz, and W. M. Simson, "High-speed circuit measurements using photoemission sampling," *Appl. Phys. Lett.*, pp. 226–228, Jul. 1986.
26. K. Yang, G. David, J.-G. Yook, I. Papapolymerou, L. P. B. Katehi, and J. F. Whitaker, "Electrooptic mapping and finite-element modeling of the near-field pattern of a microstrip patch antenna," *IEEE Trans. Microw. Theory Tech.*, vol. 48, no. 2, pp. 288–294, Feb. 2000.
27. J. T. L. Tong, "Transit time effect in electron beam testing voltage measurements," *Meas. Sci. Technol.*, vol. 3, pp. 827–837, Sep. 1992.
30b-EMC Test Systems, L.P, "RF Test Systems: E&H Near Field Probes,"
online: [Http://www.emctest.com](http://www.emctest.com)
28. " IEEE Standard Methods for measuring electromagnetic field strength of sinusoidal continuous waves, 30Hz to 30GHz, " IEEE std. 291-1, IEEE, New York, 1991.
29. " IEEE Standard Methods for Measuring Electromagnetic Field Strength for Frequencies Below 1000 MHz in Radio Wave Propagation", IEEE std. 302, IEEE, New York, 1969.

30. M. Kanda, " Standard probes for electromagnetic field measurements", *IEEE Transactions on Antennas and Propagation*, vol. 41, no. 10, pp. 1349-1364, Oct. 1993.
31. M. Kanda, " Analytical and numerical techniques for analyzing a linear dipole with a non-linear load", *IEEE Transactions on Antennas and propagation*, vol. AP-28, pp. 71-78, Jan. 1980.
32. J. Randa and M. Kanda, " Multiple-source, multiple-frequency error of an electric field meter ", *IEEE Transaction on Antennas and Propagation*, vol. Ap-33, pp. 2-9, Jan. 1985.
33. M. Kanda, " A relatively short cylindrical broadband antenna with tapered resistive loading for picosecond pulse measurements," *IEEE Transactions on Antennas and Propagation*, vol. Ap-26, pp. 439-447, May 1978.
34. M. Kanda, " Time-domain sensors and radiators," in *Time Domain measurements in Electromagnetics*, E.K. Miller, ed. New York: Van Nostrand, 1986.
35. M. Kanda and L. D. Driver, " An isotropic electric-field probe with tapered resistive dipoles for broadband use, 100KHz to 18GHz, " *IEEE Transactions on Microwave Theory Technology*, vol.MTT-35, pp. 124-130, Feb. 1987.
36. T. T. Wu and R. W. P. King, "The cylindrical antenna with nonreflecting resistive loading," *IEEE Transactions on Antennas and Propagation*, vol. Ap-13, pp. 309-373, May 1965.
37. (2013) Concept - II homepage. [online]. Available: <http://www.tet.tu-harburg.de/concept/index.en.html>.
38. (2013) CST- CST MWS, Germany. [online]. Available: <http://www.cst.com/Content/Products/MWS/Solvers.aspx>.

39. A. Boros, *Measurement Evaluation*, English Translation Gabor, Amsterdam: Elsevier, pp. 34-42, 1989.
40. A. C. Newell, "Error analysis techniques for planar near-field measurements", *IEEE Transactions on Antennas and Propagation*, vol. 36, no. 6, pp. 754-768, June 1988.
41. P. Billingsley, *Probability and Measure*, 3rd edition, New York: Wiley, 1995.
42. A. Nothofer, Cross-Polar Coupling in GTEM Cells used for Radiated Emission Measurements, PhD Thesis, University of York, York, 2000.
43. S. Jarrix, T. Dubois, R. Adam, P. Nouvel, B. Azaïs and D. Gasquet, "Probe Characterization for Electromagnetic Near-Field Studies," *IEEE Trans. on Instrumentation and Measurement*, Vol. 59, No. 2, pp. 292-300, 2010.
44. D. Van Labeke, "*Microscopie optique en champ proche*", Techniques de l'Ingénieur, chapter 862.
45. A. Newell, "Error analysis techniques for planar near field measurements," *IEEE Trans. Antennas Propagat.*, vol. AP-36, no. 6, pp. 754-768, Jun. 1988.
46. J. Dunsmore, "Comparison of mixer characterisation using new vector characterisation techniques," in *Proc. 32nd European Microwave Conf.*, vol. 1, pp. 163-166, Sep. 2002.

Chapter 4

Equivalent Dipole Modelling Applications and Limitation

4.1 Introduction

This Chapter is on the applications of the equivalent dipole modelling (EDM). This also discusses the conditions for reliable performance and validity of this technique with illustrations on its limits especially in characterising practical problems.

The computational requirements for electromagnetic simulations of electronic devices are increasing due to increasing functionality and component density. Often, it is not possible to fully simulate a complete electronic system in reasonable time frame even using the most advanced computers.

A simple analytical model based on equivalent dipoles was used in [1][2] to predict the electromagnetic properties of devices within a reasonable time therefore avoiding the expensive computational requirement. In this Chapter, the limitation of the conventional equivalent dipole model (EDM) in characterizing the practical PCB will be shown. Firstly, its application in characterizing PCB in free space, PCB over infinite ground plane and PCB over finite ground plane will be demonstrated. These will then be compared with full field simulation results of the same problem (i.e. PCB in free space, PCB over infinite ground plane and finite ground plane respectively). By so doing, the limitation of the EDM can clearly be shown. Furthermore, a model that combines

diffraction solutions as implemented in a full wave solution and EDM technique will be presented.

Equivalent Dipole Model

The conventional EDM model as derived in Chapter 2 and is given by the expression

$$[H] = [G][D] \quad (4.1)$$

Where H , G and D are the magnetic field, coefficient matrix and the equivalent dipole moment vector respectively.

The LHS of (4.1) is the magnetic field which is extracted either through near field measurement as presented in Chapter 3 or electromagnetic simulation package. The coefficient matrix G is computed through (2.15) – (2.17) for electric dipoles and (2.18) – (2.20) for magnetic dipoles. The unknown which is the dipole moment vector can then be evaluated by solving the inverse problem. The SVD as presented in Chapter 2 is used to solve the inverse problem.

4.2 Equivalent Dipole Modelling in Free Space

Firstly, a simple radiating element in form of a square loop of 20cm perimeter, was designed using an MoM-based Concept-II numerical code [3] as shown in Fig. 4.1. The loop is excited with a 0dB source at the centre of the right edge along the y -axis at 900MHz. Transverse magnetic near-field samples H_x and H_y were computed at 10mm above the loop along the z -axis. For a 41×41 sampling points, over a 28cm perimeter enclosing the entire loop both the amplitude and the phase of the near field were extracted from the complex valued fields.

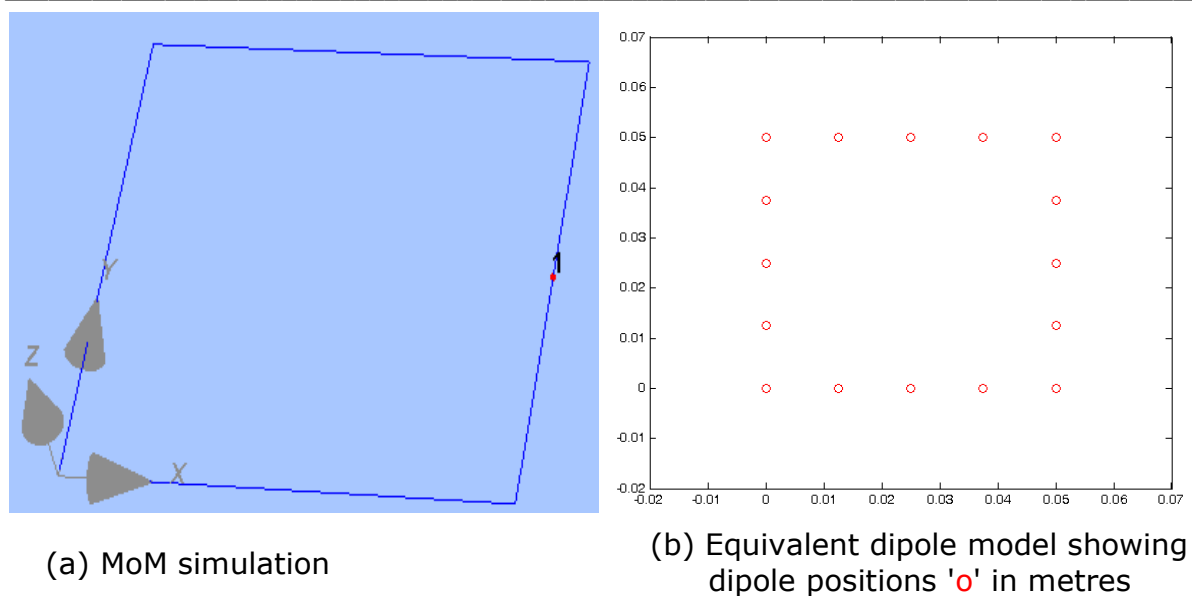


Fig. 4.1. Square loop radiator in free space.

They were then used as the input for the LHS of (4.1). Furthermore the first term of the RHS of (4.1), the coefficient matrix, was also computed using the expressions (2.15)-(2.17) by aligning a total of 20 electric dipoles uniformly separated along the entire perimeter of the loop (i.e. 5 dipoles/side) as shown in Fig. 4.1b. The dipole resolution and locations were chosen as the radiation sources on this particular problem are known (i.e. the conducting ring). However, ways of determining the dipole resolution and locations for characterising unknown radiation problems will be presented later in section 4.5.4. The SVD as presented in Chapter 2 was used to solve the inverse problem and the deduced dipole vector then used to reproduce the transverse fields at 10mm above the xy -plane and to predict the longitudinal magnetic field, H_z . The results are shown in Fig. 4.2 for the MoM and equivalent dipole model.

Figure 4.2 shows a good agreement between the MoM results and equivalent dipole model result with a maximum relative error max_{δ} , better than -20dB.

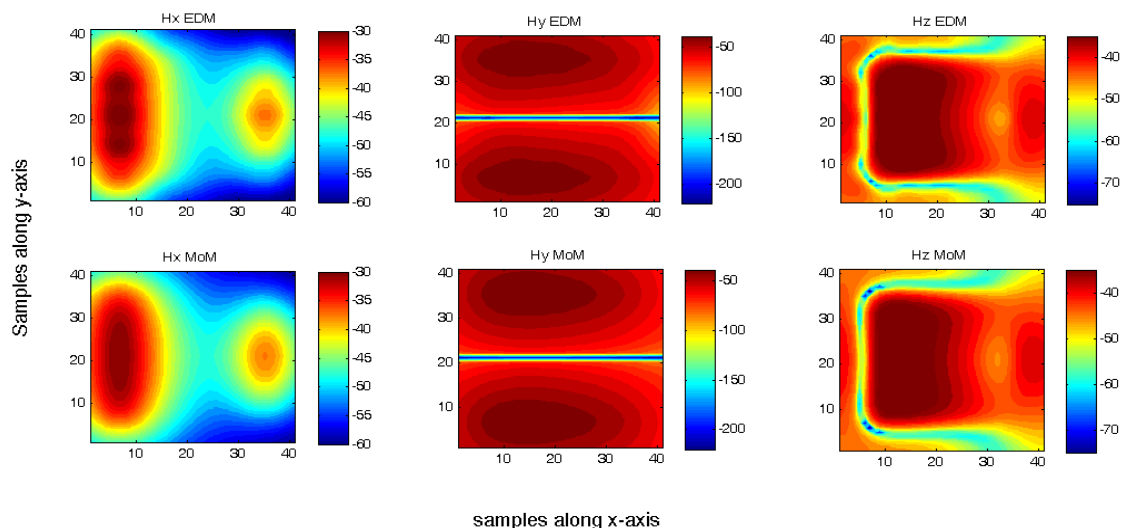


Fig. 4.2. Loop magnetic field radiation in free space at 10mm observation point computed using the MoM simulation and EDM code in dBA/m for 900MHz.

This maximum relative error for N field points was evaluated through the expression

$$\max_{\delta} = \max \left(20 * \log \left[\left(\frac{H_s^T - H_m^T}{H_s^T} \right) \right] \right)_N \quad (4.2)$$

$$H^T = \sqrt{H_x^2 + H_y^2 + H_z^2} \quad (4.3)$$

where H_s^T and H_m^T are the total magnetic fields computed on the MoM code and equivalent dipole model respectively.

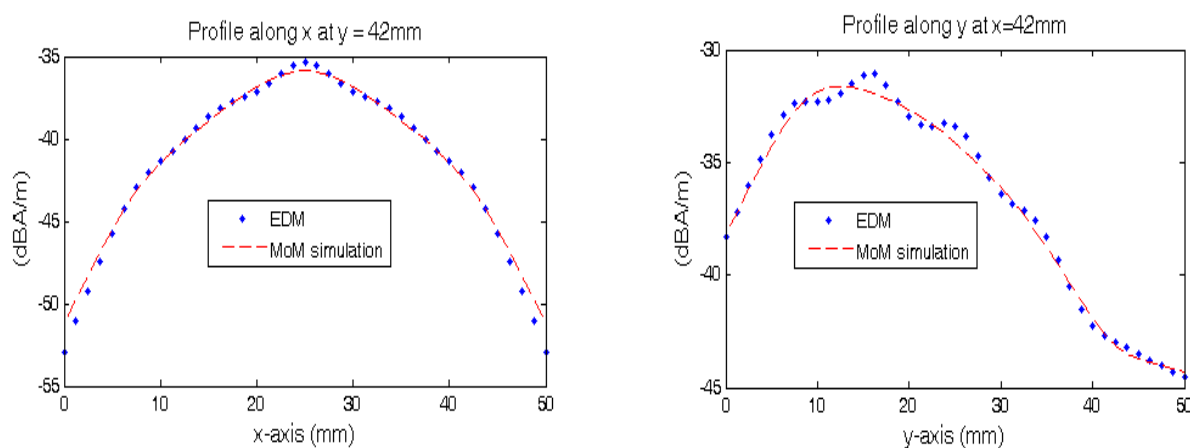


Fig. 4.3. Profiles of H^T along x -axis and y -axis at 10mm above the xy -plane.

Also in Fig. 4.3 the field profile along a 1D plot for both x -axis and y -axis shows good correlation. The figure shows a strong agreement for the profile of a y -point (at $y=42mm$) along x -axis. However, more deviation is observed while comparing the EDM and MoM results for the profile of an x -point (at $x=42mm$) along y -axis. The same is true for the Fig. 4.2 as relatively more differences are observed especially for the H_x component (which is the strongest contributor to the H^T according) for x -points along y -axis.

4.3 Ground Plane Approximation

Most PCBs are designed with a conducting ground plane which strongly affects the radiation of a PCB. There is a need to account for the scattering of electromagnetic waves due to the ground plane. This often leads to reflection and diffraction. The former being caused by the reflective properties of a perfect conductor and the latter caused by extra currents induced at the edges of the ground plane or roughness of the conductive plane. The following sections will now apply the EDM in characterising the EM properties of PCB on an infinite ground and on a finite ground plane.

4.4 Infinite ground plane approximation

The infinite ground plane principle has been demonstrated in [4]-[7] to sufficiently characterize radiating sources. This approach was used to characterize a 3D radiator above an infinite ground plane. It is also assumed here that the only significant effect of the scattering due to the conducting ground plane is the directly reflected waves. Therefore the total magnetic field H_t , at any observation point, is given by

$$H_t = H_d + H_r \tag{4.4}$$

where H_d and H_r are the direct and reflected wave respectively.

The first term on the RHS of (4.4) is easily evaluated using the expression for free space dipole in (2.15)-(2.22). This has been provided for a z oriented electric dipole in (2.15) - (2.17) and magnetic dipole in (2.18) - (2.20). The remaining field component H_r , in (4.4), is then evaluated through the principle of image theory.

4.4.1 Image theory

To compute the component of the reflected rays, a virtual source is assumed. This is derived from the established image theory according to [8]-[10]. The two field components (actual and virtual sources) due to direct and reflected rays are then added to determine the total field radiated by the dipole at any observation point, P_o .

Figure 4.4(a) shows the positions of the sources from the observation point, P_o . The virtual source (or image source) and the actual source positions are denoted by the P_i and P_a respectively. The actual and virtual sources are separated by the same distance h , from the ground plane but in opposite sides of the ground plane.

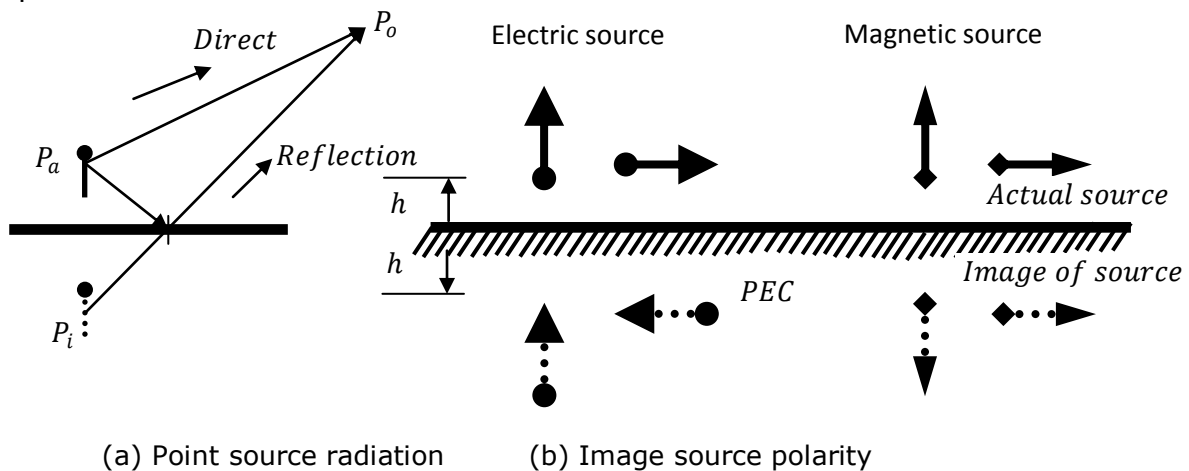


Fig. 4.4. Electromagnetic sources on a perfect electric conductor [11].

The polarities of the virtual sources are determined from the orientations of the actual sources and the nature of the ground plane. For electric and magnetic sources on a perfect electric conducting (PEC) ground plane, the polarity of the images are as shown in Fig. 4.4(b) [11].

For the assumption of an infinite ground plane, reflection is sufficient for approximating the scatterings due to ground plane. This leads to a closed form unique solution. This assumption can also be used for DUTs where the electromagnetic sources are remote from the edges of the ground plane. Taking into consideration the ground effect leading to reflection, the equivalent dipole model for N sampling points as given in (2.21) - (2.22) is then extended to

$$\begin{bmatrix} H_x \\ H_y \\ H_z \end{bmatrix}_N = \sum \begin{bmatrix} G'_x & G'_y & G'_z \\ G'_x & G'_y & G'_z \\ G'_x & G'_y & G'_z \end{bmatrix}_{NxM} \begin{bmatrix} D_x \\ D_y \\ D_z \end{bmatrix}_M + \begin{bmatrix} G''_x & G''_y & G''_z \\ G''_x & G''_y & G''_z \\ G''_x & G''_y & G''_z \end{bmatrix}_{NxM} \begin{bmatrix} D_x \\ D_y \\ D_z \end{bmatrix}_M \quad (4.5)$$

Further simplification is also possible therefore leading to

$$[H] = [G'] [D] + [G''] [D] , \quad (4.6)$$

Or

$$[H] = [G] [D] . \quad (4.7)$$

where G' and G'' are the coefficient matrix evaluation for the direct wave and reflected wave respectively.

4.4.2 Radiating loop over a large plane

The problem in section 4.2 was used to validate this model. However the radiating loop element was computed over a large ground plane of 5 times the size of the loop using the MoM-based code [3]. The simulation was carried out over a square ground plane with sides of 1m as shown in Fig. 4.5a. The square sampling plane of 28cm side lengths was kept at 10mm directly above the loop

and parallel to the ground plane. The loop was excited in similar way as in section 4.2. Figure 4.5b shows the current excitation on the ground plane.

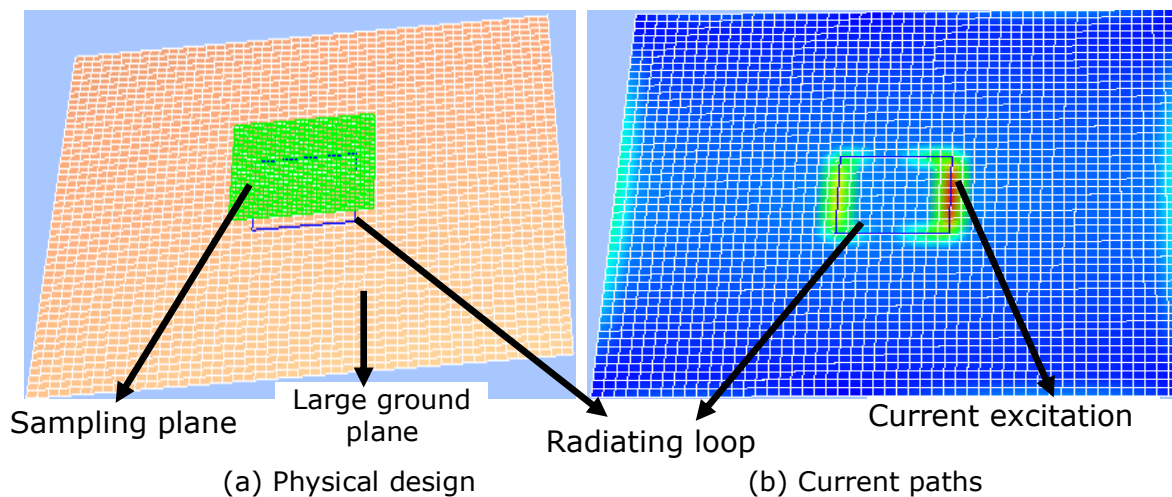


Fig. 4.5. Radiating loop element of a large ground plane.

The transverse fields H_x and H_y , required as the input for the dipole modelling (4.5) - (4.7) were then computed. Figure 4.6 shows the positions of the dipoles used in the model for two different dipole resolutions.

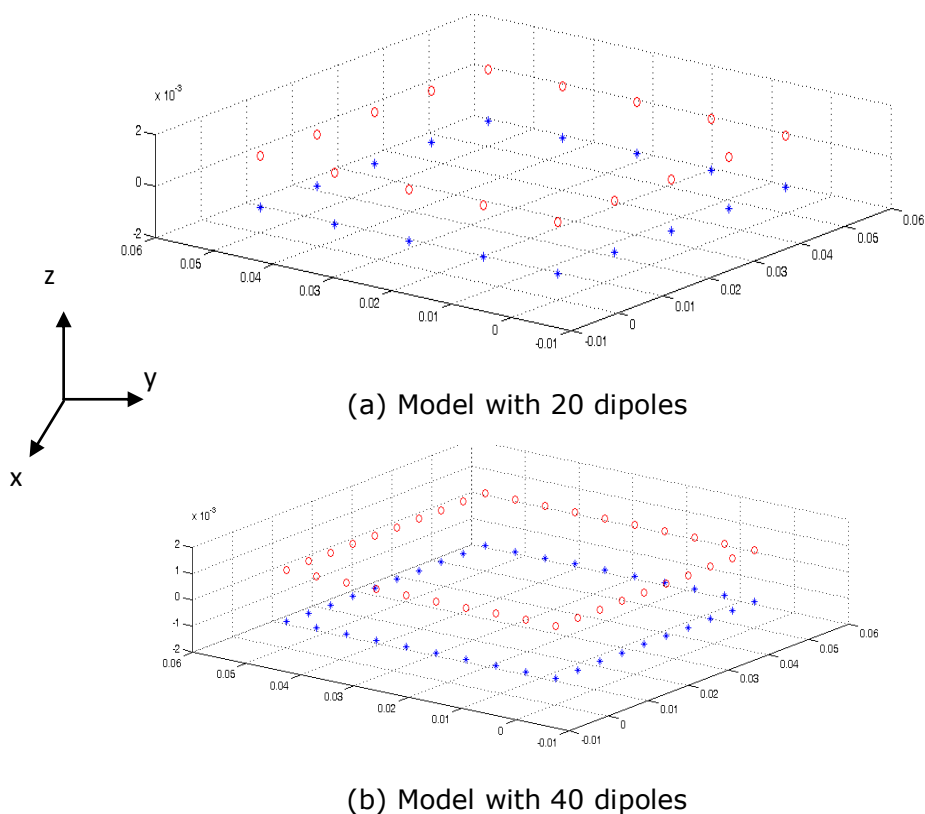


Fig. 4.6. Dipole positions 'o' and '*' represent the positions for the actual dipole sources and the image sources respectively.

The results as shown in Fig. 4.7 show that the model with 20 dipoles that can accurately reproduce the electromagnetic fields from a radiating loop in free space is no longer sufficient when a ground plane is involved. The presence of a conducting ground plane increases the complexities of the electromagnetic near fields hence requiring more dipoles for a more accurate characterisation.

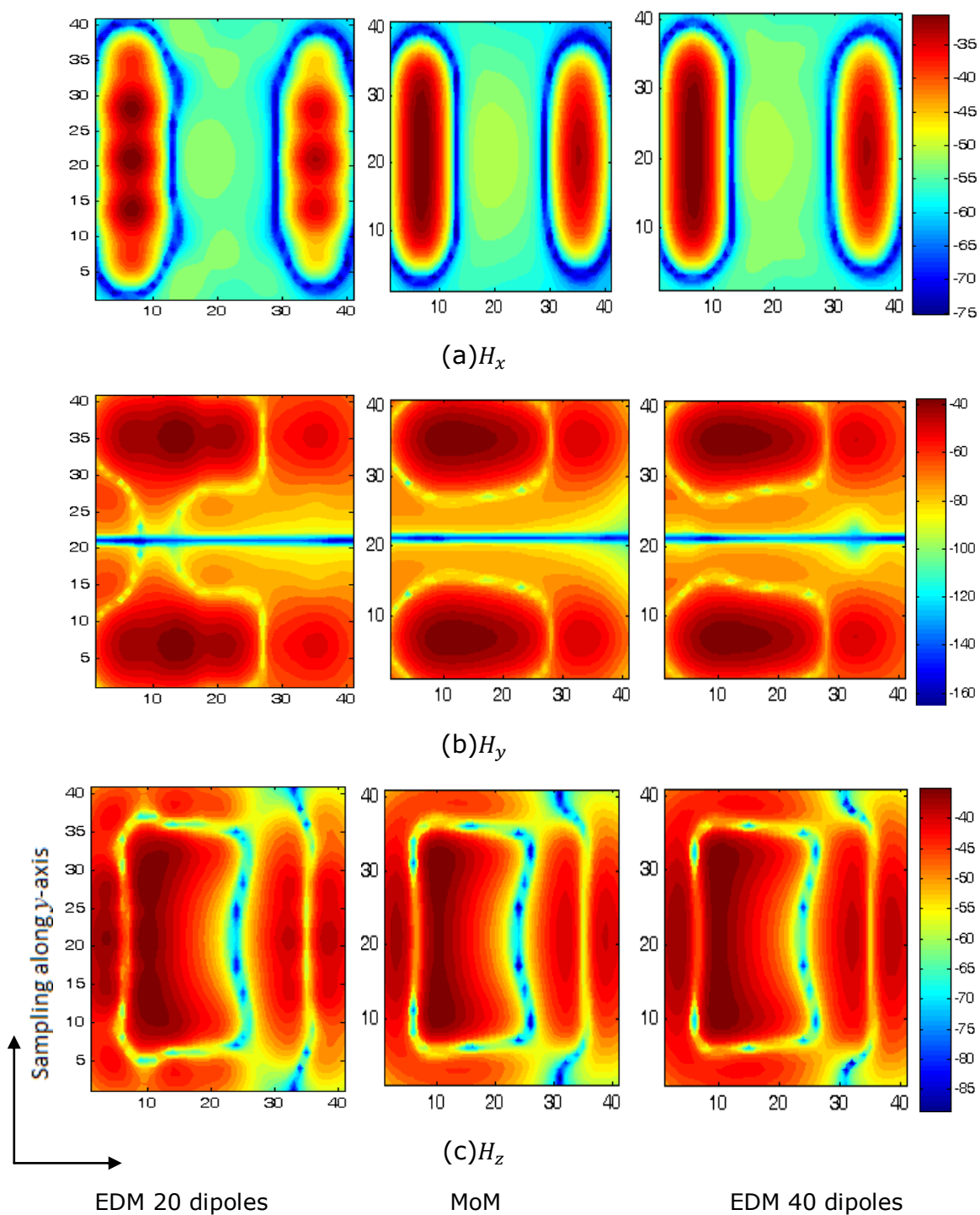


Fig. 4.7. Near-field results of the radiating loop over a large ground plane (dBA/m) (a) H_x (b) H_y (c) H_z

The field distribution reproduced and predicted with the dipole models and MoM code are presented in Fig. 4.7. The maximum relative error computed against the MoM simulation using the expressions in (4.2) and (4.3) were 26% and 3% for the 20 dipole model and 40 dipole models respectively. The purpose here is to demonstrate the effect of the inclusion of the ground plane. The result agrees with the assertion in [1],[4] also provided in Appendix B, that increasing the number of dipoles improves the characterization of the radiator. The experiment to establish the optimal number of dipoles required in equivalent dipole modelling will be presented in section 4.5.2.

4.4.3 3D radiator over an infinite ground plane

In [5]-[7] and previous sections, only the sampling along the z-plane was required to fully characterize a radiating element. However, for problems with significant vertical structures as commonly seen in PCB motherboards comprising several daughter boards, there is also a need to characterize the radiations along the sides. An experiment that characterizes a 3D radiating element is described. A monopole aligned along the z-axis with dimension 105mm x 5mm (i.e. height x radius) was designed using CST microwave electromagnetic code [12] as shown in Fig. 4.8.

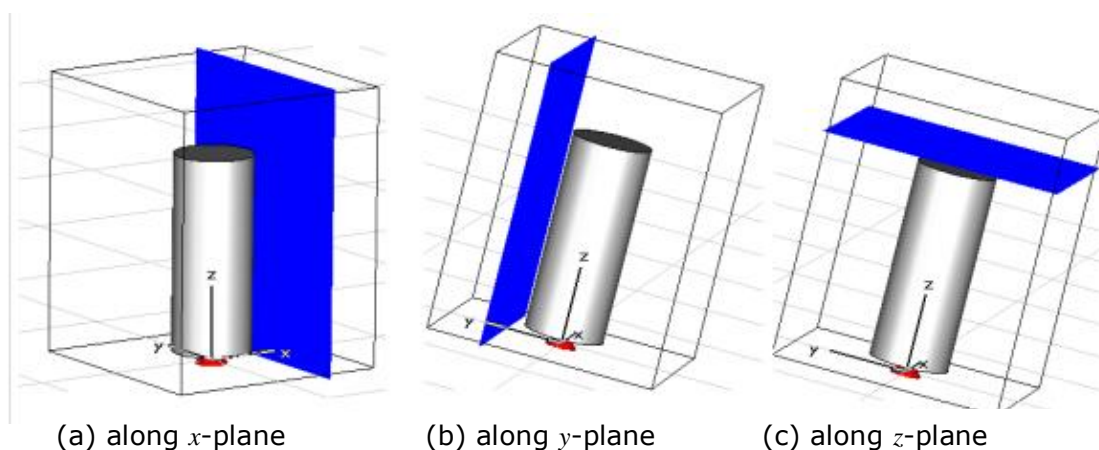
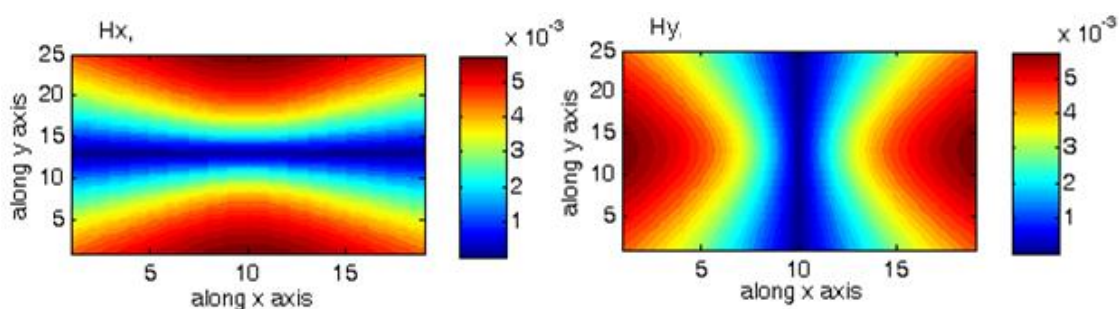


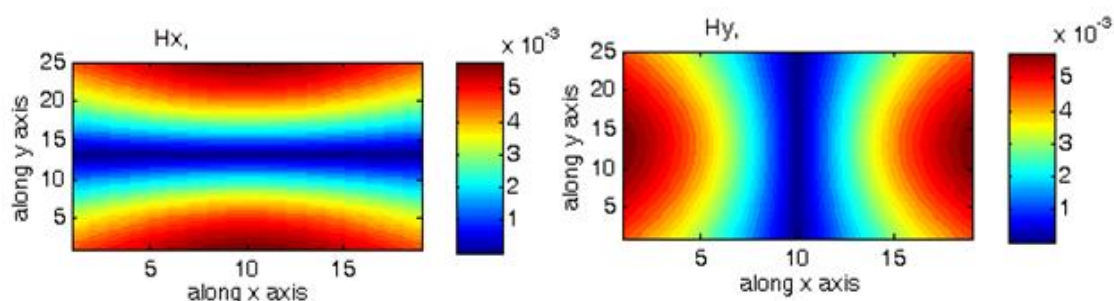
Fig. 4.8. Monopole antenna design over an infinite ground plane showing the three near field observation planes.

The monopole was excited at the bottom centre with 0dB source at a given frequency. In this 3D problem significant fields are expected to surround the DUT. Consequently, to accurately determine the equivalent dipole model capable of characterizing this problem, sufficient field information are extracted all around the DUT as shown in Fig. 4.8. Note that the first resonant frequency of the structure is around 600MHz.

Figure 4.9 compares the results for characterizing the monopole using EDM and CST simulation at 900MHz. The near field was first computed at a cubic plane enclosing the monopole with the monopole at the centre. Each individual plane of the cube is 10mm from the monopole. The fields beneath the ground plane are assumed to be zero for an infinite ground problem. So only the five Cartesian planes surrounding the DUT were used.



(a) Equivalent dipole model



(b) CST microwave simulation

Fig. 4.9. Magnetic near field of a monopole antenna over infinite ground plane at 900MHz, in A/m.

The model here is similar to that derived from (2.15) - (2.20), however an

appropriate vector transformation is applied and the fields from all the planes are combined and used as the RHS term of (4.3). The coefficient matrix is computed in similar manner as before and SVD technique was used to solve the inverse problem. The dipole moment vector is then evaluated. Taking into consideration the symmetric nature of the DUT and which is also modelled as a perfect electric conductor, 7 electric dipoles centralised along x and y axes with uniform spacing were used for the modelling. This characterized the transverse magnetic fields with an error less than 2% as shown in Fig. 4.9. The error, ζ was computed as the average of the r.m.s error, ζ_{rms} in reproducing the two transverse fields as given in the expression

$$\zeta_{rms} = \sqrt{\frac{\sum_{i=1}^N (H_s - H_m)^2}{\sum_{i=1}^N H_s^2}} \quad (4.8)$$

where H_s , H_m and N are the magnetic fields computed using numerical code, magnetic field reproduced using the EDM and the total number of sampling points respectively.

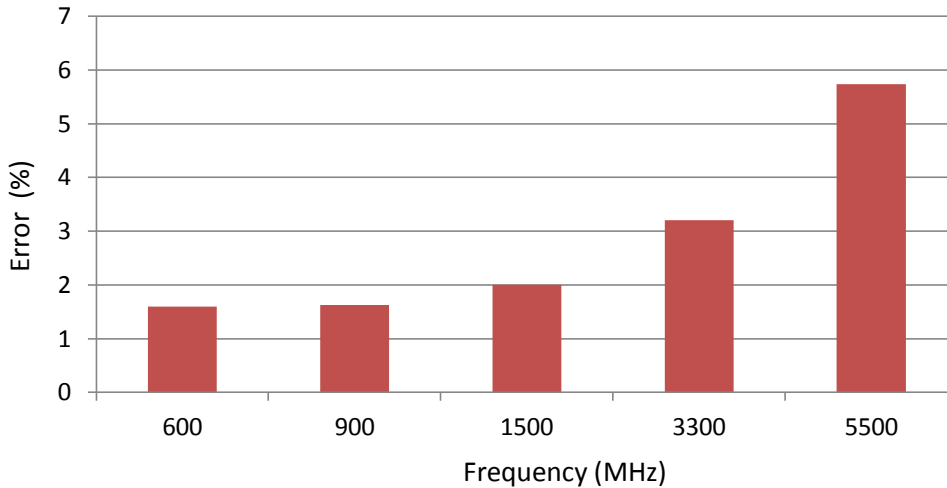
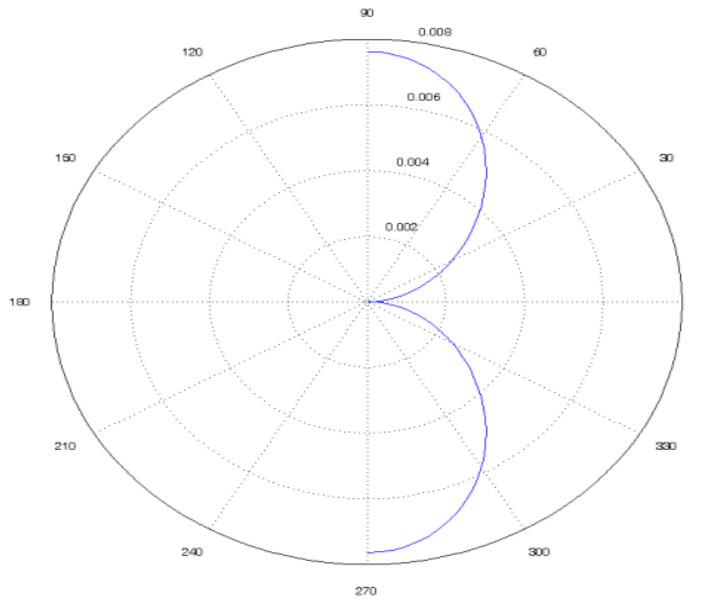


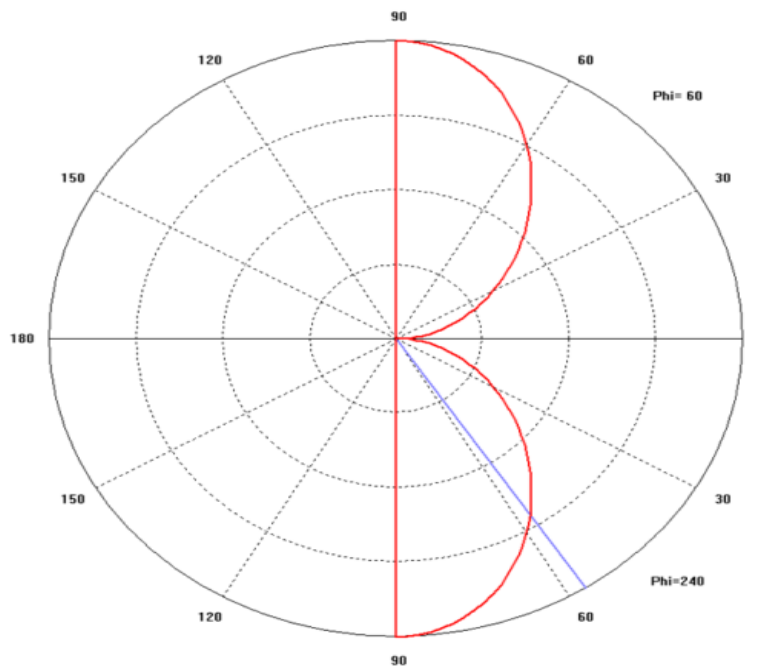
Fig. 4.10. Broadband response.

The same model was used to characterize the monopole antenna over the frequency range [600-5500MHz]. Figure 4.10 shows there is good agreement with actual simulation. The error is shown to increase with frequency. This is because more dipoles are required as the wavelength reduces to maintain same

error level. In the same manner the computation of the far-field radiation was carried out at a distance of 10λ and presented in Fig. 4.11. This also shows good agreement with a maximum field of 0.076A/m .



(a) Equivalent dipole model (max. field= 0.076A/m)



(b) CST microwave simulation (max. field= 0.076A/m)

Fig. 4.11. Far-field results at 10λ .

4.5 Sources of Error in Equivalent Dipole Modelling

As both the amplitude and the phase of the measured transverse fields are required as inputs to the dipole modelling, (4.7) can then be decomposed into its vector amplitude and phase components

$$[\vec{H}e^{i\vec{\phi}}] = [G^{i\vec{\theta}}][\vec{D}e^{i\vec{\theta}}] \quad (4.9)$$

where \vec{H} and $\vec{\phi}$ are vectors of the amplitude and phase of the measured field and \vec{D} and $\vec{\theta}$ are vectors of the amplitudes of the dipole moment.

In cases where a close form solution is possible, the coefficient matrix, G can be said to be an exact value. However information extracted at near field $\vec{H}e^{i\vec{\phi}}$, contains errors $\overline{\Delta H}$ and $\overline{\Delta \phi}$ which adds to the total error in computing the dipole moments. Errors due to near field measurement have been extensively presented in Chapter 3 and [1, Chapter 3] shows also that the accuracy of the inverse problem is affected by measurement errors. Matrix ill-conditioning of the inverse problem can also bring about errors in dipole modelling. Singular value decomposition technique (SVD) as already presented offers a good solution in solving ill-conditioned inverse problem hence reducing significantly numerical errors.

4.5.1 Deviation in modelling height

Modelling errors are also introduced by incorrect positioning of the measurement probes and other human parallax errors. To investigate this, an error due to modelling height variance from the actual measured height is investigated. The simulation in [section 4.4.2, Fig. 4.5] for a radiating loop was used to carry out this study. Particularly, the dipole model in Fig. 4.5 was used. The fields

obtained at a sampling height of 12.5mm were modelled at various planes with Δh variations. The result in Fig. 4.12 shows that, though the error ζ_{rms} (4.8) increases as the modelled height deviates from the actual height, however, the rate is not rapid. The plot shows that it will require a high deviation of up to 2.5mm to introduce an error of about 20% or more. But for robotic positioner of 10 μ m resolution, as used in this work, high deviation is more likely due to human introduced errors for example parallax and positioning of the DUT can be possible sources for this deviation. Therefore sufficient care is required in DUT positioning and in recording measurement positions to ensure minimal deviation. The deviation Δh , between the actual measured height, h_{mea} and the modelled height, h_{mod} is given by

$$\Delta h (mm) = h_{mea(mm)} - h_{mod (mm)} \quad (4.10)$$

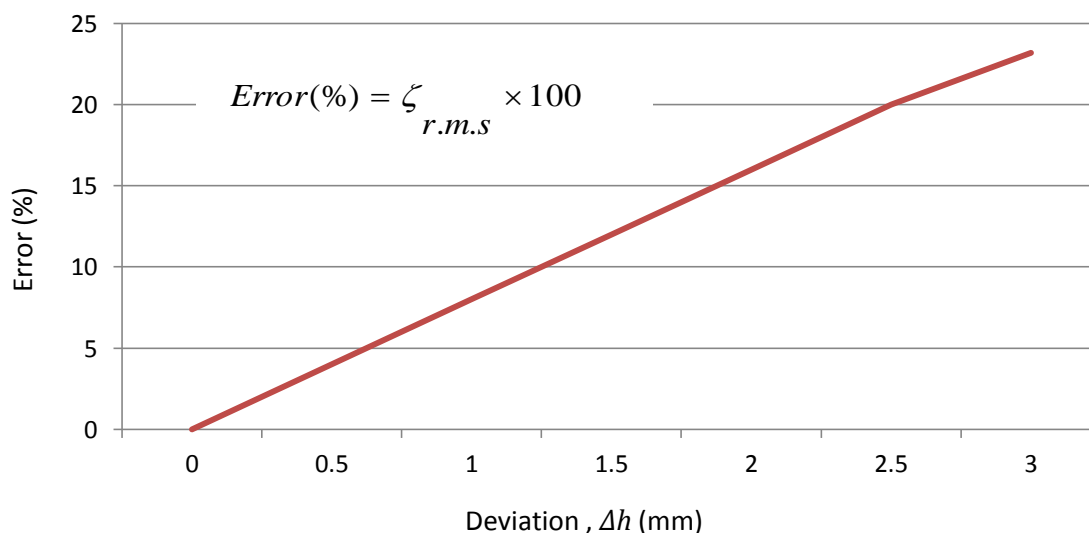


Fig. 4.12. Error due to deviation in dipole modelling from actual position.

The principle of information theory [22]-[23] in minimizing the mean square error in data transfer and communications, can be applied in extracting sufficient information at near field that is capable of representing the electromagnetic

behaviour of the radiating element. An adequate scanning height should be selected in such a way that probe is sensitive enough in picking up sufficient information without perturbing the experiment as discussed in Chapter 3. In addition near field scan should be carried out over sufficient plane size and with fine resolution so as to pick up all the spatial variances and evanescence. An experiment was carried out to show the dependence of equivalent dipole modelling on sampling resolution and sampling plane size. The experiment presented in section 4.4.2, Fig. 4.5 for a radiating loop was used over a frequency range between 100MHz and 3000MHz. A dipole resolution of 2.5mm was used in the experiment.

4.5.2 Sampling resolution

Sufficient information is normally required from near field measurement for determining the properties of the equivalent dipoles capable of characterizing radiating elements. This often requires a fine resolution. However, a fine resolution also results in high computational cost. Therefore, there is need to optimize the sampling resolution in dipole modelling for an acceptable degree of accuracy with minimized computational cost. The required sampling resolution has been found to depend on the scanning height. The experiment presented in [section 4.4.2, Fig 4.5] for a radiating loop was also used to investigate this. Magnetic field samples with different resolutions, Δs were extracted at various heights, h . Each magnetic field sample for a given sampling resolution was then used in the equivalent dipole modelling to predict the far field at 3m.

The correlation coefficient ρ_{sm} at far field, computed using the equivalent dipole modelling method and full field simulation, is now used as a normalised degree of accuracy. This is to enable comparison with previous work [1]. Correlation

coefficient is a measure of how the far field results reproduced using the equivalent dipole model and the far fields extracted directly through a full field simulation are linearly related. The correlation coefficient is defined as:

$$\rho_{sm} = \frac{\sum_{n=1}^N (H_{sf} - \bar{H}_{sf})(H_{mf} - \bar{H}_{mf})}{\sqrt{\sum_{n=1}^N (H_{sf} - \bar{H}_{sf})^2 \cdot \sum_{n=1}^N (H_{mf} - \bar{H}_{mf})^2}} \quad (4.11)$$

where \bar{H}_{mf} and \bar{H}_{sf} are the mean of the magnetic far-field computed using equivalent dipole modelling (H_{mf}) and full field simulation (H_{sf}) respectively for an N sampling points.

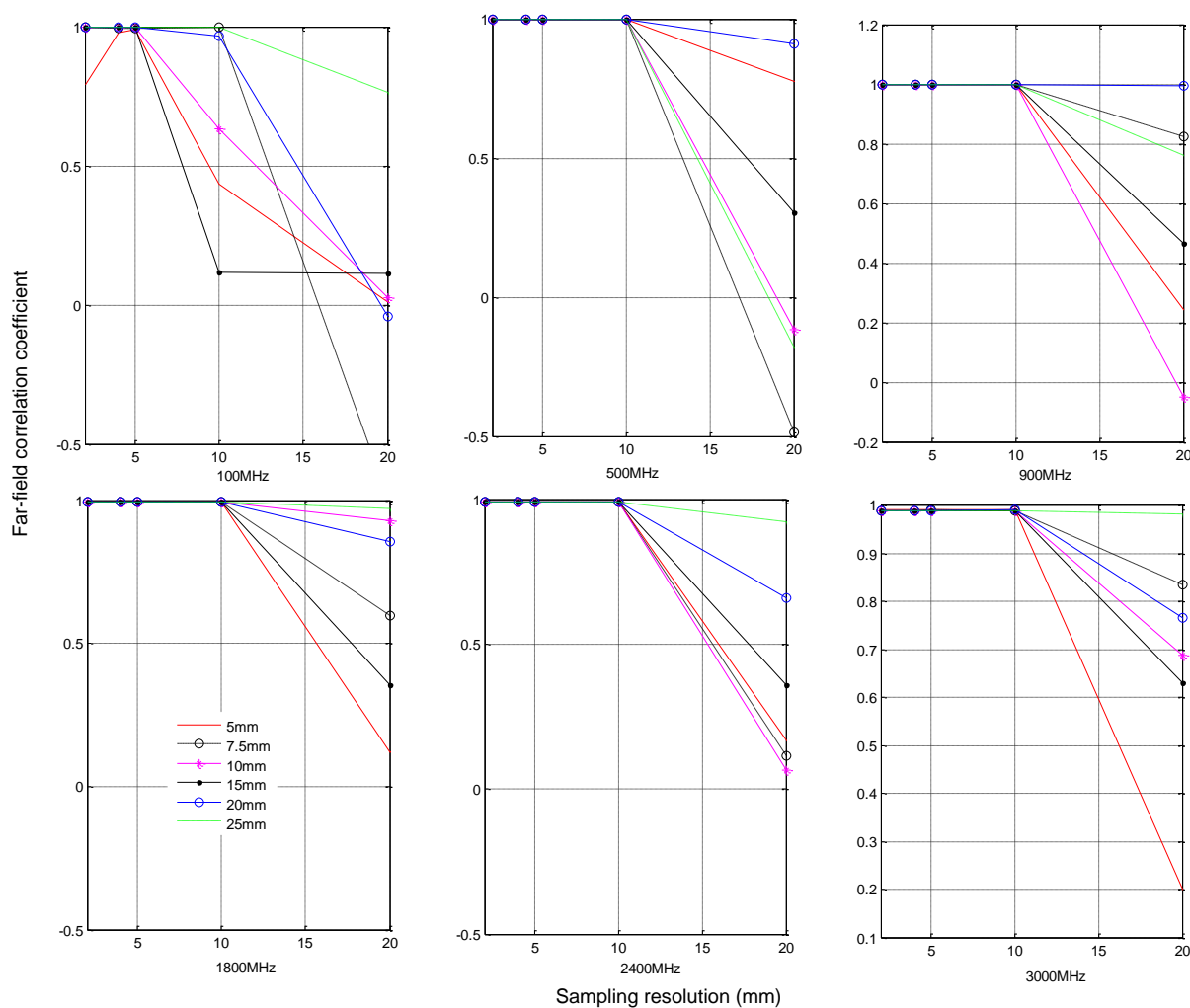


Fig. 4.13. Near field sampling resolution dependence on the scanning heights at different frequencies.

In Fig. 4.13 the correlation coefficients for the far field (3m) computed as a result of various near field sampling resolutions (2.5mm-20mm) using the equivalent dipole modelling and the MoM simulation are given for various frequencies. Each compares the correlation coefficient computed at different scanning heights of 5mm, 7.5mm, 10mm, 15mm, 20mm and 25mm. It shows that as the sampling height reduces, a finer resolution or smaller dipole separation is required to retain a good performance at the far-field for the dipole model (i.e. $\Delta s \propto h$).

The sampling resolution is also a function of the wavelength with an upper limit of half wavelength (i.e. $\Delta s \leq \frac{\lambda}{2}$) for far field measurement where no evanescent wave is present. However, near-field measurement is carried out in the region of space that contains evanescent waves. Therefore a finer resolution than half wavelength is required. According to [24] the maximum sampling resolution required for extracting sufficient information in a planar near field scanning is given by

$$\Delta s = \frac{\lambda}{2\sqrt{1+\left(\frac{\lambda}{d}\right)^2}} \quad (4.12)$$

where λ and d are the wavelength and the scanning height respectively.

For $\lambda \gg d$,

$$\Delta s \approx \frac{d}{2} \quad (4.13)$$

The results presented in Fig. 4.13 approximately confirm (4.13). This is also in agreement with the results shown in the previous work [1, section 3.7.1]. Therefore for a 10mm scanning height, which has been determined to be the optimal scanning height for the loop probe used in this work, a maximum

sampling resolution of 5mm is required. A finer resolution can even be used to improve the accuracy.

4.5.3 Sampling plane

The accuracy of the dipole modelling also depends on the extent of information surrounding the DUT that were collected. This also implies that the more information collected, the more accurate the computation of equivalent dipoles that are able to represent the electromagnetic sources becomes. An experiment similar to that presented in [1, section 3.7.2] was carried out over an n number of planes, each having an area of $L_p \times W_p$, as given in Table 4.1. This was performed over a broad range of frequencies for a DUT of size 50 x 50mm ($L_D \times W_D$).

Table. 4.1 Sampling plane dimensions

n	Dimension (mm)	(Area P/Area D)^{0.5}	$\Delta d = L_D - L_p = W_D - W_p$ (mm)
1	50 × 50	1	0
2	60 × 60	1.2	5
3	70 × 70	1.4	10
4	75 × 75	1.5	12.5
5	100 × 100	2	25
6	120 × 120	2.5	37.5
7	150 × 150	3	50

(Area P = surface area of the sampling plane; Area D= surface area of the DUT)

Figure 4.14 shows mean square error (4.8) as a result of modelling with different sampling plane size. There is an improvement in the modelling accuracy as the plane size increases. However, this improvement becomes very marginal and often insignificant beyond an optimal point. This can be explained as near field decays rapidly with $\frac{1}{r^2}$ and $\frac{1}{r^3}$. Also the plot shows a consistent frequency response.

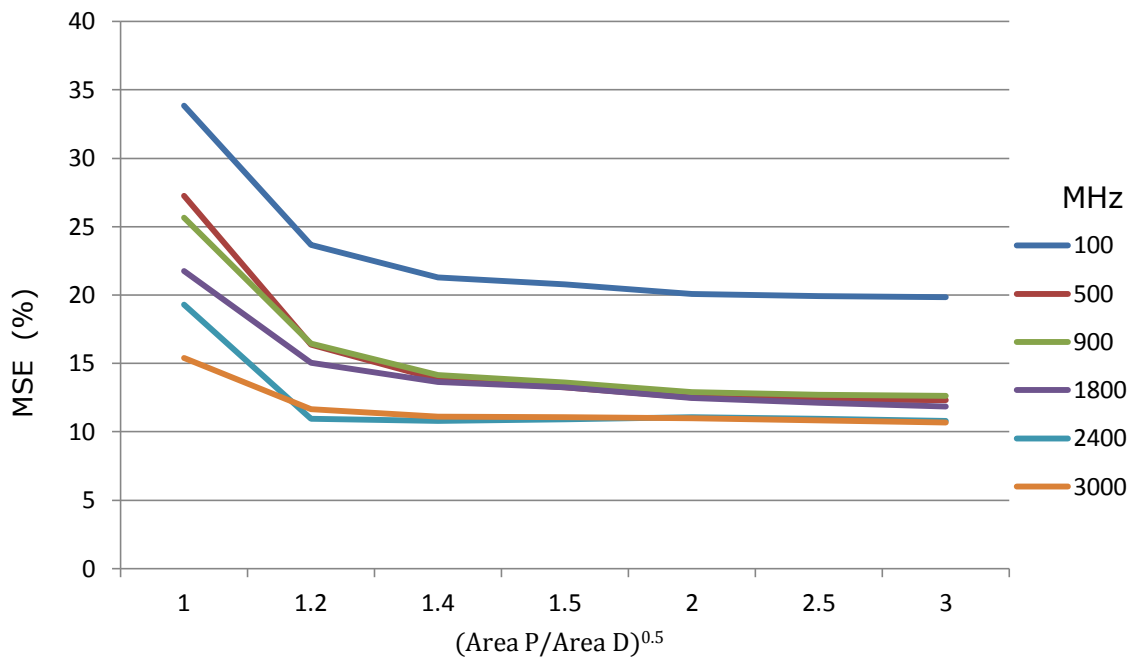


Fig. 4.14. Dependence on sampling plane size.

Therefore beyond a scanning plane 10mm away from the edge of the planes surrounding the DUT (i.e. $\Delta d = 10\text{mm}$), little improvement is seen. Hence it can be said that a scanning of an area that extends 10mm away from the edges of the DUT is enough to collect sufficient information required for equivalent dipole modelling.

4.5.4 Dipole spatial resolution

The accuracy of equivalent dipole model improves with increase in the number of dipoles used which implies higher resolution. However, increase in the dipole resolution also increases the modelling run time. Figure 4.15 shows the effect of the number of dipoles used in equivalent dipole modelling and the run time. This is demonstrated for the problem involving a loop on a large ground plane in Fig. 4.5 and the run time is shown to significantly increase for finer dipole resolutions. The task was performed on a computer with specifications Intel i7 3.07/3.06GHz processor, 6GB RAM and running on Windows 7 64 bits operating system.

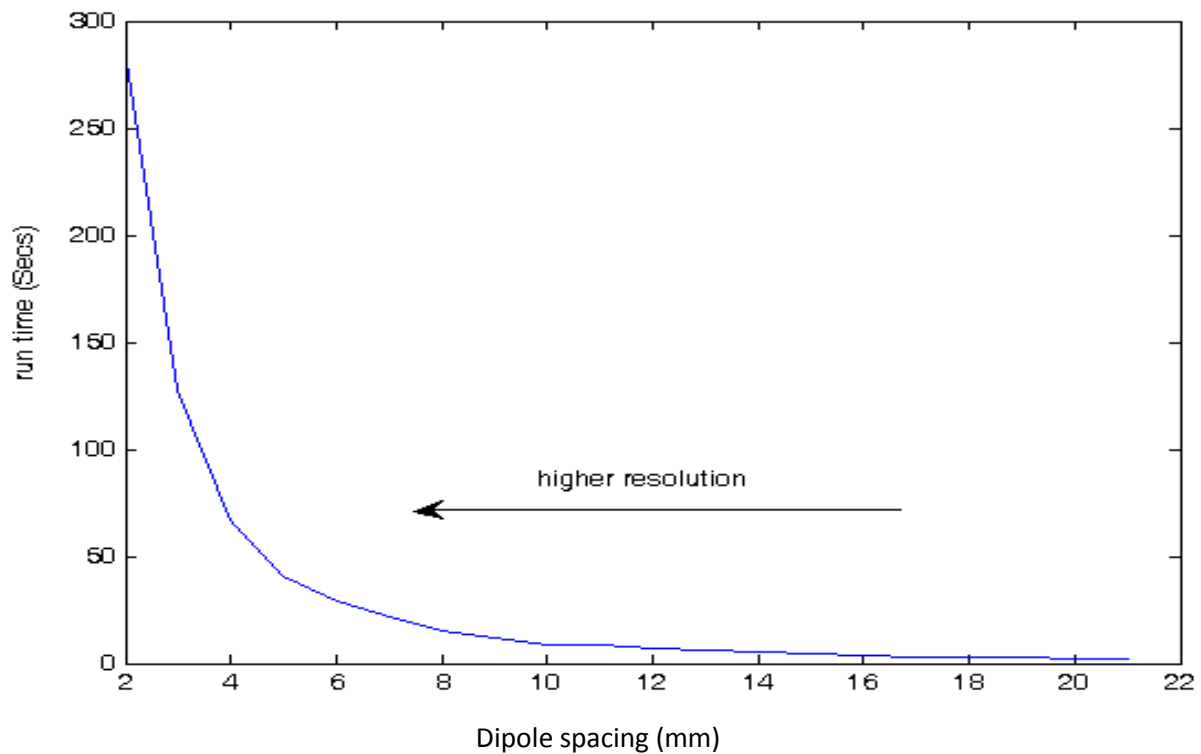


Fig. 4.15. EDM run time as a function of dipole numbers.

For a more complex problem involving dipole positioning along 3D geometry, the total modelling time will be running into several minutes. There is therefore the need for a good compromise between the dipole resolution and the level of accuracy required for a considerable run time. An experiment was carried out to estimate the dependence of the EDM accuracy to the dipole resolution. This was done by comparing the near and far field predicted using the EDM with various resolution to the actual simulation results. The same experiment as used in section 4.4.2, Fig. 4.5 was used, however, with different dipole resolution. The magnetic near and far fields were computed at 10mm and 3m respectively with the same scanning heights as used in the near field measurement. The near field results were then used to determine the dipole moment vectors for various dipole resolutions. These were then used to predict the fields at near and far fields and then compared with the actual simulation.

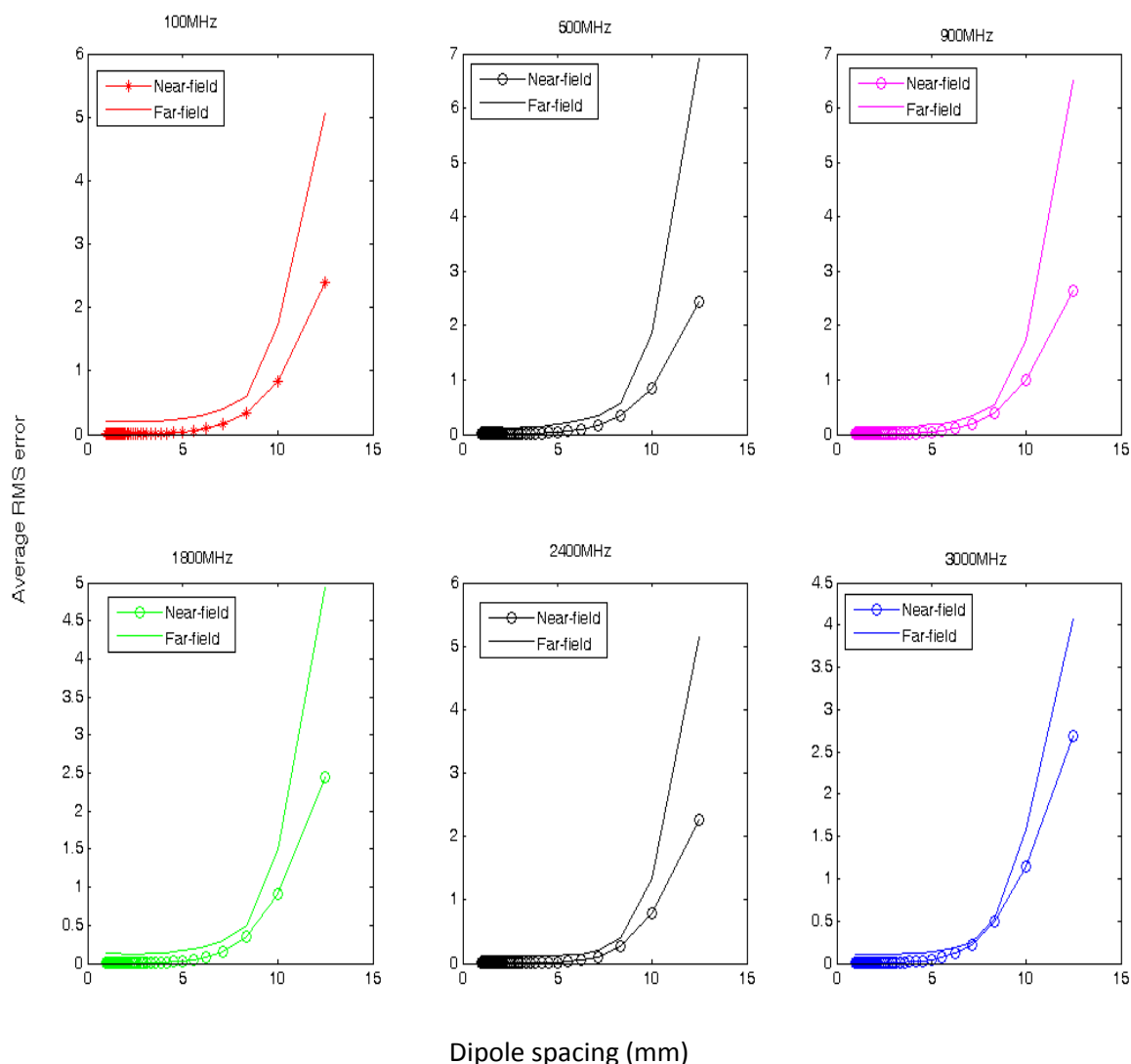


Fig. 4.16. Average RMS error near-field and far-field predictions.

Figure 4.16 shows that as the dipole spacing increases, resulting in a fewer number of dipoles (i.e. low resolution), the average RMS error (4.8) also increases. This worsens as the predictions are made at higher distances from the DUT up to far-field. Therefore, for an accurate far field prediction, sufficient number of dipoles of spacing much less than a wavelength is required.

From the far field correlation in Fig. 4.17, for a scanning height of 10mm, between the equivalent dipole modelling results and simulation, a dipole resolution of about 10mm or fewer results in a high correlation as calculated

using (4.11). The correlation degrades with increase in frequencies as finer resolution will be required as the wavelength reduces.

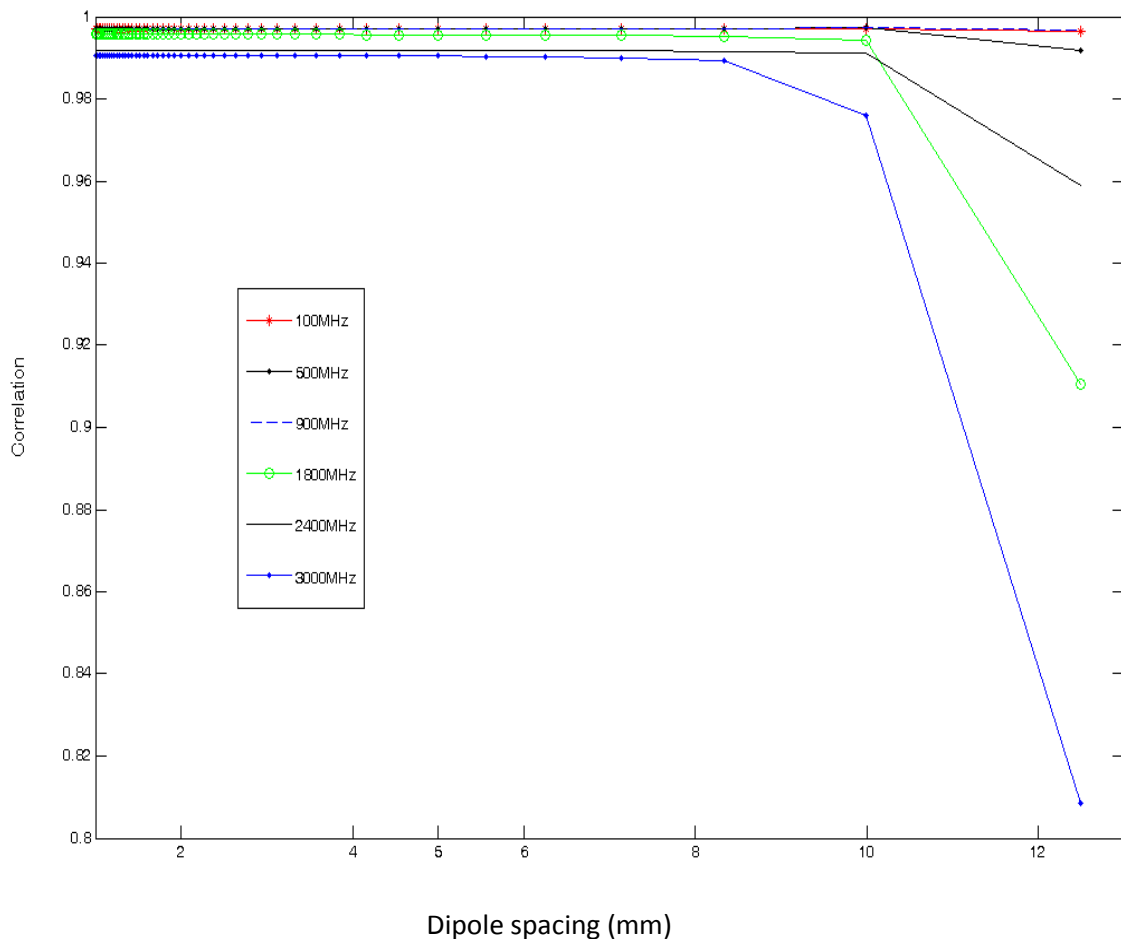


Fig. 4.17. Far field correlation.

4.6 Finite ground plane approximation

In the preceding section, reflection has been shown to be sufficient in approximating the scattering effect due to an infinite conducting ground plane. The image theory was used to approximate this effect and by combining it with the direct wave yields an accurate, close form solution for characterizing electromagnetic properties of a radiating element above an infinite ground plane. This is also applicable for problems involving current sources that are well isolated from the edges of the PCB. However, most practical PCBs or other

electrical and electronic devices often involve current sources very close to the edges of a finite conducting ground plane. The result of this is that extra currents are induced at the edges of the ground plane due to its finiteness and further leading to diffraction.

In [13]-[14], radiations from the edges of the PCB, which are due to the via transitions of high speed signals, have been identified as a significant contributor to the total emissions from the PCB at a given observation point. Also these edge radiations increase as the emission sources are located close to the edges of the PCB. This makes the basic EDM technique adopted in [4] - [7] insufficient in representing other sources of emissions from a practical PCB of finite size. In [15], the accuracy of the basic EDM was shown to further deteriorate as the emission sources are located close to the edges. Therefore to develop a model that can fully represent a real life scenario, all the possible sources of the emissions in the PCB need to be taken into consideration. Often, this does not lead to a close form solution. In particular, this greatly increases the mathematical complexities in evaluating the contribution of diffraction to the total emission around a PCB finite ground plane. Though there are classical solutions that offer a good approximation for diffraction problems [16] - [19], however, they can be complicated analytically and often does not lead to close form solution. In [2], a hybrid technique was presented that is based on equivalent dipole model and numerical techniques, which was used to characterize emissions from an enclosure with an aperture. This is also presented later in this thesis.

Figure 4.18 shows the current excitation at an edge of a PCB due to its finiteness including other sources like the via and high speed traces. Therefore, total field H_t , at an observation point is then given by

$$H_t = H_{actual\ source} + H_{image\ source} + H_{edge} , \quad (4.14)$$

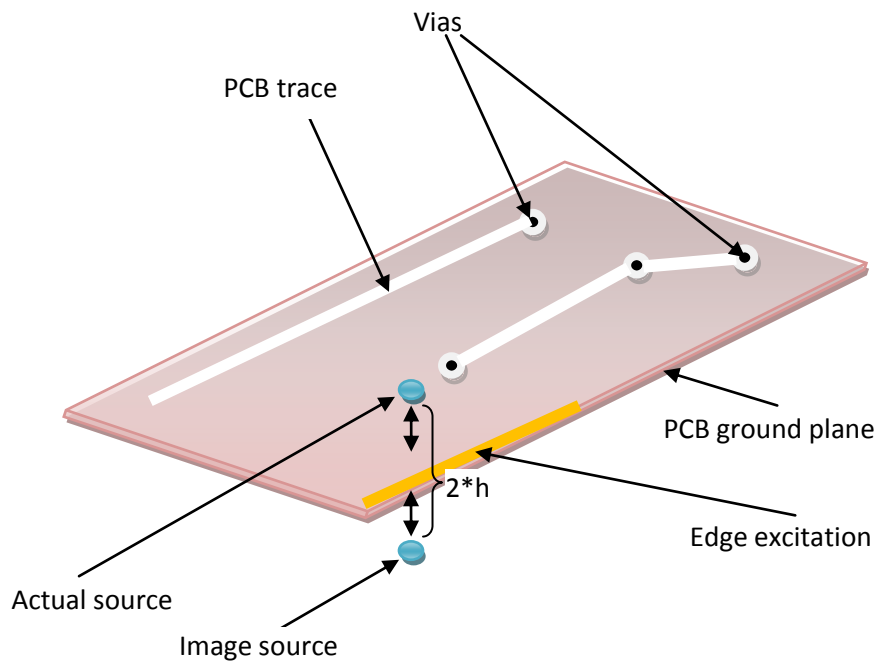


Fig. 4.18. Edge excitation and its sources in finite sized PCB.

4.6.1 Diffraction effect

The additional scattering at the edges of the ground plane due to the induced currents by the actual electromagnetic (EM) sources on the device under test (DUT) lead to diffraction. These diffraction effects if ignored as in [4] - [7], degrade the performance of the equivalent dipole modelling (EDM) especially when the EM sources are located closer to the edges. Furthermore, to evince this effect, a rectangular PCB, with a simple L trace of 30mm × 70mm, was simulated using MoM-based numerical code [3].

Firstly, the simple L trace was positioned at the centre of a large perfect electric conducting (PEC) ground plane with dimension 100mm × 160mm as shown in

Fig. 4.19(a). This is then repeated with the L trace positioned close to the bottom-right of the PEC as shown in Fig. 4.19(b). A dielectric surface of the same dimension as the PEC ($\epsilon = 4.6$) with a thickness of 1.5mm was placed in between the trace and the PEC to represent the typical FR4 properties.

For uniformity, the same discretisation as shown in Fig. 4.19 was used and the trace was excited with 0dB signal at the shorter leg while the longer leg was terminated with a 50Ω load in both cases.

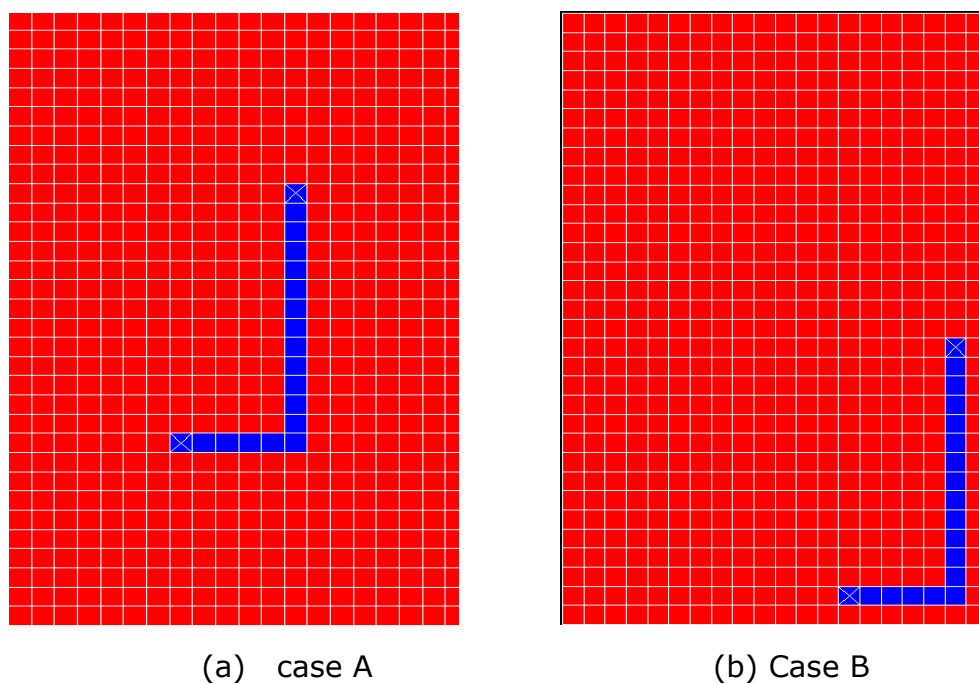


Fig. 4.19. Physical layout of a simple PCB with an L trace positioned at different locations above its dielectric layer.

The transverse magnetic field computation in the xy -plane was carried out over a range of frequencies. For consistency, the same sampling resolution and sampling height of 4mm and 10mm respectively were maintained for both cases. The transverse fields were then imported into the dipole model and were used to determine the moment vector for the equivalent dipoles required to reproduce the same fields. Similar to the approach in [6] and [7], the emissions of the EM sources were characterized using a number of infinitesimal dipoles, with 10mm

uniform separation, whose images accounted for the reflection due to the PEC. For the two cases, the same number of dipoles and dipole resolution were used. This is to enable clear comparison as the error in equivalent dipole modelling tends to reduce with the increase in the number of dipoles (see appendix B).

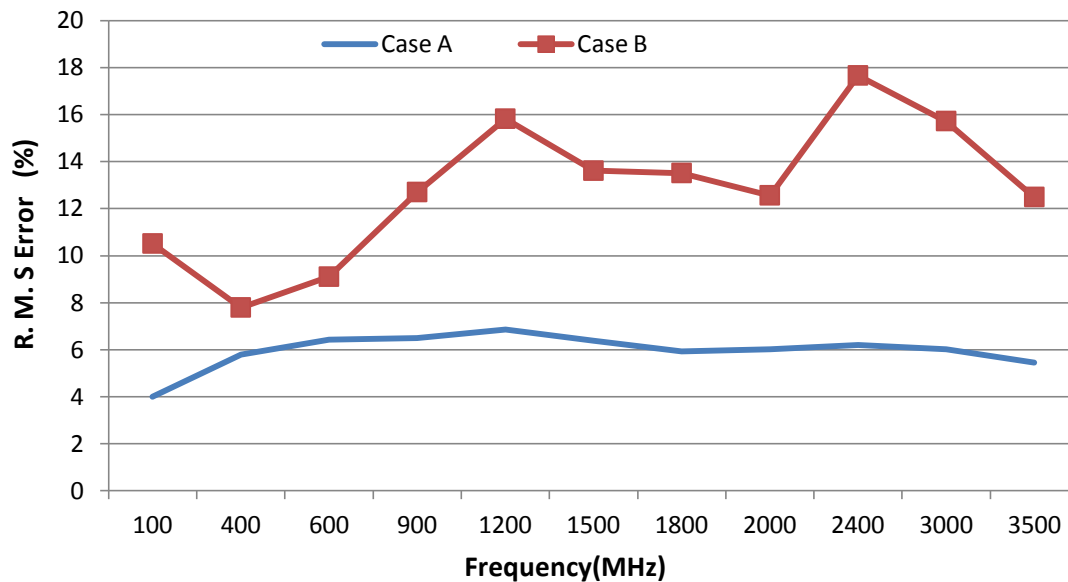


Fig. 4.20. PCB EDM results with different source positions.

Figure 4.20 compares the error in reproducing the transverse magnetic fields using the equivalent dipole model for the two cases shown in Fig. 4.19. The error significantly increases in Case B consistently across the frequencies considered. The error was computed as the average of the r.m.s error, ζ as given in (4.8). This increase in error, is due to the excited traces or the current sources being located close to the edges and hence exaggerating the diffraction at the edge. This is often the case with complex PCBs where components are placed close to the edge. This error increases as the number of the sources close to the edge increases in such a way that the images of the active sources are no longer sufficient to accurately characterize all the scattering effects due to the conducting ground plane.

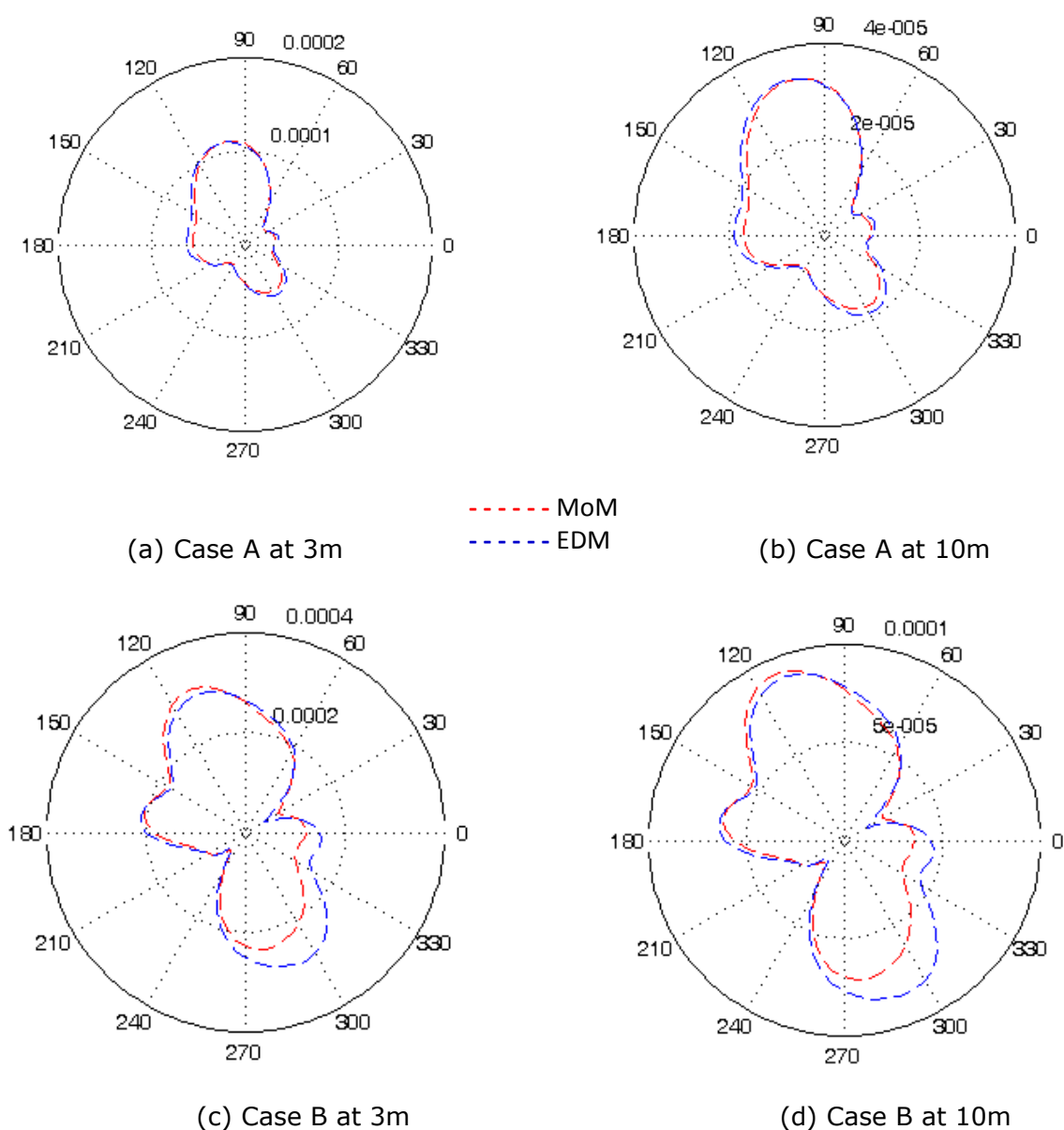


Fig. 4.21. Far-field results (Azimuthal, at $\theta=60$) for 2400MHz.

Figure 4.21 shows the azimuthal far-field results, H_θ for the 2 cases as presented in Fig. 4.19. The equivalent dipole moment vectors computed and used in estimating the r.m.s error in Fig. 4.21 for cases A and B, were then used to predict their magnetic fields at far-field distances of 3m and 10m. These fields were then compared with the MoM simulation results. More deviation is observed in case B while case A predicted the radiation pattern with high correlation. This far field result is shown for the industrial scientific and medical radio (ISM) band

2400MHz which finds its usefulness in several applications including Microwave oven, Bluetooth, WLAN, cordless phones and near-field communication.

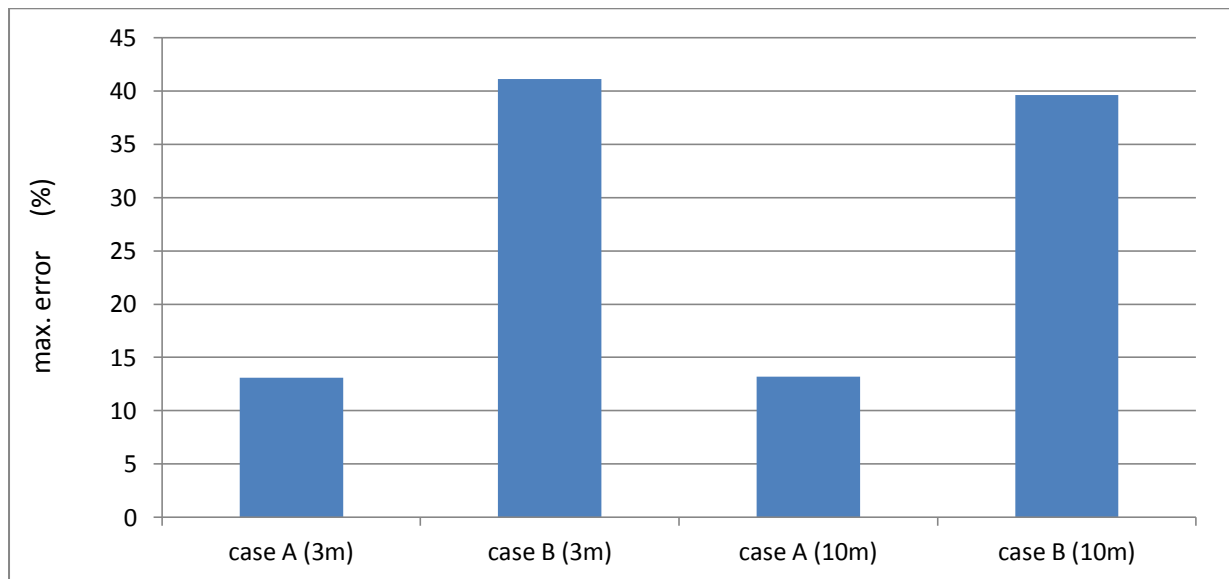


Fig. 4.22. Relative error computed at far-field for 2400MHz.

Furthermore, the maximum relative error ($\varnothing = 0$ to 360) is shown in Fig. 4.22. Maximum deviation from the simulation results are observed in modelling case B. This error increases as more current sources are located closer to the edges of the ground plane. Therefore, there is a need to characterize the additional currents at the edges of the ground plane for a finite ground and more practical problems.

4.6.2 Diffraction relative to source position

To investigate how diffraction effects vary with the position of the sources away from the edge, a simple scenario shown in Fig. 4.23 that comprises a *path A* which is a portion of the edge, a source placed at different positions away from *path A* and scanning planes (*xy* and *xz*) around the source is considered. The ground plane and the observation planes *xz* and *xy* are shown in Fig. 4.23, where the orange colour indicates the source position.

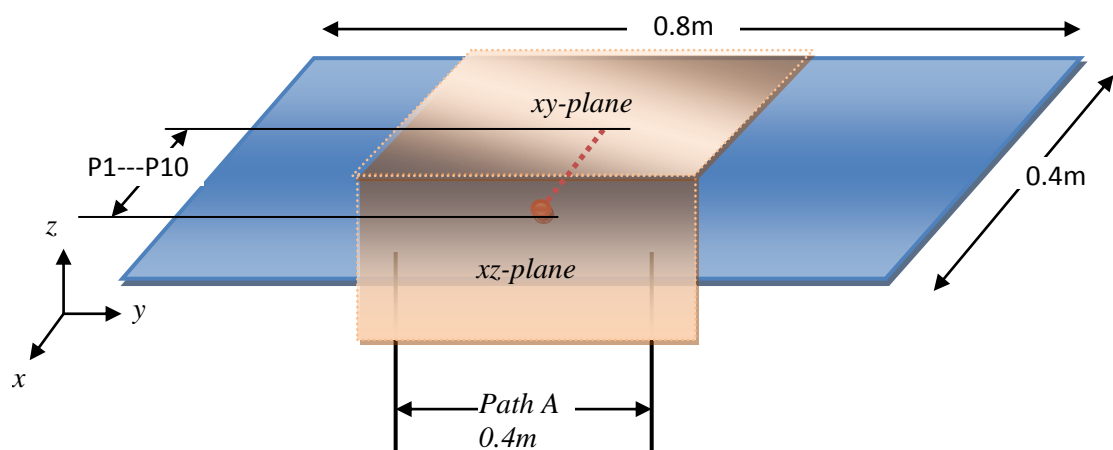


Fig. 4.23. Dipole position away from the edge.

The *path A* is assumed to be the area along the edge that has been significantly excited by the source. The sampling areas along *xy* and *xz* planes were made sufficiently wide to cover areas excited by the current source. Also in this experiment, the effect of the propagating wave and the introduction of edge dipoles are investigated.

The simulation was carried out using the MoM-based Concept-II code [3]. A large ground plane was used so as to provide sufficient isolation from other edges. A simple dipole source of frequencies 0.1-5.5GHz was then placed at 1mm above the ground plane at 10 different source positions along *x*. The computation was carried out at the *xy* and *xz*-planes as shown in Fig. 4.23.

The computed fields at the various planes were reproduced using the basic equivalent dipole modelling in section 4.4. This model was developed in such a way that the current excitations at the edges of a ground plane were not accounted for. Through this, the variation in the degree of diffraction can easily be extracted and the improvement brought about by the introduction of passive dipoles at the edges of the ground plane, easily quantified. The magnetic field comprising both amplitude and phase computed at the *xy* and *xz* planes using the MoM code were used as the input at the LHS of (4.7). The inverse problem

was then solved and the dipole moment vector was evaluated. This was then used to reproduce the fields at the two planes.

Figure 4.24 shows the r.m.s error as given in (4.6) in the xy and xz planes for different source locations P1-P10. The position of the source from the edge of a ground plane is shown to have a direct effect on the degree of diffraction observed. Figures 4.24a and 4.24b highlight this effect in characterizing emissions in the xy and xz planes respectively.

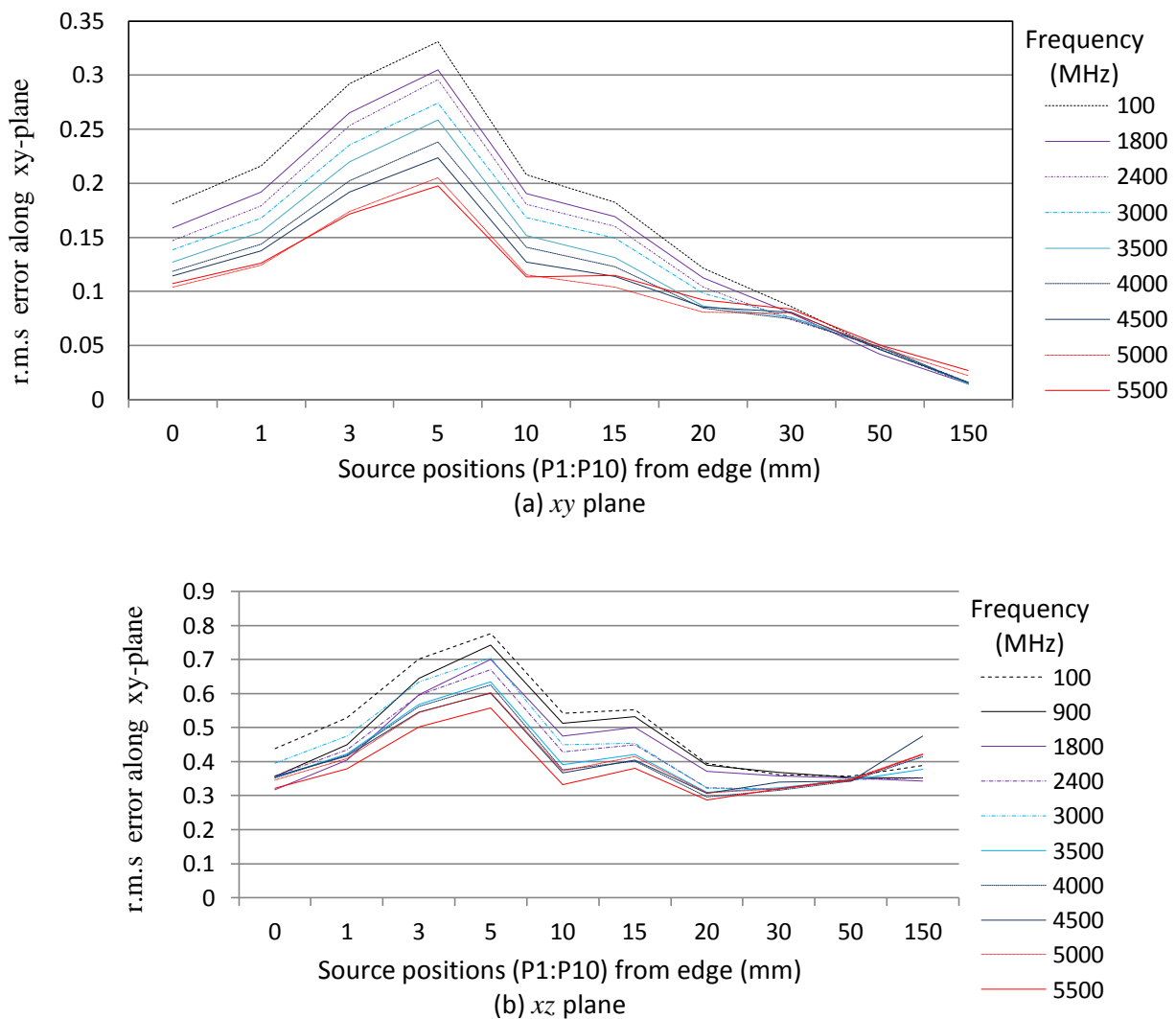


Fig. 4.24. Effects of finiteness of the ground on basic equivalent dipole modelling.

The diffraction is shown to be more significant, as expected, on the side plane xz resulting to higher r.m.s error as shown in Fig. 4.24b than the top plane xy in Fig. 4.24a. The r.m.s error was estimated from the expression (4.8).

It can also be seen from the results in Fig. 4.24, that the error due to diffraction effect reduces as the source is positioned further away from the edge of the ground plane. It is also related to the propagating wave as at higher wavelengths, the distance of the source from the edge becomes electrically small resulting to an increase in diffraction as seen in the Fig. 4.24b. For this problem, source position of about 4.5mm from the edge can be said to cause worst diffraction effect. This is unique with the problem and is dependent on the observation plane selected for the experiment and the height of the dipoles from the ground plane.

4.6.3 Solutions to diffraction

High frequency techniques

There are solutions that offer a good approximation to diffraction problems. Some of these techniques to include

- Geometric Theory of Diffraction (GTD) which is a form of the classical Geometric optics but with the introduction of the diffraction element [1],[16] as a solution to finite edge diffractions.
- Physical Theory of Diffraction (PTD) which supplements the physical optics by providing corrections due to the diffractions at the edge of the conducting surfaces [17]-[18].
- Uniform Theory of Diffraction (UTD) which remedies the GTD's erroneous predictions at and near the incident and reflected shadow regions by modifying the diffraction element [19].

These are mainly high frequency techniques whose analytical Solutions lead to very complicated integral equations as seen in the PTD [17]-[18]. To further show the complexity of some of these high frequency techniques, an example of the GTD/UTD [10] solution is presented.

Figure 4.25 shows the diffraction geometry as implemented in GTD [10], [18] for a straight edge. The source and observation points are located at distances S' and S respectively from the diffraction point Q_D where β_0' and β_0 are the phase constant of the medium. The total electric field, E^p at the observation point is therefore given by

$$E^p = E^{ip} + E^r + E^d \quad (4.15)$$

where E^p is the total field at any observation point p and E^{ip} , E^r and E^d are the incident, reflected and diffracted field components respectively at the point, p .

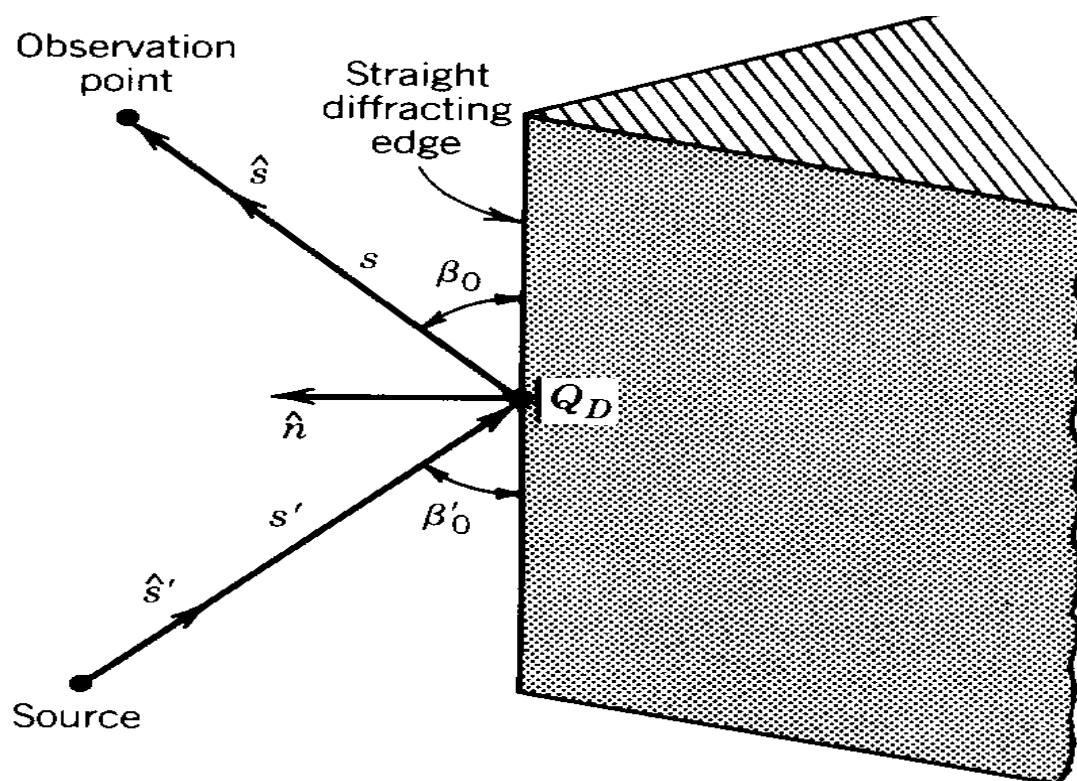


Fig. 4.25. Diffraction at the edge [10].

The solution for the incident and reflected component are easily solved through the geometric optics method. However, a more complicated approach is adopted for solving the field component due to diffraction, $E^d(s)$ as summarized below:

$$E^d(s) = E^i(Q_D) \cdot \bar{D} \cdot A(\rho_c, s) \cdot e^{-j\beta s} \quad (3.16)$$

where

- $E^i(Q_D)$ is the field at the reference point
- \bar{D} is the diffraction coefficient [10]
- $A(\rho_c, s)$ is the spatial attenuation [10]
- $e^{-j\beta s}$ is the phase factor

s is the distance of the observation point to the diffraction point, Q_D . ρ_c is the distance between the point Q_D and the second caustic (point through which all the rays of the wave pass) of the diffracted waves and is dependent on:

1. Wave front curvature of the incident field
2. Angles of incidence and diffraction, relative to unit vector normal to edge \hat{n} , at the point Q_D
3. Radius of curvature of diffracting edge at point Q_D

For straight edges as seen in simple PCBs, the ρ_c is approximated to s' , which is the distance of the source from the point of diffraction, Q_D . As can be seen from (3.16), the expression for the diffraction coefficient given in [10] does not yield a close form solution and thus presents a very complicated solution for characterizing emissions from PCBs [17], [18]. The same can be said of the Physical Theory of Diffraction technique where fictitious currents are used in computing the diffracted fields [17]-[18]. Therefore, there is a need for a more

suitable technique that approximates the diffraction problem with reduced complexity.

A hybrid technique that is based on the MoM-PO-UTD [20]-[21], Method of Moment-Physical Optics-Uniform Theory of Diffraction technique as implemented in Concept-II [3] was combined with the dipole modelling in solving diffraction problem. This is shown in the following subsection.

Characterizing of emission using EDM and numerical techniques

The example here is as presented and published in [2]. A hybrid solution based on MoM-PO-UTD is combined with the equivalent modelling for characterizing a radiating structure. As an example, metallic rectangular enclosure which is excited through an internally placed monopole was simulated on Concept II [3] in order to validate this approach.

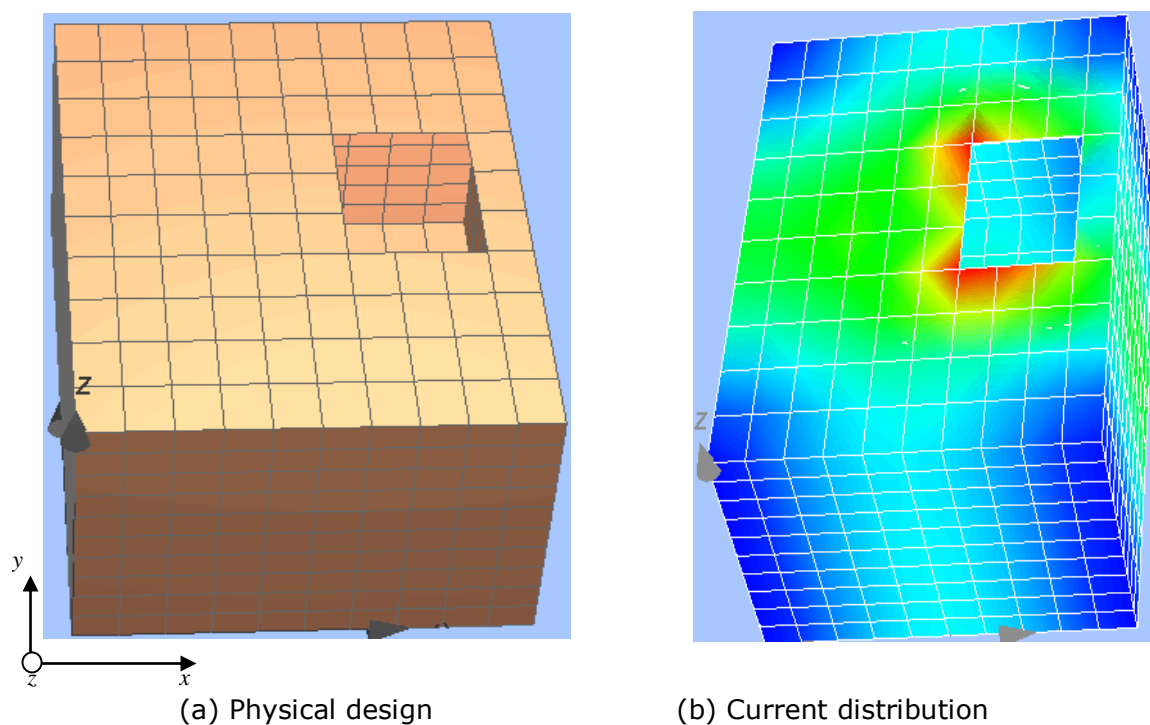


Fig. 4.26. Concept-II simulation of a metallic enclosure excited by a monopole source.

Figure 4.26a shows the physical design of the metallic enclosure whose dimensions are 30mm x 40mm x 20mm with a 9mm x 12mm slot on the top. A small monopole of dimensions 10mm by 1mm (length by radius), oriented along the z-axis is placed at the centre inside the enclosure. The simulation was carried out at 900MHz with a -5dBm excitation power. Figure 4.24b shows the current distribution on the metallic structure. These currents act as the EM sources over the entire structure.

As the sources are scattered around the entire structure, complete 3D information is required to fully characterise its emissions. The magnetic near fields (magnitude and phase) are obtained at sampling points over all the planar surfaces (at a distance of 10mm, 900MHz) that surround the structure above the ground plane. The sampling points are computed with a resolution of 2mm. Only the tangential fields to the plane are required from each plane. These fields (comprising magnitude and phase) are then used as the input in the dipole model. The field magnitude and phase information are extracted directly from the MoM-based simulation tool in this work.

Furthermore, in the dipole model, 84 dipole locations were randomly selected around the geometry of the structure with 3 orthogonal electric dipoles. A sufficient number of dipole points is required but should not be more than the sampled or measured points. Though this generates a very large matrix, it is better to maximize the dipole locations initially and then optimize them to retain the only significant contributors to the total field. This is because the accuracy of the final result from the optimization depends on the initial search options.

The coefficient matrix G is then computed at observation planes parallel to the sides of the test structure and 10mm from the surface, for all the dipoles using

the MoM-PO-UTD technique implemented in Concept-II [3], [20]-[21]. Next the dipole moment vector was calculated, from the observed fields generated from the test structure by solving the inverse problem (4.7). The SVD presented in Chapter 2 was used to solve the inverse problem. The computed dipole moment vector for the equivalent dipoles was then used in reproducing the fields at the surrounding observation planes parallel and 10mm from the sides of the test structure. The Concept-II was only used to compute the coefficient matrix which involves diffraction components for a given observation plane. Once this coefficient matrix has been computed, the equivalent dipole moment vector required for characterising any other PCB at the given observation plane was determined through the solution to the inverse problem.

Figure 4.27(a) shows the initial positions for the 84 dipoles which were later halved through an elimination process to 43 dipoles as shown in Fig. 4.27(b). The elimination process was implemented in such a way that it only retains dipoles D_i with moments M_i greater than or equal to a given percentage d , of M_{max} was used, where M_{max} is the maximum dipole moment of the initial dipole vector (i.e. $M_i \geq d \times M_{max}$).

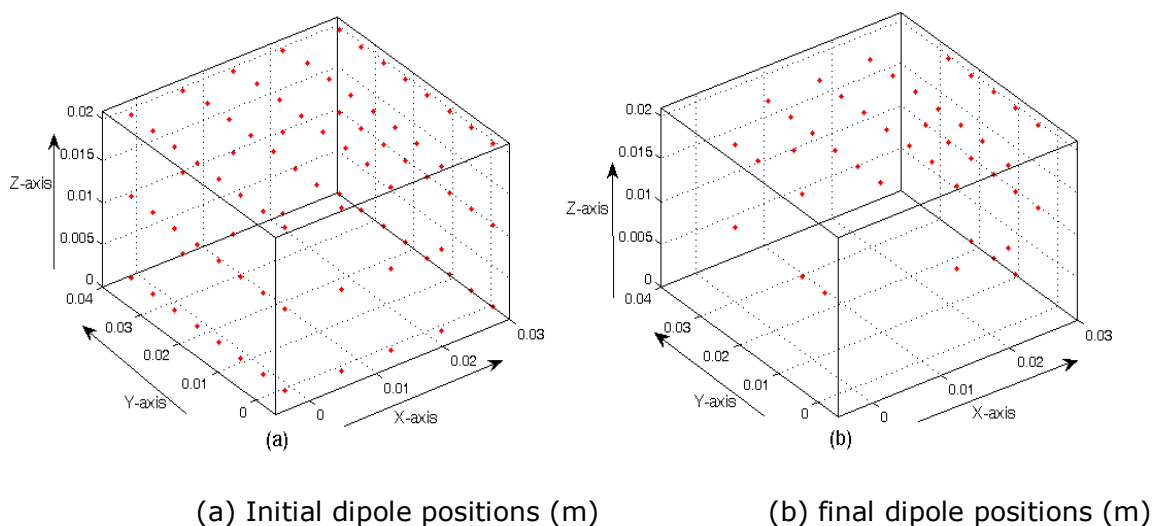


Fig. 4.27. The dipole positions about the geometry of the excited enclosure.

Any arbitrary value (in percentage) can be assigned to d however as this process reduces the total number of dipoles, the error is expected to increase with d . By assigning an arbitrary value of 10% to d , the dipole redundancy was minimized by 49%. The resulting 43 dipoles gave an error of 5.4% against 4.7% of the initial dipole array of 84 dipoles using the average R.M.S error relationship in (4.8).

Consequently, only the results from the optimized number of dipoles are included here, as the variance with the initial results is just about 15%. This implies that the optimized dipoles contain sufficient information to compute electromagnetic field results similar to the initial model. However, higher accuracy can be achieved by starting with a higher number of initial dipole positions as they serve as the accuracy benchmark for other results obtained via this basic optimization technique.

Fields reproduced at the initial plane

The dipole moment vector once calculated through the solution of the inverse problem to the equivalent dipole modelling expression (4.7), the magnetic fields at the initial planes i.e.10mm from the metallic enclosure surfaces can then be reproduced. The coefficient matrix G was computed for the 3 orthogonal magnetic field components of all the planar planes considered here (i.e. xy , yz and xz) using a hybrid technique based on MoM-PO-UTD. The fields predicted using the optimized 43 dipole positions were compared with the original fields and are presented in Figs. 4.28a, 4.29a and 4.30a. A very good agreement is observed.

Fields predicted at higher planes

Fields at different observation planes from the one used to obtain the equivalent dipoles can also be predicted using the equivalent dipoles properties calculated above (i.e. dipole moments and positions). The new coefficient matrix is computed using the hybrid of MoM-PO-UTD technique. The LHS of (4.7) can then be solved for any other higher plane. Figures 4.28b, 4.29b and 4.30b compare the fields predicted at xy , yz and xz planes 20mm from the test structure through EDM using the equivalent dipoles determined above (for characterizing the fields at 10mm) and the fields extracted directly from MoM simulation at planes 20mm parallel and surrounding the test structure (i.e. xy , yz and xz planes). These results show that the calculated equivalent dipoles can predict the electromagnetic fields at planes farther from the DUT than the observation plane used in determining them.

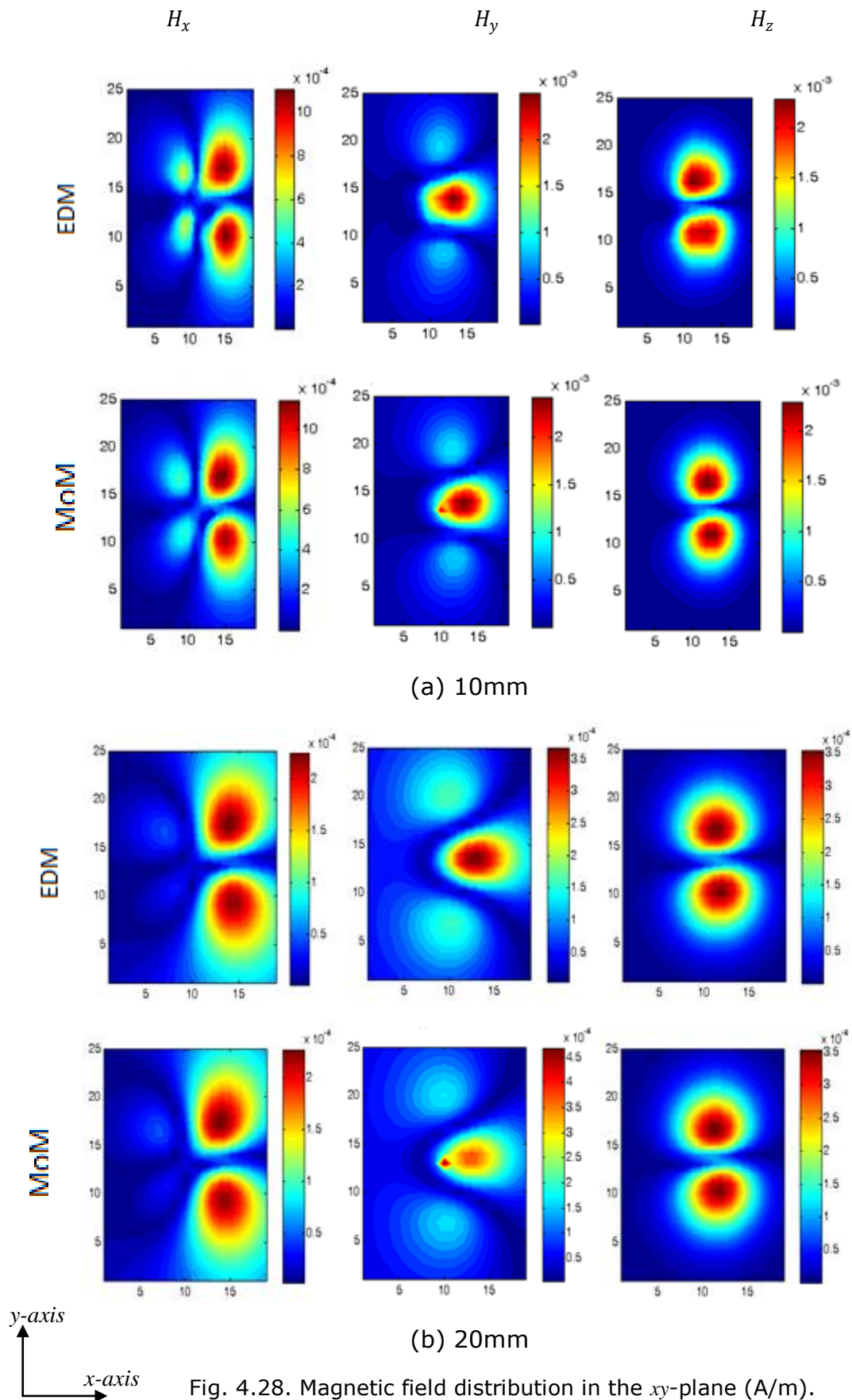
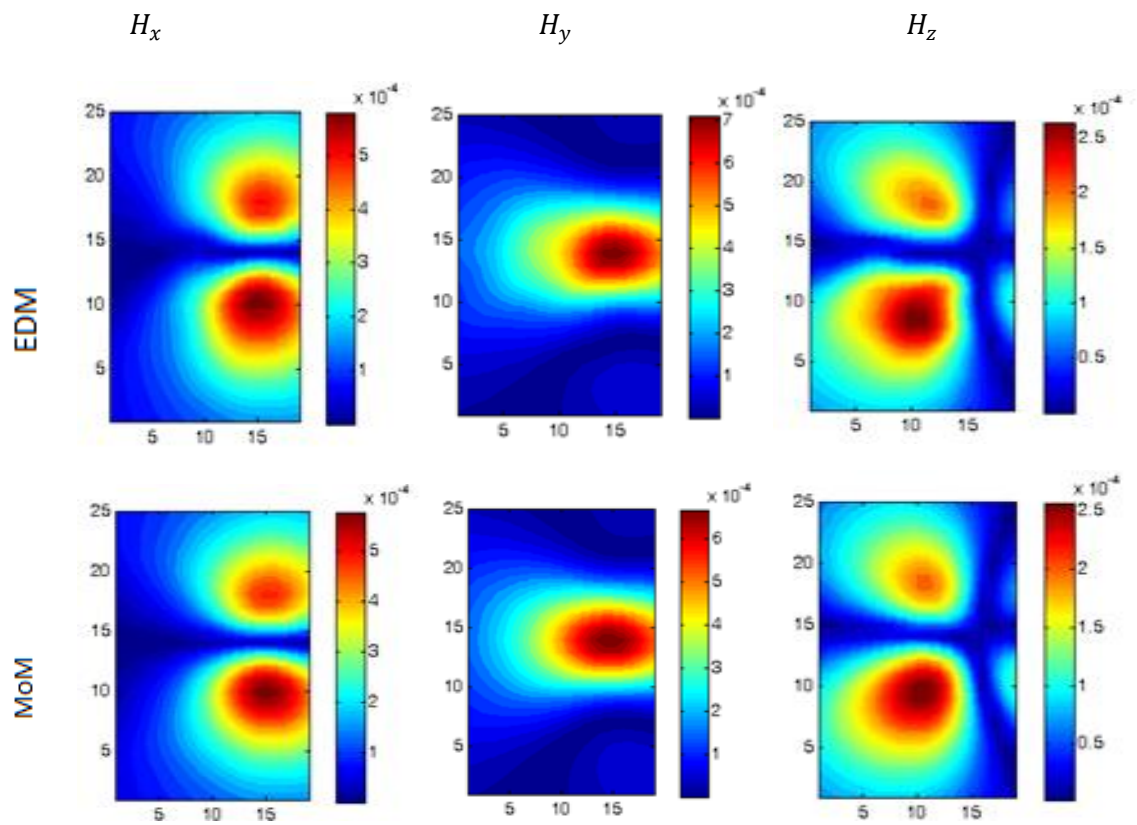
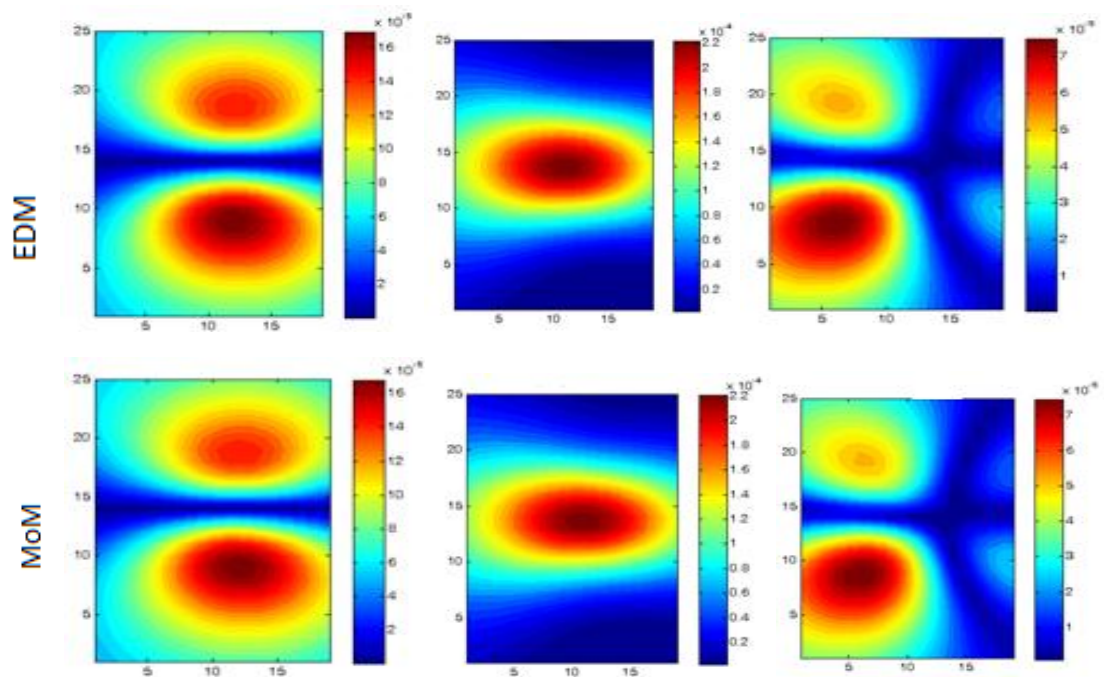


Fig. 4.28. Magnetic field distribution in the xy -plane (A/m).



(a) 10mm



(b) 20mm

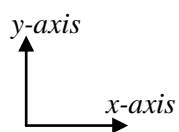


Fig. 4.29. Magnetic field distribution in the yz -plane (A/m).

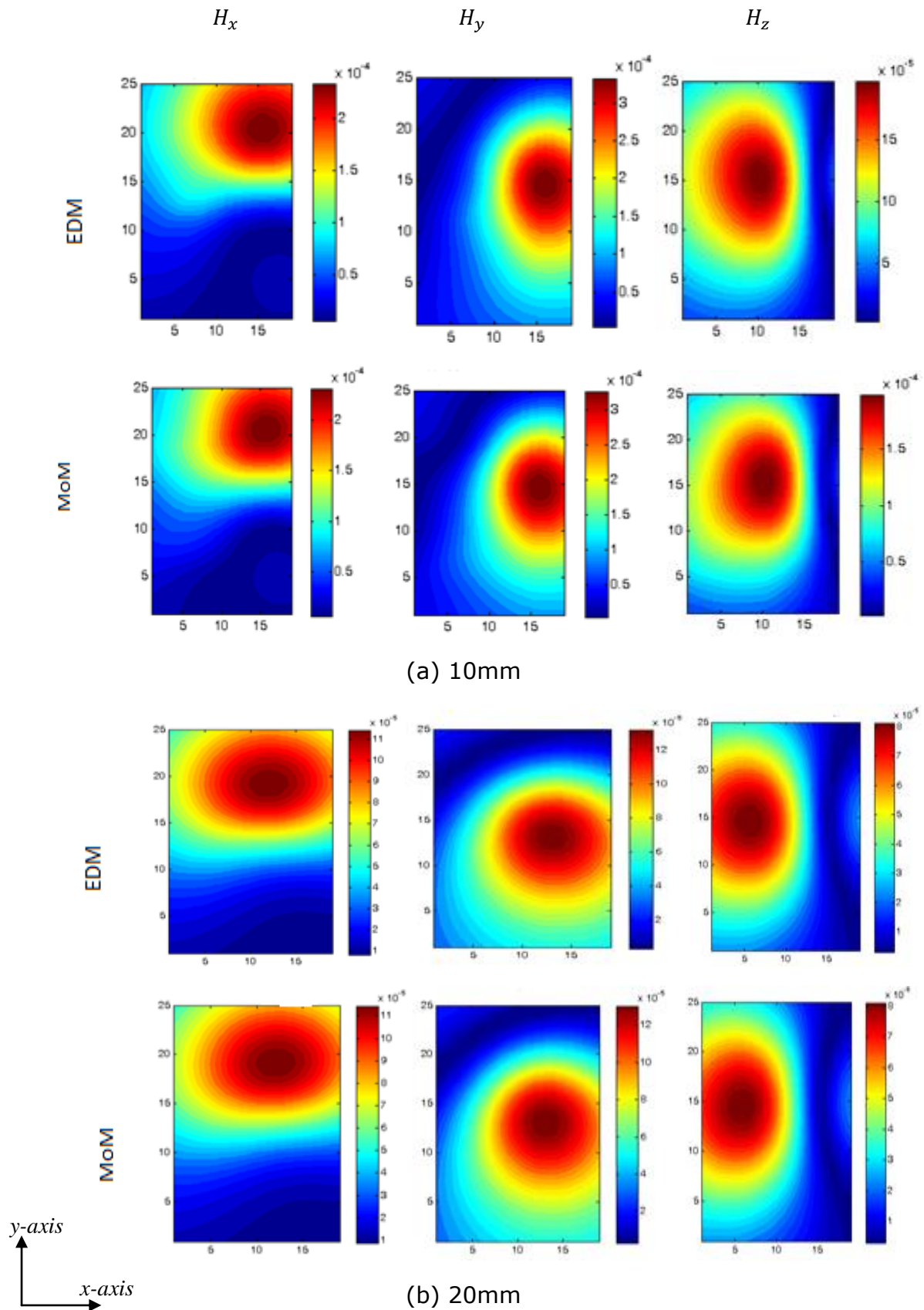


Fig. 4.30. Magnetic field distribution in the xz -plane (A/m).

4.7 Conclusion

It has been shown that an equivalent number of dipoles can be extended and used in predicting the emissions from a practical 3D radiator. Once the equivalent infinitesimal dipoles that are capable of emulating the electromagnetic properties of the actual sources are determined, the total field at any desired observation plane can be predicted. The dipoles used in this model serve as sources for computing the electromagnetic fields of interest without the need to accurately model the actual sources. The accuracy of the model improves with the number of dipoles used. It has also been shown that diffraction effects need to be accounted for in characterizing radiating elements above a finite ground plane. This is due to extra currents induced at the edges of the ground plane by the actual sources which was also shown to be more significant as the source is located closer to the edge of the finite ground plane. A hybrid model based on equivalent dipole modelling and high frequency techniques was shown to adequately characterize radiators with significant diffraction effects. The results from this approach have been compared with simulation and a good agreement was observed. Accordingly, the simulated data which served as the input for the dipole model can now be replaced by real near field measurement data from any practical test structure like a PCB, for studying its electromagnetic characteristics. This approach has been possible by combining the dipole modelling with a hybrid of MoM-PO-UTD technique. Whilst the hybrid technique was used to compute the coefficient matrix, the inverse problem of the equivalent dipole modelling was solved using the SVD to determine the equivalent dipole moment vector. This solution still presents a major problem in its high computational cost.

The next chapter looks at a simpler way of approximating the effect of diffraction through an all equivalent dipole modelling approach.

References

1. X. Tong, Simplified Equivalent Modelling of Electromagnetic Emissions from Printed Circuit Boards, PhD Thesis, University of Nottingham, Nottingham, 2010.
2. C. Obiekezie, D. W. P Thomas, A. Nothofer, S. Greedy and P. Sewell and C. Christopoulos, "Prediction of emission from a source placed inside a metallic enclosure over a finite ground plane , " EMC Europe 2012 Conf., Rome, Italy, Sept. 2012.
3. Concept-II, available [Online], 2013, <http://www.tet.tu-harburg.de/concept/index.en.html>.
4. C. Obiekezie, D. W. P Thomas, A. Nothofer, S. Greedy and P. Sewell, "Electromagnetic Characterization of 3D Radiators, " EuroEM 2012 Conf., Toulouse, France, July 2012.
5. X. Tong, D. W. P. Thomas, A. Nothofer, P. Sewell, and C. Christopoulos, "Modelling electromagnetic emissions from printed circuit boards in closed environments using equivalent dipoles", on *IEEE Trans. Electromagn. Compat.*, vol.52,no.2,pp.462-470, 2010.
6. Y. Vives-Gilabert, C. Arcambal, A. Louis, F. de Daran, P. Eudeline, and B. Mazari, "Modeling magnetic radiations of electronic circuits using near-field scanning method," *IEEE Trans. Electromagn. Compat.*, vol. 49, no. 2, pp. 391–400, May 2007.
7. Lotfi Beghou, Bing Liu, Lionel Pichon, François Costa, "Synthesis of Equivalent 3-D Models from Near Field Measurements - Application to the

- EMC of Power Printed Circuit Boards," *IEEE Transactions on Magnetics*, vol. 45, no. 3, pp 1650-1653, 2009.
8. D.B. Davidson, *Computational Electromagnetics for RF and Microwave Engineering*, 2nd Edition, Cambridge: Cambridge University Press, 2011.
 9. R. E. Collin, *Field Theory of Guided waves*, 2nd edition, New York: IEEE press, 1991.
 10. C. A. Balanis, *Advanced engineering electromagnetics*, New York: Wiley, 1989.
 11. C. A. Balanis, *Antenna Theory Analysis and Design*, John Wiley and Sons, New York, 2005, 3rd ed.
 12. CST- CST MWS, Germany. [online]. 2013, <http://www.cst.com/>.
 13. J. S. Pak, H. Kim, J. Lee, and J. Kim, "Modeling and Measurement of Radiated Field Emission from a Power/Ground Plane Cavity Edge Excited by a Through-Hole Signal via Based on a Balanced TLM and via Coupling Model," *IEEE Trans. on Adv. Packag.*, vol. 30, pp. 73-85, Feb. 2007.
 14. W. Cui, X. Ye, B. Archambeault, D. White, M. Li, and J. L. Drewniak, "EMI Resulting from Signal via Transitions through the DC Power Bus," *IEEE International Symposium on Electromagnetic Compatibility*, pp. 821-826, 2000.
 15. C. Obiekezie, D. W. Thomas, A. Nothofer, S. Greedy, L. R. Arnaut, P. Sewell, "Extended Scheme using Equivalent Dipoles for Characterizing Edge Currents Along a Finite Ground Plane," *Applied Comp. Electromagn. Soc.*, vol. 28, nos. 11, pp. 1111-1121, Nov. 2013.
 16. J. B. Keller, "Geometrical theory of diffraction," *J. Opt. Soc. Amer.*, vol. 52, no. 2, pp. 116-130, February 1962.

17. P. Y. Ufimtsev, "Approximate computation of the diffraction of plane electromagnetic waves at certain metal bodies. Part I: Diffraction patterns at a wedge and a ribbon," *Soviet Phys.-Technical Phys.*, vol. 2, no. 8, pp. 1708-1718, Aug. 1957.
18. P. Y. Ufimtsev, "Elementary edge waves and the physical theory of diffraction," *Electromagnetics*, vol. 11, pp. 125-160, 1991.
19. R. G. Kouyoumjian and P. H. Pathak, "A uniform geometrical theory of diffraction for an edge in a perfectly conducting surface," *Proc. IEEE*, vol. 62, pp. 1448-1461, Nov. 1974.
20. H. D. Brüns, M. Sabielny, D. Leugner, H. Singer, "Application and limits of the MoM-PO-UTD Hybridization Technique", *IEEE Symp. on EMC*, vol. 2, pp. 672-677, Santa Clara, Aug. 2004.
21. H.-D. Bruns, A. Freiberg and H. Singer, *Concept-II Manual of the Program System*, 2007.
22. C. E. Shannon, "The mathematical theory of communication," *Bell Syst. Tech. J.*, vol. 27, pp. 379-423, July 1948; also *ibid.*, vol. 27, pp. 623-656? Oct. 1948.
23. E. C. Cherry, "A history of information theory," in *Proc. Inst. Elec. Eng. (London)*, vol. 98, pt. 3, pp. 383-393, Sept. 1951.
24. E. B. Joy and D. T. Paris, "Spatial Sampling and Filtering in Near-Field Measurements," *IEEE Trans. Antennas Propagat.*, vol. AP-20, pp. 253-261, May 1972.

Chapter 5

Extended Equivalent Dipole Modelling

5.1 Introduction

In this Chapter, the Extended Equivalent Dipole Modelling (EEDM) is presented. This is a simple approach that is based on equivalent dipoles only and can be said to be an extension of the equivalent dipole modelling. An additional set of dipoles is added at the edges of the ground plane to emulate the electromagnetic behaviour of the induced edge currents. The EEDM will be shown to offer a viable solution to the limitations basic equivalent dipole modelling has in characterising practical problems.

In Chapter 4 the additional induced currents along the edges of a finite ground plane, which is a more accurate representation of a practical PCB, have been shown to introduce another scattering phenomenon known as diffraction. This diffraction is also seen to increase as the current sources are located closer to the edges of the ground plane. Consequently, rendering the basic equivalent dipole modelling method of source dipoles and their images insufficient for characterizing all the possible sources of emissions in practical PCBs. A hybrid technique that is based on equivalent dipole modelling and high frequency techniques was used to characterize a radiator with significant field contributions [3] due to diffraction to an observation plane. However, this solution poses a problem as its computational cost increases with the complexity of the problem.

In this Chapter, a simple technique based on the use of passive dipoles is presented as a way of approximating the effects of diffraction.

5.2 Passive Dipoles

In this section the effects of diffraction are accounted for by introducing edge dipoles. The same problem presented in Chapter 4 section 4.6.2 is also used here. Edge dipoles are introduced to the existing equivalent dipole modelling for emulating the electromagnetic characteristics of the currents induced at the edges of a finite ground plane without requiring complicated integral expressions often adopted in approximating diffraction effects [2]. The edge dipoles D_{edge} , are passive sources as they emanate as a result of currents induced at the edges due to the active sources. Therefore the total field, H_t at any observation point p is assumed to be as a result of the contributions of the fields H_{edge} , from the passive dipoles and H_{source} from the active dipoles. The set of passive dipoles are combined with the active dipoles (i.e. representing the active sources) to generate the dipole vector required for the model. And their relationship with the total field, H_t is formulated from (4.5)-(4.7) as

$$H_t = H_{source} + H_{edge} \quad (5.1)$$

$$[H_t] = [G][D_{source}] + [G][D_{edge}] \quad (5.2)$$

$$[H_t] = [G][D_{source} + D_{edge}] \quad (5.3)$$

where the source D_{source} , comprises the direct wave and the reflected (image) wave. Using the solution to the inverse problem as described in Chapter 2, the dipole moment vector in (5.3) is evaluated and other electromagnetic problems

about the PCB can then be solved. The edge dipoles were then introduced and the same fields as in section 4.6.2 were reproduced.

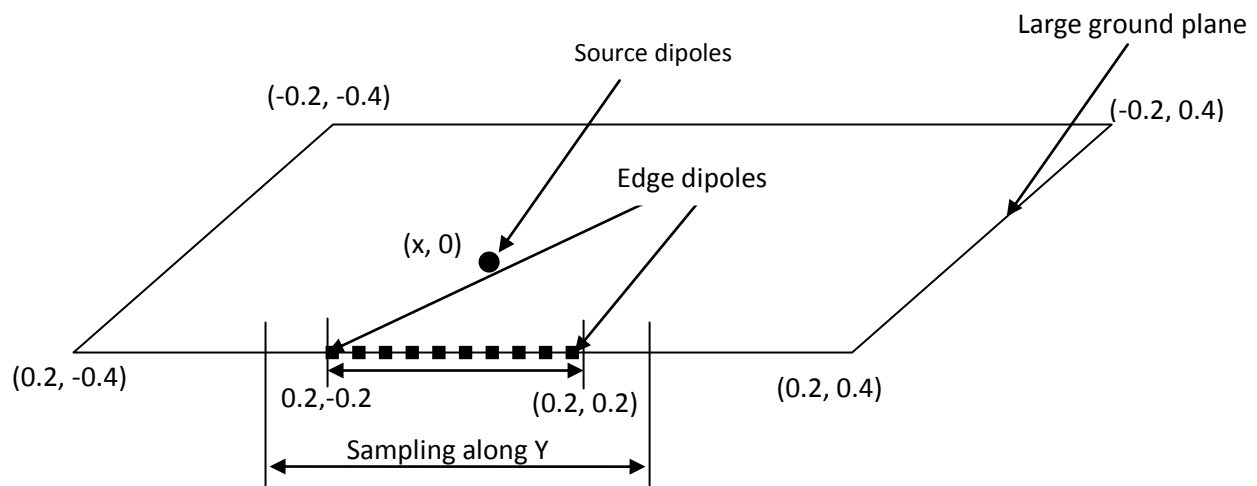


Fig. 5.1. Equivalent edge dipole model with dimensions in metres.

Figure 5.1 shows the schematic of the problem as implemented in the extended equivalent dipole modelling (EEDM). The spatial (x, y) coordinate of the dipole source is $(x, 0)$ for x values of $[0, 3, 5, 10, 15, 20, 30, 50, 100]$ mm. These were the same as the problem shown in Fig. 4.23. The edge dipoles were added as shown in Fig. 5.1 along the excited edge in the modelling. These edge dipole positions together with the already known position of the source were then used in evaluating the dyadic Greens function in (5.3). The fields on the xy and xz planes as computed using the MoM code were then used as the input to the LHS of (5.3).

The dipole moment vector, comprising the source and edge dipoles, was evaluated through the solution to the inverse problem Chapter 2. This was then used to reproduce the fields. The improvement achieved through this technique for five edge dipoles with respect to the basic equivalent dipole model (4.5)-(4.7) is then shown in Fig. 5.1. The relative improvement is used as a measure of how much the extended equivalent dipole modelling was able to reduce the

error observed using basic equivalent dipole modelling to characterize a problem. This improvement was estimated through

$$\text{Improvement (\%)} = \frac{\zeta^{edm} - \zeta^{eedm}}{\zeta^{edm}} \times 100 \text{ [\%]} \quad (5.4)$$

where ζ^{edm} and ζ^{eedm} are the r.m.s errors in reproducing the fields using the basic equivalent dipole modelling and the extended equivalent dipole modelling respectively. Only the result for xz -plane is shown here, as the total field on this plane has been shown earlier in Fig 4.24b to have stronger contribution due to diffraction effect.

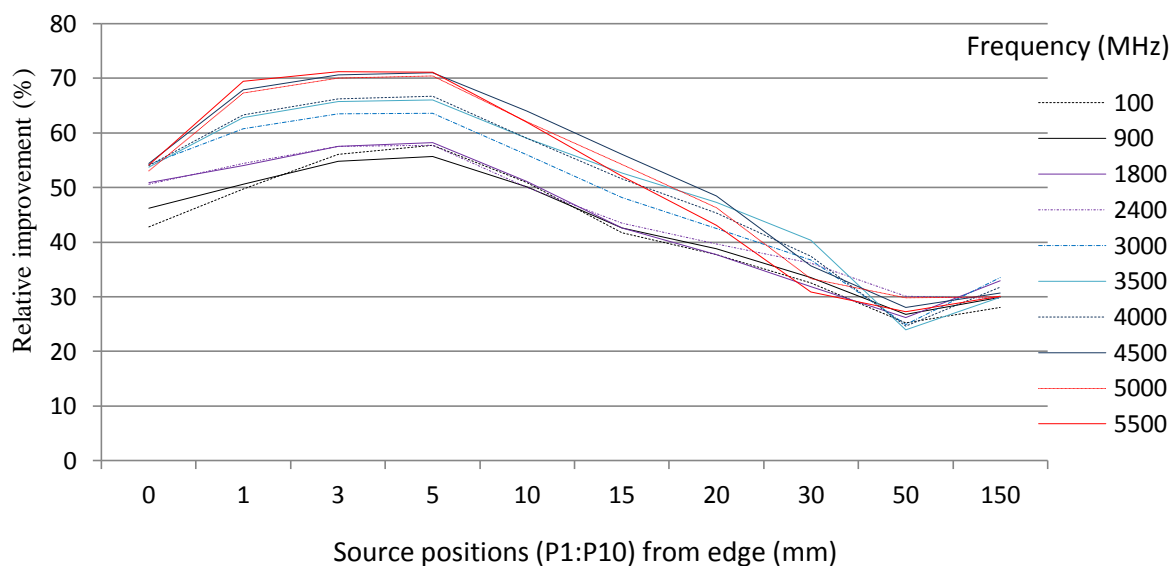


Fig. 5.2. Improvement as a result of edge dipoles for the xz -plane.

Figure 5.2 shows significant improvement across the entire band which was achieved through the introduction of five edge dipoles that are uniformly separated by 8mm.

This improvement has also been shown to reduce as the source is located further away from the edge following same shape with the plots in Fig. 4.24. This is expected as the error contribution due to diffraction reduces with source

separation from the edge which will further result to the convergence of both models and also higher improvements are achieved at the regions with higher error as seen in Fig. 5.2. Therefore, sufficient edge dipoles are required to adequately characterize the effects of the edge currents. In order to determine the optimal number of edge dipoles, different spatial resolutions were used to reproduce the fields. The errors in reproducing the fields at the yz -plane for various dipole resolutions are compared in Fig. 5.3. The result shows that with edge dipole resolutions finer than 8mm which was achieved in this problem by using 5 dipoles, the resulting improvement becomes insignificant.

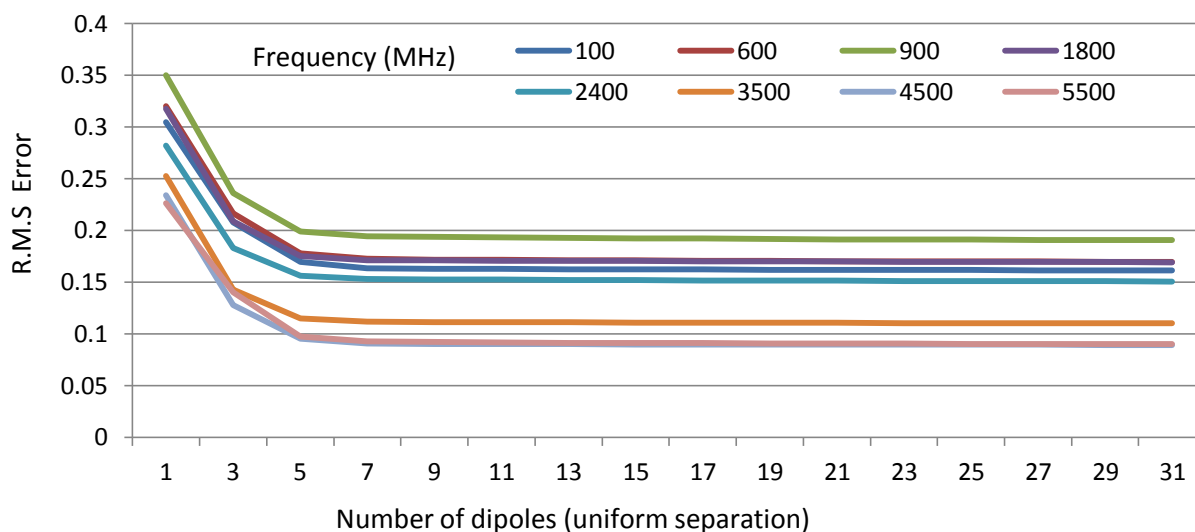


Fig. 5.3. Edge dipoles optimal uniform separation.

This behaviour is also consistent over the broad band considered in this experiment. Therefore it can be said that edge dipole resolution smaller than the wavelength can sufficiently emulate the behaviour of the additional currents excited at the edges of the ground plane by the active sources. This conclusion is also in agreement with that as obtained for characterizing active sources in [Chapter 4, section 4.4].

Generally, the accuracy in using equivalent dipole modelling to characterize radiating elements improves as the number of dipoles increases up to a certain optimal number. However, the edge dipoles as introduced above will be shown to specifically characterize emissions due to diffraction. This is demonstrated through the following experiment. Unlike the above experiment that was used to develop this model, the following experiment includes all the edges of the ground plane.

Effect of passive edge dipoles

To understand the influence of the passive dipoles, the same fields as in the two problems in [Chapter 4, Fig. 4.19] of L strip PCB on a finite ground plane were modelled using the EDM. However, unlike in the previous modelling, a number of infinitesimal dipoles were then introduced and positioned at the edges of the PEC ground plane. A sufficient number is required so as to fully emulate the current excitation at the edges. Here, infinitesimal dipoles of 10mm uniform separation were used. This is in addition to the number of infinitesimal dipoles also of 10mm uniform separation, used to characterize the actual sources.

It is necessary to distinguish the influence of the edge dipoles from just any additional dipole used for characterizing the active sources. It is expected that the increase in the number of dipoles would reduce the error. However, it is important to show that the edge dipoles particularly represent the effects due to diffraction hence will only improve cases that are affected by diffraction.

In case A, a problem with minimal diffraction effect was simulated on the MoM based Concept-II [1]. This was achieved by placing the trace at the middle of the large ground plane with good isolation from the edges. It is assumed that

through this, minimal current is induced at the edges of the ground plane by the trace. In case B, a problem involving significant amount of diffraction was simulated by placing the trace close to an edge of the ground plane. This is also shown in Fig. 4.19. In Chapter 4, section 4.6.1, the transverse magnetic fields were computed at 10mm in the xy -plane for the two test cases using active dipoles only. Furthermore, in addition to the number of active dipoles used in characterizing these problems, different dipoles (i.e. 52 passive dipoles, 31, 42, 64 active dipoles) were then added to highlight their contributions.

In order to understand the effect of each model (i.e. various dipole types and number), the improvement brought about by the introduction of the set of dipoles for each model was compared against the initial model presented in [Chapter 4, section 4.6.1]. These results are presented in Fig. 5.4 and Fig. 5.5.

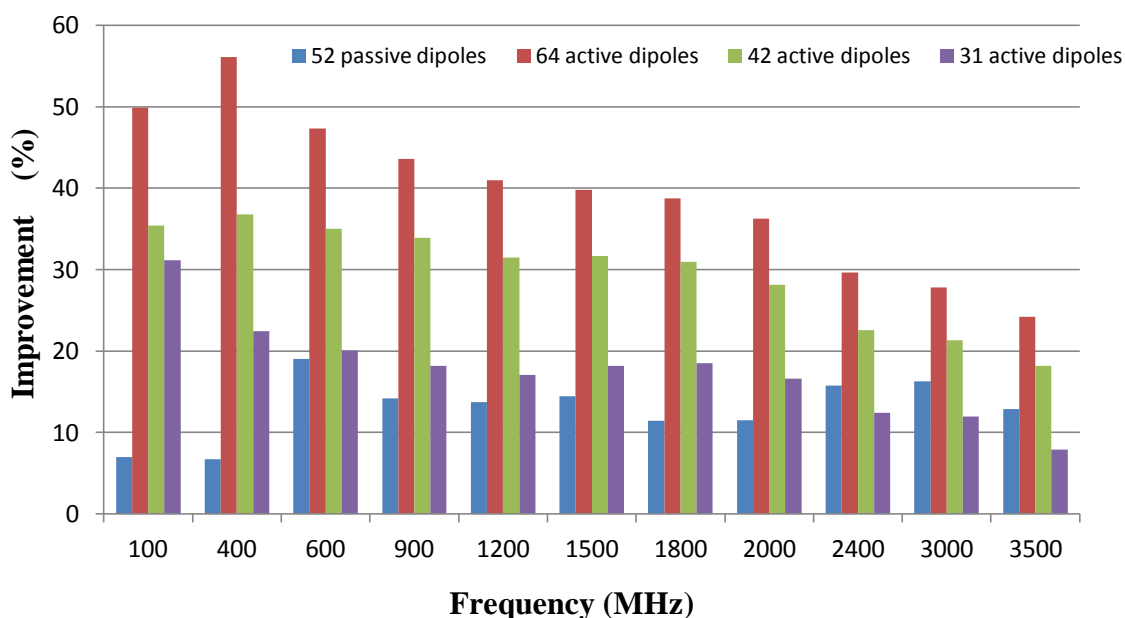


Fig. 5.4. Case A with minimal diffraction effect.

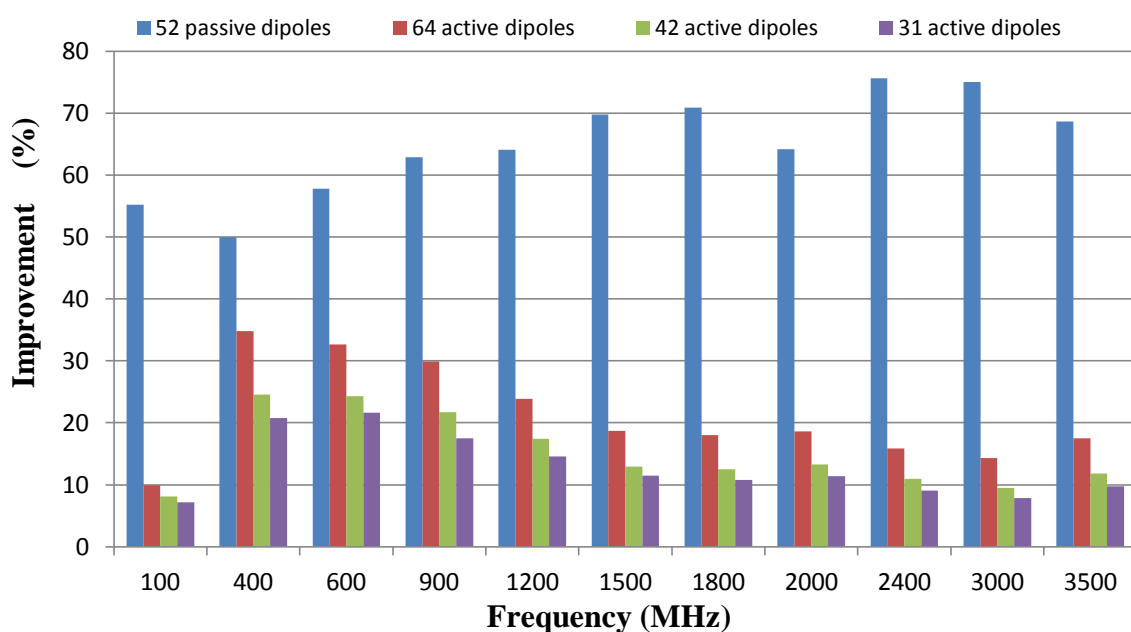


Fig. 5.5. Case B with significant diffraction effect.

Figure 5.4 shows that the introduction of passive dipoles resulted in a smaller improvement. This is shown in the plot with 42 active dipoles resulting in higher improvements than 52 passive dipoles. This is because passive dipoles are introduced to emulate the characteristics of the induced currents at the edges of the ground plane and not to characterize the active sources. This is the observation here as this case involves a problem with minimal current induced at the edge.

Conversely, Fig. 5.5 involves a problem with significant contribution due to the total field resulting from diffraction. The 52 passive dipoles are shown to bring about highest improvement. Even out-performing 64 active dipole model. This helps to show that even as the introduction of dipoles generally improves the accuracy of equivalent dipole modelling, the possible contributors to the total emissions to any observation point should also be determined for an accurate representation. The passive dipoles have been shown to accurately characterize

the emissions due to edge diffraction. This passive dipole technique (EEDM) is now used to characterize some practical problems.

5.3 EEDM Validation

5.3.1 Single layer PCB

To further show the viability of this approach, a long metallic strip over a finite ground plane (160mm x 100mm) with similar EM performance as a practical PCB was simulated using MoM code [1].

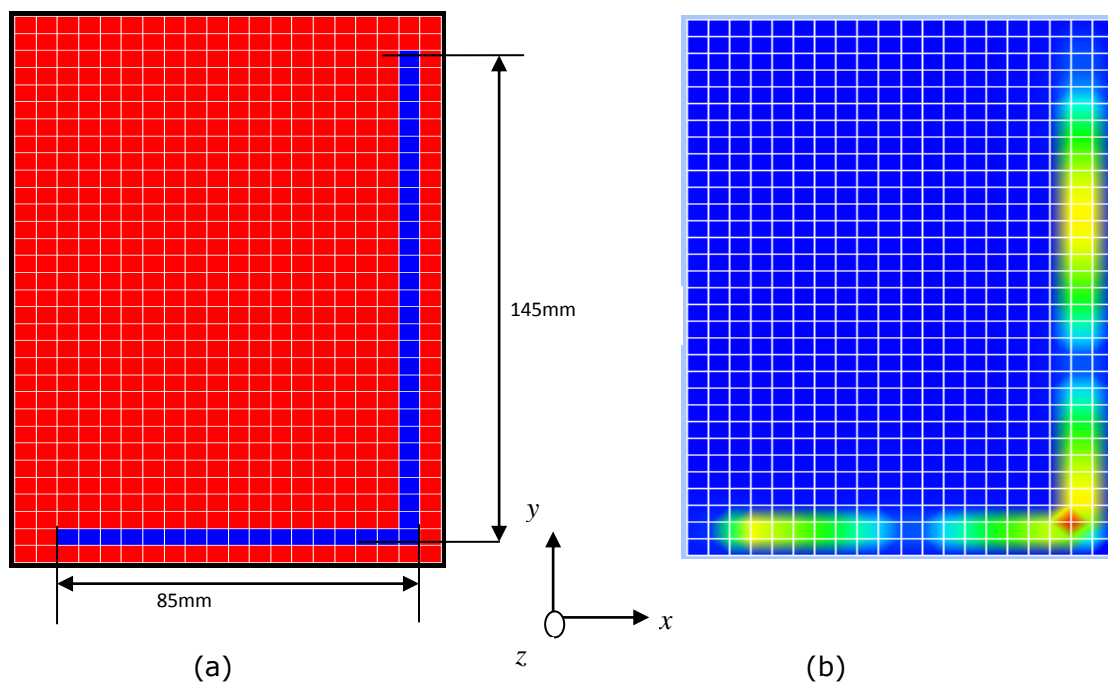


Fig. 5.6. (a) Physical design and (b) Current path on the L-shape strip.

Figure 5.6a shows the physical design with 5mm mesh size and Fig. 5.6b the current path along the L strip. The strip is excited with 8dBmW power at the tip of the shorter leg while the longer leg is terminated with a 50Ω load. This simulation was carried out at 900MHz and field results were extracted 10mm above the planes. Unlike the problem treated earlier, the transverse fields on all the planes surrounding the PCB are required in the model. This is to provide

sufficient information required to compute the moments of the passive dipoles. These passive dipoles have been shown to contribute most to the diffracted fields. Samples taken from the xy -plane only as used in sections 4.6.2 were sufficient because of the size of the trace and a smaller edge current excitation is expected. However, for a larger trace located close to the edge, significantly more edge current excitation is expected and to properly characterize these edge currents, sufficient sampling around the PCB is required.

Dipole modelling

The extracted complex-valued field strengths are then imported into the equivalent dipole model. The LHS of (5.3) comprises all the transverse fields extracted at each of the planes surrounding the structure. The first term on the RHS which includes the direct, reflected and diffracted field components, is then computed using (2.15)-(2.17) or (2.18)-(2.20) for electric or magnetic dipoles respectively. The dipole moment vector is then calculated through the solution for the inverse problem. As described in Chapter 2, the singular value decomposition technique was used. Following from the dipole expansion, 6 dipoles comprising 3 electric (D_x^E, D_y^E and D_z^E) and 3 magnetic (D_x^M, D_y^M and D_z^M) were first used to model each dipole point. This is computationally expensive and requires about 25mins to run on an Intel core i7 3GHz processor and 6GB RAM PC.

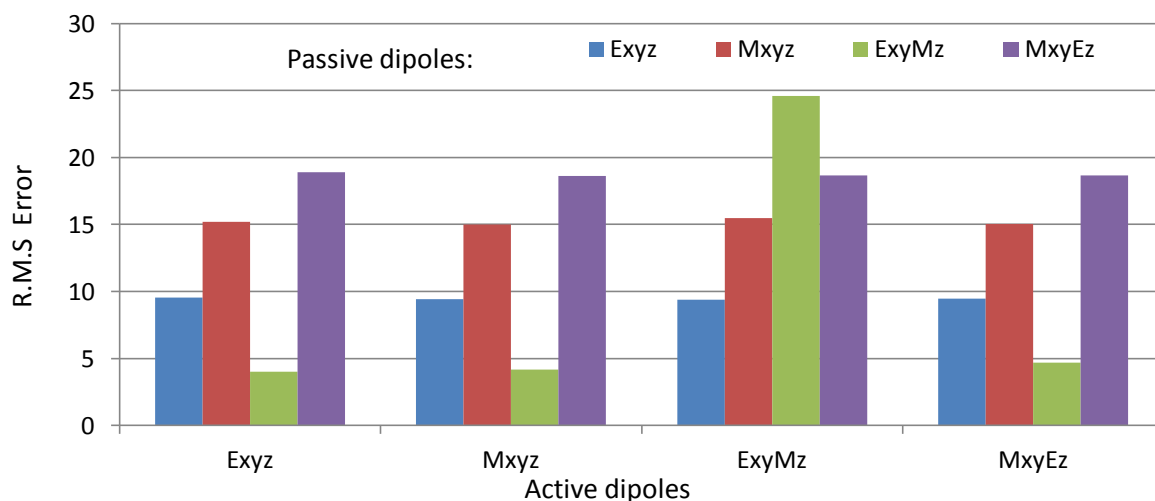


Fig. 5.7. Dipole configuration for EEDM.

Furthermore, by trying different combinations of dipoles and reducing the individual dipole moment redundancies, 3 orthogonal electric or magnetic dipoles were found to be sufficient in modelling the actual sources (active sources) while a combination of electric and magnetic dipoles were used in modelling the currents at the edges of the ground plane (passive sources). The result for the various dipole combinations for the active and passive dipoles is shown in Fig. 5.7. The result shows better performance is achieved when a combination of a vertical magnetic dipole and 2 horizontal electric dipoles are used to model the passive sources. The only exception is when similar combination is also used in modelling the active sources, which produces relatively worse result, as the dipole configuration could not characterize the direction of the excited currents. However, most combination here yielded results with r.m.s error less than 25%. It shows that for a single layer PCB, any combination of electric and magnetic dipoles can be used in characterizing both the active and passive sources on the PCB. The appropriate dipole configuration can be said to be problem specific as will be shown later for the double layer PCB. This is because various multilayer PCBs may present different current paths hence would require an appropriate

dipole configuration to be able to emulate the behaviours of the various current sources on the PCB. The single layer PCB was then characterized with the following dipole configuration

$$D_{active} = \begin{bmatrix} D_x^E \\ D_y^E \\ D_z^E \end{bmatrix} \quad (5.5)$$

$$D_{passive} = \begin{bmatrix} D_x^E \\ D_y^E \\ D_z^M \end{bmatrix} \quad (5.6)$$

Though any of the 3 orthogonal magnetic dipoles can equally be used in modelling the active sources with good accuracy, only the vertical magnetic dipoles can be used at the edges as the polarization of the horizontal magnetic dipole cannot generate currents in the direction of the actual currents induced at the edges in this particular problem. Initially, 468 dipoles were used which takes approximately 5mins run time using the same PC. The initial dipole positions are shown on Fig. 5.8.

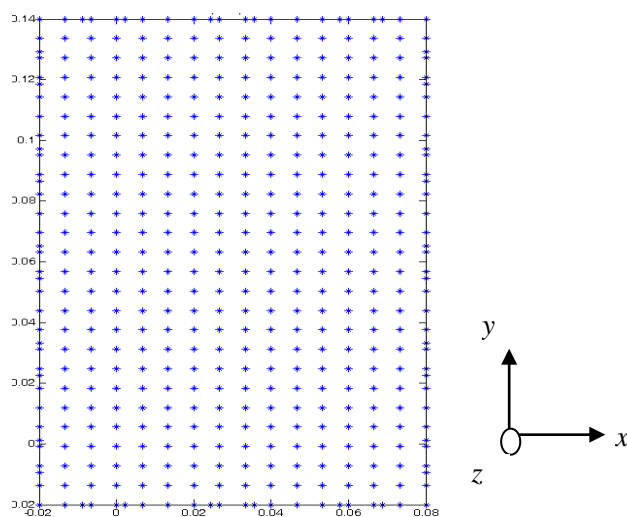


Fig. 5.8. Initial dipole positions.

Figure 5.9 shows the total field H_t , computed at the principal planes of the structure where

$$H_t = \sqrt{H_x^2 + H_y^2 + H_z^2}$$

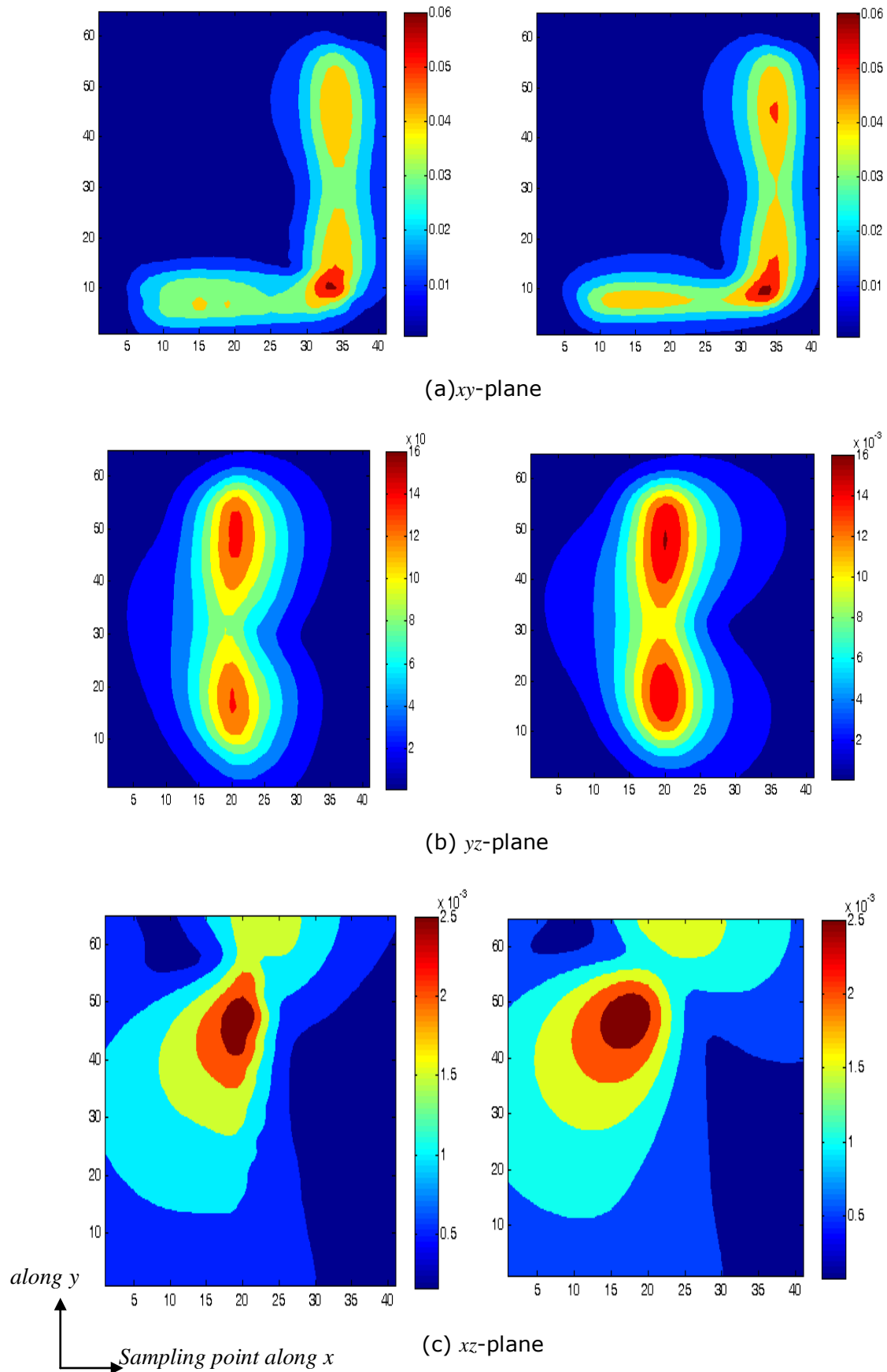


Fig. 5.9. Total magnetic fields magnitude H_t , computed at the principal planes using the EEDM (left column) and MoM (right column).

Furthermore, the redundant dipoles can be removed by retaining only the dipole moments with significant contributions, D_o (i.e. $D_o \geq p \times D_{mMax}$), to the total field observed at any given point. D_{mMax} is the maximum dipole moment in the initial dipole moment vector and p is a given proportion. This elimination technique was introduced earlier in Chapter 4 (section 4.6.3) and was applied to the metallic enclosure problem previously given in Fig. 4. 27.

Figure 5.10 then shows the optimized final dipole on the surface of the structure up to 10% of D_{mMax} (i.e. $p = 10\%$). This resulted in 102 dipoles. The active dipoles were found to align along the current path as expected. The moments of these optimized dipoles were then calculated according to (5.3) and used to predict these fields.

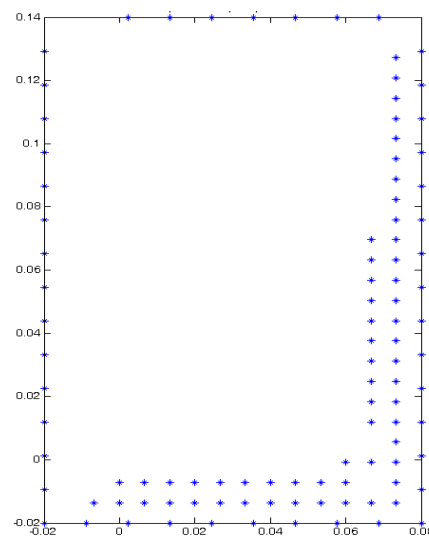


Fig. 5.10. Optimized dipole positions.

The maximum difference between the two models is observed in reproducing the fields at the xy -plane, because sufficient number of active dipoles is required to accurately model the fields parallel to the surface of the large structure. This is because the actual sources of emissions are located in this region. Again as mainly the active dipoles were reduced through optimisation the accuracy in reproducing the fields at the xy -plane reduces. Also predictions were made at

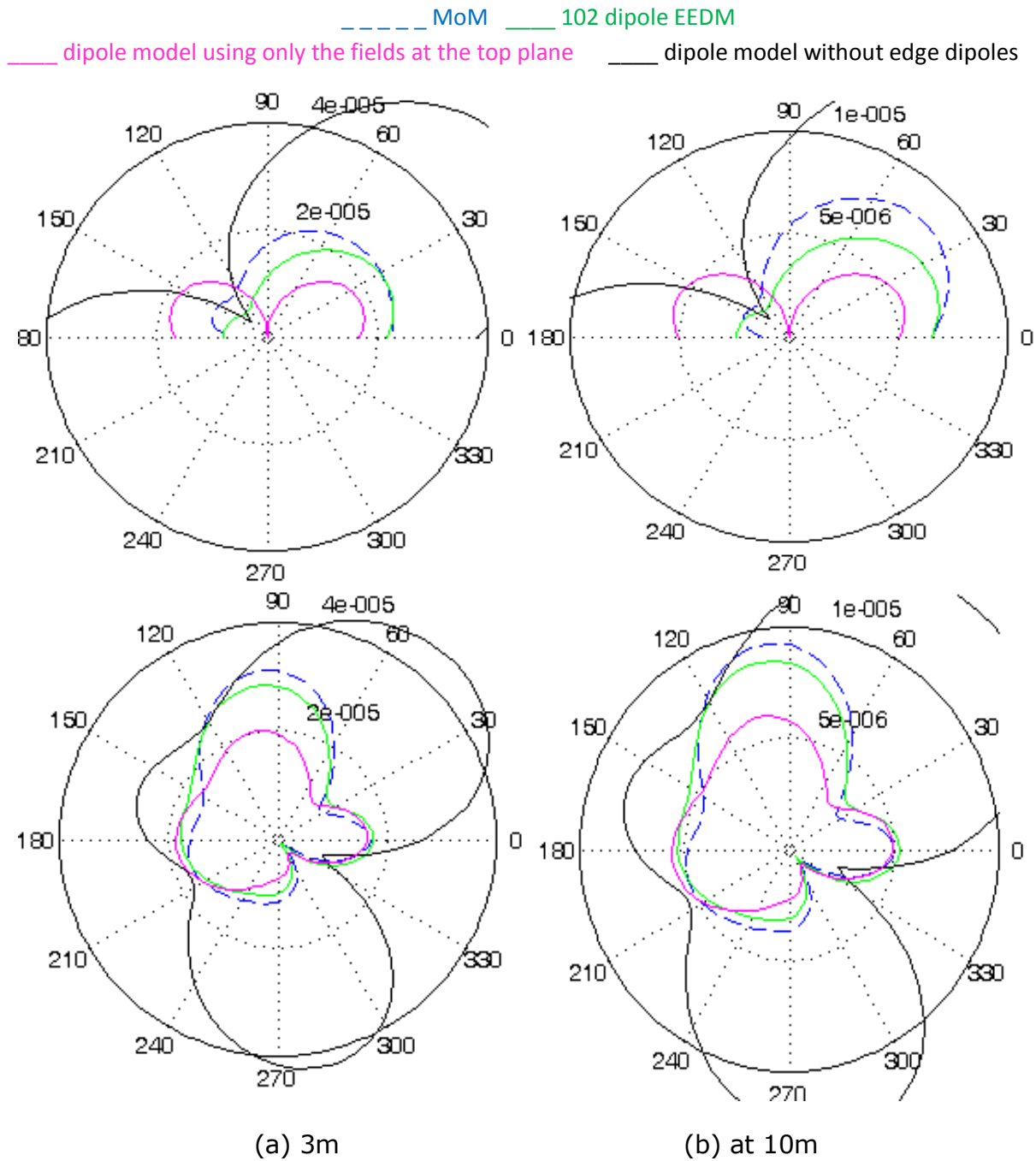


Fig. 5. 12. Field pattern of the PCB structure given in Fig. 4.8 and predicted with different equivalent dipole in A/m for H_θ (1st row) and H_ϕ (2nd row).

Dipole moments computed from the information obtained only from the top plane of the structure (i.e. xy-plane) yields higher error in predicting the far-fields. This is represented by the magenta line. By including the field information from all planes surrounding the structure to compute the dipole moment, a more accurate prediction is observed as represented in green.

5.3.2 Multilayer PCB

In a multilayer PCB, unlike a single layer PCB, more fields are expected at the sides. This is because of the multiple interactions between the PCB planes and other sources already present in a single layer PCB. The EEDM is now used to characterize a multilayer PCB with predictions up to far-field distance. Also some results are shown for various frequencies to show the consistency of this approach in yielding accurate solutions over a wide band.

Simulation

A multilayer PCB with an embedded L track was simulated using the method of moment (MoM) based simulation package, Concept-II [1]. The different layers included in the design are shown in Fig. 5.13.

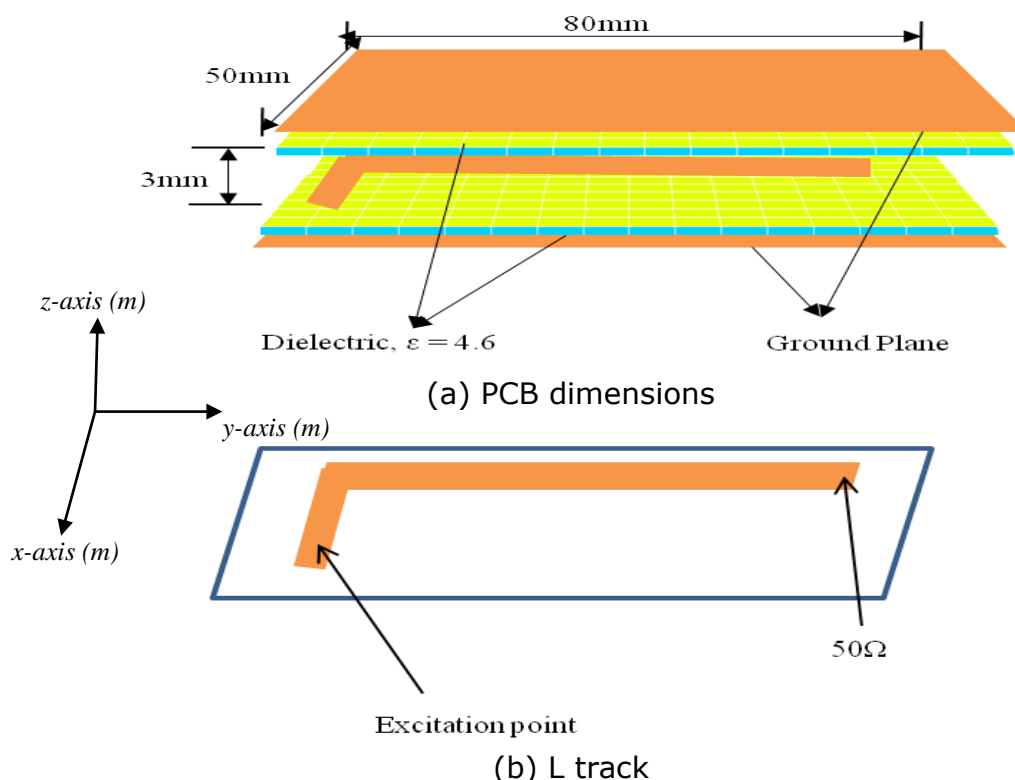


Fig. 5.13. Schematic representation of the PCB design.

The L copper track which represents the signal or power trace in a PCB, was sandwiched between the two dielectric layers of 3mm thickness. The dimension

of the copper track is 30mm x 60mm and positioned at 10mm from the edges of the ground plane.

The simulation was first carried out at 900MHz with a 0dBm CW excitation. The magnetic near field results were computed at a distance 10mm at planes surrounding the PCB. At each plane the three orthogonal magnetic field components were obtained. As mentioned earlier, the electromagnetic field information around the surfaces of the PCB are required in this model. This is to provide sufficient information for determining the number of infinitesimal dipoles needed to completely characterize the 3D structure. As also mentioned earlier in Chapter 3, an appropriate sampling resolution should be used in order to accurately determine the equivalent dipoles capable of characterizing the electromagnetic properties of the PCB. The appropriate dipole resolution is determined by the features of the problem which includes operating frequency and scanning height. The relationship was shown in the expression (4.12).

Therefore in this particular problem, a maximum sampling resolution of 5mm is required according to, however a finer resolution of about 2.5mm was used in this work. Figure 5.14 shows the magnetic field components extracted at 10mm to planes surrounding the PCB via simulation on Concept-II. It also shows the presence of strong radiation at the sides of the PCB especially for the H_x and H_y components. These hotspots are due to the currents between the source and loads connected to the ends of the trace and the current loops formed by this trace with the ground plane as shown in Fig. 5.13a.

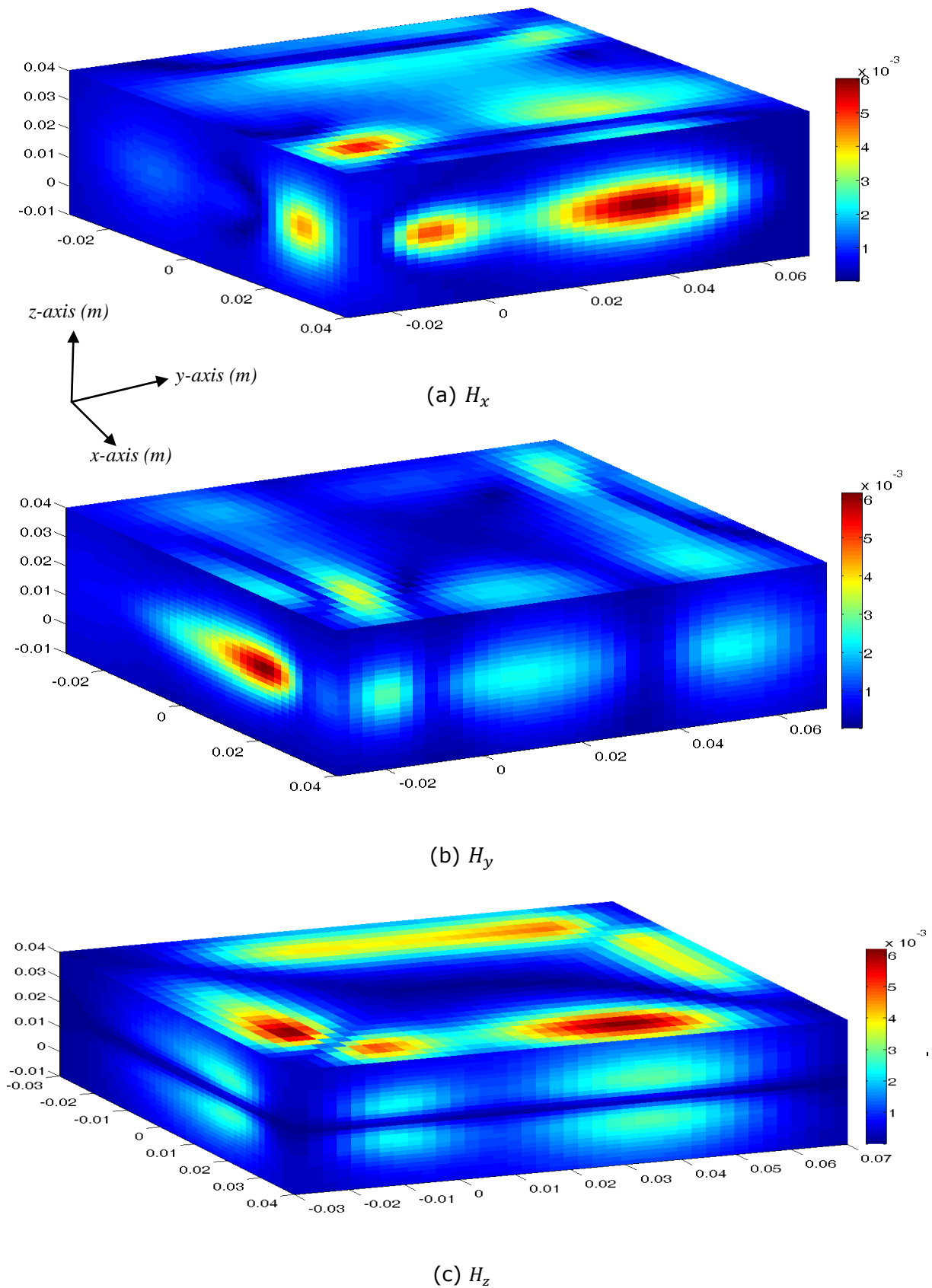


Fig. 5.14. Hotspots surrounding the multilayer PCB (H-Field in A/m).

Dipole modelling

An arbitrary number of dipoles were distributed uniformly above the ground planes positions as shown in Fig. 5.15. In modelling the active and passive sources, 5mm and 10mm uniform separations were chosen respectively. The nature of this PCB necessitated modelling over 2 parallel ground planes. The active dipoles were positioned 0.5mm away from the ground planes, towards the L-strip for the respective ground plane, and the passive dipoles were aligned along the edges of the finite ground plane.

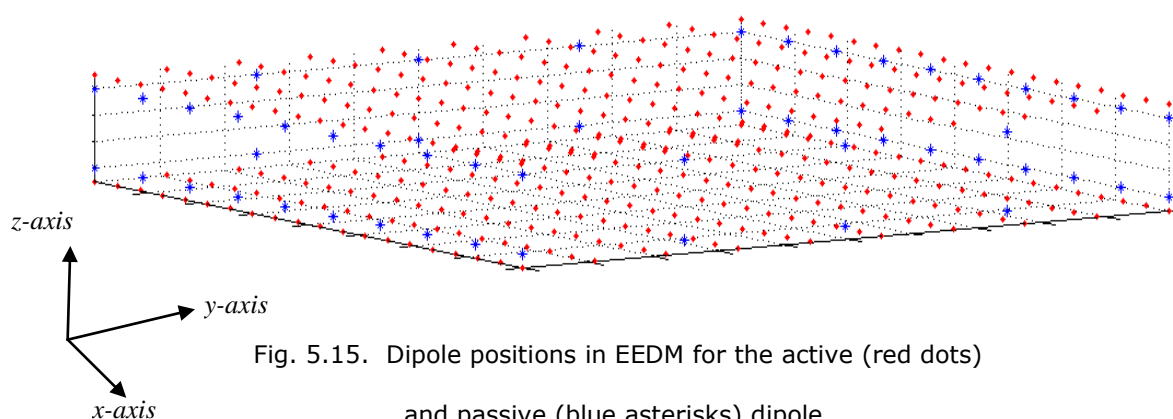


Fig. 5.15. Dipole positions in EEDM for the active (red dots) and passive (blue asterisks) dipole.

The results from the dipole model were compared with the results from the Concept- II simulation. At first, different configurations of dipoles horizontal (x, y directions) and vertical were used. The configuration details are provided in Table 5.1.

Table 5.1. Dipole configuration.

E_{xyz}	3 orthogonal electric dipoles
M_{xyz}	3 orthogonal magnetic dipoles
$E_{xy}M_z$	2 Horizontal electric dipoles and a vertical magnetic dipole
$M_{xy}E_z$	2 Horizontal magnetic dipoles and a vertical electric dipole

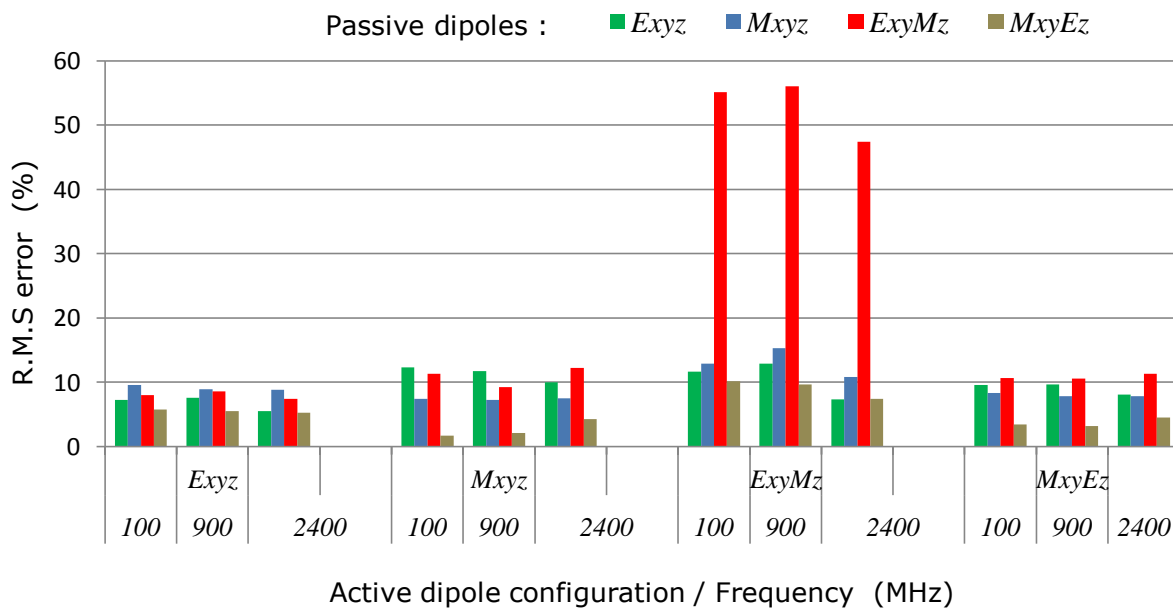


Fig. 5.16. Frequency response for various dipole configurations.

In Fig. 5.16, comparisons are made for the different dipole configurations at 100, 900 and 2400MHz frequency band. As shown, it can be deduced that using horizontal magnetic dipoles and vertical electric dipole to model the active and passive sources respectively yielded best results. Also using vertical magnetic dipoles in modelling both the active and passive sources resulted in a much higher error. These errors were estimated as the average RMS error in predicting the fields surrounding the PCB. This can be due to the fact that z component of the electric field is comparatively higher around the surfaces of the multi-layer PCB. Therefore the dipole vector as computed is given by

$$[D] = \begin{bmatrix} M^x \\ M^y \\ M^z \end{bmatrix}_{active} + \begin{bmatrix} M^x \\ M^y \\ E^z \end{bmatrix}_{passive} \quad (5.7)$$

The exact image, instead of complex image due to the dielectric layer was used and the SVD technique used to solve the inverse problem. The dipole moment vector obtained was then used to reproduce the fields and comparisons made with the results from simulation.

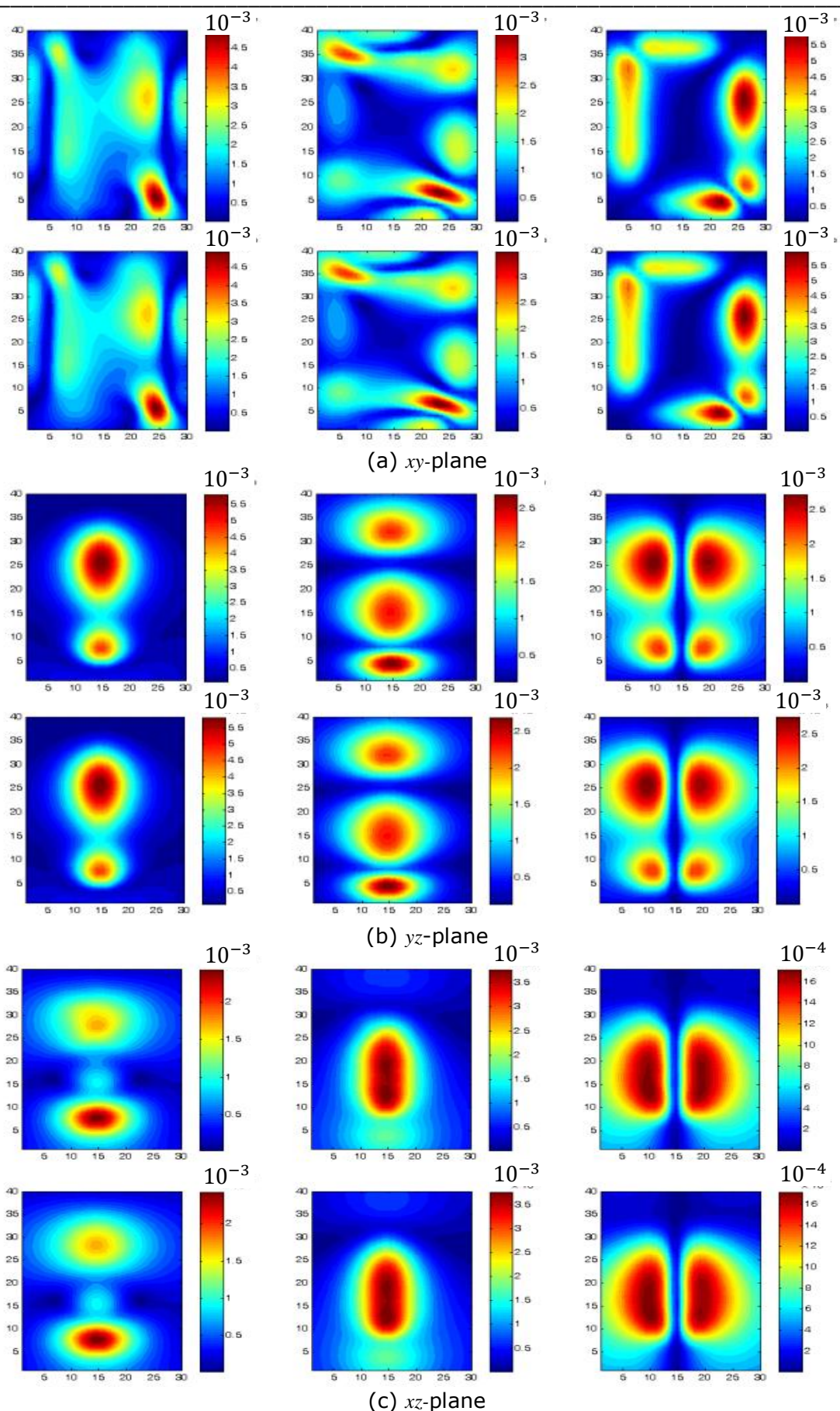


Fig .5.17. Magnetic field magnitude in A/m at the PCB's near field for EEDM (1st row) and MoM simulation (2nd row). The x , y and z field components are represented by the 1st, 2nd and 3rd columns respectively.

Figure 5.17 shows the results reproduced using the extended equivalent dipole modelling compared with those from MoM for a 30 x 40 sampling points over the principal planes of the PCB. These comprise the side planes nearest to the current track in addition to the top plane. An average error of about 2% was achieved using the EEDM in reproducing the fields at 10mm. In addition, to further show the consistency of this approach, the experiment was then carried out over a wider range of frequencies.

Comparison was also made with ordinary equivalent dipole modelling technique for predicting the total magnetic field at 10mm. The result is shown for the xz-plane in Fig. 5.18.

And total magnetic field is given by, $H_t = \sqrt{H_x^2 + H_y^2 + H_z^2}$.

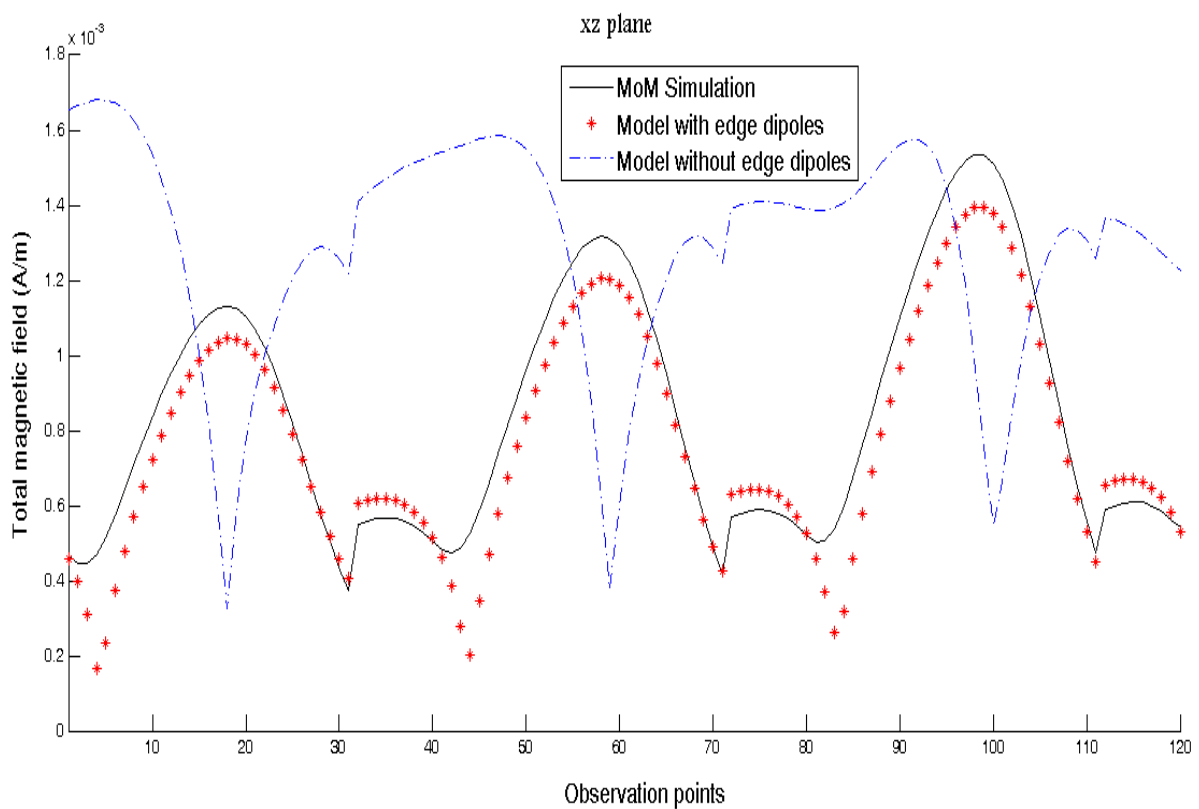


Fig. 5.18. Prediction of total magnetic field using the EEDM and EDM.

It is shown that unlike the ordinary equivalent dipole modelling method, the introduction of edge dipoles was able to characterize the total magnetic field observed at the xz -plane. And this plane was shown in Figs 5.12 and 5.13 to have significant amount of field contributions due to diffraction.

Also the EEDM was used to predict the fields across several frequency bands and the average RMS error determined. According to Fig. 5.19, good predictions of the fields were observed across different frequencies. The error is seen to increase with a decrease in the wavelength as more dipoles are required at higher frequencies. However, an error much smaller than 10% was achieved across the broad band considered in this work.

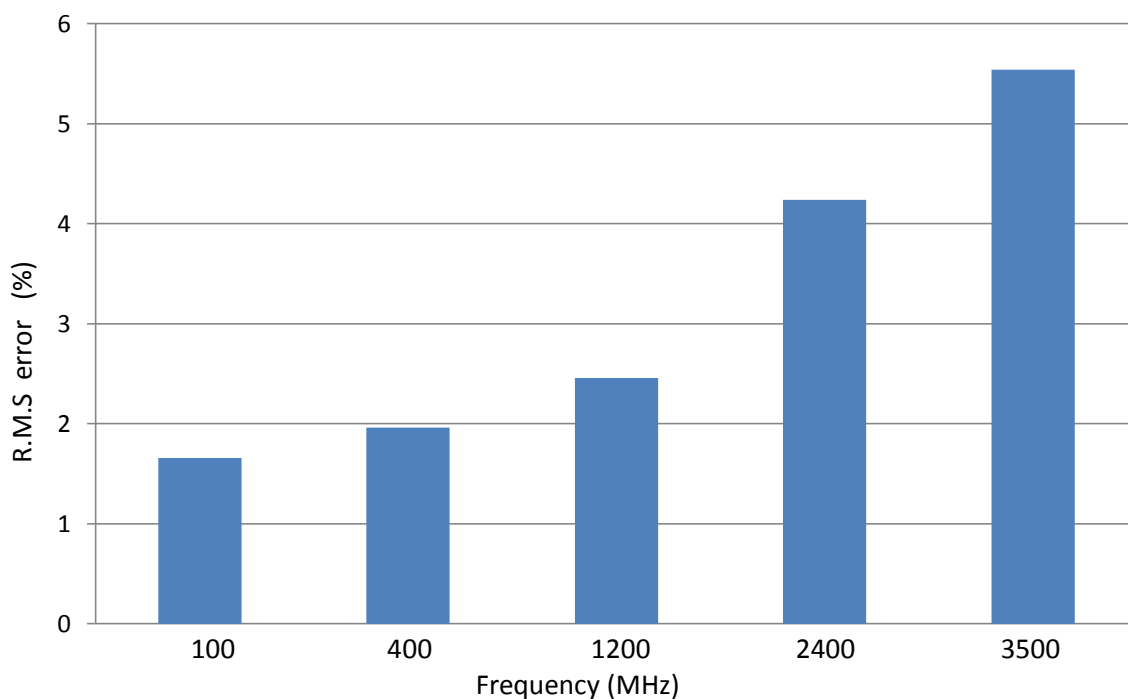
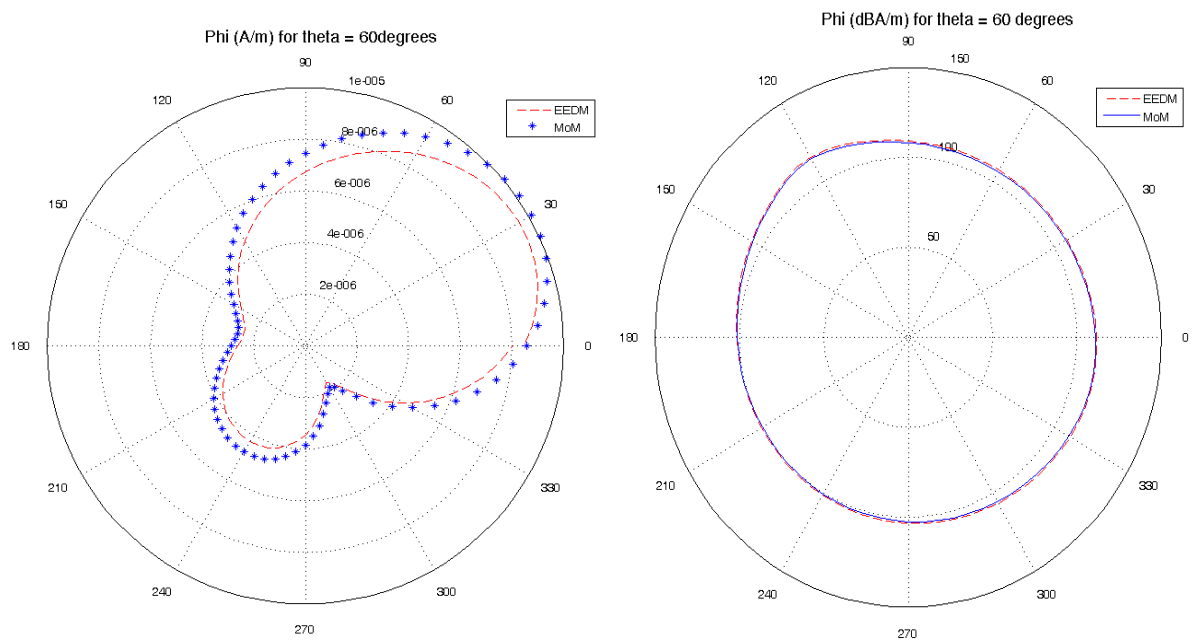


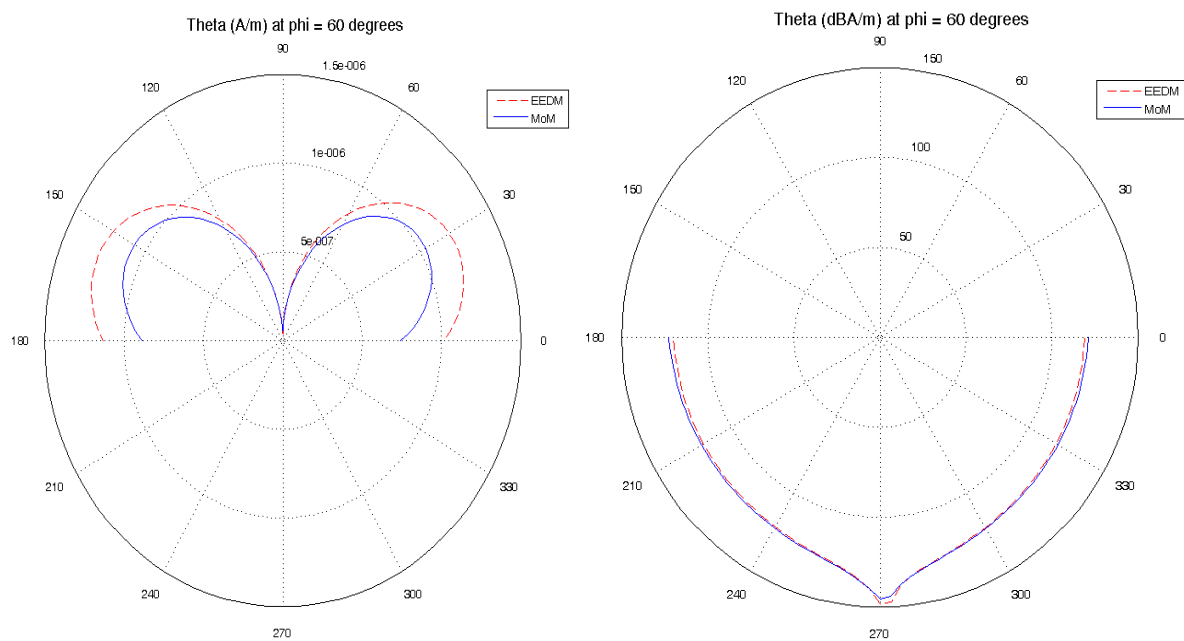
Fig. 5.19. Error over broad band.

Prediction was also made at the far-field and results are shown in Fig. 5.20 for 900MHz at 3m. Here the dipole moment vector already determined above was then used to predict the magnetic fields at far-field distance $\approx 10\lambda$. These were

then compared with fields computed at the same far-field distance using MoM technique. And as shown, there is a good agreement.



(a) H_ϕ ($\phi = 60^\circ$)



(b) H_θ ($\theta = 60^\circ$)

Fig. 5.20. Magnetic far-field components at 3m computed using EEDM and MoM.

5.3.3 A conducting enclosure with aperture

Furthermore, a useful application of the EEDM is now presented. Here an enclosure excited by a simple monopole was simulated using the MoM based Concept-II code [1] and then characterized using the EEDM approach. This structure presents a similar electromagnetic problem as a shielded PCB with aperture for other interfaces, display screens etc. The simple monopole inside the enclosure serves as the current sources (e.g. PCB) while the metallic enclosure serves as the electromagnetic shield (e.g. electronic cases). The EEDM approach was then used to characterize its emissions. Comparisons were made between predicted results using the EEDM and simulation results. Consequently, the shielding effectiveness of the enclosure can then be estimated from the predicted results.

Figure 5.21 shows the design for the metallic enclosure of dimensions $30\text{mm} \times 40\text{mm} \times 20\text{mm}$. The metallic structure encloses the monopole source of $10\text{mm} \times 1\text{mm}$ (length \times radius). The simulation was carried out at 900MHz and with

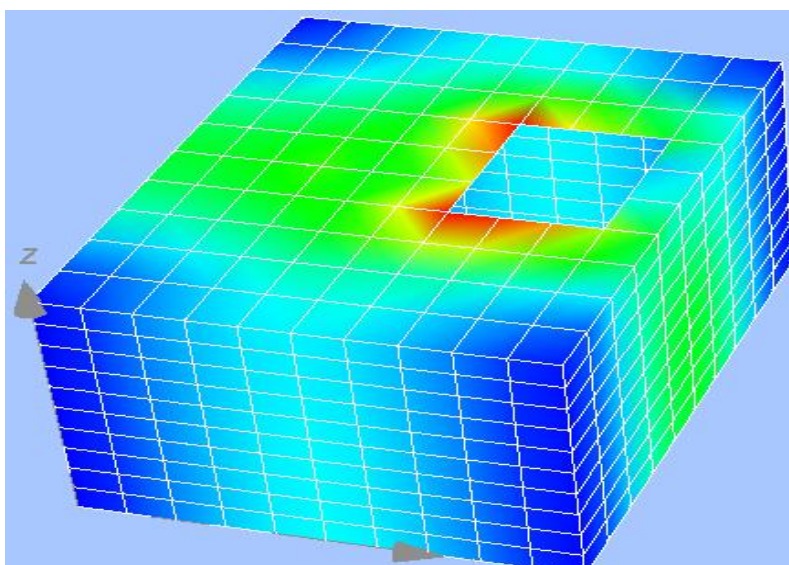


Fig. 5.21. Conducting enclosure with an aperture.

0dB input power. A 9mm \times 12mm slot was made on the xy -plane of the cubic structure. Near field measurements were obtained at planes 10mm away from the surfaces of the metallic enclosure.

Dipole modelling

Electric dipoles were used in this model and were positioned around the geometry of the enclosure as shown in Fig. 5.22. The dipoles are uniformly separated by 5mm. The fields from the active sources, as modelled using dipoles 10mm directly above the conducting planes, are computed with their images. Additional dipoles, already introduced as passive dipoles, are placed along all the edges of the structure to emulate the edge currents due to the finiteness of this radiating structure and their contributions are computed in free space.

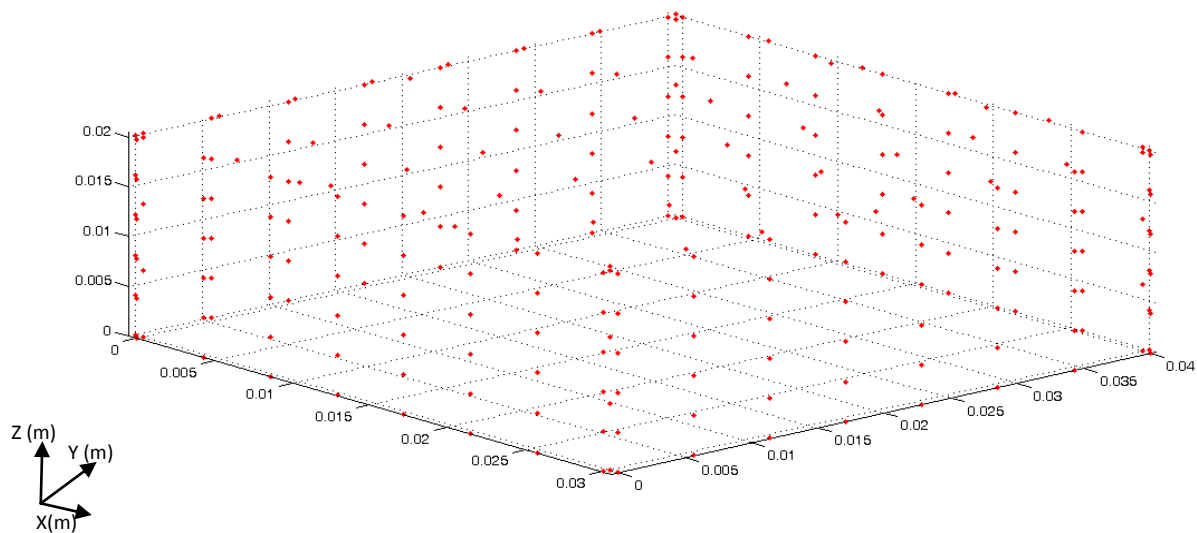


Fig. 5.22. Dipole positions.

With the left hand side of (5.3) extracted from the MoM based software, the coefficient matrix elements are then generated for the dipoles with respect to the 10mm scanning plane. As shown in Figure 5.22, equivalent dipoles are generated similar to the approach in section 4.6.3, however passive dipoles are

used here instead of the more complicated diffraction equations for approximating the effects of diffraction.

Furthermore, the dipole moment vector is evaluated using SVD to solve the inverse problem and then used to reproduce the fields. This achieved accuracy within an average error of 2%. The results are shown in Fig. 5.23.

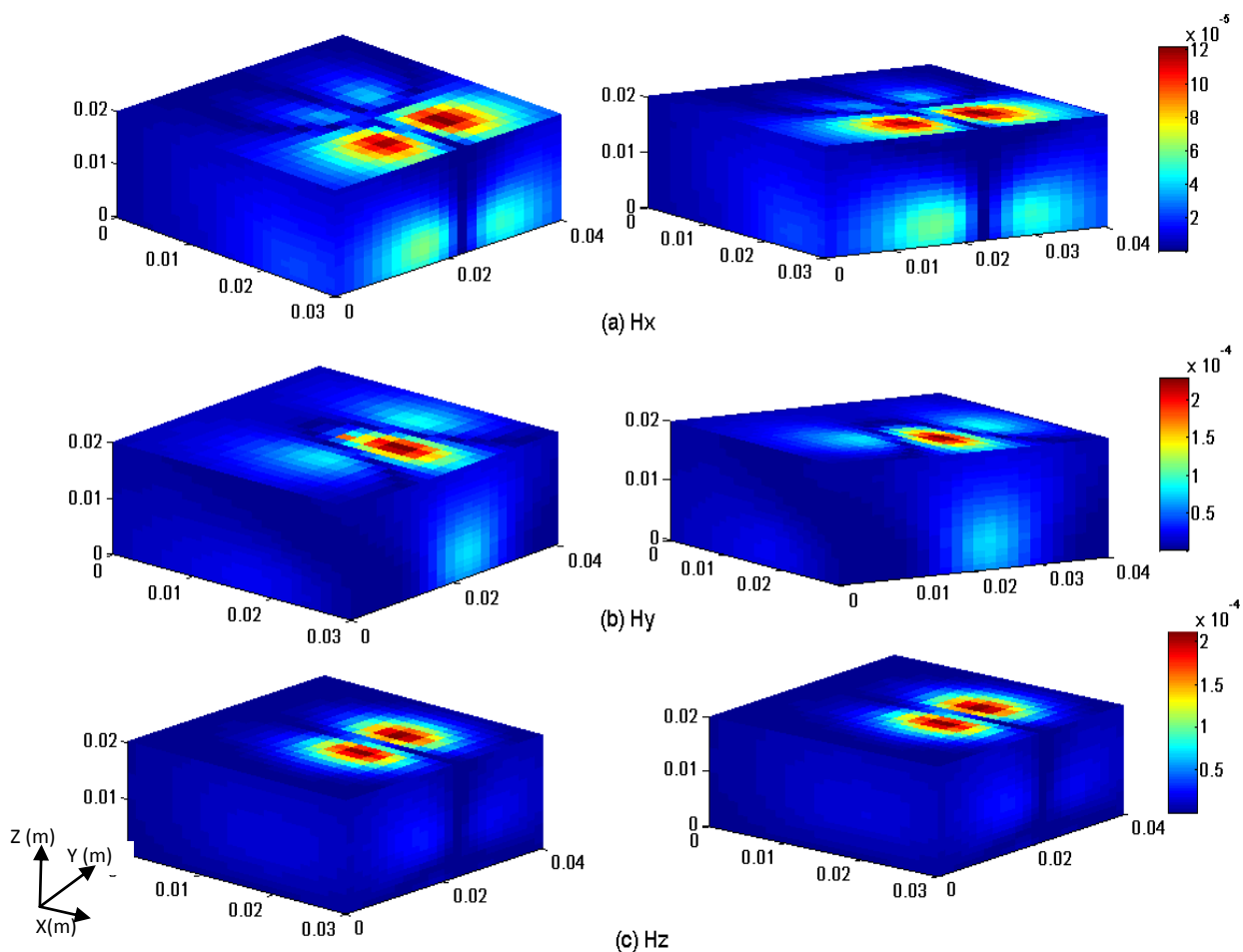


Fig. 5.23. Magnetic field results computed using MoM (left column) and EEDM

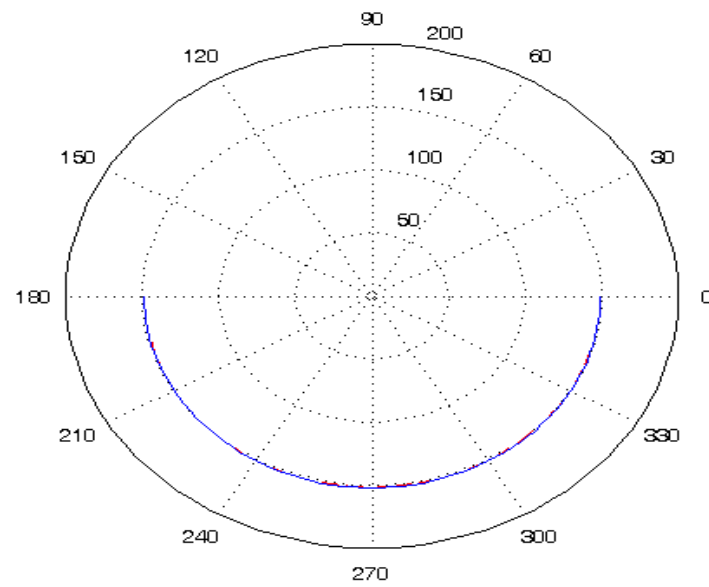
(right column), A/m.

As shown in Fig. 5.23, the EEDM was able to accurately predict the field distribution surrounding the conducting enclosure. Results at a far field distance

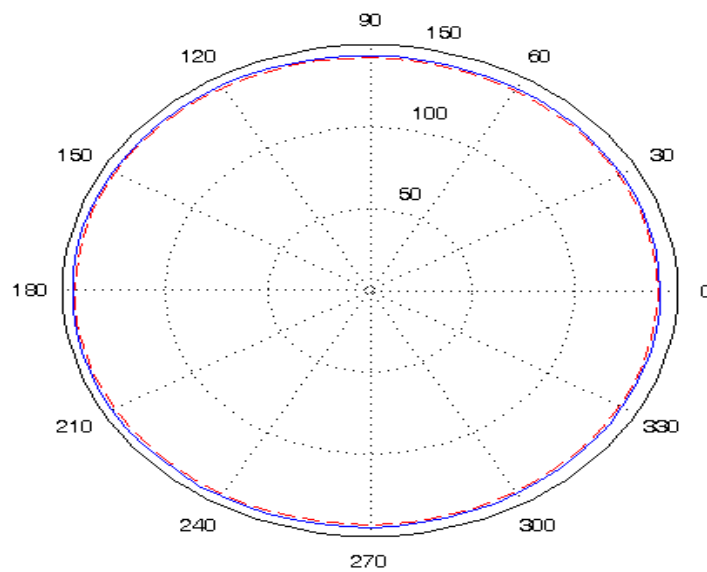
of 3m were also computed and are presented in Figs. 5.24. The results also show good correlation with the maximum fields given in Table 5. 2.

Table 5.2 Maximum field at 3m from a Monopole inside a Metallic box.

Technique	H_θ (dBA/m)	H_ϕ (dBA/m)
MoM	-140.3	-148.65
EEDM	-141.59	-148.84



(a) H_θ ($\theta = 60^\circ$)



(b) H_ϕ ($\phi = 60^\circ$)

Fig. 5.24. Far field results at 3m (in units dBA/m).

Shielding effectiveness

As the EEDM has been shown to be able to predict the magnetic fields at higher planes up to the far-field with a good degree of accuracy. Once the far-field has been computed using the EEDM without requiring the expensive far-field measurements, shielding effectiveness (S.E) of the enclosure (e.g. portable electronics like mobile phones) can be evaluated using the expression [8]

$$S.E. = 20 \times \log \frac{H_{\phi}^f}{H_{\phi}^s} \quad (5.8)$$

where H_{ϕ}^f and H_{ϕ}^s are the radiation in free space and in the shielded enclosure respectively. In this problem the H_{ϕ}^f was computed from the monopole source radiation in free space. The far-field result is then compared with that with enclosure and shown in Fig. 5.25.

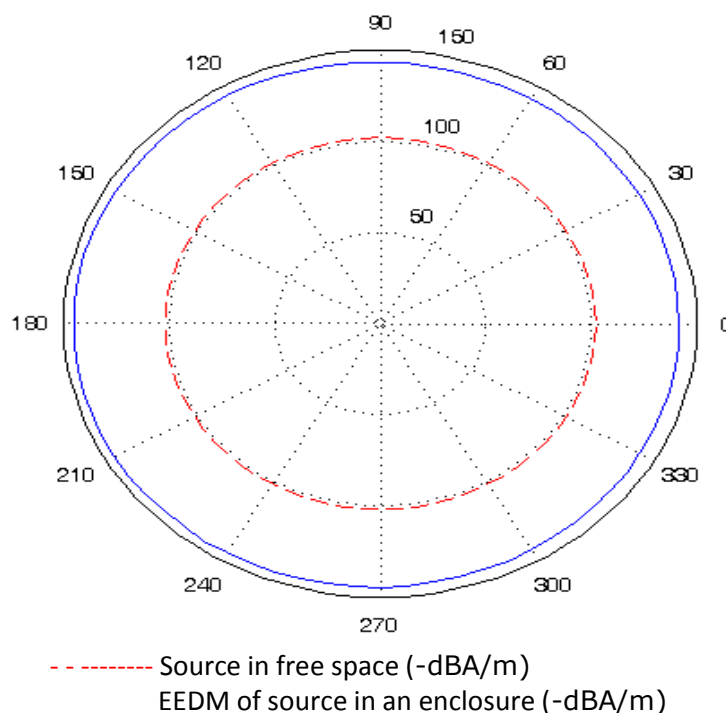


Fig. 5.25. Far Field comparison for H_{ϕ} ($\phi = 60^\circ$) for the monopole over infinite ground and with the enclosure in -dBA/m.

As expected the radiation of the source placed in a conducting enclosure is significantly lower than that in free space. The near field scanning and EEDM approach of determining the S.E has the advantage that it does not require the often expensive far field measurements.

5.4 Conclusion

The equivalent dipole modelling has been extended to account for the contributions due to diffraction to the total electromagnetic field at any observation plane in characterizing radiating elements. It has been shown that passive dipoles are able to emulate the electromagnetic behaviour of the additional currents induced at the edges of a finite ground plane. In this Chapter, several examples also published in [4]-[6] have been used to validate the extended equivalent dipole modelling. Furthermore, a field prediction based on near field modelling and inversion has also been used to demonstrate this approach [7].

Other applications of this technique have also been shown including accurate far-field predictions and estimating the shielding effectiveness of an enclosure.

References

1. Concept-II, available [Online], 2013, <http://www.tet.tu-harburg.de/concept/index.en.html>.
2. G. D. Durgin, " The Practical Behaviour of Various Edge-Diffraction Formulas," *IEEE Transactions on Antennas and Propagation*, vol. 51, no. 3, June 2009, pp. 24-35.
3. C. Obiekezie, D. W. P Thomas, A. Nothofer, S. Greedy, P. Sewell and C.

- Christopoulos, "Prediction of Emission from a Source placed inside a Metallic Enclosure over a Finite Ground Plane , " EMC Euro Conf., Rome, Italy, September 2012.
4. C. Obiekezie, D. W. P Thomas, A. Nothofer, S. Greedy, Luk. R Arnaut and P. Sewell, "Extended scheme using equivalent dipoles for characterizing edge currents along a finite ground plane," *Applied Computational Electromag. Society Journal*, vol. 28, nos. 11, pp. 1111-1121, Nov. 2013.
 5. C. Obiekezie, D. W. P Thomas, A. Nothofer, S. Greedy, L. R Arnaut and P. Sewell, "Modeling of Electromagnetic Emissions from a Multilayer PCB," IEEE EMC Int. Symp. on Electromagn. Compat., Denver, Colorado, Sep. 2013.
 6. C. Obiekezie, D. W. P Thomas, A. Nothofer, S. Greedy, Luk. R Arnaut and P. Sewell, "A Technique for Analyzing EMC Shielding Effectiveness Based on Near-Field Measurement and Equivalent Dipole Modeling," EMC Euro. Conf., Brugge, Belgium, 2013.
 7. C. Obiekezie, D. W. P Thomas, A. Nothofer, S. Greedy, Luk. R Arnaut and P. Sewell, " Accurate Prediction of Magnetic Fields at Higher Planes using Near-Field Measurement," URSI Festival of radio science, Birmingham, UK, 2013.
 8. C. Christopoulos, "Principles and Techniques of Electromagnetic Compatibility", 2nd edition, CRC Press, 2007.

Chapter 6

Techniques for Improving the Performance of Equivalent Dipole modelling

6.1 Introduction

This chapter presents the techniques that are used to further improve the performance of the equivalent dipole modelling (EDM). In the equivalent dipole modelling, more dipoles will be required for problems with larger surface areas. This becomes computationally expensive for big sized PCBs (e.g. 17 inches laptop motherboard). The complex source point (CSP) which includes the complex localisation of the dipole sources, whereby the equivalent dipoles that represent the actual sources of emissions are placed in the complex space thereby reducing the total number of equivalent dipoles required, is presented as a way of improving the performance of EDM. Furthermore, the particle swarm optimisation which is based on swarm intelligence algorithm is used to optimize the equivalent dipoles required for characterizing an EM problem. This reduces both the computational cost and time required for characterising PCBs using the equivalent dipole model.

The extended equivalent dipole modelling has been demonstrated to be able to model various PCB problems with high correlation to the actual emissions from the current sources on the PCB. The dipoles determined using the extended equivalent dipole modelling (EEDM) for any particular problem are imported into numerical software to enable further analysis e.g. detailed 3D far-field results, behaviours in another EMC environment and coupling with other radiating

elements. However, the number of the dipoles needs to be optimised for a minimized computational cost. The accuracy of the model was shown to improve with the increase in the number of dipoles. This can be explained as more dipoles are able to provide more accurate representation of all the actual sources of electromagnetic fields on any radiating element. For the frequency range considered (100-5500MHz) in Fig. 5.2, this improvement brought about by the increase in the number of dipoles, becomes quite insignificant at a certain threshold with dipole resolution finer than 5mm. However, for PCBs with large ground planes ($pcb\ area > 50cm^2$), modelling with this dipole resolution presents a high computational cost. Therefore a good compromise is required between the computational cost and accuracy of the model.

6.2 Complex Source Point

The complex source point (CSP) is now presented as a way of improving the accuracy of the model with reduction in the number of dipoles. The CSP has been shown [1]-[4] to provide a good representation of a real source. It involves the placement of the equivalent sources that characterize the real sources on a complex spatial domain. In EEDM, as well as in other dipole modelling techniques, the field at any particular observation point is assumed to be the superposition of all the contributions from the equivalent dipoles sources used in characterizing the actual sources above a ground plane. For characterizing a 2D problem using CSP, the 2D plane where these equivalent sources are modelled is analytically extended further to a complex space. In order to relate the solution to practical problems, the real observation plane is retained. This relationship is illustrated in Fig. 6.1.

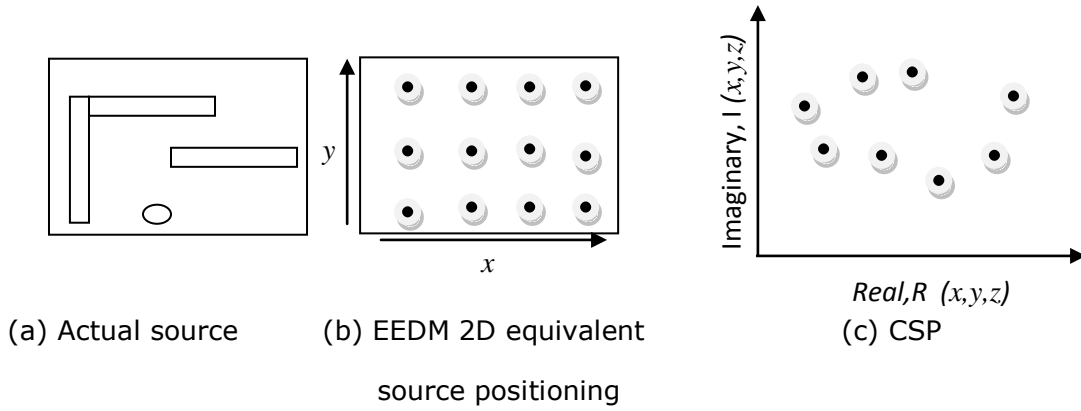


Fig. 6.1 Source position representation.

In Fig. 6.1, the resultant positions for the coordinates of the equivalent sources for characterizing the actual EM source in (a), are given as x_i, y_i at $z = a$ and x_i, y_i at $z = z_i + jz'_i, z_i = 0$ for the 2D as (b) and CSP as (c) respectively for i number of equivalent sources, are shown. Fig. 6.1c shows the basic illustration for a simple case where the complex elevation has only the imaginary component (i.e. $z = jz'_i$), resulting to $R = \sqrt{x_i^2 + y_i^2}$ and $I = jz'_i$. To understand this principle clearly, a mathematical explanation is now given.

To recount, the field B^r , observed at a position $P^r(x_r, y_r, z_r)$ due to an electric dipole source located at $P^i(x_i, y_i, z_i)$ can be derived from the expression of the coordinate form of the time harmonic Green's function in a homogenous medium given by [1]

$$B^r(\vec{p}^r, \vec{p}^i) = \frac{e^{ikR}}{4\pi R} \quad (6.1)$$

where $k = \frac{2\pi}{\lambda}$ for single frequency, time dependent factor $\exp(-i\omega t)$ and

$$R(\vec{p}^r, \vec{p}^i) = \sqrt{(x_r - x_i)^2 + (y_r - y_i)^2 + (z_r - z_i)^2} \quad (6.2)$$

The complex source point is defined as the characterization of electromagnetic sources with equivalent sources in a complex space, i.e. by making \vec{p}^i to be

complex. This means that any of the three components (i.e. x_i, y_i, z_i) can be complex.

In the EDM and EEDM presented in previous Chapters, the equivalent dipoles were placed on a 2D plane parallel to the ground plane (i.e. the orthogonal coordinates are real). However, in the CSP the dipoles are placed in the complex space with the real component of the resulting distance representing the actual 2D source position (i.e. at x_i, y_i, z_i).

In a simple 2D problem with the ground plane parallel to the xy -plane, a complex z -axis component is used (i.e. $z_i = a + jb$, for $z'_i < z_i$) as shown in Fig. 6.1 and the expression (6.1) can now be reformulated to include the complex source position and is given as

$$B^r(\vec{p}^r, \vec{p}^t) = \frac{e^{-ikR}}{4\pi R} \quad (6.3)$$

where \vec{p}^0 and R are now the complex position vector of the sources and the distance from the source to the observation point respectively. R is determined by extending the real equivalent source positions to a complex space i.e. by inserting $x_i, y_i, z = z_i + jz'_i$ in the expression for R in (6.2). The consequence of this is the inclusion of an additional arbitrary source (by adopting the complex equivalent source localization) without increasing the number of equivalent sources used [1].

6.3 CSP Validation

6.3.1 Developing the equivalent dipole model

The viability of the CSP is now demonstrated. A 3D box with an aperture, enclosing an EM source is used. The radiation pattern here involves the

divergence of the electromagnetic fields with distance from the aperture which tends to an ideal dipole electromagnetic radiation pattern. This 3D box can be said to represent a PCB in an enclosure as often seen in electrical and electronic equipment.

Near-field measurements were used to extract the magnetic field information required for the modelling as shown in Fig. 6.2. The box has a dimension 105 x 75 x 45 mm (L x W x H) while the square aperture located at the centre of the xy-plane is 20mm x 20mm. The box encloses a monopole antenna which is the primary source of the emissions. The monopole antenna is excited with a 0dBm power source using a signal generator and an amplifier at the box resonance frequency of 2.4GHz. The experiment was carried out at this resonant frequency so as to achieve a significant emissions particularly at the sides of the box due to the excitation of surrounding edges by the real sources.

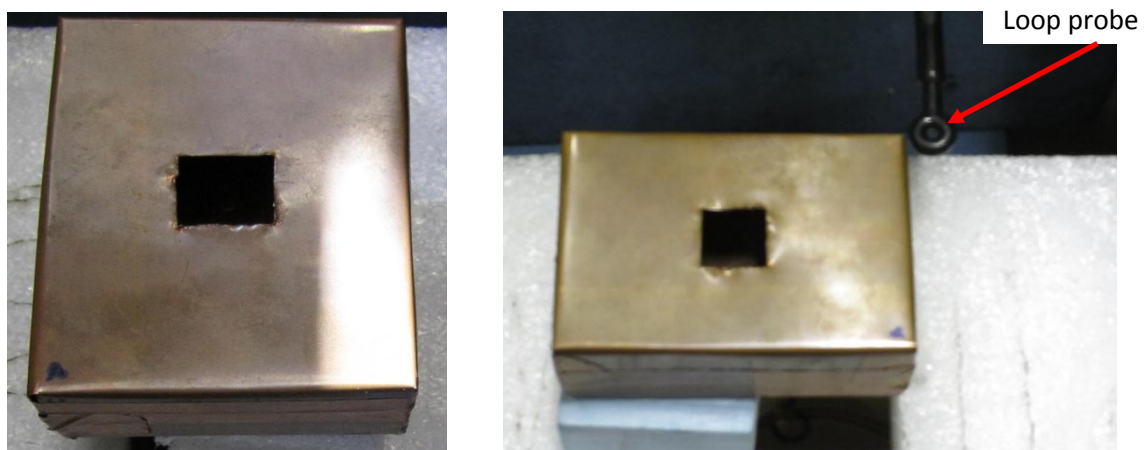
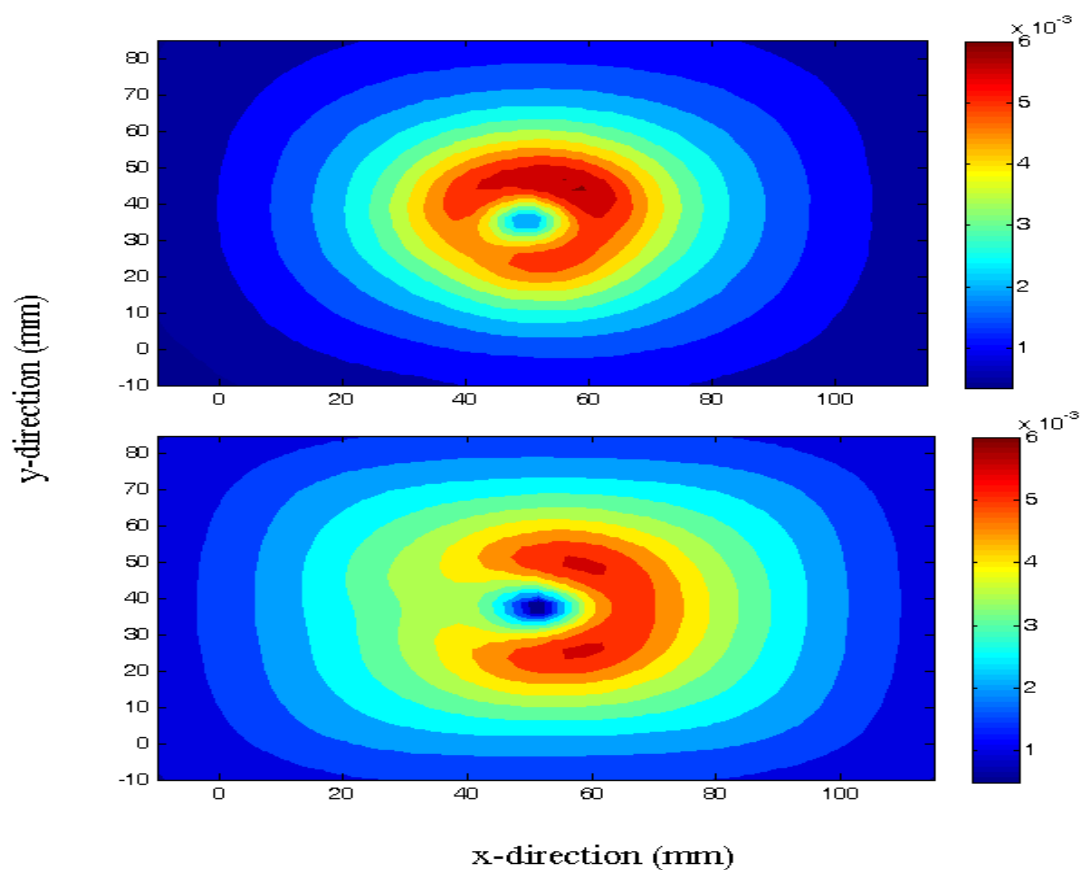


Fig. 6.2 Near-field measurement setup for the metallic box with an aperture.

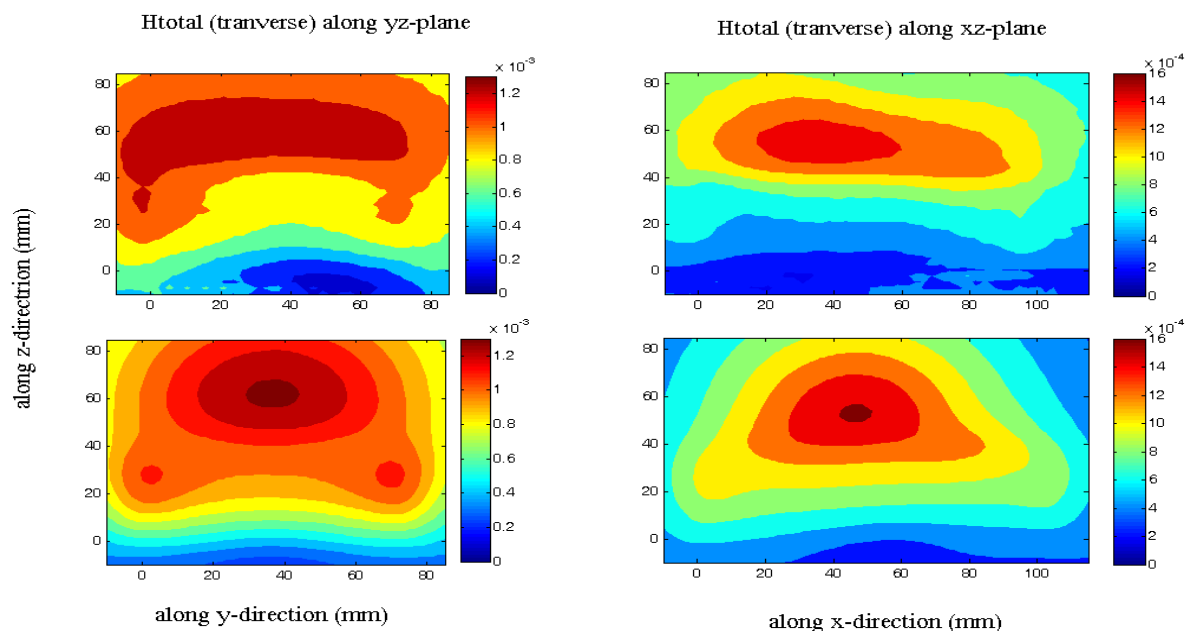
The higher emissions at resonances are due to the minimum impedance at the resonant frequency.

This structure was also simulated on the MoM base Concept-II for validating the measurement results and for far-field calculations. Fig. 6.3 compares the fields

obtained through MoM computation and near-field measurement. A maximum difference of less than 10% in amplitude was observed along the side planes between the 2 techniques. The major reason for this as presented in Chapter 3 is the probe sensitivity. The signal to noise ratio degrades at low power as seen at the side planes (yz - & xz - planes). However a relatively better correlation is seen at higher emissions as seen at the top plane (xy -plane). Pre-amplifier can be used to improve the SNR of the probe receiver. The recorded data is now characterized using the CSP technique. The simulation results were used to determine the optimal equivalent dipoles that were able to characterize the far-fields with minimal error. These determined dipole positions were then extended to complex space to further improve the accuracy of the model.



(a) top plane



(b) side planes (yz- & xz- planes)

Fig. 6.3 Total transverse magnetic field magnitude in A/m for near-field measurement and MoM computation (top and bottom respectively).

Equivalent Dipole positions

Firstly, the location of the active dipoles were determined using the basic extended equivalent dipole model (EEDM). Electric dipoles of 2.5mm resolution were uniformly distributed on a plane 10mm above and parallel to the xy -plane of the metallic structure. These were then used to reproduce the magnetic fields using the expressions for EEDM (5.1) - (5.3) as developed in Chapter 5. The active dipoles which characterized the real current sources, were then placed on a complex plane and used to reproduce the magnetic fields. The latter was then validated using the FSV technique.

Electric conducting surfaces or enclosures act as electromagnetic shields, hence no real sources of emission is expected at the side planes of this metallic enclosure. Therefore active dipoles were restricted to the xy -plane in the modelling because of the presence of an aperture at this plane. However,

accurate prediction of the far-field requires characterization of the possible emissions at the side planes. This is done by including passive dipoles along the edges of the cuboid. And as mentioned these are the only sources (passive) included at the sides to account for the finiteness of the metallic box.

Figure 6.4 compares the far-field results predicted using MoM, dipole modelling without the edge dipoles and dipole modelling with edge dipoles. This shows that including the edge dipoles improves the modelling significantly. This step was only taken to understand the desirable positions for the active sources, which are on the xy -plane of the DUT because of the presence of an aperture. Once this has been achieved the complex source technique is then investigated to further improve the accuracy of the modelling.

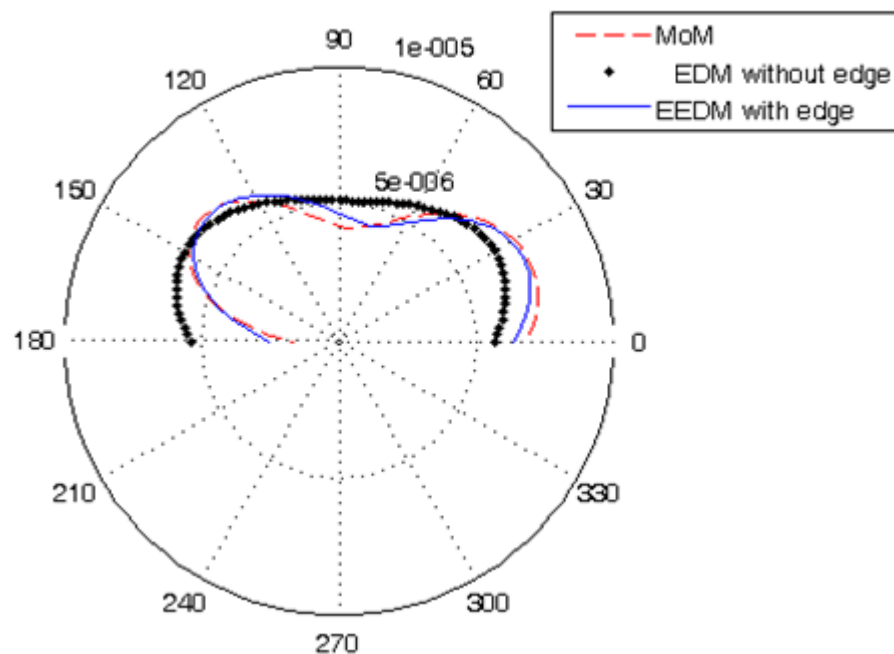


Fig. 6.4 Far field results at 3m (A/m).

It is worth noting that the EEDM result has been used to establish the basic model which comprises the number of equivalent dipoles and their respective

positions. The CSP principle will now be applied to this model and used to characterize the magnetic field extracted through the near field measurement.

6.3.2 CSP example: Experimental validation

In the CSP method, the active sources are positioned in the complex plane and used to reproduce the magnetic fields according to (5.1)-(5.3). Though the computations are performed in complex spatial domain, the results are interpreted in real spatial domain which are 2D and 3D for a 2 and 3-dimensional problem respectively. The rms error in reproducing the magnetic field using the basic EEDM and the EEDM with CSP is shown in Fig. 6.5. A significant improvement is observed by positioning the dipole sources in complex space compared to modelling with equivalent dipoles on the 2D plane. Note that in the CSP model the equivalent dipoles are mathematically positioned in the complex plane and then inserted in the EEDM model developed in Chapter 5.

The plot shows a significant reduction in the rms error as a result of positioning the active sources on a complex plane. It is also clear that more dipoles are required for the basic EEDM to match any given point on the EEDM with CSP error curve. Therefore this technique can provide a useful way of optimising the number of dipoles required to achieve any desired degree of accuracy.

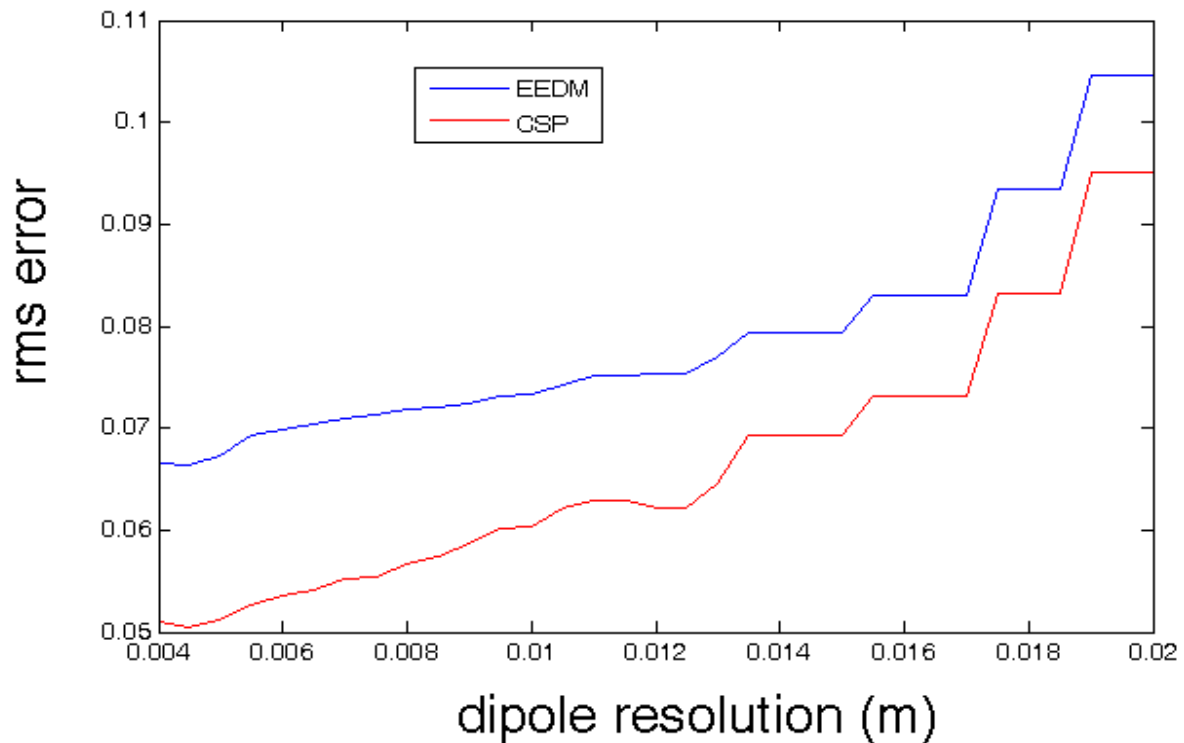


Fig. 6.5. CSP model and basic EEDM.

6.4 Particle Swarm Optimisation

In EDM and EEDM, well defined and predictable problems (in this case appropriate localization of the equivalent dipoles) are easily modelled by using fine dipole resolution. The equivalent dipoles are determined through the singular value decomposition (SVD) as presented in Chapter 2. This can lead to a high computational cost especially for electrically large structures. There is therefore a need for a more flexible approach capable of yielding results with high accuracy at low computational cost. Optimisation techniques offer ways of determining the best solution with limited computational resources. Also implementation of the solution in electromagnetic software becomes easy with reduced number of equivalent dipoles. Here the particle swarm optimisation technique is presented as a way of achieving this.

Particle swarm optimisation (PSO) is a swarm intelligent (SI) method like the ant colony optimisation (ACO) [6]-[8]. As introduced by Kennedy and Eberhart [5], it has been demonstrated to be a robust technique for a range of engineering problems especially optimisation. These include neural network training [5], [10], [11], gene clustering [12], power systems [13] multimodal biometric systems [14] and discrete problems [15]-[17].

The PSO technique is adopted here for the optimisation of the equivalent dipoles required for characterization of radiating structures. And like the evolution technique genetic algorithm (GA), it starts with random population which is updated for every optimal value. However, it does not utilize evolution operators such as crossover and mutation as presented in [25]. PSO algorithm involves a population of particles which are defined by their speed and position vectors. The particles are distributed in the searching space and they search for the minimum or maximum of a defined objective function [5], [9]. The PSO algorithm is summarized in the flowchart in Fig. 6.6.

As shown in the flowchart, the PSO arrives to its optimal solution by moving a swarm of candidate solutions around in the search space. The populations are at first selected at random and their movement are guided by their own local best position in the search space (p_{best}) as well as the global swarm best (g_{best}).

This process is repeated until a satisfactorily solution is achieved. The PSO does not use gradient information and the movements of the particle depend only on the velocity and location where good solutions have already been found by the particle itself or other neighbouring particles in the swarm [9].

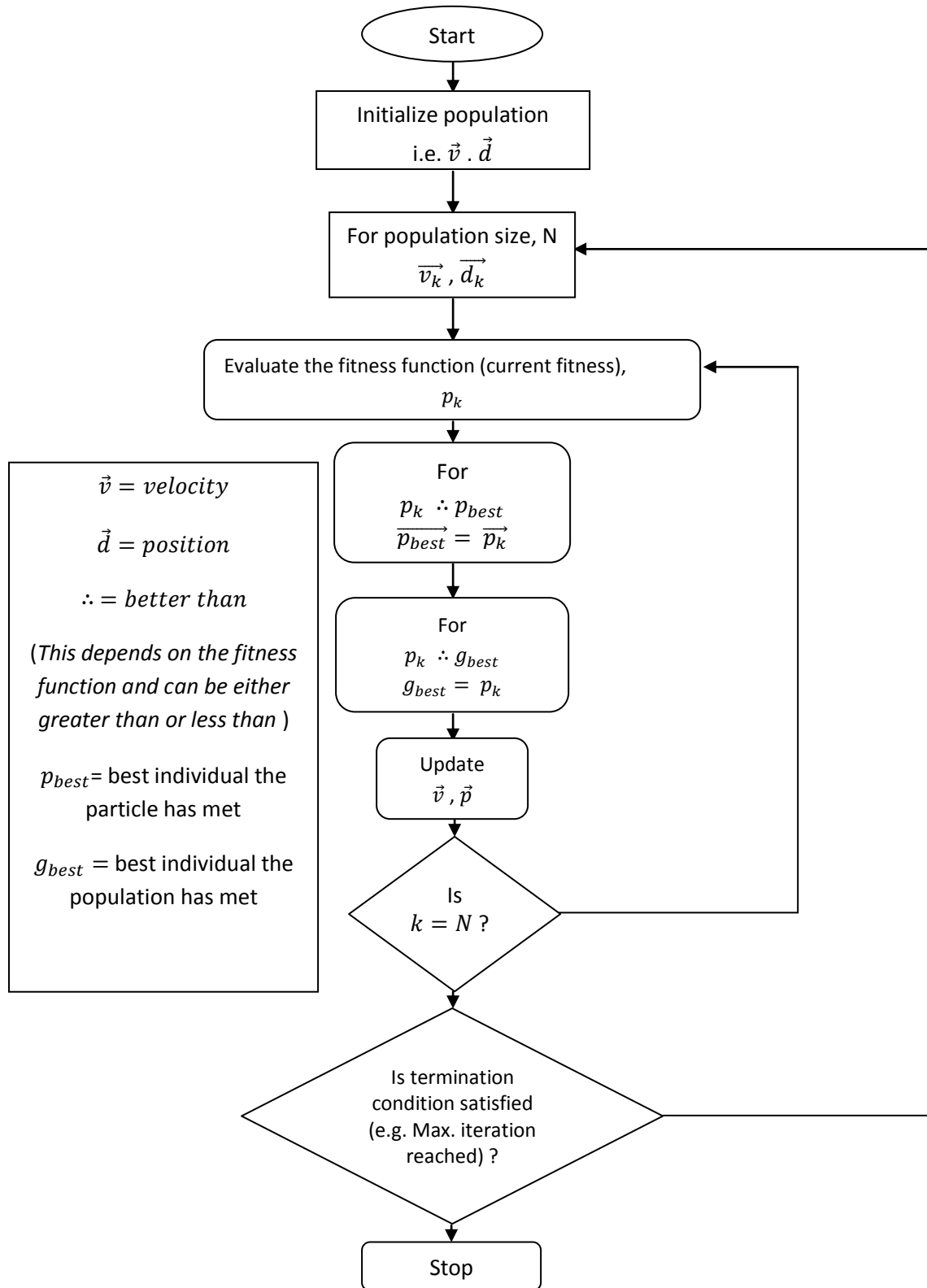


Fig. 6.6 PSO algorithm flowchart [9].

At each step, they change their positions according to the best individuals to reach a new position. Through this, the whole population evolves towards the optimum.

The new velocity of the particle k is determined through

$$\vec{v}_{k+1} = C_i \times \vec{v}_k + C_c \times r(0,1) \times (\vec{p}_{best} - \vec{P}_k) + C_s \times r(0,1) \times (\vec{g}_{best} - \vec{P}_k) \quad (6.4)$$

where $r(0,1)$ is a set of random numbers uniformly drawn from [0 1] and C_i is the coefficient of inertia which determines relative weight of a particles velocity and thus influences the direction of search. The other constants C_c and C_s are the cognitive and social acceleration parameters respectively. They are used to estimate the influence of local and global best respectively and are normally predefined by the user with typical values $C_c = C_s = 2$.

After the velocity has been updated the new position can then be determined through

$$\vec{d}_{k+1} = \vec{d}_k + \vec{v}_k \quad (6.5)$$

This iteration is carried on until the set maximum generation or other defined stoppage criteria is reached. The key terms are the:

- Position: this represents the possible solutions to the optimization problem
- Velocity: this is the information required to update the current particle's position.
- Fitness: this is the measure of the goodness of fit of a solution for a given position.

For an optimal performance of PSO, the initial population range is defined so that it closely bounds the expected domain of the feasible region. This is

automatically done for lower and upper bound constraints, but not for linear and nonlinear constraints [26].

The extent at which the solution space is explored is determined by the population size. Higher population sizes are able to yield better solutions however, they also lead to increase in the total run-time.

The PSO is then applied in the dipole modeling to determine the optimal properties of the dipoles required to characterize current sources. This is achieved by minimizing the fitness function given by

$$\zeta = H^{meas} - H^{model} \quad (6.6)$$

where H^{meas} and H^{model} represent the total measured and modelled magnetic fields respectively. The procedure is presented below.

Dipole optimization using PSO

This PSO algorithm is now used to optimize the number of dipoles required to characterize the metallic enclosure with an aperture in Fig. 6.2. In this model, only 20 equivalent active dipoles (electric dipoles) were used to characterize the active sources. The edge dipoles as used in section 6.2.1 were retained so as to characterize the finiteness of the problem. Also the same set of field information was used as reference. This follows the same principle of dipole modelling of radiating sources. However, the inverse problem is solved stochastically rather than an analytical approach like the SVD. The properties of the dipoles, also known as the positions in PSO, were initially selected randomly and were used as the initial population for the algorithm. These properties include the 3 orthogonal coordinates (x , y and z) and also their dipole moments

$(P_x^r, P_y^r, P_z^r, P_x^i, P_y^i \text{ and } P_z^i)$, where P^r and P^i are the real and the imaginary components of the dipole moments. A complex z -coordinate was used as in the complex source position technique presented in section 6.2. The PSO was then used to determine the optimal active dipole properties (i.e. dipole positions and dipole moments). It is worth mentioning that the number of equivalent dipoles was fixed in this algorithm but the properties as mentioned above changed at every generation until an optimal set of equivalent dipoles was achieved.

In PSO algorithm, early convergence which presents a false solution can be avoided by using sufficient population size. In this case, population size of 60 was used. Fig. 6.7 shows the PSO algorithm performance over 100 iterations. The score is estimated for the fitness function (6.6).

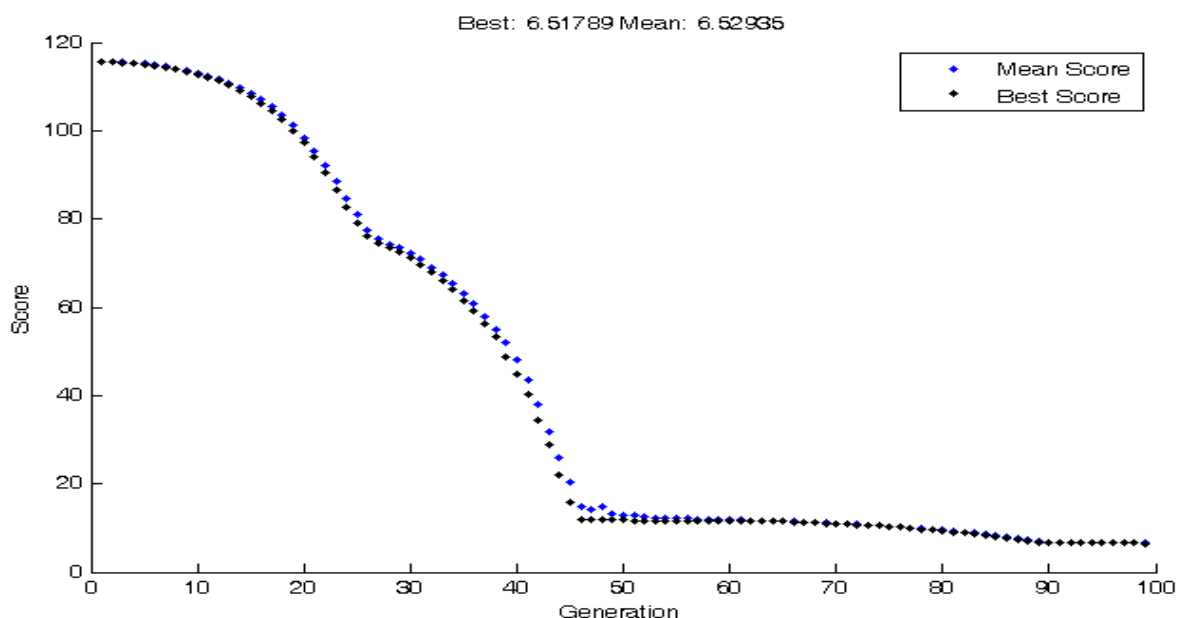


Fig. 6.7. PSO optimization for 100 iterations.

The optimal solution was obtained after the 90th generation (iteration). The result from the PSO was then used to compute the field at the xy -plane and an r.m.s error of about 6% was achieved. This shows a significant improvement against the analytical solutions presented in Fig. 6.5. According to Fig. 6.5, a

10mm dipole resolution will be required to achieve an accuracy of 6% for the CSP model presented earlier. This means approximately 75 dipoles against the 20 dipole-optimized CSP model using PSO. The accuracy can also be increased further by adding more active dipoles. The viability of this approach is also validated using the feature selective validation technique. This approach is now presented.

6.5 Feature Selective Validation

Many comparison techniques e.g. cross correlation, root-mean-square (R.M.S) etc have been used in estimating the degree of agreement between two data sets (i.e. between measurement, simulation and (or) dipole modelling). However, it is difficult to relate the result from these comparison techniques to what the human 'expert' would decide with a visual inspection of the data sets which can be quantified according to the IEEE Std 1597.1 which is the standard for validation of computational electromagnetics computer modelling and simulations [24]. The IEEE Std 1597.1 recommends the approach to be used to formally validate computer based modelling and simulations used in electromagnetic compatibility/signal integrity design and analysis. The feature selective validation (FSV) achieves a better indication of the agreement between two data sets by comparing and combining two of their aspects.

According to [19]-[23] these aspects are the amplitude based comparison, Amplitude Difference Measure (ADM) and the feature based comparison, Feature Difference Measure (FDM). They are evaluated by decomposing the original data into trend information and feature information. The results are presented at range of levels from a point-by-point analysis to a single figure of merit. They

are also combined into a Global Difference Measure (GDM). This technique continues to evolve through heuristic approach. The FSV focused on producing a range of outputs from simple summary 'Goodness-of-fit' factors to detailed point-by-point diagnostics. The outputs are presented in categories comprising natural language descriptors as given in Table 6.1.

Table 6.1. FSV output categories.

FSV value (quantitative)	FSV interpretation	FSV Visual six point scale
$x < 0.1$	Excellent	1
$0.1 \leq x \leq 0.2$	Very good	2
$0.2 \leq x \leq 0.4$	Good	3
$0.4 \leq x \leq 0.8$	Fair	4
$0.8 \leq x \leq 1.6$	Poor	5
$x > 1.6$	Very poor	6

The basic 1D FSV formulation [23] is derived in Appendix D. The FSV technique is now used to compare the total magnetic field on the xy -plane for the problem in Fig. 6.2. The comparison was made between the results reproduced using 20 active dipoles (whose properties were determined using the particle swarm optimisation and positioned on the complex plane) with the measured magnetic field. The results are presented in Fig. 6.8 – Fig. 6.10.

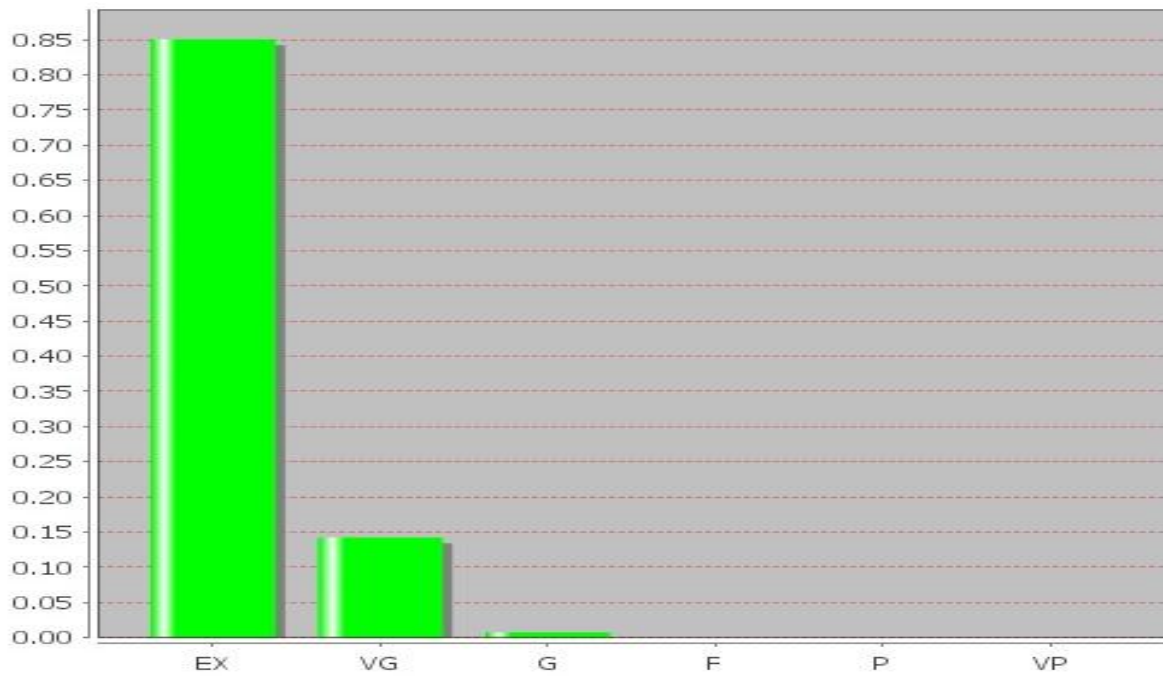


Fig. 6.8 Amplitude difference measure result (ADM) for PSO.

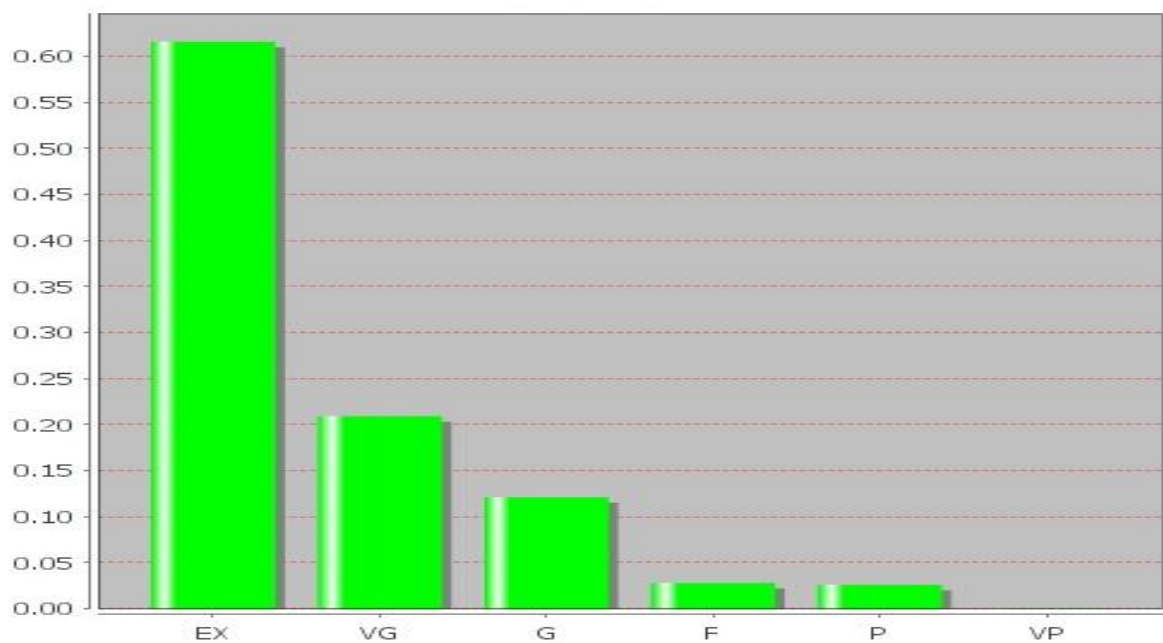


Fig. 6.9 Feature difference measure result (FDM) for PSO.

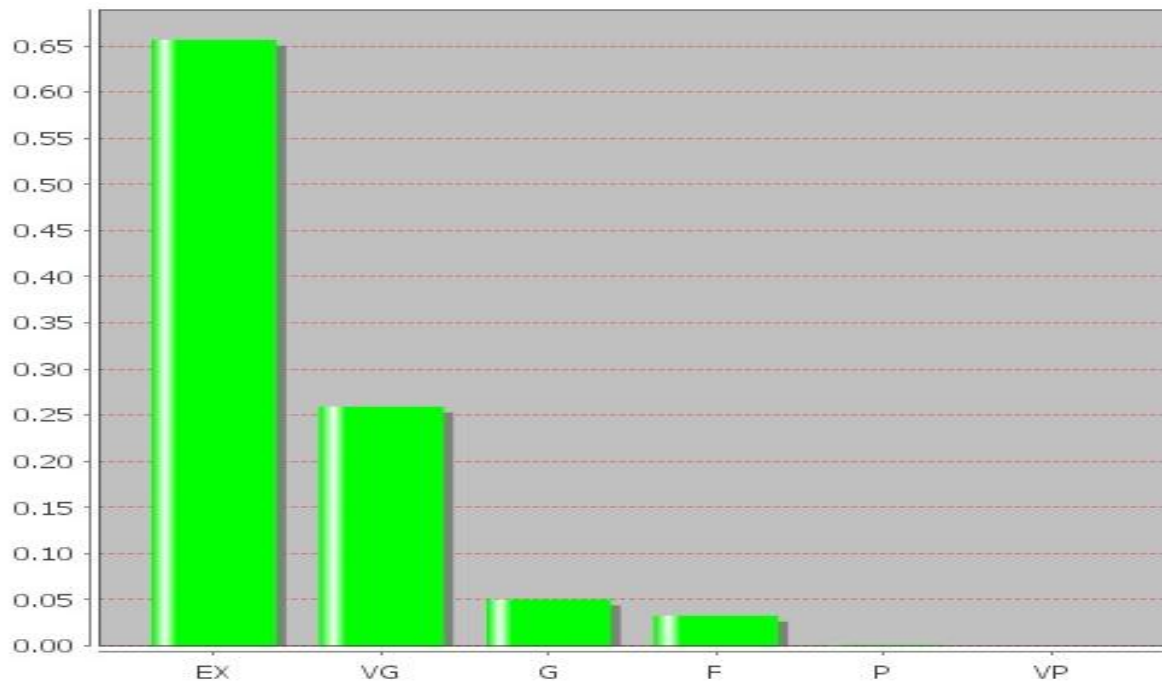


Fig. 6.10 Global difference measure result (GDM) for PSO.

The excellent bar is the most significant of all the indicators in the validation measures shown above. This implies an excellent correlation both in feature and amplitude. The particle swarm has been shown to be a good alternative for the solution to an inverse problem. Its main advantage over other solutions to inverse problem like the SVD, is the ability to achieve minimal error for a smaller number of equivalent dipoles. As there is no a priori information about the sources, sufficient dipoles are required in SVD with respect to the size of the problem for proper characterization. This is not the case with the PSO as any desired amount of dipoles can randomly be chosen and the algorithm searches for the best fit.

6.6 GA vs PSO

The PSO performance here is now compared with that of the Genetic Algorithm (GA). The same problem presented in Fig. 6.2 whose near field result is given in

Fig. 6.3, was optimized using the GA algorithm. The population size of 100 and 60 generations were used. The magnetic near field of the metallic enclosure with an aperture for 50x38 observations points and 10mm above the xy -plane, were reproduced using 20 active dipoles. Edge dipoles were also retained as before to characterize the finiteness of this problem. The active dipoles were randomly chosen and the GA algorithm was then used to search for the best fit. This was done by minimizing the same objective function used in the PSO algorithm and given by the expression (6.6). The performance of the GA in optimizing this problem is now compared with the PSO.

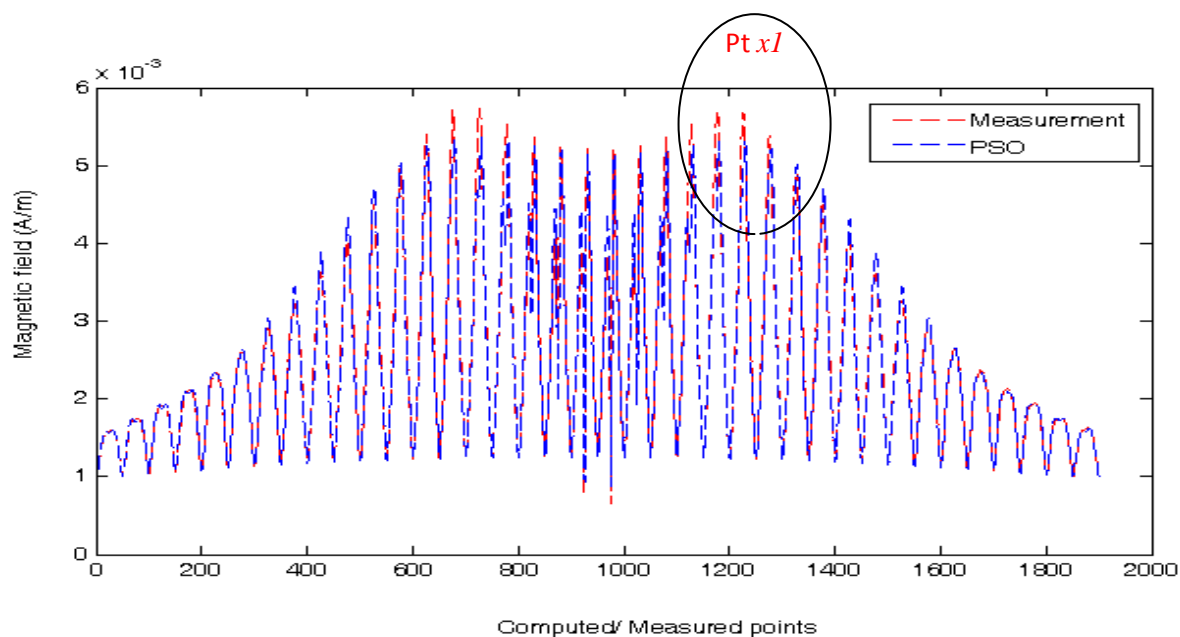
Table 6.2 Optimisation algorithm performance.

Algorithm	r.m.s error (%)	Correlation	Run-time(mins)
GA	7.6	0.9855	106
PSO	6	0.9913	50

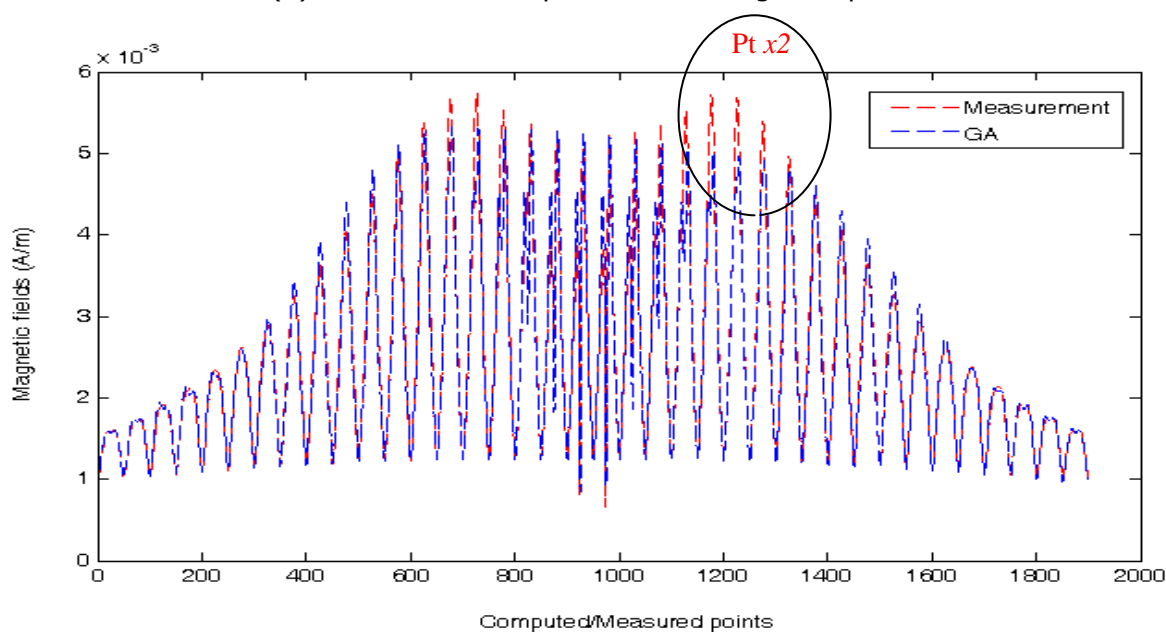
From Table 6.2 it is shown that the PSO has relatively better performance than the GA. A slightly higher accuracy of about 21% was achieved with PSO algorithm for about halve the run time when compared with the GA for the same problem. The algorithms were executed in Matlab ver. 2011 and on a computer with specifications Intel i7 3.07/3.06 processor, 6GB RAM and windows 7 64-bit operating system.

These results are further plotted in Fig. 6.11 for the (a) PSO and (b) GA algorithms. The plots in Fig. 6.11a and Fig. 6.11b compare the results computed using PSO and GA respectively against measurement for all the 50x38 observation points in the xy -plane used in developing the model. This umbrella-like behaviour of the plot is due to the profile of the field distribution on the xy -plane as given in 2D plot of Fig. 6.3a. However, in Fig. 6.11, the 1900 (50x38) observation points from measurement and modelling (GA or PSO models) are

overlaid in a 1D plot so as to clearly show the distinctness of the two models when compared with the results from near field measurement.



(a) Particle swarm optimisation using 20 dipoles



(b) Genetic algorithm using 20 dipoles

Fig. 6. 11 Total magnetic field in the xy-plane.

In Fig. 6.3a, higher fields are concentrated on the centre along the x-axis which is also the position for the various peaks seen in Fig. 6.11 i.e. at points that are odd multiples of 25 (as the scan comprises 50 points along x for 38 different

positions along y , where each position along y represents a uniform increment from the previous y position).

Though both correlated well with the measured field, however relatively more deviations are observed at the 1200th and 1300th points in the GA model than the PSO model as seen at pt $x2$ and pt $x1$ respectively.

However, for more discrete problems, the efficiency of the basic PSO reduces this is because according to the Heisenberg uncertainty principle, the position and velocity of a particle cannot be simultaneously determined accurately. A PSO technique based on quantum individuals, being time dependent is capable of overcoming this limitation [26].

6.7 Conclusion

It has been shown that by the positioning of equivalent current sources in the complex space, fewer sources will be required to attain any given error when compared with 2D positioning, characterizing radiating elements. The real axis represents any (real) 1D direction in the actual 2D source plane. This has been demonstrated using equivalent dipoles to characterize the electromagnetic emissions from a metallic box with an aperture. It was shown that edge dipoles were able to characterize the finiteness of the box.

However, this may result to higher number of dipoles for physically large problems. Optimization techniques were presented as a way of determining the optimal number of dipoles required in equivalent dipole modelling. The particle swarm optimization has been presented in detail and applied to the same problem as in above. A significant reduction (of about 70%) in the number of equivalent dipoles required was achieved using the PSO algorithm. The feature

selective validation (FSV) was demonstrated as an effective way of visually identifying the extent of agreement between data sets for an electromagnetic problem. The PSO was also shown to yield a better performance than the genetic algorithm in optimizing the same problem. The PSO is able to achieve slightly better accuracy than the GA at a reduced run-time.

Finally, the combination of CSP and PSO technique can be said to be a robust and simple way of optimizing the performance of the dipole modelling.

References

1. N. Norris, "Complex point-source representation of real sources and the Gaussian beam summation method," *Journal of the Optical Society of America*, vol. 3, pp. 2005-2010, 1986.
2. K. Tap, P. Pathak, and R. Burkholder, "An exact CSP beam representation for EM wave radiation," in *Electromagnetics in Advanced Applications. International Conference on*, September 2007, pp. 75-78.
3. E. Martini, G. Carli, and S. Maci, "A non redundant complex source expansion derived by using spherical modes," in *Antennas and Propagation Society International Symposium*, 2009, pp. 1-4.
4. A. Toccafondi, S. M. Canta, and D. Erricolo, "Recent Advances in the Incremental Theory of Diffraction for Complex Source Point Illumination," *URSI General Assembly and Scientific Symposium*, 2011, pp. 1-4.
5. Kennedy, J. and Eberhart, R. *Particle Swarm Optimization*, IEEE International Conference on Neural Networks, (Perth, Australia), IEEE Service Center, Piscataway, NJ, IV: 1942-1948, 1995.

6. Bauer, A., Bullnheimer, B., Haiti, R. F. and Strauss, C, 1999, An ant colony optimization approach for the single machine total tardiness problem, *Proc. CEC'99*, IEEE, Piscataway, NJ, pp. 1445-1450.
7. Bonabeau, E., Dorigo, M. and Theraulaz, G., 1999, *Swarm Intelligence: From Natural to Artificial Systems*, Oxford University Press, Oxford.
8. Bullnheimer, B., Hartl, R. F. and Strau, C. A., 1999, New rank based version of the Ant System: a computational study. *Central Eur J. Open Res. Econ.*7:25-38.
9. Blum, C. and D. Merkle :*Swarm Intelligence - Introduction and Application Natural Computing Series*, Springer, 2008.
10. van den Bergh, F. and Engelbrecht, A. P., 2000, Cooperative learning in neural networks using particle swarm optimizers, *S. African Comput. J.* 26:84—90.
11. Conradie, A., Miikkulainen, R., and Aldrich, C, 2002, "Adaptive control utilizing neural swarming, *Proc. Genetic and Evolutionary Computation Conf. (GECCO 2002)*," Morgan Kaufmann, San Mateo, CA, pp. 60-67.
12. Xiao, X., Dow, E. R., Eberhart, R., Ben Miled, Z. and Oppelt, R. J., 2003, "Gene clustering using self-organizing maps and particle swarm optimization," in: *Online Proc. 2nd IEEE Int. Workshop on High Performance Computational Biology (HICOMB 2003)*.
13. Yoshida, H., Kawata, K., Fukuyama, Y, Takayama, S., and Nakanishi, Y, 2000, A particle swarm optimization for reactive power and voltage control considering voltage security assessment, *IEEE Trans. Power Syst.* 15:1232-1239.

14. Veeramachaneni, K., and Osadciw, L., "Adaptive multimodal biometric fusion algorithm using particle swarm," in: Proc. SPIE Aerosense 2003 (Orlando, FL), pp. 211 - 222, 2003.
15. Kennedy, J. and Eberhart, R. G., 1997, "A discrete binary version of the particle swarm algorithm," Proc. 1997 Conf. on Systems, Man, and Cybernetics, Piscataway, NJ: IEEE Service Center, pp. 4104-4109.
16. Ko, P.-G. and Lin, P.-G., 2004, "A hybrid swarm intelligence based mechanism for earning forecast," in: Proc. 2nd Int. Conf. on Information Technology and Applications (ICITA 2004).
17. Hu, X., Eberhart, R. and Shi, Y., 2003, "Swarm intelligence for permutation optimization: a case study on n-queens problem," in: Proc. IEEE Swarm Intelligence Symp. 2003 (Indianapolis, IN).
18. Said Mikki and Ahmed Kishk, "Investigation of the quantum particle swarm optimization technique for electromagnetic applications", Antennas and Propagation Society International Symposium, 2005 IEEE Vol. 2A, pp. 45-48, 3-8 July 2005.
19. V. Rajamani, C.F. Bunting, A. Orlandi and A. Duffy, "Introduction to feature selective validation (FSV) ," IEEE International Symposium Antennas and Propagation, 2006, pp.601-604.
20. A.P.Duffy, A.J.M.Martin, A.Orlandi, G.Antonini, T.M.Benson, and M. S. Woolfson, "Feature selective validation (FSV) for validation of computational electromagnetics (CEM): Part I. The FSV method," IEEE Trans. Electromagn. Compat. , vol. 48, no. 3, pp. 449-459, Aug. 2006.
21. A. J. M. Martin, "Quantitative data validation," Ph.D. dissertation, De Montfort Univ., Leicester, U.K., 1999.

22. A. Orlandi, A. P. Duffy, B. Archambeault, G. Antonini, D. E. Coleby, and S. Connor, "Feature selective validation (FSV) for validation of computational electromagnetics (CEM): Part II. Assessment of FSV performance," *IEEE Trans. Electromagn. Compat.* , vol. 48, no. 3, pp. 460–467, Aug. 2006.
23. A. Orlandi, G. Antonini, C. Polisini, A. Duffy and H. Sasse, "Progress in the development of a 2D Feature Selective Validation (FSV) method," *IEEE International Symposium on EMC*, 2008, pp. 1-6.
24. 1597.1 IEEE Standard for Validation of Computational Electromagnetic Computer Modelling and Simulations, Standards Development Committee, USA, 2009.
25. X. Tong, Simplified Equivalent Modelling of Electromagnetic Emissions from Printed Circuit Boards, PhD Thesis, University of Nottingham, May 2010.
26. Said Mikki and Ahmed Kishk, "Investigation of the quantum particle swarm optimization technique for electromagnetic applications," *Antennas and Propagation Society International Symposium*, 2005 IEEE Vol. 2A, pp. 45-48, 3-8 July 2005.

Chapter 7

Conclusion and Future work

7.1 Conclusion

The aim of this thesis was to develop a simple way of characterizing the electromagnetic emissions from practical electrical and electronic devices. A PCB and also a box with an aperture were used as the main sources of electromagnetic field in this study. In characterising such a practical problem, there is the need to include all the possible sources of emission. These have been addressed in this work. The novelty of this work includes:

-the development of a simplified analytical model based on equivalent dipoles only, that fully characterize a practical PCB taking into consideration the finiteness of such PCBs. In previous work the equivalent dipole approach was only for PCB that could be approximated by modelling on infinite ground plane. With the approach presented in this work, the effects of diffraction were sufficiently approximated without requiring the classical diffraction solutions. This avoids the complicated integrals as seen in the high frequency technique. It is obvious from the discussions that this offers a practical way of approximating the diffraction effects.

-the improvement of the equivalent dipole model through the complex localization of the equivalent dipoles. It was shown that more dipoles will be required in the basic dipole modelling (i.e. 2D positioning of equivalent dipoles) to attain any specific error criterion level, than the number required for the

model with equivalent dipoles positioned in a complex space. This required number of equivalent dipoles was further reduced through PSO algorithm.

The technique presented in this work is based on near field measurements or full wave simulations and equivalent dipole modelling. The equivalent dipoles are determined through direct fitting to the measured near field data. The singular value decomposition was shown to be adequate in solving the ill-conditioned inverse problem.

In Chapter 2, the equivalent dipole modelling was developed from the basic principle of source equivalence. The processes involved in developing the appropriate equivalent dipole modelling for characterising the electromagnetic emissions from a PCB including near field scanning were introduced.

In Chapter 3, a set-up for the planar near field measurement was presented. The 3D near field information required for adequate characterizing of the side emissions from a practical PCB, were collated from the individual planar near field scans on the surrounding surfaces. Two different techniques were presented for extracting the near field magnitude and phase data. Firstly, for the self-powered device, spectrum analyzer is used while for the externally excited device, the vector network analyzer is used. Both techniques showed good correlation with simulated results. These measurements were carried out using near field probes. The exact field at the locations where the near field probes are inserted is related to the output of the probe through the probe performance factor. For the 10mm loop probe used in this work, the probe separation of 10mm was found to be the optimal for the near field measurement. This was necessary so as to minimize the coupling between the loop probe and the DUT being characterized.

In Chapter 4, the principle of equivalent dipole modelling as developed in Chapter 2, was used in characterising PCBs in free space and above the ground plane. The application for this model was demonstrated to be limited to problems with EM sources isolated from the edges of the PCB. Furthermore, it was shown that by combining the basic dipole modelling with a ray-based technique, this limitation can be overcome. However, higher computational resources were required.

In Chapter 5 the basic equivalent dipole modelling was extended to account for the finiteness of a practical PCB without requiring a ray-based technique. This unique approach as presented here is based on dipole only modelling. Passive dipoles which themselves are not active current sources, were used to emulate the behaviours of the wave diffraction at the edges. An accuracy of about 2% r.m.s error was achieved through this approach.

Fundamentally, the accuracy of equivalent dipole modelling is improved by increasing the number of dipoles used in the model. However, in Chapter 6, the complex localization of equivalent sources was presented as a way of achieving better improvement up to 20% without increasing the number of dipoles.

Also in Chapter 6, the particle swarm optimization (PSO) was demonstrated as a technique to further optimize the properties of equivalent dipoles (i.e. dipole positions and moments) required in the model as an alternative to inverse problem. The PSO was shown to have 21% and 52% better performance, in accuracy and run time respectively, than the genetic algorithm for the same problem as presented in the Chapter. The PSO can search the optimal dipoles required for an accurate characterization of a PCB.

7.2 Future Work

Modern electric and electronic equipment are required to perform well in their electromagnetic environment without introducing electromagnetic noise. This is often carried out by their radiated and conducted emissions characterisation from dc to 3GHz. This means performing measurements over thousands of frequency points, the effect of which is measurement time running into several hours.

Time domain EMI measurement systems sample the broad-band EMI signal with GHz sampling rates and compute the EMI spectrum by digital signal processing technique e.g. fast Fourier transform (FFT) [1]. Through this the measurement time is significantly reduced. Early works on time domain measurements are published in [1]-[4].

The spectrum function and time function are related to each other through the Fourier integral analysis.

As has been discussed and presented in Chapter 1 and Chapter 2 for the frequency domain measurements, the time domain measurements also finds its applications in conducted and radiated EMI measurements using current clamps and broadband antennas respectively.

Therefore replicating this model presented in this thesis in time domain will serve as a useful tool for the EMC and system design engineers in understanding the noisy behaviour of various PCB circuits. The expressions given in [5] and [6] relate the equivalent sources to the fields observed at any given point. The magnetic field at a distance r of a vertical polarized source is expressed as

$$H_x(t) = \frac{-1}{4\pi} \left(\frac{y}{r^3} I \left(t - \frac{r}{c} \right) + \frac{y}{cr^2} \frac{\partial I \left(t - \frac{r}{c} \right)}{\partial \left(t - \frac{r}{c} \right)} \right) \quad (7.1)$$

$$H_y(t) = \frac{-1}{4\pi} \left(\frac{x}{r^3} I \left(t - \frac{r}{c} \right) + \frac{x}{cr^2} \frac{\partial I \left(t - \frac{r}{c} \right)}{\partial \left(t - \frac{r}{c} \right)} \right) \quad (7.2)$$

$$H_z(t) = 0 \quad (7.3)$$

Therefore, from the knowledge of the actual field at any point, where $\left(t - \frac{r}{c} \right)$ is the retarded time, measured or simulated using a time domain solver, the equivalent dipoles required for the model can then be determined from the solution to the inverse problem (7.1) - (7.3). This time domain equivalent dipole model will then be used in the future for characterizing transients, impulsive signals and high rise times often observed in PCBs with high clock speeds.

Also stochastic approach has been presented in [7]-[9] as an alternative to the often measurement based deterministic approach. The former requires minimal amount of measurements in characterizing radiating structures.

This approach although is more complex than frequency domain approaches, is necessary for complex mixed signal devices with many uncorrelated sources.

References

1. P. Russer, "EMC measurements in the time-domain," in General Assembly and Scientific Symposium, 2011 XXXth URSI IEEE, Aug. 2011, pp. 1-35.
2. E. L. Bronaugh, "An Advanced Electromagnetic Interference Meter for the Twenty-First Century," in 8th International Zurich Symposium On Electromagnetic Compatibility, Zurich, Switzerland, 1989, 1989, pp. 215-219, no. 42H5.

3. E. L. Bronaugh and J. D. M. Osburn, "New Ideas in EMC Instrumentation and Measurement," in 10th International Zurich Symposium On Electromagnetic Compatibility, Zurich, Switzerland, 1993, 1993, pp. 323–326, no. 58J1.
4. A. Schütte and H. Kärner, "Comparison of time domain and frequency domain electromagnetic compatibility testing," in Proceedings of the 1994 IEEE International Symposium on Electromagnetic Compatibility, Aug. 22th–26th, 1994, pp. 64–67.
5. E.T Pereira, D. W. P Thomas, A. F Howe and C Christopoulos, "Computation of Electromagnetic Switching Transients in a Substation," Int. Conf. on Comp. Electromagn., pp. 331-334, London, Nov 1991.
6. M. A Uman, D. K McCain and E. P. Krider, "The Electromagnetic radiation from a finite antenna," *Am. J. Phys*, vol. 43, pp. 33-38, Jan. 1975.
7. L. R. Arnaut and C. S. Obiekezie, "UWB radiation modes of printed circuit boards based on principal component analysis," Proc. 2013 ICEAA Int. Conf. Electromagnetic Adv. Applic, Torino, Italy, Sep. 2013.
8. L. R. Arnaut and C. S. Obiekezie, "Stochastic analysis of wideband near-field emissions from integrated antennas and circuits," *IEEE Trans. On Electromagn.*, vol. 54, nos. 1, pp. 93-101, 2014.
9. L. R. Arnaut, C. S. Obiekezie and D.W.P. Thomas, "Empirical Emission Eigenmodes of Printed Circuit Boards," *IEEE Trans. On Electromagn.*, vol. pp, nos. 99, pp. 1-11, 2013.

Appendix. A

System Automation

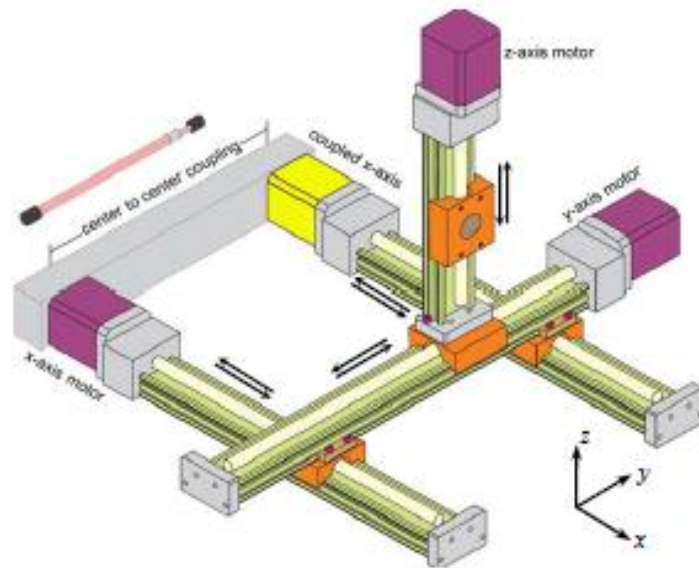
A.1 3-D Positioner

The physical structure for the near-field test bench comprises the robotic arms, stepper motors, stepper drives and power module. These were purchased and assembled *in the George Green Institute* for Electromagnetic Research (GGIEMR). Table A. 1 provides more details on these subsystems.

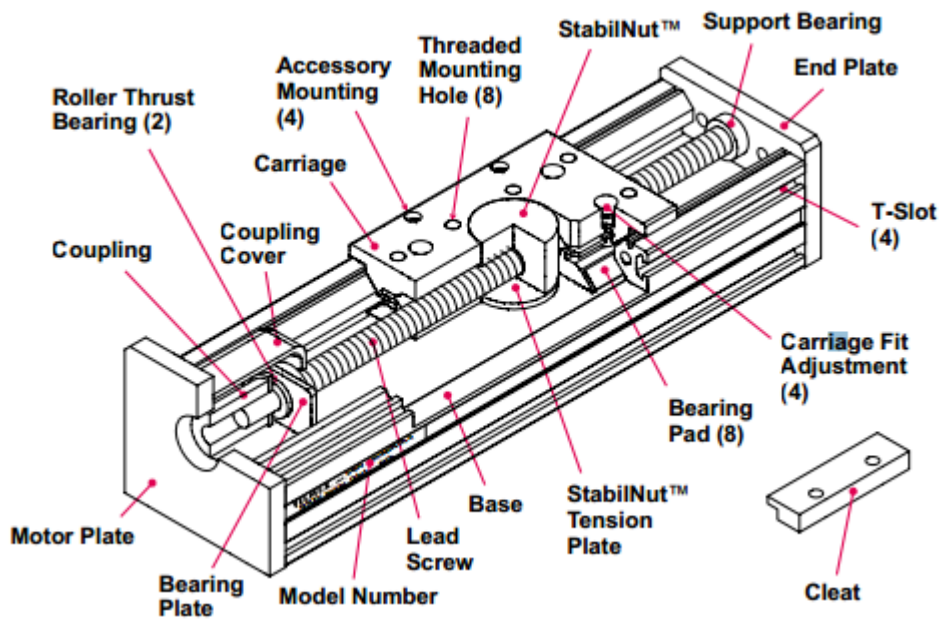
Table A. 1 Near-field test bench subsystem

Subsystem	Vendor	Model (Quantity)
Robotic arms	Velmex	Motorized Bislide (4)
Programmable stepper motors	Parker Hannifin	SY872 (1) SY563(2)
Stepper drive	Parker Hannifin	ViX500 (3)
Power supply unit	LG motion	PSU1 (1)

One of the key advantages of this assembling is its scalability and upgradability. Doing the cause of carrying out the studies for this work, the vertical arm was upgraded to a longer slide. The intention of this was to increase the degree of freedom along the z-axis likewise isolating the measurement domain from the metallic slides. Through the adjustment the scanning domain was doubled in size providing more isolation for the near field measurement. The mechanical details are provided in Fig. A. 1.



(a) Mechanical details for the Velmex slide



(b) Lead connectors on the Velmex slide

Fig. A. 1 Velmex slide

The performance of the positioning system can be affected by the Load capacity and motor torque. The maximum speed for a good performance tend to reduce with increase in load. This is shown in Fig. A. 2. Exceeding this load limits will result in rapid lead screw and nut wear [3].

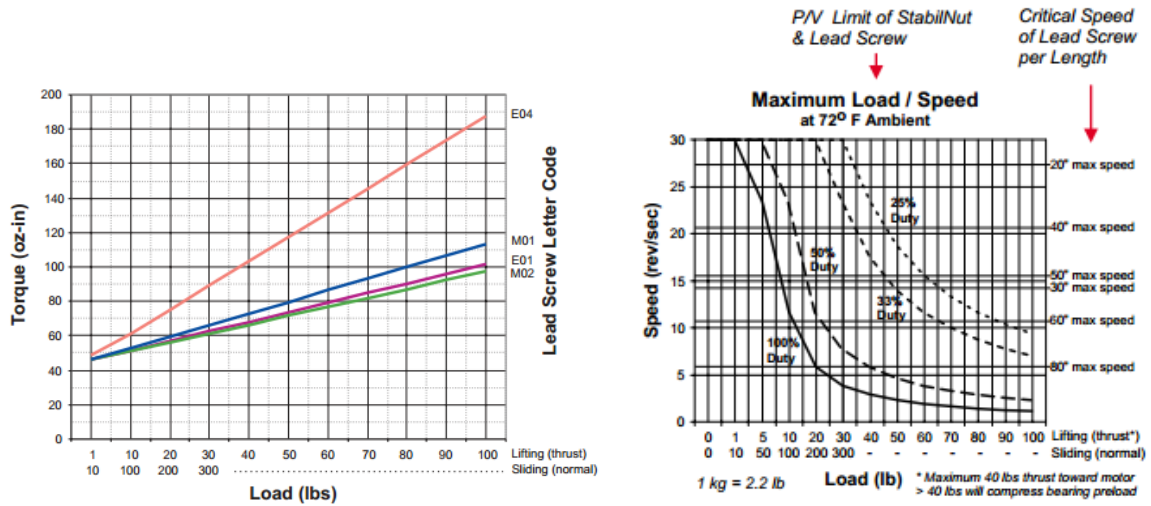


Fig. A. 2 Effect of load on (a) torque (b) speed

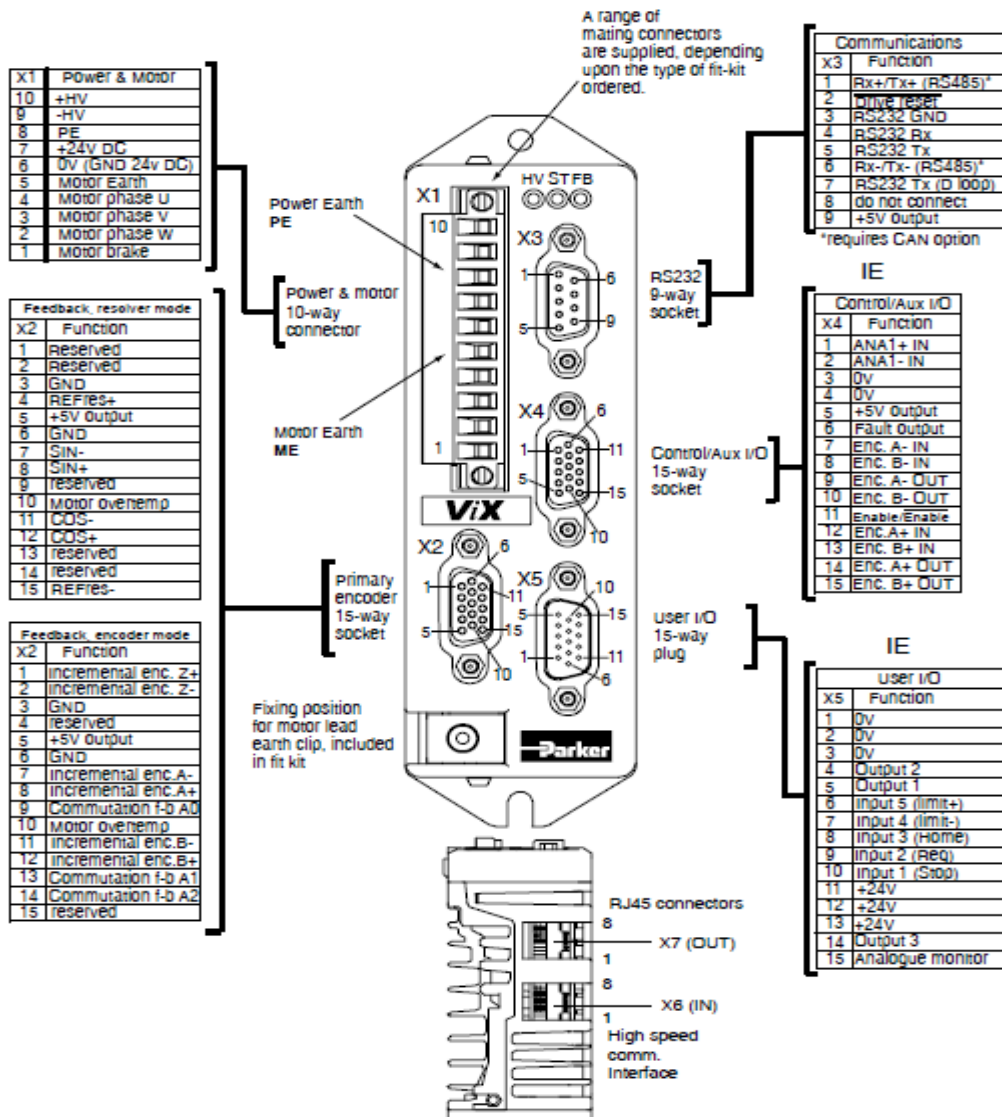


Fig. A. 3 ViX stepper drive Connector Pin Layout [1]

A.2 Programming

Labview is a graphical programming tool used for the motion control and the data-aquisitions in this work. The basic labview functions are shown in Fig. A. 4.

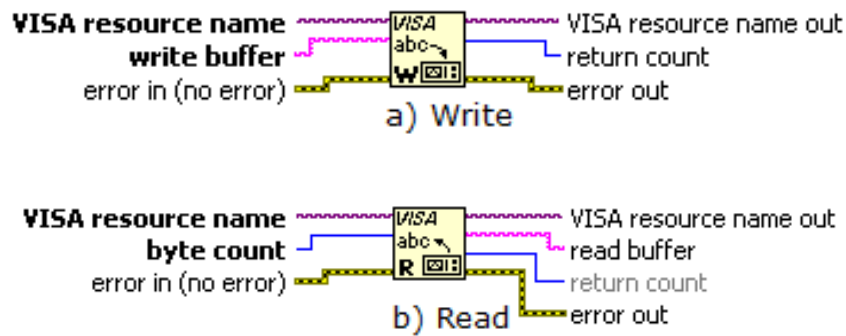


Fig. A. 4 Labview basic control function

The write (and read) command(s) are used in instructing (and reading the response from) the object. The details of their interface functionalities are shown in Table A. 2.

Table A. 2 Write and Read Interface functionality

Objects	Functionality
VISA resource	Instrument interface
Write buffer	Writing to the instrument
Read buffer	Contains the data read from the instrument
Error in	Describes error conditions that occur before the node
Error out	Contains error information
Byte count	The number of bytes to be read
Return count	Contains the actual number of bytes written

The use of labview functions in a simple instrument control program via a serial port is shown in Fig. A. 5.

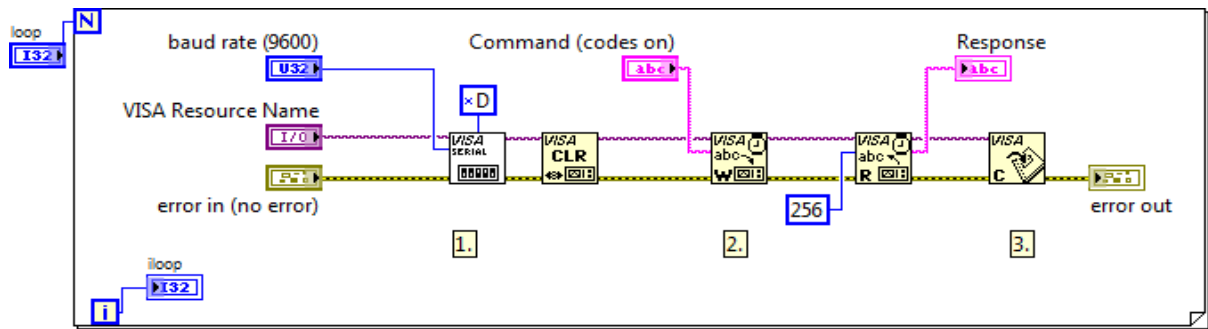


Fig. A. 5 Labview instrument control via serial port

The first stage opens and configures the instrument interface. In our example it is a serial port with basic configuration as shown in Table A. 3.

Table A. 3 Serial Port Configuration

Configuration	Value
Baud rate	9600
Data bits	8
Parity	None
Stop bits	1
Flow control	None
Time out	10000
Termination character	\r

The clear function is used to free up the interface making it available for use by newer programs. The write and read command as already mentioned earlier is used to write to the instrument and read from the instrument respectively.

Then this interface is closed using the close function. By doing this, the resource is made available for other programs to access. This is highly recommended for labview programming best practice [1].

A.3 Motion Control

The program for controlling the 3-D positioner follows similar sequence with the example given above in Fig. A. 6. The stepper drive VIX500IM, from Parker Hannifin, is used to control the motors for the three axes [2]. Customized machine language is used to communicate with this stepper drive as shown in Table A. 4.

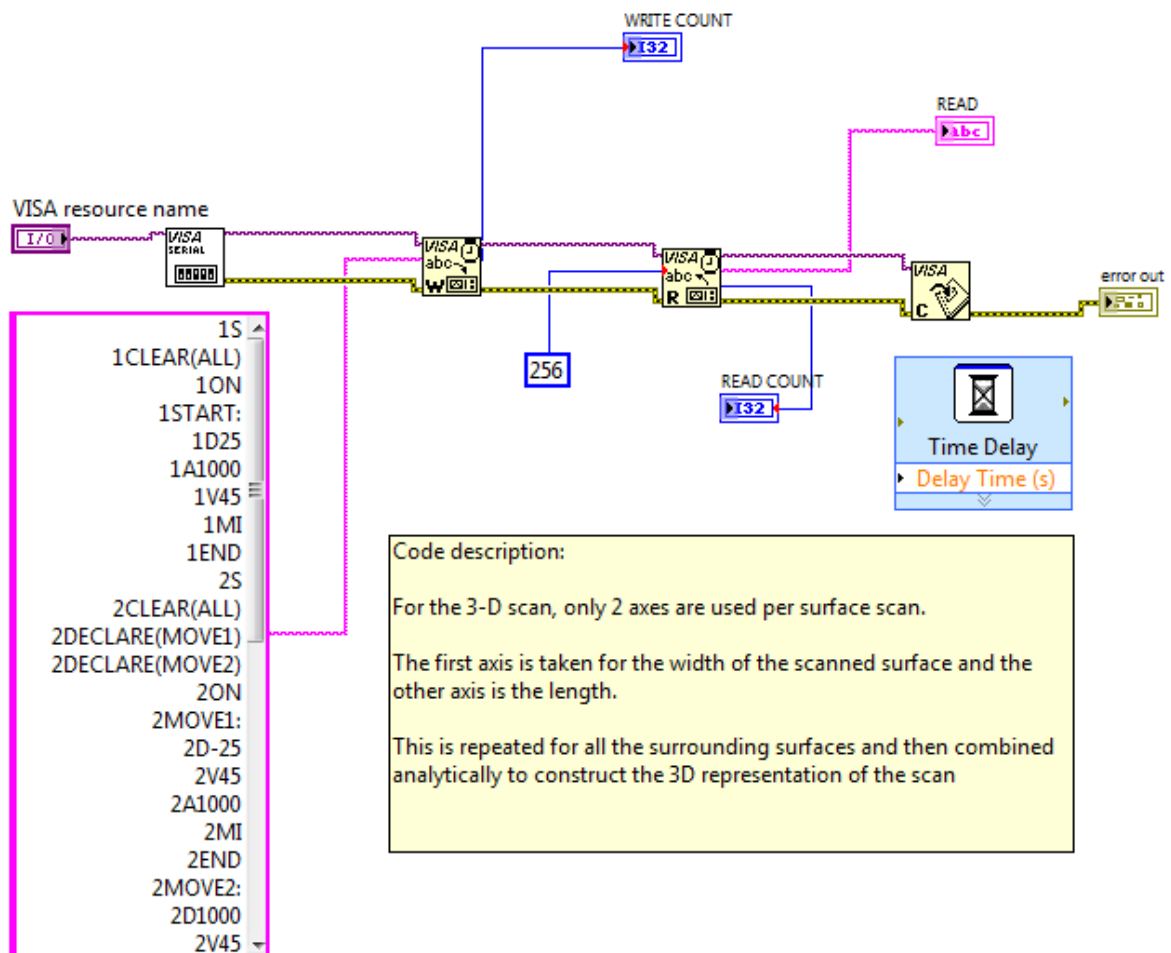


Fig. A. 6 Labview initialization code for motion control

Table A. 4 Command syntax for VIX500IM stepper drive

Command syntax	Interpretation
1ON	On axis 1
1A25	Set axis 1 acceleration to 25 revolutions/s ²
1V25	Set the velocity to 25 revolutions/s
1D250000	Set the distance to 250000 equivalent to 10mm
1MI	Set to incremental movement mode
1G	Make a move by the above configurations
1S	Stop axis 1
1OFF	Turn off axis 1

These commands are sent to the drive through the write function on labview on software level and through an RS232 serial cable on hardware level. The receipt axis for each command precedes each of the command syntax. The commands for axis 1 has been demonstrated in Table A.3 above.

A.2.1 Data Acquisition

Data acquisition is an automated way of triggering measurements from instruments like Network analyzer. The NI GPIB-USB interface was used to connect the pc physically to the network analyzer. The model in use is Agilent PNA E8362B. The program is on Standard Command for Programmable Instrument (SCPI) [3] or IEEE 488.2. This program is used to instruct the PNA on the following:

- what type of measurement and when to take a measurement
- the location to save the measured data
- the data type and format

Appendix A

Fig. A. 7 shows the program used to control the measurement readings from the network analyzer. This program contains other sub-programs that configures the measurement type and formats the measured data.

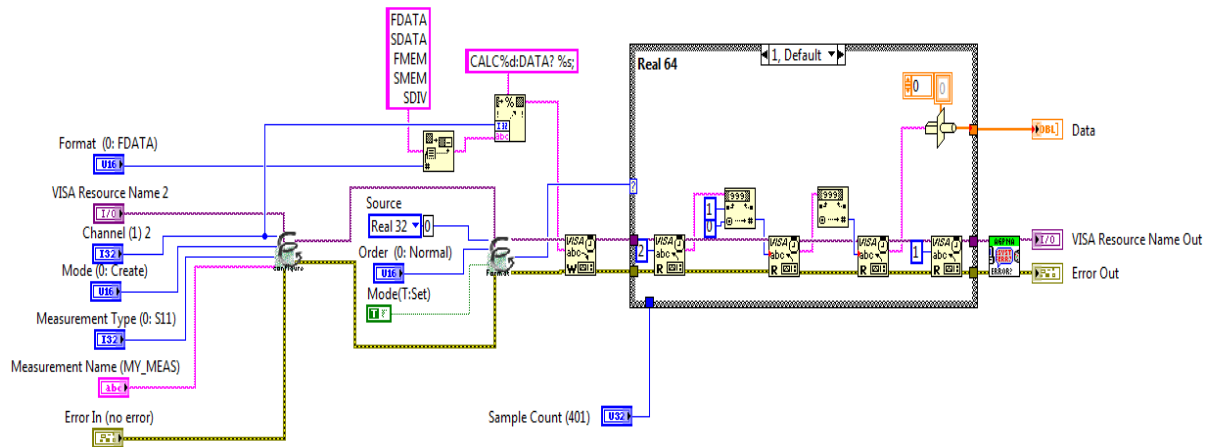


Fig. A. 7 Labview program to take reading using network analyzer PNA E8362b

The labview program for configuring the type of measurement and setting up a specific measurement format is shown in Fig. A. 8. The possible types of measurements include the four s-parameters for the 2-port network analyzer and the data format can be either ASCII, REAL32 or REAL64 [4].

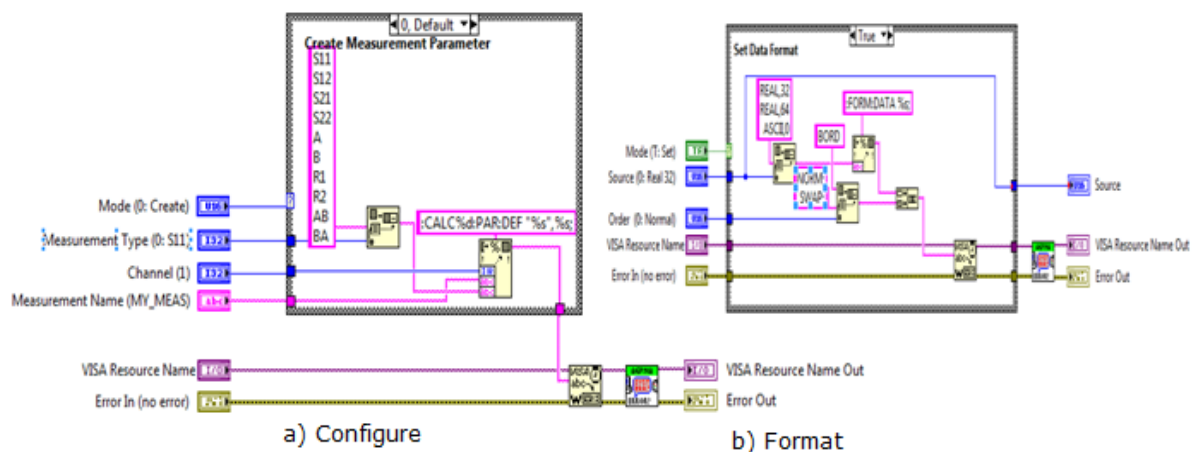


Fig. A. 8 Labview program for configuring and formatting the measurement parameters

The Table A. 5 shows some of the relevant programs used and are presented in the following manner:

- Delete the previous measurements created if required
- Create a new measurement
- Select the required measurement.

Table A. 5 SCPI command for controlling VNA E8362B

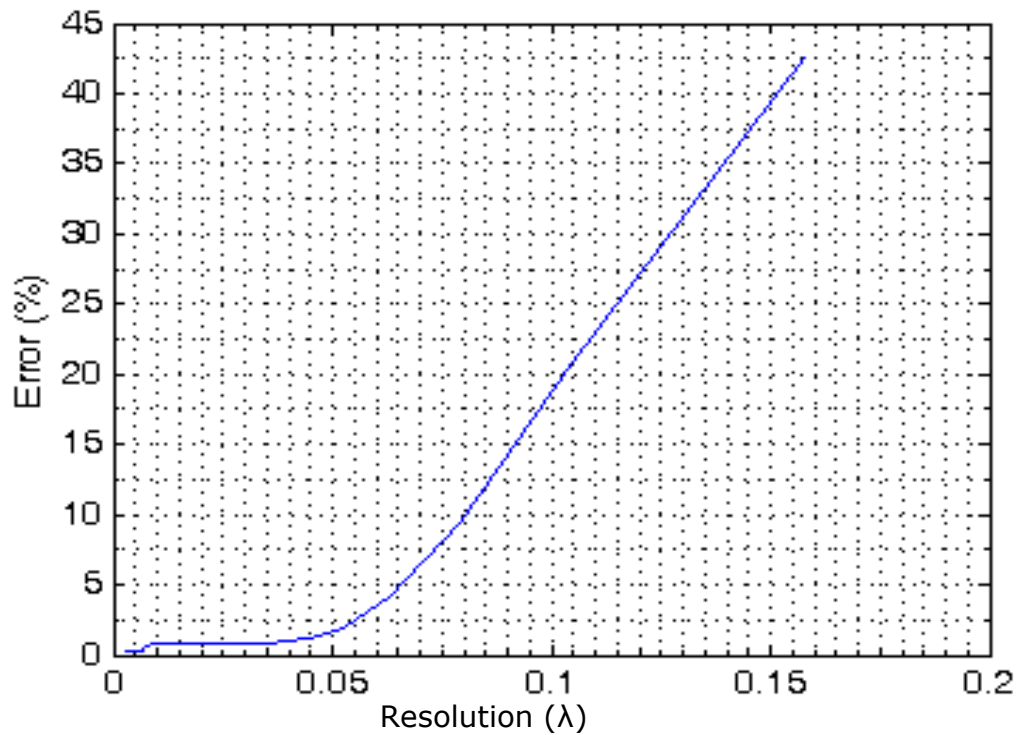
Functions	Command syntax	example
Delete a specific old measurements	CALCulate<cnum>:PARAmeter:DELeTe[:NAME] <Mname>	CALCulate1:PARAmeter:DELeTe:Scan1,s11
Delete all old measurements	CALCulate:PARAmeter:DELeTe:ALL	
Create a new measurement	CALCulate<cnum>:PARAmeter:DEFine <Mname>,<param>[,port]	CALCulate1:PARAmeter:DEFine Scan2,s21
Select the required measurement	CALC<cnum>:PAR:SEL <mname>	CALC1:PAR:SEL scan2
To read or write measurement data	CALCulate<cnum>:DATA <char>,<data>	CALCulate1:DATA FDATA,<data>
To format measured data	FORMat[:DATA] <char>	FORMat:DATA real 64
To set the display of the preferred measurement	CALCulate<cnum>:FORMat <char>	CALCulate1:FORMat POLar

Reference

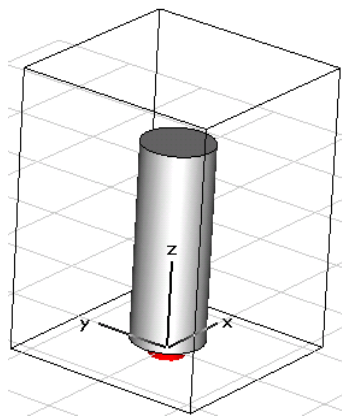
1. *ViX 250/500IM Stepper Drivers User Guide*, Parker Hannifin Eletromechnical Division Europe, Offenburg, Germany, 2004.
2. A.1. P.A. Blume, *Labview style book*, 1st Edition, New Jersey: Prentice hall, March 2007.
3. Velmex Inc, BiSlides Assembly, [Online], 2013, <http://www.velmex.com/pdf/bislides-pdf/users-guide-bislides.pdf>.
4. Agilent Technologies, *PNA Series Network Analyzer*, December 2007.

Appendix B

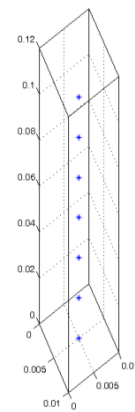
Equivalent dipole modelling accuracy dependence on dipole resolution



(a)



(b) Simulated monopole antenna



(c) Dipole positions for equivalent dipole modelling

Fig. B.1. Error as a function of number of dipoles used (defined as dipole resolution given as proportion of wavelength, λ at 900MHz).

References

1. C. Obiekezie, D. W. P Thomas, A. Nothofer, S. Greedy and P. Sewell, "Electromagnetic Characterisation of 3D Radiators, " EuroEM 2012 Conf. accepted for publication, April 2012.

Appendix C

Infinitesimal dipole radiation with distance

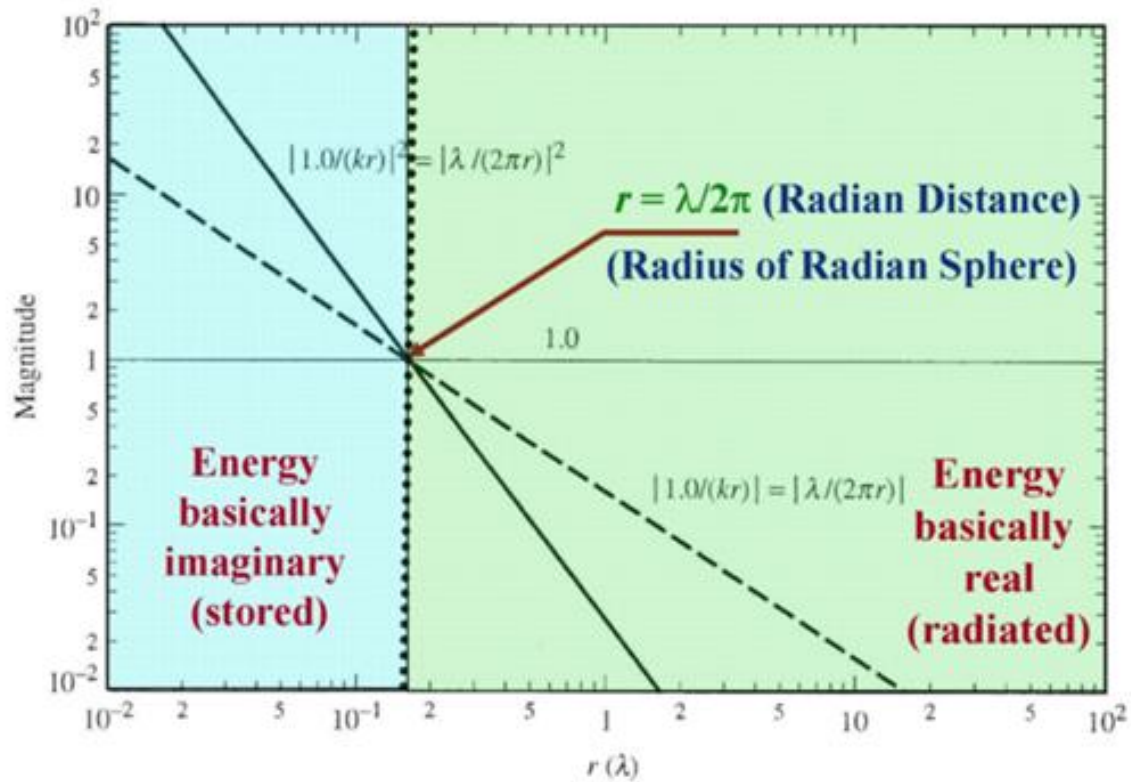


Fig. C.1 Magnitude variation, as a function of radial distance, of the field terms radiated by an infinitesimal dipole [1].

Reference

1. C. A. Balanis, *Antenna Theory Analysis and Design*, John Wiley and Sons, New York, 2005, 3rd ed.

Appendix D

Basic 1-D FSV formulation [1]

1. Fourier transform the original data sets
2. Take the DC term and the first four points either side and low and high pass filter the remaining data in the transformed domain. Inverse transform these into low (Lo) and high (Hi) pass data in the original domain for both data sets to be compared.
3. The ADM is calculated for each of the data point in the data set using

$$ADM(n) = \left| \frac{\alpha}{\beta} \right| + \left| \frac{\gamma}{\delta} \right| \exp\left(\left| \frac{\gamma}{\delta} \right|\right) \quad (D.1)$$

where

$$\alpha = (|Lo_1(n)| - |Lo_2(n)|)$$

$$\beta = \frac{1}{N} \sum_{i=1}^N (|Lo_1(i)| - |Lo_2(i)|)$$

$$\gamma = (|DC_1(n)| - |DC_2(n)|)$$

$$\delta = \frac{1}{N} \sum_{i=1}^N (|DC_1(i)| - |DC_2(i)|)$$

n is an n th data point and the subscripts 1 and 2 represents the data sets being compared for a total of N data points. The mean value ADM which gives a single-figure measure of the goodness-of-fit can then be calculated from

$$ADM = \frac{\sum_{n=1}^N ADM(n)}{N}$$

4. Create a Feature Difference Measure (FDM) from the normalised difference of a combination of derivatives of the low and high pass data.

$$FDM_1(n) = \frac{|Lo_1'(n)| - |Lo_2'(n)|}{\frac{2}{N} \sum_{i=1}^N (|Lo_1'(i)| + |Lo_2'(i)|)} \quad (D.2)$$

$$FDM_2(n) = \frac{|Hi'_1(n)| - |Hi'_2(n)|}{\frac{6}{N} \sum_{i=1}^N (|Hi'_1(i)| + |Hi'_2(i)|)} \quad (D.3)$$

$$FDM_3(n) = \frac{|Hi''_1(n)| - |Hi''_2(n)|}{\frac{7.2}{N} \sum_{i=1}^N (|Hi''_1(i)| + |Hi''_2(i)|)} \quad (D.4)$$

$$FDM(N) = 2(FDM_1(n) + FDM_2(n) + FDM_3(n)) \quad (D.5)$$

5. Combine the ADM and FDM to obtain the GDM through

$$GDM(n) = \sqrt{(ADM(n))^2 + (FDM(n))^2}$$

6. Obtain confidence histograms

Reference

1. A. Orlandi, G. Antonini, C. Polisini, A. Duffy and H. Sasse, "Progress in the development of a 2D Feature Selective Validation (FSV) method," IEEE International Symposium on EMC, 2008, pp. 1-6.